Development and Characterisation of Graphene-Based Composite Coating on Metal Substrate for Tribological Applications

By

Yingdi Feng



UNIVERSITY OF BIRMINGHAM

A thesis submitted to the University of Birmingham

for the degree of

DOCTOR OF PHILOSOPHY

School of Metallurgy and Materials

College of Engineering and Physical Sciences

University of Birmingham

2025

UNIVERSITY OF
BIRMINGHAM

University of Birmingham Research Archive

e-theses repository

This unpublished thesis/dissertation is copyright of the author and/or third parties. The intellectual property rights of the author or third parties in respect of this work are as defined by The Copyright Designs and Patents Act 1988 or as modified by any successor legislation.

Any use made of information contained in this thesis/dissertation must be in accordance with that legislation and must be properly acknowledged. Further distribution or reproduction in any format is prohibited without the permission of the copyright holder.

Synopsis

Nano-scale experimental and theoretical studies have shown the excellent tribological and corrosion-resistant properties of graphene. As interest in using these unique properties grows, there is an ever-increasing demand for producing thick and large area graphene-based coatings with strong bonding to the substrate and high load bearing capacity for real industrial applications. However, there has been limited research on metal-based graphene-reinforced composites in surface engineering. This study was focused on using electro-brush plating (EBP) technique to create cost-effective and scalable Cu-based composite coatings on metallic substrates, with relatively inexpensive graphene oxide (GO) as the reinforcement.

In this research, graphene oxide (GO) was utilised as the coating precursor, with the EBP method employed to apply the GO/Cu composites coatings on 316 stainless steel and brass substrates. Comprehensive processing studies and systematic characterisation of the coatings were conducted to explore the optimal EBP parameters and to demonstrate the feasibility of producing dense, uniform, and strongly bonded GO/Cu composite coatings using the advanced EBP technology.

Low friction and high wear resistance are essential properties for sliding bearings. In this research, advanced GO/Cu nanocomposite coatings were developed using the brush plating method to enhance the tribological performance of brass-based materials for sliding bearing application. To this end, a series of brush plating experiments were conducted under varying voltages and GO concentrations. The tribological behaviour of the GO/Cu composite coatings was evaluated using dry ball-on-plane tribological tests. The experimental results demonstrated

that GO was successfully incorporated throughout the composite coating layer. The GO/Cu composite coatings significantly reduced friction and increased wear resistance of brass by two orders of magnitude, primarily due to the self-lubricating properties of the GO within the coatings. The experimental results have also shown that the GO-Cu composite coating can also enhance the electrochemical corrosion properties. It is thus anticipated that the novel GO/Cu coatings developed from this research could also have good corrosion-wear properties.

The development of novel self-lubricating and corrosion-resistant coatings great potential for sliding bearing and other tribological applications. The systematic investigation into the underlying mechanisms by which graphene oxide (GO) is effectively incorporated into copper coatings and improvements in tribological performance and enhanced corrosion resistance have also advanced scientific understanding.

Acknowledgements

I would like to start by expressing my grateful to my supervisors, Prof. Hanshan Dong and Dr. Xiaoying Li, for their consistent support and invaluable contributions throughout this study. Their insights and guidance during our frequent and meaningful discussions were essential in shaping and advancing this project. I am also particularly thankful to both of them for their significant assistance during the application process of this PhD degree.

I must express my deep appreciation to everyone at the Doctoral Training Centre for Innovative Metal Processing (IMPaCT) for their support. I am also grateful for the generous financial support provided by the Engineering and Physical Sciences Research Council (EPSRC; EP/F006926/1), which has greatly contributed to both my research and personal life.

I would also like to express my gratitude to the Surface Engineering Research Group, including Dr. Shaojun Qi, Dr. Behnam Dashtbozorg, Mr. Yepeng Yang, Dr. James Alexander, Dr. Yana Liang, Dr. Zhiyuan Jing, Dr. Chang Che, Dr. Mikdat Gurtaran, Miss Xueqi Zhu, and Miss Diandian Wu, for their invaluable support. Additionally, I extend my appreciation to the staff of Metallurgy and Materials, including Dr. Daniel Reed and Miss Amy Newell, for their sincere help with Raman spectroscopy and XRD, as well as to Mr. Ludwig Schneider, Mr. Paul Stanley, and Mrs. Theresa Morris for their assistance with SEM.

I would like to thank our International Student Team (IST) for their warm and invaluable support throughout my studies, especially during the challenges of the COVID-19 pandemic.

Finally, I would like to express my love and gratitude to my parents and grandparents for their unwavering support and encouragement. I also wish to acknowledge my late grandfather, whose

love and guidance continue to inspire me from a special place. And I want to thank my precious friends, especially Mrs. Qi Tang our friendship last for over 16 years which is more than half of my life, you aways cheers me up when I felt down.

Finally, I would like to express my love and gratitude to my parents and grandparents for their unwavering support and encouragement. I also wish to acknowledge my late grandfather, whose love and guidance continue to inspire me from a special place. Additionally, I want to thank my cherished friends, especially Mrs. Qi Tang. Our friendship, spanning over 16 years, more than half of my life, has been a constant source of strength.

Publication

- Y. Feng, X. Li, H. Dong, The Development of Novel Cu/GO Nano-Composite Coatings by Brush Plating with High Wear Resistance for Potential Brass Sliding Bearing Application, Materials 17 (2024) 2623. https://doi.org/10.3390/ma17112623.

Contributions of authors to this paper: Conceptualisation, Hanshan Dong (H.D.) and Xiaoying Li (X.L.); methodology, Yingdi Feng (Y.F.); validation, Y.F. and X.L.; formal analysis, Y.F.; investigation, Y.F.; resources, H.D.; data curation, Y.F.; writing—original draft preparation, Y.F.; writing—review and editing, Y. F. and X. L.; visualisation, Y. F. and X.L.; supervision, X.L. and H. D.

Text and figures from this paper has been incorporated directly into the following sections:

1 Introduction

3.3 Production of Composite Coating

3.5.2 Tribological tests

4.3.1 Brass substrate GO/Cu composite coating system

4.3.2 Surface Morphology of Copper Control Group on Brass Substrate

4.3.6 Roughness Comparison between Cu and GO/Cu Sample Coating Surface

5.2.2 The Improvement of Wear

5.2.3 Optimal Brush Plating Conditions for Wear Resistant Coating

List of Contents

Chapter 1 Introduction 1
Chapter 2 Literature Review 5
2.1 The History of Graphene Research 5
2.2 The Structure and Basic Properties of Graphene 7
2.2.1 The Formation of Graphene Structure 7
2.2.2 Mechanical Properties 10
2.2.3 Electronic Properties 12
2.2.4 Chemical Properties 14
2.2.5 Derivatives of Graphene and Their Properties 16
2.3 Substrate Materials 18
2.3.1 Stainless Steel 18
2.3.2 Copper and Its Alloys for Bearings 21
2.4 Techniques for Producing Graphene Based Coatings 23
2.4.1 Chemical Vapour Deposition (CVD) 23
2.4.2 Electrophoretic Deposition (EPD) 26
2.4.3 Electro Brush Plating (EBP) 30
2.4.4 GO Reduction Techniques 33
2.4.5 Reduction of Graphene Oxide 33
2.5 Graphene-related Materials for Surface Protection 37
2.5.1 Tribological Applications of Graphene 37
2.5.2 Impermeability and Corrosion Barrier 43
2.6 Summary of Literature Review 43
Chapter 3 Experimental 45
3.1 Substrate Materials 45
3.2 Graphene Oxide Material 46
3.3 Production of Composite Coating 49
3.4 General Characterisation 53

3.4.1 Raman Spectroscopy 53
3.4.2 X-ray Diffraction (XRD) 54
3.4.3 Fourier Transform Infrared (FTIR) Spectroscopy 56
3.4.4 Surface Roughness Measurement 56
3.4.5 Scanning Electron Spectroscopy (SEM) 56
3.4.6 Energy Dispersive X-ray Spectroscopy (EDX) 57
3.4.7 Glow Discharge Optical Emission Spectroscopy (GDOES) 58
3.5 Mechanical and Tribological Property Assessments 58
3.5.1 Micro-hardness 58
3.5.2 Tribological tests 59
3.6 Corrosion Property Evaluation 60
3.6.1 Preparation of Samples and Equipment 60
3.6.2 Preformation of Open Circuit Potential (OCP) 61
3.6.3 Potentiodynamic Polarisation Test 62
3.7 Summary of Experimental 62
Chapter 4 Results 64
4.1 Raw Materials 64
4.1.1 Graphene Oxide Produced 64
4.2 GO/Cu Coatings on Stainless Steel 316 Substrate 69
4.2.1 Influence of GO and Plating Voltages on GO/Cu Coatings 69
4.2.2 Cross-sectional Layer Structure for Cu6 and GO/Cu Sample Coatings 73
4.2.3 Composition Depth Profile of GO/Cu Sample 78
4.2.4 Raman Results on GO/Cu Composite Coatings 81
4.2.5 Comparison of Surface Layer Phase Compositions 83
4.2.6 Surface Micro-hardness 85
4.3 GO/Cu Coatings on Brass Substrate: Material Characteristics 87
4.3.1 Brass Substrate GO/Cu Composite Coating System 87
4.3.2 Surface Morphology of Copper Control Group on Brass Substrate 88
4.3.3 Surface Morphology of GO/Cu Composite Coating with 0.2 g/L of GO 91
4.3.4 Graphene Oxides at Surface Morphology under SEM and EDX 94
4.3.5 Surface Morphology of GO/Cu4 and GO/Cu5 Samples 96
4.3.6 Roughness Comparison between Cu and GO/Cu Samples Coating Surfaces 99
4.3.7 Cross-sectional View SEM Images of Pure Cu Control Group 102

4.3.8 Cross-sectional SEM Images of GO/Cu Composite Coating (0.2 g/L GO) .. 104
4.3.9 Cross-sectional View of GO/Cu4-5 Samples with 0.4, 0.6 and 0.8 g/L GO . 107
4.3.10 Microhardness Comparing with Sample with and without GO Addition 110
4.3.11 Raman Spectroscopy to Reveal GO on Outmost Coating Region 113
4.3.12 X-ray Diffraction (XRD) Comparisons on Different Coatings 115
4.3.13 GDOES Results of Carbon Concentration 120
4.4 Tribological Properties 122
4.4.1 Tribological Comparison of Pure Cu and GO/Cu-Brass Samples..... 122
4.4.2 Comparison of the GO/Cu Samples under Different GO Concentrations..... 143
4.5 Electrochemical Corrosion Properties 159
4.5.1 Potentiodynamic Polarisation of GO/Cu and Brass at Varying GO 159
4.5.2 The SEM and Elements Analysis on Corroded Sample Surface 164
4.6 Summary of Results 174
Chapter 5 Discussion..... 175
5.1 Incorporation of Graphene Oxide into Copper Based Coating 175
5.1.1 Comparison of GO Incorporation Mechanisms in Bath and Brush Plating .. 175
5.1.2 Successfully GO Introduction into Cu Coating on 316 Stainless Steel..... 178
5.1.3 The Influence of Graphene Oxide Concentration..... 180
5.2 Improved Tribological Properties..... 183
5.2.1 The GO Impact on Friction Coefficient 184
5.2.2 The Improvement of Wear..... 185
5.2.3 Optimal Brush Plating Conditions for Wear Resistant Coatings..... 189
5.2.4 Wear Mechanisms..... 190
5.3 Corrosion Protection..... 193
5.3.1 GO concentrations Impact on Corrosion Behaviour 193
5.3.2 Influence of Brush Plating Voltage on Corrosion..... 196
5.3.3 Corrosion Mechanisms for GO/Cu Composite Coating..... 199
5.4 Summary of Discussion..... 201
Chapter 6 Conclusions and Future Work 202
6.1 Conclusions 202
6.2 Proposed Future Work 205
Reference 207

List of Figures

Figure 2.1.1 Two versions of theorical stimulation of graphene: (a) the model with long range order and (b) the improved model [24].

Figure 2.1.2 Various carbon allotropes derived from graphene honeycomb structure [36].

Figure 2.2.1 Schematic of carbon structure: (a) energy level of carbon outer electrons in normal state; (b) exited state of carbon electron energy level; (c) sp2 hybrids formation; (d) graphene lattice showing A and B belong to different sublattice; (e) showing the sp2 hybridisation from the bonding [39].

Figure 2.2.2 (a) Schematic of graphene edge orientation [38] and (b) Scanning Tunnelling Microscopy (STM) image of graphene the blue arrow denoted as armchair and yellow is zigzag orientation [43].

Figure 2.2.3 An art work of inspiring from the stiffness of graphene, it could not be torn even four elephants dragged at the corners with defect which is remained the strongest material [49].

Figure 2.2.4 Schematic of nanoindentation test applied on defective graphene atomic force microscopy (AFM) [54].

Figure 2.2.5 Brillouin zone of graphene and denoted symmetry points [38].

Figure 2.2.6 Schematics of graphene functionalisation [78].

Figure 2.2.7 The process of converting graphene to graphene oxide (GO) and then to reduced graphene oxide (rGO). [91].

Figure 2.2.8 Spectrum of an exampled FTIR result for single layer of graphene oxide [13].

Figure 2.3.1 The stainless-steel family showing with their compositions and related properties [101].

Figure 2.4.1 Schematic of microwave plasma CVD fabricating large-scale graphene films [119].

Figure 2.4.2 Procedures of wet CVD transferring using polymethyl methacrylate (PMMA) [121].

Figure 2.4.3 The schematic of formation of electric double layer from negatively charged particle in a suspension [135].

Figure 2.4.4 Schematic of electronic brush plating (EPB) [148].

Figure 2.4.5 Fabrication of rGO composite with only one-step of electrochemical reaction [188].

Figure 2.5.1 Schematic of nano-scale friction test under AFM Si tip [196].

Figure 2.5.2 The friction coefficient change under different loads and graphene fractions in GO/Al composite materials [214].

Figure 3.2.1 Images taken during reactions: (a) stage 1 of oxidation reaction; (b) stage 2 of oxidation reaction; (c) stage 3 of oxidation reaction; (d) after removed retained $KMnO_4$.

Figure 3.3.1 Image of electro-brush plating equipment.

Figure 3.3.2 (a) 3D design model for the working table holding stainless steel specimens and (b) working picture.

Figure 3.4.1 Photo of the Raman spectroscopy used for graphene oxide and copper oxides measurement.

Figure 3.4.2 Photo of the Proto AXRD diffractometer utilised for pure Cu control group and GO/Cu composite coating surface.

Figure 3.6.1 Electrochemical working station configuration.

Figure 4.1.1 SEM image of graphene oxide produced by Hummer's method on silicon carbide (SiC) wafer.

Figure 4.1.2 Raman spectrum of graphite powder and graphene oxide flakes.

Figure 4.1.3 Raman spectrum and its fitted curves for graphene oxide flakes.

Figure 4.1.4 Comparison on FTIR spectra for graphite and graphene oxide.

Figure 4.2.1 Pictures of post brush plating surface for (a) the Cu6 specimen and (b) the GO/Cu4-0.2, GO/Cu6-0.2 and GO/Cu8-0.2 specimens.

Figure 4.2.2 Surface morphology on GO/Cu plated samples: (a) Cu-6; (b) GO/Cu4-0.2; (c)

GO/Cu6-0.2; (d) GO/Cu8-0.2; (e) higher magnification of Cu6 sample and (f) GO discovered under higher magnification for GO/Cu4-0.2.

Figure 4.2.3 Surface roughness on grinded stainless steel and plated samples.

Figure 4.2.4 Cross-sectional images show coating structure of copper plated and GO/Cu composite plated samples: (a) Cu6-0.2; (b) GO/Cu4-0.2; (c) GO/Cu6-0.2; (d) GO/Cu8-0.2.

Figure 4.2.5 SEM images from cross-sectional view to discover the graphene oxides distribution: (a) general view of etched GO/Cu4-0.2 and (b) GO structure; (c) GO found with Cu plating structure and (d) detailed view of GO on GO/Cu6-0.2; (e) GO structure at the outermost area and (f) the bottom of coating structure of GO/Cu8-0.2.

Figure 4.2.6 Glow discharge optical emission spectroscopy of GO/Cu4-SS316 sample.

Figure 4.2.7 SEM images on argon produced crater bottom surface: (a) general observation of crater created around 20 seconds; (b) one special abrupt observed graphene like structure; (c) graphene oxides with ripples feature shown.

Figure 4.2.8 Comparing Raman spectra among GO/Cu plated under different working potentials.

Figure 4.2.9 XRD patterns for GO/Cu composite plated sample surface and standard XRD peaks for pure copper.

Figure 4.2.10 XRD pattern of GO/Cu6 with detailed phase indexing.

Figure 4.2.11 Comparing of micro-hardness for neat copper plated and GO/Cu composite plated specimens on their near surface region.

Figure 4.3.1 Surface changing with the brush plating procedure for pure Cu2 sample.

Figure 4.3.2 Surface microstructure for Cu coating samples: (a) Cu2-Brass; (b) Cu3-Brass; (c) Cu4-Brass; (d) Cu5-Brass and (e) Cu6-Brass.

Figure 4.3.3 Surface morphology of GO/Cu composite coatings with 0.2 g/L of GO on the brass substrate: (a) GO/Cu2-Brass; (b) GO/Cu3-Brass; (c) GO/Cu4-Brass; (d) GO/Cu5-Brass, (e) GO/Cu6-Brass and (f) GO/Cu5-Brass EDX line scan on one of the cauliflower-like structure with dark area on the top and results.

Figure 4.3.4 Graphene oxides found with SEM and EDX results: (a) SEM image for GO/Cu3-

Brass and (b) two graphs of EDX results by AutoID mode; (c) SEM image for GO/Cu4-Brass and (d) graphs of Spectrum 5 and 6.

Figure 4.3.5 Carbon and copper with colour-chemi SEM images for GO/Cu5-Brass samples: (a) red shows carbon rich areas; (b) red and yellow show carbon and copper rich areas.

Figure 4.3.6 Surface morphology of GO/Cu4 and 5 samples deposited with 0.4, 0.6 and 0.8 g/L GO concentrations: (a) GO/Cu4-0.4; (b) GO/Cu5-0.4; (c) GO/Cu4-0.6; (d) GO/Cu5-0.6; (e) GO/Cu4-0.8 and (f) GO/Cu5-0.8.

Figure 4.3.7 Bar charts for roughness comparisons for: (a) pure Cu and GO/Cu samples deposited with 0.2 g/L GO suspension; (b) GO/Cu samples deposited with 0.4, 0.6 and 0.8 g/L GO suspension.

Figure 4.3.8 Cross-sectional view for pure Cu control group to investigate how the voltage would influence the layer structure of Cu brush plating coating: (a) Cu2-Brass; (b) Cu3-Brass; (c) Cu4-Brass; (d) Cu5-Brass; (e) Cu6-Brass and (f) Cu4-Brass-EDX.

Figure 4.3.9 Cross-sectional view of GO/Cu brush plating coatings deposited with 0.2 g/L GO concentration: (a) GO/Cu2-Brass; (b) GO/Cu3-Brass; (c) GO/Cu4-Brass, (d) GO/Cu5-Brass and (e) GO/Cu6-Brass.

Figure 4.3.10 Comparison of layer thickness for pure Cu control group and GO/Cu-Brass samples.

Figure 4.3.11 SEM images of cross-sectional view of GO/Cu4 and 5 samples deposited with 0.4, 0.6 and 0.8 g/L GO concentrations: (a) GO/Cu4-0.4; (b) GO/Cu5-0.4; (c) GO/Cu4-0.6; (d) GO/Cu5-0.6; (e) GO/Cu4-0.8 and (f) GO/Cu5-0.8.

Figure 4.3.12 Comparing the layer thickness with GO differential GO concentrations under 4 volts and 5 volts.

Figure 4.3.13 Microhardness comparison of GO/Cu samples with (a) different voltages and (b) different GO concentrations.

Figure 4.3.14 Raman spectroscopy for GO/Cu composite coating on Brass substrate deposited with different GO concentrations: (a) 0.2 g/L GO concentration and (b) 0.4 g/L GO concentration.

Figure 4.3.15 XRD patterns from coating surface of (a) Cu control group and (b) GO/Cu-Brass materials.

Figure 4.3.16 Detailed XRD patterns of GO/Cu samples at lower positions.

Figure 4.3.17 GDOES results of carbon concentrations for samples deposited with different GO additions: (a) 0.2 g/L; (b) 0.4 g/L; (c) 0.6 g/L and (d) 0.8 g/L.

Figure 4.4.1 (a-b) Friction coefficient curves comparing among grinded brass and pure Cu control group: (a) within initial 100 cycles and (b) 2000 cycles.

Figure 4.4.2 The influence of GO addition on the friction coefficient: (a) plated under 4 volts; (b) plated under 5 volts; (c) plated under 6 volts and (d) summarised friction coefficient results.

Figure 4.4.3 (a) 2D scan comparison of worn track on brass, Cu control group and GO/Cu sample under 0.2 g/L of GO; comparing of Cu coating and GO/Cu coating samples: (b) Cu4 and GO/Cu4-Brass; (c) Cu5 and GO/Cu5-Brass and (d) Cu6 and GO/Cu6-Brass.

Figure 4.4.4 The comparison of wear volume among brass, pure Cu control group and GO/Cu composite coatings.

Figure 4.4.5 Comparison of SEM and colour-chemical results for wear track and wear counter ball on GO/Cu5 and Cu5: (a) Cu5-Brass wear track; (b) GO/Cu5-Brass wear track; (c) Cu5-Brass wear counterpart; (d) colour-chemical image of Cu5-Brass counter ball; (e) GO/Cu5-Brass wear counter ball to reveal the carbon component; (f) colour-chemical image of GO/Cu5-Brass counter ball.

Figure 4.4.6 (a-b) SEM images of worn track of Cu5-Brass plated coating under 316 stainless steel counter ball in air under 5N load.

Figure 4.4.7 SEM images and EDX mapping results on worn surface of GO/Cu5-Brass sample.

Figure 4.4.8 EDX results in 3D bar chart for the on the wear track of Cu and GO/Cu5: (a) Cu5-wear track; (b) Cu5-EDX; (c) GO/Cu5-wear track and (d) GO/Cu5-EDX.

Figure 4.4.9 Raman spectroscopy of worn tracks of Cu5-Brass and GO/Cu5-Brass and their optical images: (a) Cu5-p1, (b) Cu5-p2, (c) GO/Cu5-p1 and (d) Raman spectroscopy of pointed out position.

Figure 4.4.10 The friction coefficient comparing among the GO/Cu4 and GO/Cu5 samples deposited with different GO concentrations including 0.2, 0.4, 0.6 and 0.8 g/L: (a) GO/Cu4 samples and (b) GO/Cu5 samples under different GO concentrations; (c) COF for GO/Cu4 and 5 samples.

Figure 4.4.11 Comparison of 2D wear scar scans for (a) GO/Cu4 and (b) GO/Cu5 samples deposited with 0.2-0.8 g/L of GO concentrations using profilometer along with (c) comparing GO/Cu4-0.4 and 0.8.

Figure 4.4.12 Bar chart of wear volume for GO/Cu4 and 5 samples deposited with different GO concentrations.

Figure 4.4.13 Optical images of worn counter ball for GO/Cu4 and GO/Cu5 samples deposited with 0.4-0.8 g/L GO concentrations: (a) GO/Cu4-0.4, (b) GO/Cu5-0.4, (c) GO/Cu4-0.6, (d) GO/Cu5-0.6, (e) GO/Cu4-0.8 and (f) GO/Cu5-0.8.

Figure 4.4.14 Wear area estimated on counter ball by ellipse area calculated.

Figure 4.4.15(a-f) Comparisons for wear tracks of GO/Cu4 and 5 samples deposited with different GO concentrations of 0.2, 0.4, 0.6 and 0.8 g/L: (a) GO/Cu4-0.2, (b) GO/Cu5-0.2, (c) GO/Cu4-0.4, (d) GO/Cu5-0.4, (e) GO/Cu4-0.6 and (f) GO/Cu5-0.6.

Figure 4.4.16 SEM after EDX tests for (a) worn GO/Cu5-0.6 and (b) its EDX results; (c) GO/Cu4-0.4 SEM image denoted spectra and (d) its EDX 3D bar charts.

Figure 4.4.17 Raman spectroscopy on different areas of wear surface of GO/Cu4-0.4 to reveal the GO and oxides: (a) GO/Cu4-0.4 worn area with possible graphene spots and (b) the Raman spectra of spectra 1 to 3; (c) GO/Cu4-0.4 worn area with possible oxides and (d) its Raman spectrum

Figure 4.5.1 Potentiodynamic polarisation curves for (a) GO/Cu4-0.6 and (b) GO/Cu5-0.6 samples showing the repeatability.

Figure 4.5.2 The comparisons of potentiodynamic polarisation curves for samples deposited with various GO concentrations in (a) GO/Cu4 and (b) GO/Cu5 series versus brass substrate.

Figure 4.5.3 The corroded surface of bare brass: (a) the edge of corrosion and (b) a detailed view of the corrosion region.

Figure 4.5.4 EDX mappings on (a) the corroded brass surface with (b) Cu, (c) O and (d) C elements and (e) elements summarised results.

Figure 4.5.5(a-f) The SEM images of corroded surfaces for GO/Cu4 series of samples: (a, b) GO/Cu4-0.2; (c, d) GO/Cu4-0.4; and (e, f) GO/Cu4-0.6.

Figure 4.5.6(a-f) The SEM images of corroded surface for GO/Cu5 series of samples: (a, b)

GO/Cu5-0.2; (c, d) GO/Cu5-0.4; and (e, f) GO/Cu5-0.6.

Figure 4.5.7 EDX mapping on corroded GO/Cu4-0.4 sample showing the (a) SEM image and mapping with (b) Cu, (c) O, (d) C and (e) Cl elements.

Figure 5.1.1 Electro-chemical reaction schematics on the conventional GO/Cu co-plating process with Ni interlayer.

Figure 5.1.2 3D bar charts showing the effects of GO addition and brush plating voltage on the crystalline size calculated from XRD results.

Figure 5.1.3 Surfaces of two different coating showing (a) Pure Cu coating surface, (b) GO/Cu coating with lower GO and (c) GO/Cu sample with higher GO.

Figure 5.2.1 Raman spectroscopy on the worn track of GO/Cu4-0.4 and wear debris of GO/Cu4-0.2.

Figure 5.2.2 Typical wear tracks of brass and coating samples: (a) Brass (in insertion, EDX mapping showing brass transferred to the count-part stainless steel ball surface); (b) coating GO/Cu5. Sliding direction is shown by arrows.

Figure 5.2.3 SEM images of wear tracks from (a) Cu5 and (b) GO/Cu5 samples. (c) EDX composition (carbon and oxygen only) analysis from wear tracks (denoted as 1, 2 in (a), (b)) and wear debris (denoted as 3, 4 in (a), (b)), and Raman spectra from wear tracks of Cu and GO/Cu5 samples.

Figure 5.2.4 Typical SEM images of (a) well-developed columnar structures of GO/Cu samples showing (b) GO within the lamellar layers.

Figure 5.2.5 The graphene oxide performed as lubricants on the middle of the wear track on GO/Cu5-0.2.

Figure 5.2.6 Schematics of wear mechanisms on (a-c) pure Cu coating and (d-f) GO enhanced Cu composite coating.

Figure 5.3.1 Corrosion situation of (a) brass substrate, (b) GO/Cu composite coating of GO/Cu5-0.4 and (c) GO/Cu5-0.8 sample.

Figure 5.3.2 (a) Potentiodynamic polarisation curves of GO/Cu samples deposited with 0.6 g/L GO concentrations and corroded surface of (b) GO/Cu4-0.6 and (c) GO/Cu5-0.6.

Figure 5.3.3 Schematics of the corrosion mechanism for (a) brass and (b) GO/Cu composite

coating.

Figure 5.3.4 Corroded surface of GO/Cu samples with colour-chem image with (a) 0.2 g/L and (b) 0.8 g/L of GO.

List of Tables

Table 3.1.1 Chemical compositions of the 316 stainless steel substrate: nominal values and EDX measurements.

Table 3.1.2 Nominal and measured chemical composition of brass substrate material.

Table 3.3.1 Electronic brush plating procedures for applying Cu coating and GO/Cu composite coatings on 316 stainless steel.

Table 3.3.2 Brush plating process for applying Cu coating and GO/Cu composite coating on brass.

Table 4.1.1 Data of Raman pattern fitting of graphene oxide particle.

Table 4.2.1 EDX of GO like structure elements composition charts.

Table 4.3.1 Electric brush plating procedures for applying Cu coating and GO/Cu composite coatings on brass.

Table 4.5.1 Tafel fitting data from potentiodynamic polarisation curves of bare brass, GO/Cu4 and GO/Cu5 samples of different GO concentrations.

List of Abbreviations

CNT	carbon nanotubes
COF	coefficient of friction
CVD	chemical vapour deposition
DC	direct current
E	Young's modulus
EBP	electro brush plating
E_{corr}	corrosion potential
EDX	energy dispersive x-ray spectroscopy
EPD	electrophoretic deposition
FESEM	field emission scanning electron microscopy
FTIR	Fourier transform infrared spectroscopy
FWHM	full width half maximum
GDOES	glow discharge optical emission spectroscopy
GIC	graphite intercalation compound
GN	graphene nano-sheet
GO	graphene oxide
H_v	hardness
I_{corr}	corrosion current
I_D/I_G	intensity ratio of the D to G Raman bands
IPA	iso-propyl acrylate
OCP	open circuit potential
PECVD	plasma enhanced chemical vapour deposition
PEEK	Polyetheretherketone
PMMA	polymethyl methacrylate
R_a	roughness
SEM	scanning electron microscopy
UHMWPE	x-ray diffraction
XRD	ultrahigh molecular weight polyethylene

Chapter 1 Introduction

Graphene has attracted great attention of researchers during the past two to three decades, owing to its remarkable properties. and its outstanding electronic properties have positioned graphene research into the centre of the post-silicon era [1,2]. Moreover, graphene possesses great light transmittance and monolayer graphene (pristine graphene 97.7% [2]) and multilayered graphene also possesses light transmittance [3]. Additionally, graphene is of great mechanical strength owing to its strong sp^2 hybridised carbon-carbon (C-C) bonds, which makes graphene the thinnest and strongest material [4]. On top of those extraordinary properties, graphene was developed different types of applications for optoelectronic and electronic without further strengthening requirements, such as wafer-scale photonic devices [5], field-effect transistors [6,7] and solar cell electron transport layer [8].

Despite the significant attention it has received in these fields, relatively little research has been conducted to explore its potential in enhancing the tribological properties of materials, specifically in reducing friction and wear in tribological systems such as bearings. Notably, studies have demonstrated that graphene can exhibit lubricity comparable to bulk graphite on a microscale [9]. This finding has prompted investigations into using few-layer graphene as a self-lubricating coating for engineering materials. However, challenges such as low interface adhesive strength and thinness of the coating have limited the load bearing capacity and durability of graphene coatings for industrial applications.

Brass is one of the most commonly used lead-free alloys for the manufacturing of sliding bearings [10,11]; however, it possesses moderate tribological properties. Consequently, there is

growing interest in the development of self-lubricating components with enhanced wear resistance, which could offer a more sustainable and efficient solution for tribological applications.

Research has been conducted on improving the solid lubricant properties and wear resistance of copper (Cu) nanoparticles [12–14] primarily by incorporating Cu particles into oil-based lubricants or combining them with graphene oxide (GO) particles through mechanical bonding. Limited layer thickness and relatively weak bonding to the substrate have hindered their application, especially in demanding tribological applications [15,16]. Therefore, how to produce a self-lubricant coating on brass with sufficient layer thickness and strong bonding to the substrate presents both a technological and scientific challenge, which formed the theme of this research.

As graphene oxide (GO) possesses great hydrophilicity, it can be dissolved into aqueous-based electrolyte solutions. Moreover, their electronegative property in aqueous enables its movement within an electric field. Hence, applying GO-based coatings by electrochemical deposition techniques is possible in principle [17]. There are mainly two electro-deposition techniques to produce GO containing coatings, which are electro-plating deposition (EPD) [18] and electro-brush plating (EBP) [19].

The conventional electro-plating deposition (EPD) technique produces GO/metal composite coating by deposition of positively charged metal ions (such as Ni ions in Ni plating) together with GO to the substrate (cathode) [19]. The bonding introduced by the electric field is stronger than the graphene coatings produced by solution-flow or CVD transferring methods. However, the agglomeration of GO particles in aqueous solutions such as CuSO4 solution significantly

reduce the uniformity of GO in the GO/metal composite coating with aggregated GO particles mainly enriched in the surface. This problem could be addressed by EBP mainly because the continuous brush movement can improve the uniformity of the GO suspension in Ni plating solution as reported in [20].

However, no work has been reported on the development of graphene/copper nanocomposite coating using electro-brush plating (EBP). Therefore, the current research was directed at developing novel GO/Cu composite coatings by electro-brush plating technique with low friction and high wear resistance for potential sliding bearing applications. To this end, a series of EBP processes were conducted to study the effects of the processing parameters and GO concentration in plating solution; the coating microstructure was characterised and their tribological properties were evaluated to advance scientific understanding and for the optimisation of the EBP processing conditions for optimal GO/Cu coatings for potential brass sliding bearing applications.

Therefore, the aim of this PhD project was to develop novel GO/Cu composite coatings with low friction, high wear resistance and good corrosion performance through investigating the optimal parameters of EBP technology for the cost-effective and scalable production of GO/Cu composite coatings for potential sliding bearing applications. The specific research objectives of this PhD project were as follows:

1. To assess the feasibility of developing GO/Cu nanocomposite coatings on metal substrates using electro-brush plating.
2. To characterise the Cu/Go coatings produced using a range of material research methods including the phase structure, microstructure and chemical compositions.

3. To evaluate the mechanical and tribological properties of the coatings, with particular emphasis on their tribological behaviour at the macro scale, to gain insights into how GO can enhance the tribo-performance of the GO/Cu composite coatings.
4. To investigate the corrosion behaviour of the GO/Cu composite coatings and study the mechanisms by which GO contributes to improved corrosion properties.

A brief overview of the following chapters is stated below:

- **Chapter 2** provides a comprehensive literature review, beginning with an overview of the brief history, structure, and key properties of graphene. It then explores various techniques for producing graphene-based coatings followed by examining the functional applications of graphene, particularly in enhancing tribological performance and corrosion resistance.
- **Chapter 3** details the production and characterisation of the GO/Cu coatings, covering the preparation and fabrication of the coatings. It also describes the characterisation techniques used to analyse the specimens.
- **Chapter 4** presents the results of the study, focusing on the GO/Cu composite coatings produced by electro-brush plating. This chapter reports the surface morphology, chemical composition, microstructure and layer-structure of the coatings, and their mechanical, tribological and corrosion properties.
- **Chapter 5** is devoted to the discussion of the results reported, with a primary focus on analysing the tribological and corrosion behaviour of the GO/Cu composite coating and the mechanisms involved to advance scientific understanding. It also covers the identification of the optimal parameters for achieving the best performance.
- **Chapter 6** concludes the thesis by summarising the key findings and proposes promising areas for future scientific investigation.

Chapter 2 Literature Review

2.1 The History of Graphene Research

Graphene is typically recognised as a single layer of carbon atoms arranged in a honeycomb lattice. This atomic structure could be considered as a single layer of graphite. For many years, graphite, composed of laminated structure, has been utilised in pencils. People might accidentally produce graphene, though no one has reported it. Despite this, little attention was given to the single-layer hexagonal structure within graphite until twenty centuries. There were chances for the earlier discovery of graphene before 2004 [21].

Theoretical research was first conducted in 1947 with firmly packed hexagonal structures stuck together on a strictly flat surface, as illustrated in Figure 2.1.1a [22,23]. This model predicted hyperthermal fluctuations, suggesting that graphene could not exist due to the instability of its two-dimensional (2D) crystalline structure [23–26]. Despite this theoretical prediction, the experimental research of two-dimensional (2D) materials has never been interrupted. Interest in few-layered graphite began in the 1960s, driven by the pioneering experimental work of Boehm et al. [27–29]. In 1986, Boehm and his colleagues introduced the term "graphene" to describe a single carbon layer within graphite intercalation compounds (GICs) [30,31]. Research into graphene oxide (GO) and GICs dates back to around 1840 [32,33]. It was discovered that ultrathin graphite lamellae could be produced from graphene oxide through a reduction reaction in an alkaline suspension. Those GICs materials could be denoted as a few layers of graphene in nowadays research.

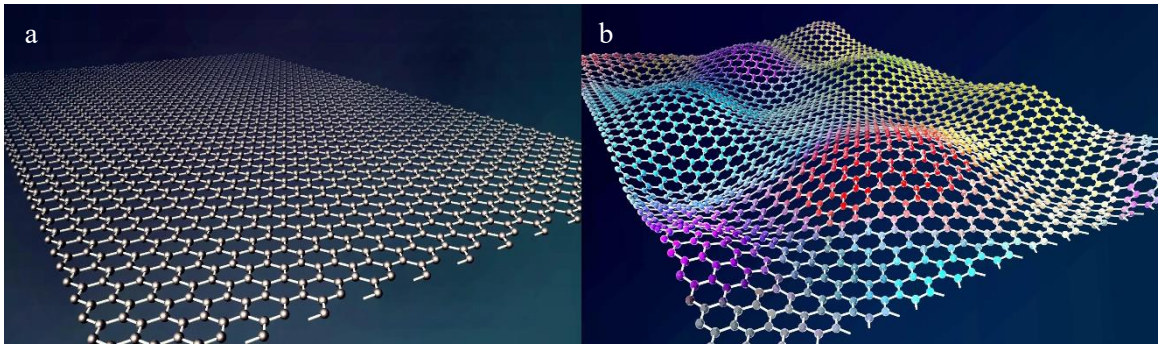


Figure 2.1.1 Two versions of theorical stimulation of graphene: (a) the model with long range order and (b) the improved model [25].

After several years of exploration, high-quality graphene was first exfoliated using "scotch tape" by Novoselov et al. in 2004 [34,2]. The improved theoretical research on the structure of graphene, as depicted in Figure 2.1.1b, was conducted in 2007 [25,35]. This structure would be further discussed at the next session. This foundational single-layer structure serves as a precursor to other significant carbon allotropes, facilitating transformations into zero-dimensional (0D) fullerenes, one-dimensional (1D) carbon nanotubes, three-dimensional (3D) graphite and diamond, as shown in Figure 2.1.2 [23,36,37]. Over the years, numerous researchers have explored the production of not only graphene itself but also its related allotropes. These efforts have led to breakthroughs in the unique properties of this 2D material across various fields.

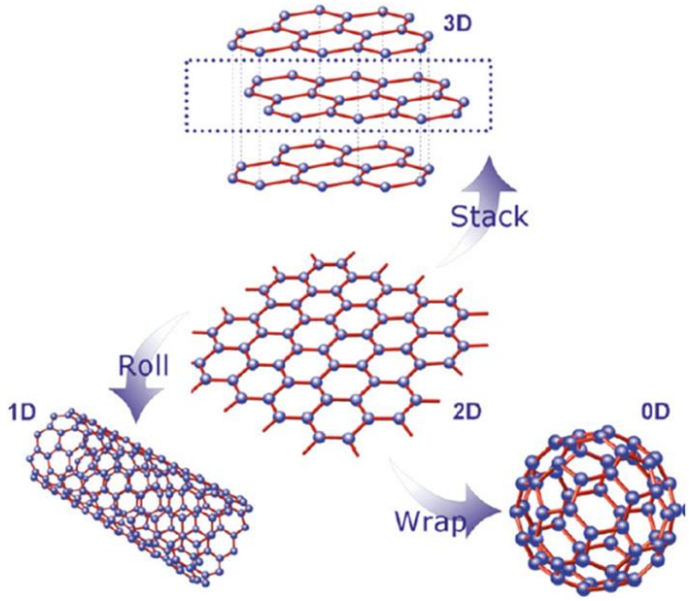


Figure 2.1.2 Various carbon allotropes derived from graphene honeycomb structure [37].

2.2 The Structure and Basic Properties of Graphene

2.2.1 The Formation of Graphene Structure

It could be illustrated in the periodic table that the ground-state electronic configuration of carbon is $1s^2 2s^2 2p_x^1 2p_y^1 2p_z^0$ and the exited-state would be $1s^2 2s^2 2p_x^1 2p_y^1 2p_z^1$, as shown in Figure 2.2.1a and b [38]. The exited $2s^1$, $2p_x^1$, $2p_y^1$ and $2p_z^1$ belong to the valence shell which could perform new bonds with hybridisation, showing in three types sp (linear), sp^2 (trigonal planar) and sp^3 (Tetrahedral) hybridisation. The honeycomb structure of graphene is performed by sp^2 hybridisation, as shown in the Figure 2.2.1c. It could be seen that there are three neighbour carbon atoms sharing their sp^2 electrons with angle of 120° [38]. Figure 2.2.1d illustrates the graphene crystal unit cell or triangular sublattice fixed with 2.46 Å (0.246 nm) lattice constant [39,40]. The denoted A and B are from the two different sublattice [39,41]. The sp^2 hybrids, shown in Figure 2.2.1e, exhibit two neighboured carbon atoms combined with sp^2 hybridised ($2s^1$, $2p_x^1$, $2p_y^1$) orbitals forming sigma (σ) bond (~ 1.42 Å), while $2p_z$ orbitals

combined to form the pi (π) bond.

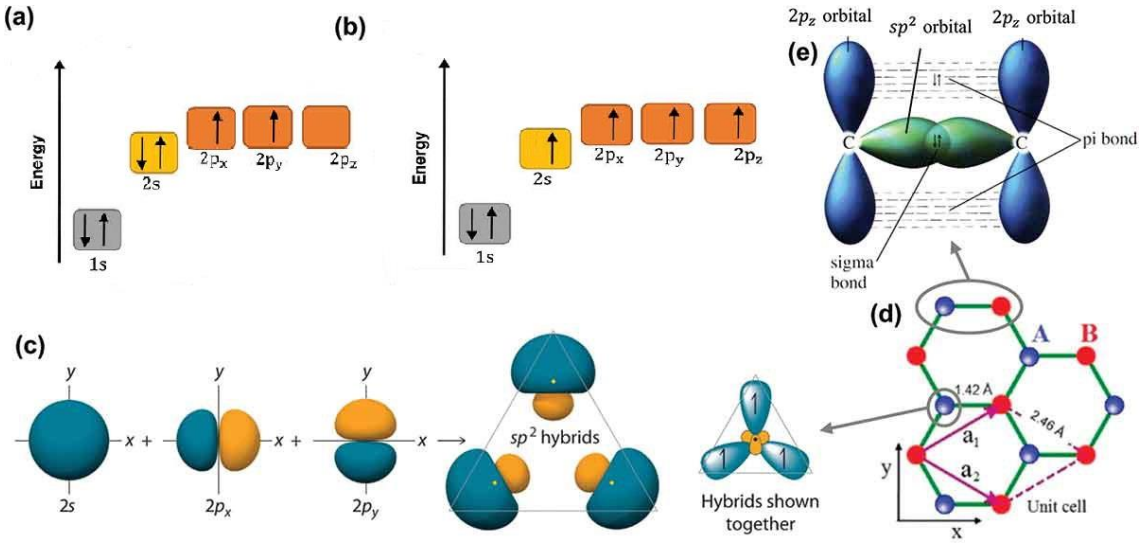


Figure 2.2.1 Schematic of carbon structure: (a) energy level of carbon outer electrons in normal state; (b) exited state of carbon electron energy level; (c) sp2 hybrids formation; (d) graphene lattice showing A and B belong to different sublattice; (e) showing the sp2 hybridisation from the bonding [40].

It is interesting that this sp^2 hybridised σ bond presents shorter distance than the C-C bond within the diamond with sp^3 hybridisation, which is also proved of stronger strength (615 kJ/mol) than diamond (345 kJ/mol) by experiment [4,42,43]. Owing to this strong σ bond, graphene could be utilised in mechanical applications. As a type of 2D material, graphene would be able to provide mechanical enhancement with ultra-thin thickness. The remaining $2p_z$ orbitals, occupying the orbital perpendicular to basal plane, form π bond with significantly lower binding energy than the above mentioned σ bond [42]. This lead to the easy shearing of graphite lamellae, which explains why the physical exfoliation of graphene from graphite is possible. Moreover, owing to the high freedom of this π bond, the graphene possesses different types of electronic properties.

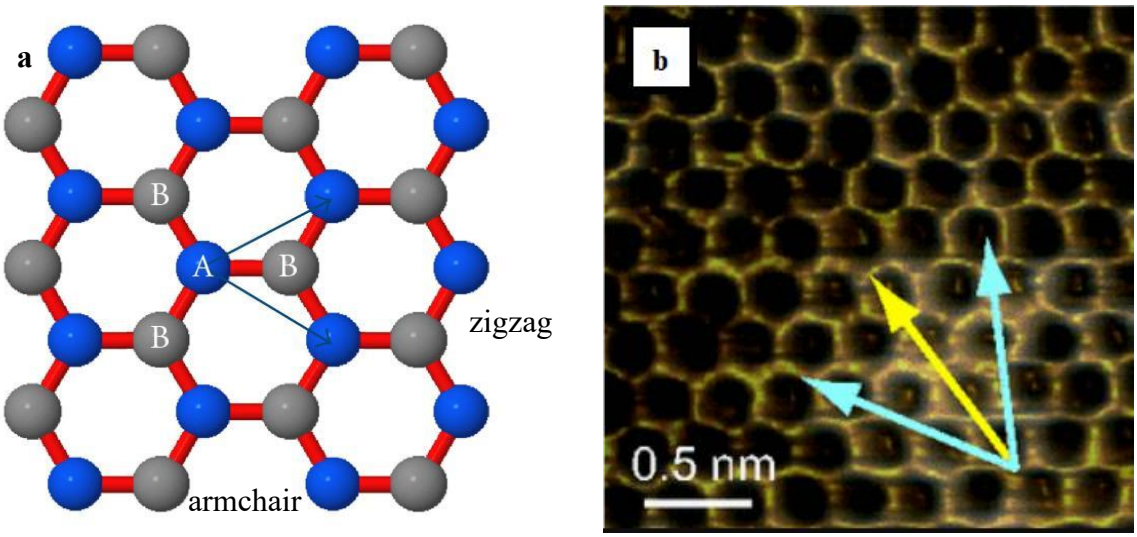


Figure 2.2.2 (a) Schematic of graphene edge orientation [39] and (b) Scanning Tunnelling Microscopy (STM) image of graphene the blue arrow denoted as armchair and yellow is zigzag orientation [44].

As mentioned before, the A and B sublattice could also be seen on the graphene hexagonal lattice. Owing to some better performance compared to the basal plane, the edge of graphene lattice is interesting to study. There are two types of edge zigzag and armchair, as depicted in Figure 2.2.2a. It is interesting to note that the chemical reactivity at the edge of graphene would be twice than that on basal plane, as proved by spectroscopic test [45]. The edges of graphene lattice would be more important when studying such chemical reactions as oxidation and doping other elements. It was discovered that the breaking of graphene would tend to occur at the grain boundary thus creating the edge mentioned above through mechanical exfoliation [46–49]. The preferred tearing orientations of graphene sheet are illustrated in Figure 2.2.2b under applied mechanical force. Hence, the graphene under mechanical usage needs more attention to the edge and it would be further discussed later.

2.2.2 Mechanical Properties

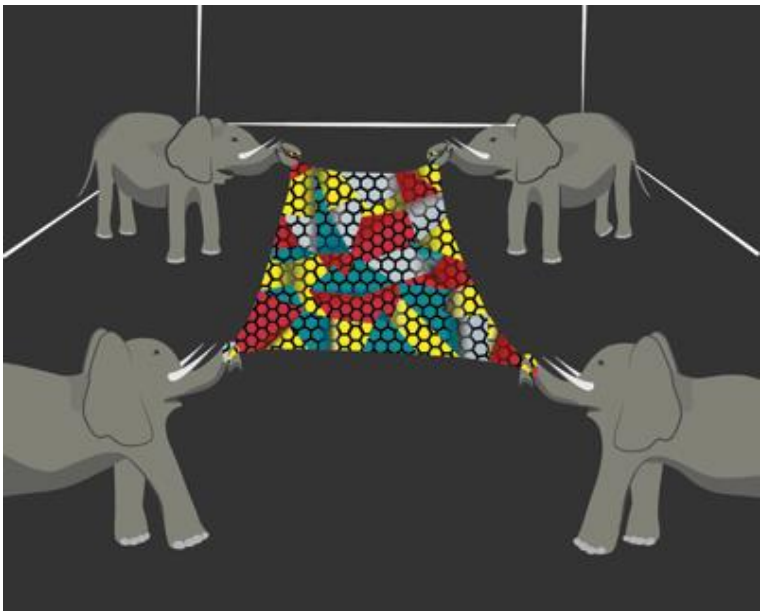


Figure 2.2.3 An art work of inspiring from the stiffness of graphene, it could not be torn even four elephants dragged at the corners with defect which is remained the strongest material [50].

Despite the presence of defects, graphene remains the strongest material known, with a thickness of only one atom [2,50]. Its mechanical strength is attributed to its sp^2 hybridised chemical bonds, which are stronger than those found in diamond. Pristine graphene exhibits a very high elasticity as it possesses as high as approximately 1.0×10^3 GPa of Young's modulus (E) and 130 GPa of intrinsic strength on defect-free single layer graphene [51,52], which are 200 times stronger than that of structural steels [53]. However, the pristine graphene without defect would only exist in small area. Consequently, graphene in most applications would be combined with different graphene grains, as illustrated in Figure 2.2.3. It is noteworthy that the graphene with many grain boundaries remains very strong, which indicates that the grain boundary of graphene also possesses great strength [50]. The intrinsic strength has been tested around 100 GPa, which is still quite close to that of pristine defect-free graphene (130 GPa) [54,55].

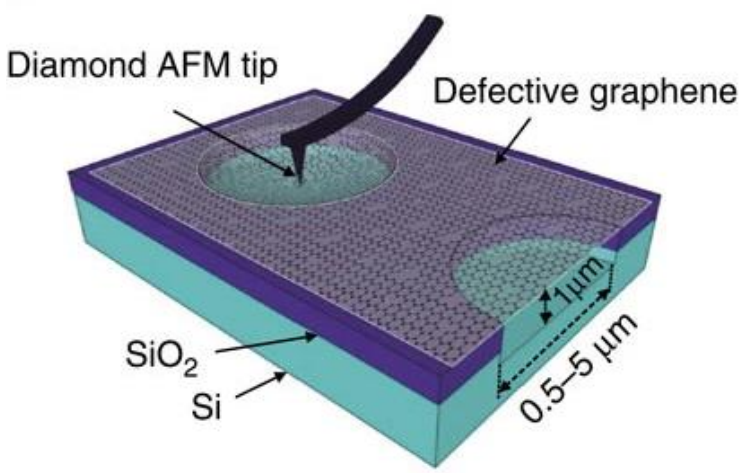


Figure 2.2.4 Schematic of nanoindentation test applied on defective graphene atomic force microscopy (AFM) [55].

In addition to the grain boundaries, graphene sheets may also exhibit sp^3-type and vacancy-type defects, both of which can impact mechanical strength. It was discovered that the atomic force microscopy (AFM) could be utilised to detect the intrinsic strength of graphene on silicon-based holder, as demonstrated in Figure 2.2.4. Figure 2.2.4 shows schematic of nanoindentation test applied on defective graphene atomic force microscopy (AFM) [55]. Sp^3-type defects result in a minor reduction in strength compared to defect-free pristine graphene, with a decrease of approximately 14% [55]. In contrast, vacancy-type defects lead to a significant decrease in strength. Hence, in order to optimise mechanical strength, it is important to focus on minimising vacancy defects during the development of graphene-related high-strength materials, particularly on a large scale. For composite applications, it is essential to ensure strong adhesion between the graphene reinforcement and the matrix to fully utilise the exceptional mechanical properties of graphene [56].

One-atom-thick graphene is recognised as a 2D structure; however, even two-atom-thick graphene retains its classification as a 2D material. A few-layer graphene, which includes structures with two to ten layers, is also considered graphene [57]. This type of a few-layer

graphene demonstrates excellent lubricity, similar to that of graphite, which is widely known for its use as a solid-state lubricant [58]. Consequently, integrating few-layer graphene into material systems can significantly enhance their tribological properties. Additionally, graphene exhibits remarkable impermeability to almost all molecules, including hydrogen. This property makes graphene an ideal passivation film, capable of preventing the penetration of corrosive agents into the materials it is applied to, thereby mitigating potential corrosion damage [59].

2.2.3 Electronic Properties

As illustrated in Figure 2.2.5, graphene's Brillouin zone is hexagonal and includes several high symmetry points: Γ, M, K, and K'. The boundary points K and K' are referred to as Dirac points. Utilising a tight-binding approach, the band structure of single-layer graphene is demonstrated in Figure 2.2.5 [39]. Here, the π electron orbitals of neighbouring atoms overlap, causing the valence (π electron occupied) and conduction (vacant) bands to intersect precisely at the Dirac points.

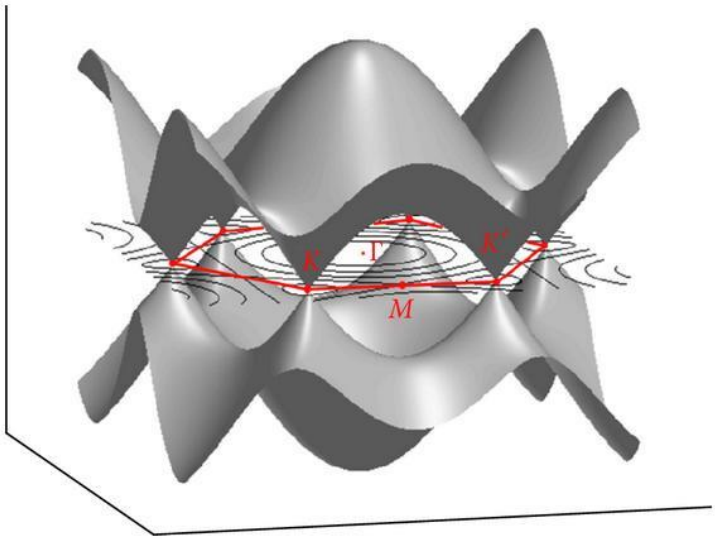


Figure 2.2.5 Brillouin zone of graphene and denoted symmetry points [39].

The conductance bands of neighboured atoms meet at the Dirac point, as the orbital of neighboured π electrons overlapped, for monolayer graphene. Hence, monolayer graphene could be used as zero band gap semiconductor [46]. Moreover, graphene possesses extremely high mobility of charge carrier (up to 100,000 $cm^2V^{-1}s^{-1}$) which could be used in producing supercapacitors [21,42,60]. For comparison, certain semiconductors like InSb can reach a room temperature carrier mobility of 78,000 $cm^2V^{-1}s^{-1}$, achieved using bulk materials without chemical doping [61]. Doping is typically used to modulate the band gap for logic applications in the semiconductor industry or to enhance electrical activity for electrochemical applications such as supercapacitors and batteries. Additionally, single-layer graphene exhibits the half-integer quantum Hall effect (QHE) at room temperature, and its conductivity never drops below the minimum threshold of e^2/h [39,62,63]. With unique electronic properties, graphene could be used in electronic applications.

2.2.4 Chemical Properties

As mentioned in Section 2.2.1, graphene is densely compacted hexagonal lattice forming honeycomb structure with a large surface-volume ratio and low mass density [64]. Although graphene possesses excellent electronic properties, the chemical property would be alike to graphite which is near inert. It is interesting that graphene also possesses high hydrophobicity comparable to graphite, and the water wettability would also be influenced by the ambient environments (i.e. temperature, absorbent hydrocarbon species and contaminations on graphene surface) [65–67]. As previously discussed the p_z orbitals are combined with relatively weaker bond which is approachable to reunite with other elements such as carbon [68], such as hydrogen (H) [69], nitrogen (N) [70–72] and boron (B) [73]. Defect-free graphene is considered as impermeable to all the liquids and gas [74–76]. Hydrogen is an exception, as it can be absorbed on the ripples of graphene and dissolved on the other side of the graphene membrane [77]. Due to its impermeability, graphene can serve as a superior barrier to prevent the penetration of corrosive species and oxygen gas. A more detailed discussion on this topic will be provided in the corrosion section.

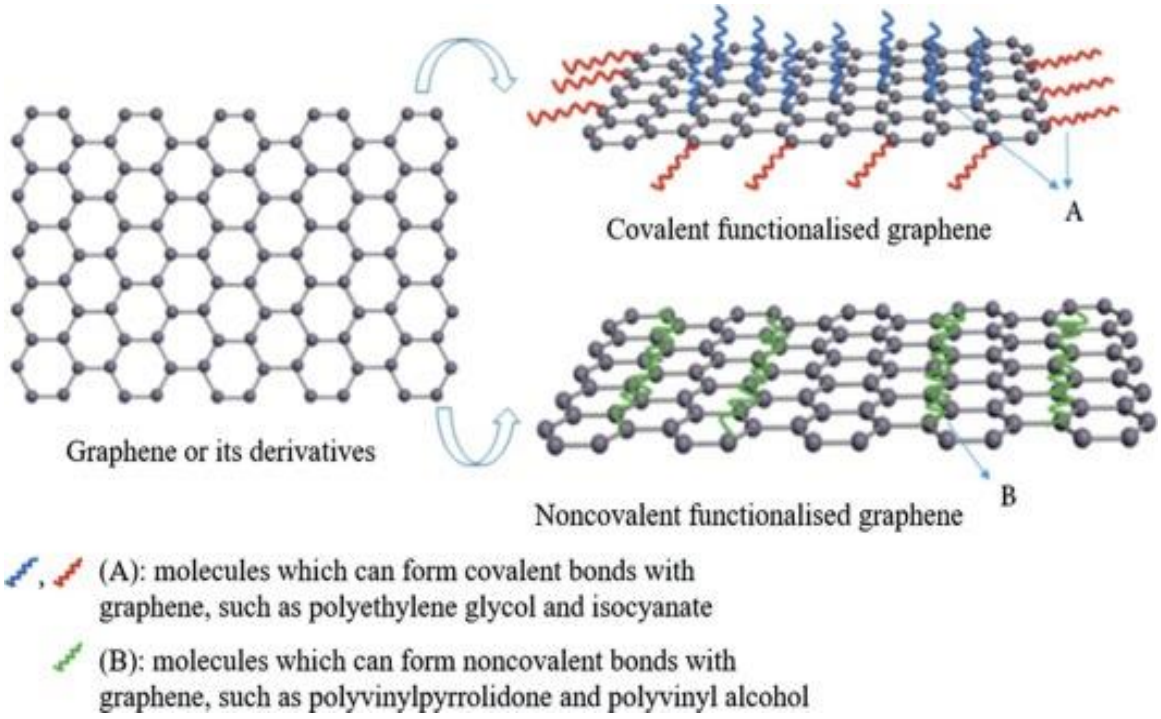


Figure 2.2.6 Schematics of graphene functionalisation [78].

Functionalising graphene opens up a wide array of possibilities for enhancing its chemical reactivity and exploring its potential in various chemical applications, such as advancing biomedicine [79–81], creating biosensors [82–84], developing electrochemical catalysts [85–87] and modulating electronic bandgaps [88,89]. Graphene can be functionalised through either non-covalent or covalent methods, as demonstrated in Figure 2.2.6 [78,90]. Non-covalent functionalization is typically achieved through van der Waals forces or π-π stacking interactions between the graphene surface and external aromatic molecules [90]. Non-covalent functionalization minimally affects the π-conjugated structure of graphene, thereby preserving its intrinsic electronic and mechanical properties to the greatest extent. In contrast, covalent functionalization involves the transition from sp^2 to sp^3 hybridisation, often resulting in the creation of graphene derivatives, which will be discussed in detail in the next section.

2.2.5 Derivatives of Graphene and Their Properties

2.2.5.1 Graphene oxide and reduced graphene oxide

Graphene oxide (GO) and reduced graphene oxide (rGO) are the most commonly studied derivatives of graphene, as demonstrated in Figure 2.2.7. There are well-established methods for cost-effective manufacturing of GO and rGO in both laboratory and industry.

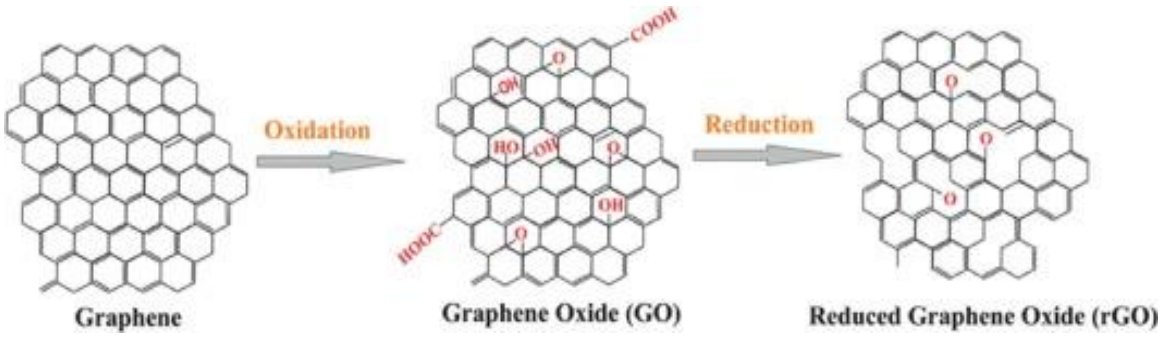


Figure 2.2.7 The process of converting graphene to graphene oxide (GO) and then to reduced graphene oxide (rGO). [91].

Broadly speaking, GO is a type of unique material with one single molecular layer of graphite structure combined with several different types of oxygen-containing groups including hydroxyl (-OH), epoxide (C-O-C), carbonyl (C=O) and carboxyl (COOH) groups (Figure 2.2.8) [92]. These functional groups tend to lose their proton within water, so that they will present as electrical negative in aqueous solutions. With those functional groups, GO will exhibit electrical negative within an aqueous solution. Hence, these GO particles will expel each other in water, which leads to great dispersibility. Owing to this great dispersibility, graphene oxide could be introduced into solutions such as plating solution for electronic plating applications. As graphene does not possess such functional groups, GO is superior to graphene in this kind of application. Comparing to graphene, however, these oxygen-containing functional groups and other sp^3 on GO are structural defects. The mechanical properties of graphene oxide are inferior

to graphene but still superior to many other materials.

Reduced graphene oxide (rGO) is produced by removing the oxygen-containing groups from GO via reduction reaction using various methods. However, even if all the oxygen bonding is removed, defects within graphene honeycomb structure remain. Accordingly, the excellent properties of graphene could not be fully recovered.

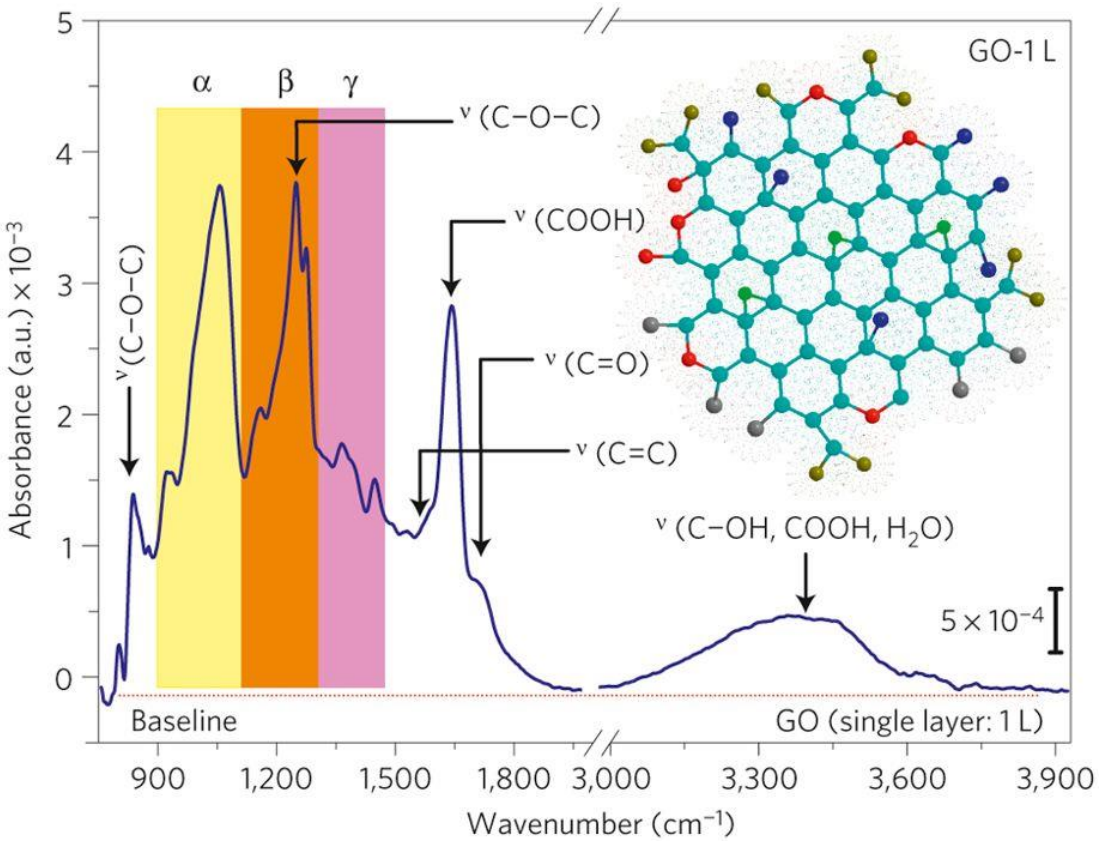


Figure 2.2.8 Spectrum of an exampled FTIR result for single layer of graphene oxide [13].

2.2.5.2 Other doping derivatives

Graphene can be modified with various elements, such as hydrogen, fluorine, and nitrogen. Like the formation of GO, these doping processes disrupt the C-C sp^2 bonds to incorporate the doping atoms into the lattice or replace carbon atoms. There are two types of graphene doping which are water vapour induced p-type and ammonia caused n-type doping [93]. Hydrogen-doped and fluorine-doped graphene are known as graphene and fluorographene, respectively [94]. Nitrogen-doped graphene, as p-type doping, is particularly noteworthy due to its significant potential in applications such as graphene-based sensors, electronics, and electrochemical reaction catalysts [95,96].

2.3 Substrate Materials

2.3.1 Stainless Steel

The use of stainless steel started in the World War I, after Harry Brearley's discovery of the first commercial useful stainless steel (containing 12.5 wt.% of chromium) [97]. According to the microstructure, stainless steel could be broadly divided into four groups which are austenitic, ferrite, martensitic and duplex stainless steels. As mentioned before, chromium (Cr) is essential for all stainless steel, which can continuously produce a dense passivation film to protect the substrate from corrosive hazard in aqueous environments.

As for austenitic stainless steels, it is FCC structured and non-magnetic materials with great toughness though relatively lower hardness than martensitic steels. Moreover, austenitic stainless steels present better corrosive resistance than other types of stainless steels [98]. Therefore, austenitic stainless steels require less maintenance which presents high commercial values in crucial corrosive environments.

2.3.1.1 300 Series Austenitic Stainless Steels

Austenitic stainless steels with chromium (Cr) and nickel (Ni) as main additions are identified as 300 series stainless steels [99]. 304 stainless steel has a composition of 18 wt.% of Cr and 8 wt.% of Ni, which is a conventional type of 300 series stainless steels [100]. Other austenitic stainless steels have different additions to further increase their corrosion properties. For example, 321 stainless steel contains titanium constituent to prevent the formation of carbides, thus slightly improving corrosive resistance [100]. 316 and 316L stainless steels are the second commonly used form of austenitic stainless steels.

2.3.1.2 316 Stainless Steel

Aforementioned all 300 series austenitic stainless steels possess great corrosive resistance, ductility, high temperature strength, high weldability and great impact resistance [99]. Those are common advantages of 316 stainless steels, and further advantages will be discussed in the next paragraph. 316 stainless steels has better weldability than other 300 series, as no annealing process is required to weld thin sections, as depicted in Figure 2.3.1. Compared with other types of stainless steels, 316 austenitic stainless steel contains about 3% Mo, which gives it better corrosive resistance (especially pitting corrosion resistance) than other types in 300 series. 316 stainless steel presents great corrosive resistance in many corrosive circumstances and a range of atmospheric environments; however, it is still subjects to pitting corrosion in warm chloride (Cl) environments. As chloride ions (Cl^-) deplete chromium oxide (CrO_2) films when contact with the stainless-steel surface.

Those outstanding properties, especially their excellent corrosive resistance, lead to their applications in transportation, medical, chemical and architectural industrial sectors to produce specific parts, such as chemical containers, medical devices, threaded fasteners and boats

fittings. However, like other types of stainless steels, 316 stainless steels also present poor tribological properties mainly due to its low hardness and high plasticity. As almost practical used parts are required to have some wear resistance, these poor properties hindered their applications in many industrial fields, such as bearings and other tribological parts. Graphene is one of the most efficient materials to improve the surface tribological properties, which will be discussed later in Section 2.5.

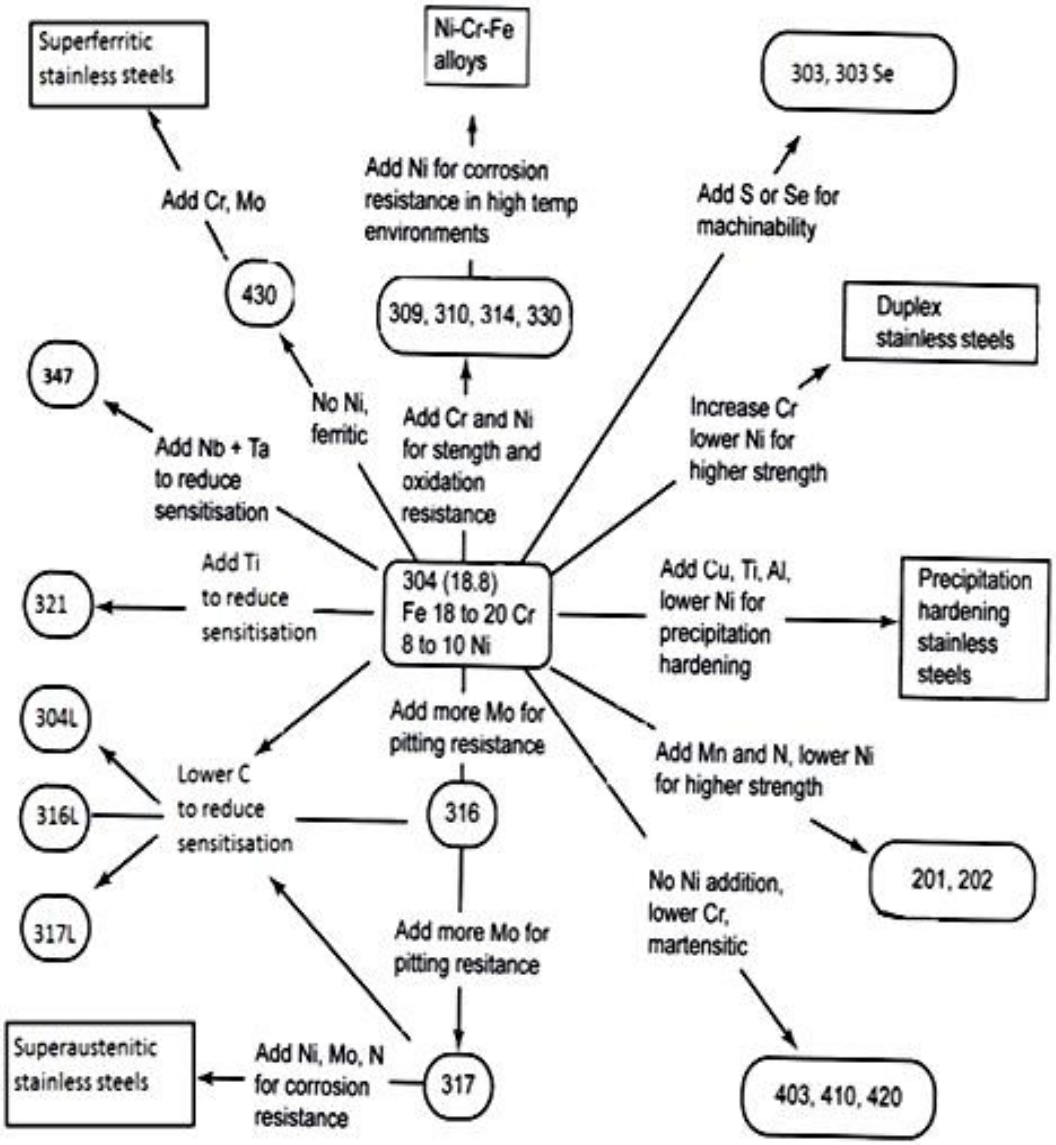


Figure 2.3.1 The stainless-steel family showing with their compositions and related properties [101].

2.3.2 Copper and Its Alloys for Bearings

It is known that copper-based sliding bearings are commonly used in many industrial fields, such as gas turbines, large size electric motors, crankshaft bearings used in diesel and petrol engines. In normal stable service, sliding bearing are used under hydrodynamic lubrication or electrohydrodynamic lubrication conditions with a hydrodynamic film separating the tribo-pairs thus reducing friction and avoid wear. However, direct contact between the tribo-pair will

occur at the start or stop when the hydrodynamic film is not thick enough to separate the tribo-pairs.

With various additives, copper and its alloys could be improved on the wear resistance to meet different demands from applications [102]. There are different catalogues of copper-based sliding bearing materials such as low phosphor bronze, brass and leaded bronze. Due to enhancement on machinability with small addition, lead is used in almost all sliding bearing materials [103]. Concerning of environmental and health issues, invention of lead-free copper-based bearings with adequate wear resistance is important to meet the need of environmentally friendly world. Clearly, new solutions should be developed to enhance the wear resistance of Cu-based bearing materials without adding lead. To this end, graphite [104,105] and/or graphene nanosheet [106,107] is used to reinforce copper matrix through powder metallurgy to form composites with improved tribological property.

As for a bearing, the whole part should be relatively stiff to ensure their serving life, and its surface needs good tribological property or even self-lubricity. Those two requirements could be satisfied cost-effectively by surface engineering. Therefore, surface engineering is a more cost-effective solution to improve tribological properties of working surface, comparing to the bulk powder metallurgy approach [108,109].

As mentioned before, copper has been widely used for sliding bearing and hence it is important to use it as the matrix of coating systems. Moreover, the lubricating ability of few-layer graphene could also be used to enhance the lubricity of the material. Additionally, graphene has been demonstrated for its excellent performance as passivation film with chemical inertness to both liquid solutions and oxidising gases [59]. Therefore, a composite coating system could be

introduced to improve tribological property for bearing application.

2.4 Techniques for Producing Graphene Based Coatings

Solution flow-based approaches include several different coating techniques [110], such as vacuum filtration [111], spray coating [112], spin coating [113,114] and dip coating [110]. These techniques are facile to be carried out with low cost and high efficiency. However, these graphene coatings are applied to the substrate surface by physical approaches. Hence, there are only physical bonding between the graphene coating and the substrate so that the adhesive strength of these coating systems is much weaker than the coating systems with chemical bonding. Therefore, the mechanical and tribological properties of such coatings are too poor to be used for tribological applications. The main purpose of this section is to review the graphene-based coatings with a certain level of bonding for mechanical and tribological applications.

2.4.1 Chemical Vapour Deposition (CVD)

2.4.1.1 Fundamental of CVD

As the market share of CVD-grown graphene expands [115,116], it becomes increasingly important to develop and refine methods for transferring CVD graphene films onto a variety of substrates for subsequent applications [117,118]. This is mainly because CVD graphene coatings can be generated only on some substrate materials, including silicon wafers, nickel, and copper. Accordingly, recent advancements in this field encompass methods such as solution flow techniques and the transfer of CVD-synthesised graphene films onto the surface engineering materials.

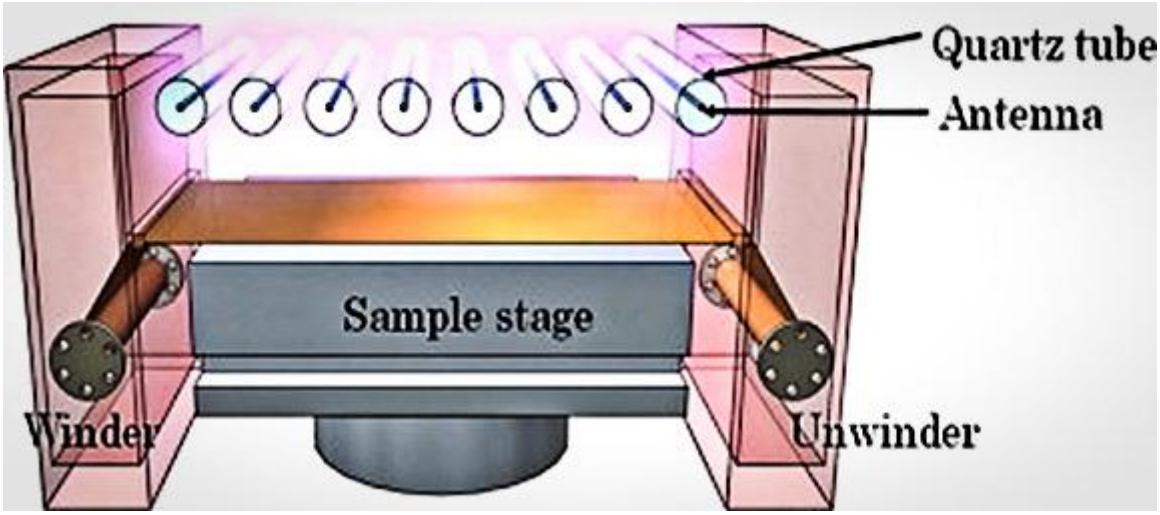


Figure 2.4.1 Schematic of microwave plasma CVD fabricating large-scale graphene films [119].

Conventional chemical vapour deposition (CVD) and plasma-enhanced chemical vapour deposition (PECVD) are widely used for producing monolayer or multilayer graphene films [120]. Recent studies have demonstrated that large-scale graphene films can be fabricated on copper or nickel substrates with dimensions of 294-297 mm or A4 size, using microwave plasma CVD, as depicted in Figure 2.4.1 [119,120]. A significant advantage of CVD techniques is their ability to produce graphene films with minimal molecular defects. As a result, graphene coatings created through CVD exhibit significantly lower gas and liquid permeability and higher light transmittance compared to those produced by other chemical methods. However, it is important to highlight that the CVD method is currently limited to depositing graphene coatings on Si, nickel or copper substrates.

2.4.1.2 CVD Graphene transferring techniques

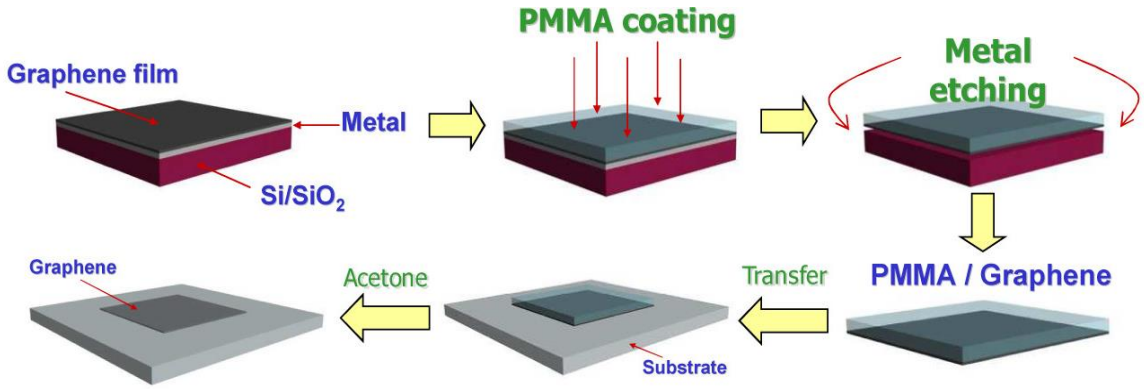


Figure 2.4.2 Procedures of wet CVD transferring using polymethyl methacrylate (PMMA) [121].

To utilise graphene as coating, it is important to expand the substrate materials from only Cu, Ni and Si wafer. It requires graphene transferring from where it was grown to the new substrate material through certain adhesive methods. The most commonly used method for this transfer is wet chemical transfer, which typically involves an intermediate carrier material such as polymethyl methacrylate (PMMA) [117,122,123]. Figure 2.4.2 depicts this transfer process [121], and the typical steps are:

1) Applying a PMMA layer on the graphene grown on a Cu substrate.
2) Etching with chemical etchant like acidic $FeCl_3$ to remove the Cu substrate.
3) Rinsing to remove the retained etchant with deionised (DI) water on PMMA-coated graphene and then it was transferred to the target substrate.
4) Removing the PMMA layer using organic solvents such as acetone.
5) Eliminating chemical residues with drying and annealing on the graphene coating.
6) Completing the transfer.

Several variations of this procedure have been investigated, including the direct transfer using isopropanol (IPA) droplets [124,125], substituting fragile PMMA with more robust polymers like PET film, allowing for the roll-to-roll transfer of graphene over 100 meters in length [126], and methods such as electrochemical bubbling delamination and transfer [127,128], etc.

However, the transfer process often introduces defects into the graphene thin film, which compromises the integrity of the coating. These defects can result in the degradation of several important properties, such as the relatively great friction [129] and corrosion resistance [130]. In addition, the bonding between the transferred graphene film and the substrate is extremely weak. Consequently, the tribological properties of the graphene coatings produced by this technique are rather poor, especially under the tangential forces generated by sliding. High tribological performance is crucial for developing high-quality sliding bearing surfaces, and thus this technique is unsuitable for such applications. Moreover, CVD graphene coatings are too thin for long-term use in sliding bearings. To address these issues, composite coatings that combine a metal matrix with graphene reinforcement could be a viable solution.

2.4.2 Electrophoretic Deposition (EPD)

There is a growing demand for techniques that enable large-scale production of graphene-based functional coatings and composites. An effective and practical approach should allow for the homogeneous and cost-efficient fabrication of graphene-related materials. Electrophoretic deposition (EPD) presents a promising solution in this regard.

EPD is a colloidal process where charged particles are driven by an electric field to move towards and deposit onto an electrode with the opposite charge [131]. After deposition, the wet layer is dried or sintered to create a dense coating. This technique enables the deposition of

particles of various sizes, ranging from nano to micro scales, and can be applied to nearly all material types, including ceramics, polymers, metals, glasses [132,133], and carbon nanotubes (CNTs) [133,134], provided that a stable suspension of the particles is maintained.

Although they may look similar, the key differences between electrophoretic and electroplating deposition are as follows:

a. In EPD, a liquid medium with low conductivity is preferred because the suspended particles and ions compete with each other during the process. Conversely, successful electroplating typically requires an electrolyte with a high ion concentration and conductivity.

b. In electroplating, the charge carriers are ions in the electrolyte, such as Ni^{2+} ions in nickel plating, which move towards the electrode to form the coating. On the other hand, in EPD, the deposition is primarily governed by the movement of solid particles, rather than free ions, within the solution.

c. Although aqueous suspensions can be utilised in EPD, organic liquid media are generally favoured. This is due to the potential for water electrolysis and Joule heating (heat accumulation near the electrodes) during the EPD process, which can arise from the low conductivity of the electrolyte [132]. In contrast, water-based electrolytes are commonly employed in electrodeposition processes.

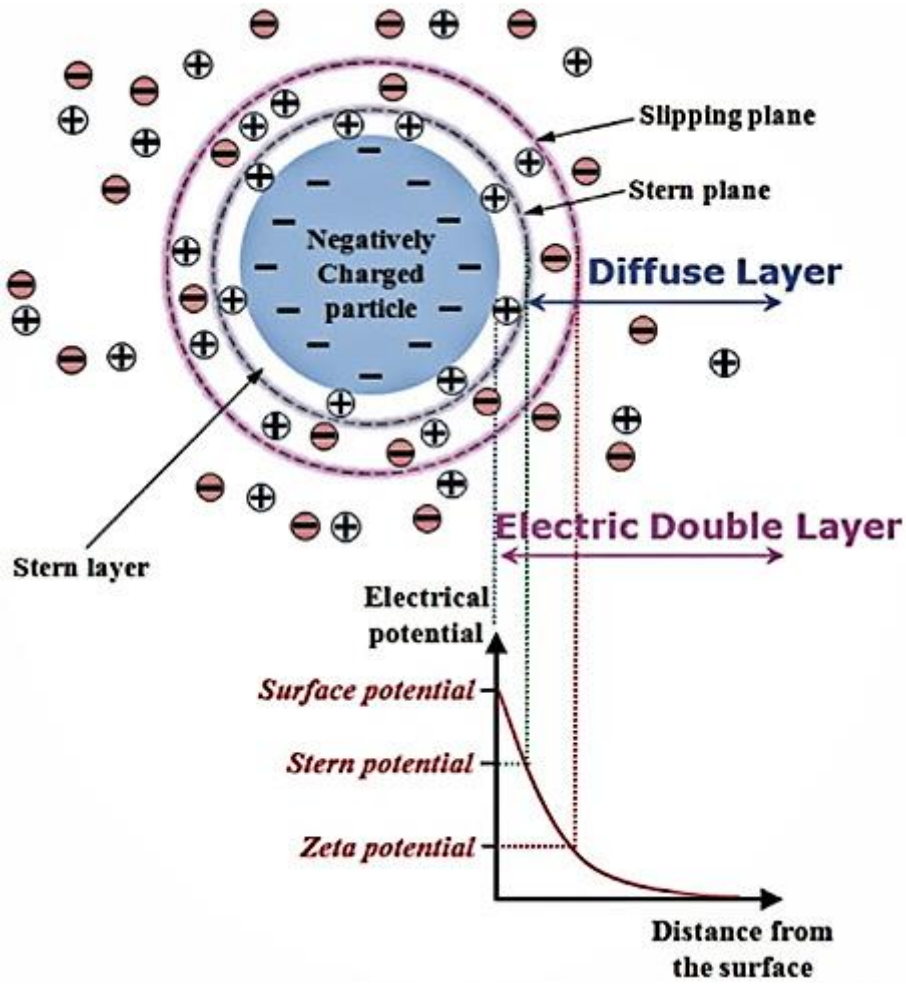


Figure 2.4.3 The schematic of formation of electric double layer from negatively charged particle in a suspension [135].

To utilise EPD in certain applications, there would be some important factors: the conductivities of both the suspension and the substrate, the particle electrophoretic mobility and the voltage applied to. Electrophoretic mobility is directly related to the zeta potential (ζ) of the particles within a given colloidal system, which is dependent on the permittivity and viscosity of the solvent [136]. The zeta potential is closely linked to the electric double-layer that forms around a charged particle, as depicted in Figure 2.4.3 [135]. It represents the potential difference between the slipping plane (the boundary where the liquid moves with the particle) and the bulk fluid [135]. This potential determines both the strength of repulsion between particles and their

direction of movement, and positively charged particles, for instance, will migrate towards and deposit on the cathode. Generally, a higher zeta potential indicates greater suspension stability and increased particle mobility. Research suggests that to prevent coagulation or flocculation of the particles, the absolute value of the zeta potential should be at least 30 mV [137].

When charged particles reach the electrode, several deposition mechanisms have been proposed [138], including particle flocculation near the electrode, particle charge neutralisation, electrochemical particle coagulation, and the distortion and thinning of the electric double-layer. A widely accepted view is that deposition largely depends on the loss of short-range order, meaning a decrease in suspension stability and electrophoretic mobility near the electrode. As particles approach the electrode, their zeta potential is reduced, suppressed by either local ions, neighbouring particles, or direct contact with the oppositely charged electrode. This reduction leads to the particles coagulating, accumulating and ultimately depositing onto the electrode.

To sum up, several strength and limitations of EPD could be identified. The advantages could be demonstrated below:

1) The coating could be easily controlled with changing the applied field [139].
2) Approachable for composite coating production by co-deposition process with different types of metal [131,140] and particles [141,142].
3) Managed to be applied onto complex structures, such as porous structures and mesh.
4) Relatively approachable equipment and cost-effective.
5) Safety selection. Ambient temperature and non-strong acid desired.

The disadvantages:

1) Limited the substrate material from electric conductive and non-resolvable to aqueous solutions, though non-conducting materials could be utilised in some situations [143].
2) Electrolytic decomposition of water in aqueous electrophoretic deposition, where the electric power would be waste.
3) It might require further procedure after EPD, such as sintering to dense the coating.
4) Anodes could be dissolved under electrochemical reactions.
5) Agglomeration of graphene in some cases is difficult to prevent [144].

2.4.3 Electro Brush Plating (EBP)

2.4.3.1 Principle of EBP

Electro brush plating (EBP) has emerged as a significant method for fabricating composite coatings and has attracted considerable attention from both industry professionals and nanotechnology researchers due to its simplicity, rapid deposition rate, and broad compatibility [145–147]. EBP is also named as selective electroplating because of its flexibility for plating selected areas rather than coating the whole surfaces by conventional tank electroplating. Hence, this technique is widely utilised for elective coating, component repair and remanufacturing [145–147].

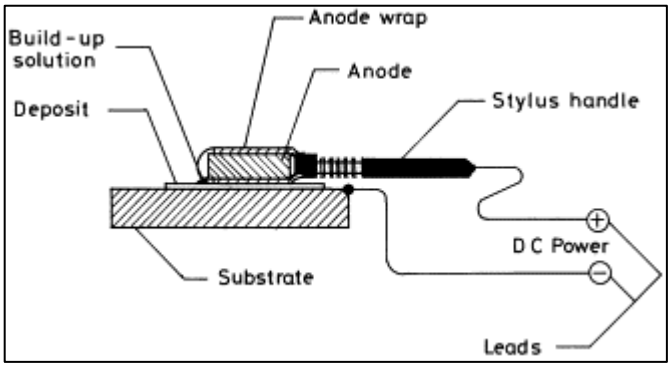


Figure 2.4.4 Schematic of electronic brush plating (EPB) [148].

Electro brush plating is a refined derivation of conventional electroplating, characterised by the establishment of an electric field between two electrodes submerged in an electrolyte solution (e.g. a copper salt solution for copper plating). In both techniques, the coating typically forms at the cathode, which is the target object. The primary difference between these methods lies in the mobility of the electrodes: while traditional electroplating involves stationary electrodes immersed in a tank containing the electrolyte for plating [149–152]. EBP (as depicted in Figure 2.4.4) [148], like electroplating, also requires two electrodes with one of the electrodes as the plating pen wrapped with absorbent cloth that holds the plating solution. During the electro brush plating process, the operator manually guides the anode pen across the surface of the workpiece at a consistent speed. Deposition occurs only when the anode pen contacts the workpiece, with the power supply remaining continuously active [145]. Coating is plated with continuous movement of the plating pen on sample surface, under certain parameters. There are electrical chemical reactions of positive ions during the plating process, such as plating of Cu or Ni to certain substrate. A GO containing composite coating can be produced by the EBP treatment [153,154]. One of the significant advantages of electro brush plating is its ability to achieve targeted deposition, thereby conserving both electrical energy and plating solution. In addition, the mechanical movement of the pen can help to address the issues of aggregation of nano particles during conventional electroplating thus ensure even distribution of nano

reinforcements (such as GO) within the composite coatings.

2.4.3.2 Applications of EBP

Owing to the super close electric electrode distance working, the Electro Brush Plating (EBP) shows significant potential for creating nano-composite coatings. A range of particles, such as zirconia (ZrO_2) [155], silicon carbide (SiC) [156], tungsten carbide (WC) [157,158], molybdenum disulfide (MoS_2) [159], alumina (Al_2O_3) [160,161], as well as nano nickel and carbon particles [162], can be introduced into the plating solution and subsequently embedded within the deposit. Additionally, EBP is capable of depositing composites that contain carbon nanotubes (CNTs) [163]. Compared to traditional electro co-deposition methods, EBP offers advantages such as producing more compact coatings with enhanced adhesion [164]. Furthermore, the movement of the anode pen across the substrate surface allows particles to be physically "pushed" into the deposit, in addition to the electrolytic deposition process, thereby increasing particle incorporation. While there have been some studies on the electrodeposition of graphene-based composites [165–170], the limited application of EBP for the fabrication of these composites has been explored [171–174].

Recent researchers based on GO/Ni composite coating produced by this technique shows better adhesive strength and uniformity than EPD method [175]. The GO/Ni composite coating presents higher adhesive strength than coatings produced by EPD technique, owing to the chemical bonding between Ni and steel substrate produced by the plating process. Moreover, the continuous brush plating process resulted in relatively high uniformity of the GO suspension in plating solution. However, except for our recent paper, there is no other published work on developing Cu/GO composite coating with desirable tribological property (low friction and high wear resistance) for sliding bearing application using the EBP technique.

2.4.4 GO Reduction Techniques

There are mainly two catalogues of electrochemical deposition techniques to produce GO coatings, which are electro-phoretic deposition (EPD) [176,177] and electro-brush plating (EBP) [178].

Conventional EPD technique produces GO coating by deposition of positively charged GO to the substrate (cathode) [108]. There are researches introducing other particles to produce composite deposition coating, such as introducing nano-copper particle [176,177] and silver nano-particles [179]. This is a facile technique, and the deposition of GO and other nanoparticles is controllable. Furthermore, the bonding introduced by the electric field is stronger than the graphene coatings produced by solution-flow or CVD transferring methods. However, the agglomeration of GO particles in aqueous solutions such as $CuSO_4$ solution will significantly influences the uniformity of GO or GO composite coating. This problem has resulted in relatively poor mechanical and chemical performance of those coatings.

2.4.5 Reduction of Graphene Oxide

Among the various applications of graphene and graphene-enhanced composite materials, one of the most cost-effective approaches is the utilisation of graphene oxide (GO). As graphene oxide (GO) possesses great hydrophilicity, it can be dissolved into aqueous-based electrolyte solutions. Moreover, their electronegative property presents in aqueous enable its movement obeying certain direction within an electric field. Hence, applying GO coatings by electrochemical deposition techniques is applicable [110].

Reduced graphene oxide (rGO) has become widely recognised as a primary resource for producing graphene suitable for laboratory applications. The reduction of GO generally

involves three key steps: graphite oxidation, then exfoliating of graphite oxide and subsequent reducing of graphene oxide. In the initial stage, oxidative ions and molecules intercalate and expand the graphite's layered structure, leading to the formation of graphite oxide. Through exfoliation, graphene oxide can be produced by overcoming the weakened van der Waals forces, which has resulted from the increased interlayer distance in the expanded graphite structure. With various reduction methods, reduced graphene oxide is generated before utilised in their applications with better properties than the GO.

2.4.5.1 Chemical reduction of GO

Hydrazine (N_2H_4) was among the first reduction agents reported for the reduction of graphene oxides (GO), which is broadly used owing to the efficiency of the reduction degree of GO [180]. The reduction procedure would occur with certain concentrations suspended into the solution containing graphene oxide under a temperature 80-100ºC for 3-24 hours [180,181]. The carbon-to-oxygen (C/O) ratio of GO could be increased by about 3 times to 5 times, depending on the parameters applied [181,182].

Hydrazine is highly effective at removing oxygen; however, its use as a reduction agent has limitations. Specifically, it can lead to the agglomeration and precipitation of reduced graphene oxide (rGO) sheets from the solution [180,181]. Furthermore, in order to improve the C/O ratio, other chemicals should be introduced to reduce the influence of hydrate in the hydrazine, such as potassium hydroxide (KOH) [183], incorporating ammonia [184] or adding a polymer before reaction [181]. Although hydrazine is highly effective in reducing GO components, its major drawback is its high toxicity, which presents serious risks to both researchers and environmental sustainability.

Alternatively, other chemicals like L-ascorbic acid (Vitamin C) [185], hydroiodic acid (HI) [186], and sodium borohydride ($NaBH_4$) [187], are recognised as effective reducing agents. Vitamin C is particularly noteworthy due to its human safety and environmental friendliness.

2.4.5.2 Thermal reducing GO

Graphene oxide (GO) can be reduced through a thermal shock process involving high temperatures in environments such as vacuum, inert gases (like argon), or reducing gases (such as hydrogen). Studies indicate that GO experiences significant mass loss in the temperature range of 200ºC to 250ºC due to the breakdown of its oxygen-containing groups [181]. At temperatures below 100ºC or above 250ºC, only minimal mass loss is observed, primarily attributed to the evaporation of water molecules adsorbed on the GO [181]. For effective exfoliation of GO layers, it is generally necessary to heat at a rate of 2000ºC/min and maintain temperatures above 1000ºC [188,189]. The annealing process is usually performed under vacuum, with inert gases, or in vacuum. Although thermal reduction can produce reduced graphene with high electrical conductivity, it has the disadvantage of high energy requirements and is not suitable for substrates with low melting points, such as polymers.

2.4.5.3 Electrochemical reduction

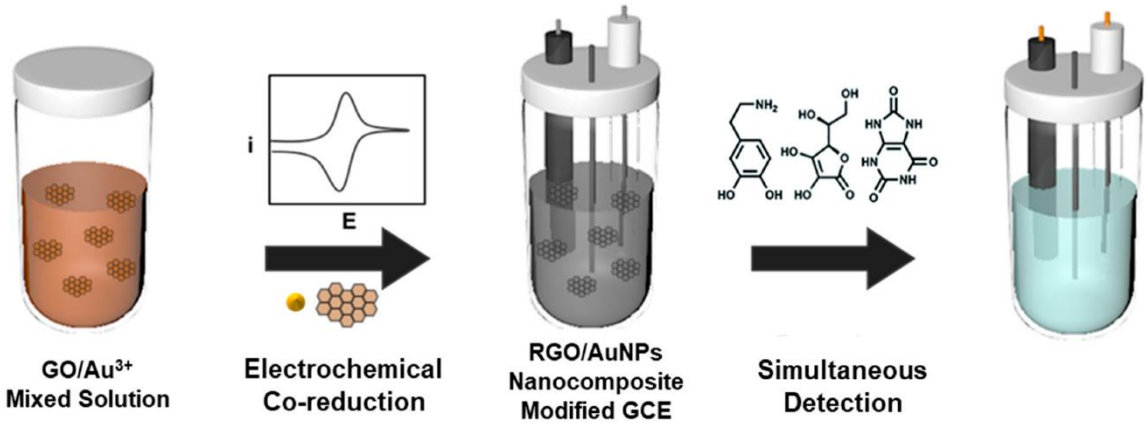


Figure 2.4.5 Fabrication of rGO composite with only one-step of electrochemical reaction [190].

The GO electrochemical reduction presents a highly efficient, non-destructive and eco-friendly approach. This method is characterised by its rapid processing, cleanliness, and low energy requirements. It operates via electron transfer between GO and a counter electrode, eliminating the need for aggressive chemicals, elevated temperatures, or complex vacuum apparatus; typically, a standard electrochemical cell at ambient temperature is adequate. This technique is particularly beneficial for the in-situ reduction of GO coatings applied to substrates such as ITO glass, PET films, metallic surfaces and silicon wafers [191–194], thereby avoiding issues related to the re-dispersion of reduced graphene oxide (rGO).

Electrochemical reduction can be performed using either cyclic voltammetry (CV) or constant voltage (DC) methods. For example, Lee et al. [195] employed cyclic voltammetry (depicted in Figure 2.4.5), immersing GO-coated electrodes and counter electrodes in a 0.8 mM $HAuCl_4$ solution and conducting a scan at a scan rate of 10 mV/s between 1.5 and -1.0 V. Alternatively, Peng et al. [196] documented the reduction of solid GO films at a constant voltage of -1.1 V in a 0.5 M $NaNO_3$ solution. In both cases, the resulting electrochemically reduced GO displayed

electrochemical activity that was comparable to, or even surpassed, that of chemically reduced GO. However, it should be pointed out that it is difficult, if not impossible, to reduce GO within composite coatings on relatively large components.

2.5 Graphene-related Materials for Surface Protection

2.5.1 Tribological Applications of Graphene

2.5.1.1 Tribological property of graphene on nano-scale

In an earlier study conducted by Lee et al. in 2009 [197], the frictional behaviour of mechanically exfoliated graphene with varying layer numbers was systematically examined using friction force microscopy (FFM) and atomic force microscopy (AFM) techniques. The study revealed a steady decrease in frictional force with an increasing number of graphene layers, ultimately approaching the frictional characteristics of bulk graphite [197].

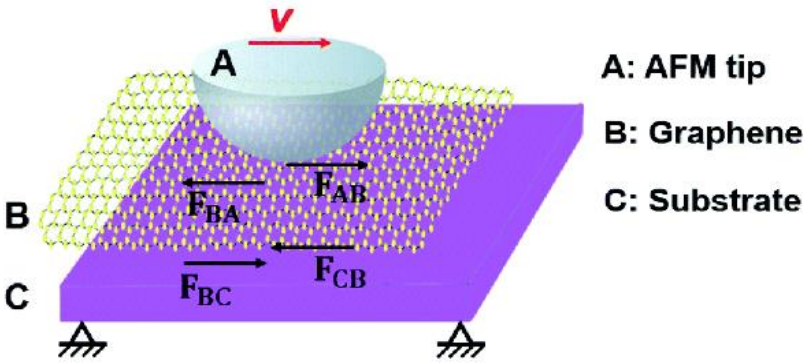


Figure 2.5.1 Schematic of nano-scale friction test under AFM Si tip [198].

Earlier TEM observations have shown that graphene monolayers, which exhibit intrinsic ripples, are not perfectly flat, due to their thermal stability [35]. This led to the proposal of the "rippling-

rug" mechanism [199,200], where the increased contact area between the tip and the graphene sheet, caused by out-of-plane ripples (Figure 2.5.1), results in higher friction. However, the effect diminishes significantly when the graphene is strongly adhered to the substrate or when the sheet is thicker and more rigid. Marchetto et al. [201] conducted a microscale investigation into the friction and wear properties of single-layer graphene epitaxially grown on silicon carbide (SiC), utilizing a multi-asperity FFM equipped with Ruby sphere tips. Their study revealed an exceptionally low initial friction coefficient of 0.02, which increased to 0.08 after 100 cycles of reciprocating sliding. This outstanding lubricating performance was attributed to the rigid SiC substrate and the strong interface bonding, which inhibited out-of-plane deformation, thereby reducing the contact area and consequently lowering the friction.

2.5.1.2 Tribological properties of GO derives of graphene

Due to the presence of defects, deformations, and functional groups within the graphene lattice, the tribological properties of graphene products often differ significantly from the theoretically predicted values. Peng and colleagues [202] have studied the nanotribological properties of multilayer reduced graphene oxide (MRGO), multilayer graphene oxide (MGO) and mechanically exfoliated multilayer graphene (MEMG) after being deposited on SiO_2 substrates. The investigation, conducted using AFM under ambient conditions, demonstrated that all three types of graphene layers exhibited lower friction compared to bare SiO_2 substrates. The friction values increased in the following order: MEMG, MRGO, and MGO. MEMG displayed the lowest friction coefficient, attributed to its perfectly planar lattice and hydrophobic nature. In contrast, the presence of oxygen functional groups on MGO resulted in a hydrophilic surface, leading to increased friction. The wear of graphene oxide (GO) decreases as the C/O ratio increases, suggesting that by tailoring the structure of GO, it is possible to achieve tribological properties similar to those of graphene.

It is important to note that some studies have shown bulk graphite exhibits lower friction than graphene with fewer than five layers [197,203,204]. Conversely, other researchers have reported higher friction for that bulk graphite [205–207]. Such seemingly contradicting results are most probably due to the fact that tribological tests can be influenced by various factors, including the purity and quality of graphite and graphene [208]. Besides, the variance in tribological testing conditions and the adhesive strength between graphene and its substrate could also influence the results [198].

2.5.1.3 Tribological properties of graphene-based materials in macro-scale

Although the above nano/micro-scale studies, typically conducted using AFM or tribometers with loads under 1000 nN, have significantly advanced our understanding of graphene's tribological properties, it is crucial to also examine graphene and graphene-based materials on a macro scale under a relatively high load more relevant to engineering applications. This involves using reciprocating or unidirectional sliding tribometers to gain insights more applicable to practical applications. Research into the macro-scale friction and wear of graphene has focused on graphene-based coatings, graphene/GO-reinforced composite coatings, and graphene-based lubricant additives. However, the latter is beyond the scope of this project. For large-scale applications of graphene-based materials, two primary approaches are considered in this review: the use of large-area graphene sheets on specific substrates and the development of graphene-enhanced composite materials. As discussed in Section 0, chemical vapor deposition (CVD) is the most widely employed method for producing graphene sheets at large scale. However, the weak adhesion between the transferred graphene and the substrate materials excludes its application in macro-scale under relatively high load. Consequently, it will focus on graphene/GO-based composite materials, which would offer more desired performance for real engineering applications.

There is growing interest among researchers in graphene-based materials reinforced composites to overcome the challenge of weak bonding in graphene coatings on large material surfaces (such as biomaterials), and researchers have developed graphene/GO-based composite coatings and investigated their tribological properties [209–216].

Graphene and its derivatives have demonstrated exceptional tribological performance in polymer, ceramics and metal-based composites. For the polymer composite, Roy et al. [213]

demonstrated that GO reinforcement into polyimide (PI) would not only enhance the tribological and mechanical properties but also improve the thermal stability of the composite. The improvement was attributed to the oxygen functional groups in GO, which facilitate a strong interface with the PI matrix. The high aspect ratio and intrinsic strength of GO sheets further reinforced the composites. Likewise, Thangavel and colleagues [214] investigated the tribological and structural properties of poly (vinylidene fluoride) (PVDF) nanocomposite thin films reinforced with GO. They evaluated the tribological behaviour of these coatings using a reciprocating tribometer with a stainless-steel counter ball under a 10 mN load. GO, and the addition of the second phase into the polymer coating was found to reduce both friction and wear of the PVDF. However, beyond an optimal GO content, both the friction coefficient and wear rate began to increase. Other types of polymers have also been studied as matrices for GO-reinforced lubricant materials, including the polyvinyl alcohol (PVA) [217], polyaniline (PANI) [218] and epoxy [219] composites.

Prashantha Kumar et al. [220] developed an aluminium (Al) 6061 metal-graphene composite using microwave sintering, with graphene uniformly dispersed in the alloy through ultrasonic assistance. The aluminium alloy, composed of 2-10 μm particles, was reinforced with 0.2-0.4 wt% graphene. This addition significantly reduced the friction coefficient from approximately 0.40 to 0.25 as the applied load increased from 50 to 150 N, as shown in Figure 2.5.2. The improved tribological performance is likely attributed to the presence of graphene clusters, which reduce friction through a self-lubricating mechanism.

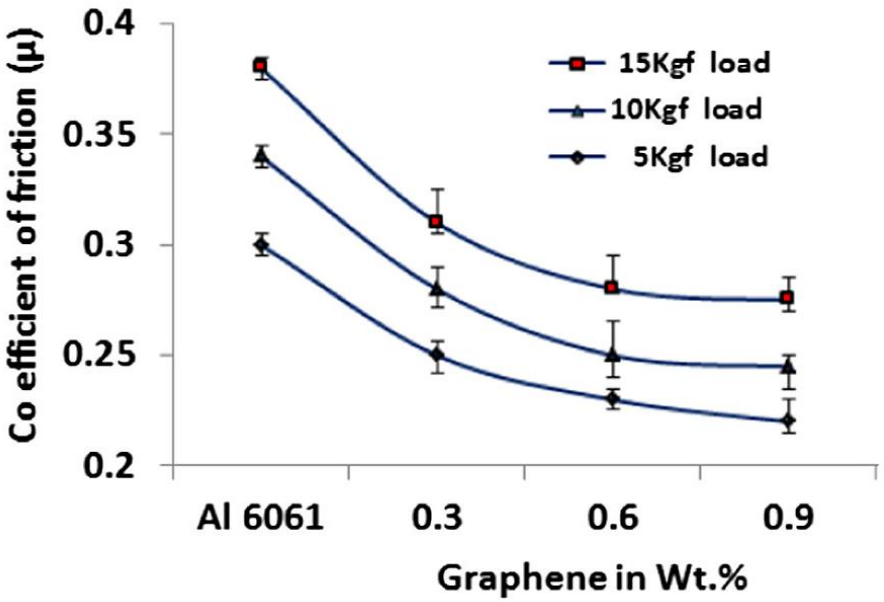


Figure 2.5.2 The friction coefficient change under different loads and graphene fractions in GO/Al composite materials [216].

Graphene oxide (GO) appears to be a more suitable option than pristine graphene for reinforcing bulk composites, largely because its oxygen groups improve interaction with the composite matrix. Additionally, GO's lower cost and greater availability make it an attractive choice. However, the majority of studies on GO composites [221–227] have primarily examined their mechanical properties, with limited attention given to their tribological performance.

Filizzola et al. [228] investigated the production of graphene oxide (GO) reinforced epoxy resin composite coatings on stainless steel substrates. Their findings revealed that the addition of just 0.5% GO significantly improved both the wear resistance and Young's modulus of the composite. The GO composite was observed to follow a transfer layer mechanism, contributing to the enhanced wear resistance [229,230]. However, as the concentration of GO increased, a slight rise in friction was reported, similar to what has been observed in CNT/UHMWPE composites [231]. Despite this minor increase in friction, the GO/epoxy composites demonstrated a notable improvement in wear resistance [232]. Nevertheless, research on metal-

graphene composites remains limited, highlighting the need for further studies focused on the fabrication and evaluation of the mechanical and tribological properties of graphene-reinforced metallic composites [146].

2.5.2 Impermeability and Corrosion Barrier

Although only one atom thick, theoretical defect-free graphene membranes can be considered perfect non-permeable materials [233]. As mentioned in Section 2.2.1, the compact hexagonal carbon lattice, with a mere 0.142 nm distance between C-C bonds, is the primary reason for this exceptional impermeability. The geometric pores of a pristine graphene lattice would be 0.246 nm in diameter if only the nuclei are considered. When accounting for the van der Waals (vdW) radius of carbon atoms (0.11 nm), this diameter further reduces to just 0.064 nm. Interestingly, hydrogen gas molecules, the smallest gas molecules, measure 0.074 nm, which is larger than the pores of pristine graphene. Additionally, the basal plane of graphene repels foreign atoms and molecules while remaining transparent to electrons [234]. Consequently, graphene has the potential to develop the thinnest corrosion barriers [235] and selective permeable membranes [77]. Pristine graphene has also proved impermeability by experiments [77,234]. GO as one of the most important graphene derivatives, has reported also possesses impermeability [236].

2.6 Summary of Literature Review

In this chapter, the history of graphene research is reviewed in Section 2.1, followed by the unique properties of graphene related to the structure of graphene review before (Section 2.2). Graphene oxide (GO) and reduced graphene oxide (rGO) hold significant promise for various engineering applications, particularly where exceptional electronic properties are not critical, due to their cost-effective synthesis and scalability for mass production.

In Section 2.3, the advantages and limitations of various substrate materials are examined, laying the groundwork for the introduction of specific coating techniques aimed at enhancing their characteristics and properties. Section 2.4 explores potential methods for manufacturing graphene-based coatings. While graphene coatings produced via the transfer of CVD films or solution-flow methods (Section 2.4.1) exhibit great physical properties, their mechanical applications are hindered by insufficient adhesive strength. On the other hand, GO coatings deposited through EPD demonstrate slightly enhanced adhesion to the substrate but are limited by their thickness and low load bearing capacity. The EBP technique (Section 2.4.3) emerges as a more promising approach, offering both increased adhesive strength, thickness and load bearing capacity. There is limited research focused on metal graphene composite coating using EBP technique and no work has been reported by other researchers on the development of GO/copper composite4 coatings.

The main applications of graphene would be located in tribological and corrosion resistance which is review in Section 2.5. Although graphene possesses extraordinary tribological properties in both nano and macro scale, the low adherent strength of transferred graphene coating is not suitable for tribological applications such as copper-based sliding beatings. Hence, this PhD research project was directed at developing novel GO/Cu composite coatings using the highly flexible and cost-effective brush electroplating technique for Cu-based sliding bearing applications.

Chapter 3 Experimental

3.1 Substrate Materials

Two types of substrate materials, 316 stainless steel and brass, were used in this study. 316 austenitic stainless-steel sheets with a thickness of 2.5mm were used as the substrate material mainly for coating development and process optimisation. The nominal chemical composition provided by the material supplier and the composition measured by EDX in this study are shown in Table 3.1.1 below. It can be seen that except for carbon, all other elements are within the range of the nominal composition. However, the measured carbon content is higher than its nominal value. This is mainly due to the large measurement error of EDX for light elements and partially due to potential contamination of the sample and the SEM chamber. 316 stainless-steel samples were cut from the sheets into 30 × 60 × 2.5 mm with an alumina cutting wheel and then wet ground from grit 120 to grit 1200 with silicon carbide grinding paper. Prior to electro-brush plating, samples were cleaned with soapy water then acetone in an ultrasonic cleaner (200 W, Ultrawave U2500H) and dried by hot air.

Grade CZ121M brass rod purchased from RS Components Ltd was used as the substrate material for the coatings mainly for property evaluation and the nominal chemical composition provided by the supplier is shown in Table 3.1.2. The received brass rods of 21 mm in diameter were cut to 5 mm in thickness using alumina blades with Struers Accutom-5 machine. Those discs were ground to grit 1200 with SiC paper, then immersed into the acetone for ultrasonic cleaning for 15 minutes and finally dried with hot air before applying coatings in order to remove grease and contaminations that would hinder the electrical conductivity for brush

plating and reduce the bonding between the coating and the substrate.

Table 3.1.1 Chemical compositions of the 316 stainless steel substrate: nominal values and EDX measurements.

Elements	Fe	C	Cr	Ni	Mo	Mn	Si	P	S
wt.% (nominal)	balance	<0.03	16-18.5	10-14	2-3	<2	<1	<0.045	<0.03
wt.% (EDX)	balance	0.88±0.23	17.48±0.17	10.03±0.19	2.1±0.34	1.29±0.12	0.38±0.05	0.03±0.03	0.02±0.01

Table 3.1.2 Nominal and measured chemical composition of brass substrate material.

Elements	Zn	Cu	Pb
wt.% (nominal)	balance	57-59	<0.1
wt.% (EDX)	balance	57.58±0.29	1.01±0.14

3.2 Graphene Oxide Material

Graphite flakes (Alfa Aesar, -325 mesh, 99.8%) were oxidised using a modified Hummer's method [237,238], and subsequently exfoliated through ultrasonication. In this procedure, 1.0 g of graphite flakes was combined with 6.0 g of potassium permanganate ($KMnO_4$). This mixture was then gradually introduced into a solution consisting of 120 mL of concentrated sulfuric acid (H_2SO_4) and 13 mL of phosphoric acid (H_3PO_4) in a 9:1 ratio. To ensure controlled conditions, the reaction was carried out in a water bath maintained at 50°C, with continuous stirring for 12 hours. The reaction vessel was then left to cool to room temperature overnight. To conclude the oxidation process, the mixture was placed in an ice-water bath, and 3 mL of 30% hydrogen peroxide (H_2O_2) was carefully added to the reaction.

The production of graphene oxide (GO) from graphite is a critical step in the process of creating graphene oxide coatings. Photographs were taken at various stages of the Hummer's oxidation process to document the changes in the reaction mixture, as illustrated in Figure 3.2.1. Initially, at the start of the oxidative reaction (Figure 3.2.1a, stage 1), the mixture appeared dark green. As the reaction progressed to stage 2 (Figure 3.2.1b), the liquid turned a chocolate brown colour. By stage 3 (Figure 3.2.1c), the mixture had changed to dark yellow. After the removal of excess $KMnO_4$, the resulting liquid became light yellow, as depicted in Figure 3.2.1d. Upon completion of the oxidation process, graphite oxide was formed within the reaction mixture.

The mixture was first filtered using filter paper, and the solid material collected on the filter was carefully separated. This solid residue was then subjected to repeated washing with 30% hydrochloric acid (HCl) using a centrifuge, with each wash cycle repeated 15-20 times. During each cycle, the sample was centrifuged at 5000 rpm for 10-15 minutes to efficiently remove SO_4^{2-} ions. After centrifugation, the supernatant was discarded, leaving a slurry at the bottom of the tube. The complete removal of SO_4^{2-} was verified by the absence of a precipitate upon the addition of barium chloride (BaCl) to the supernatant.

Following this, the residue underwent approximately 20 washes with ethanol, again using the centrifuge under the same conditions. After the washing steps, the slurry was dried and then re-dispersed in deionised water in beakers. The graphite oxide was then exfoliated using an ultrasonic bath (200 W, Ultrawave U2500H) for 2-3 hours. This process helped break down the graphite oxide into finer layers. The resulting suspension was then centrifuged at 1000 rpm to separate the exfoliated material.

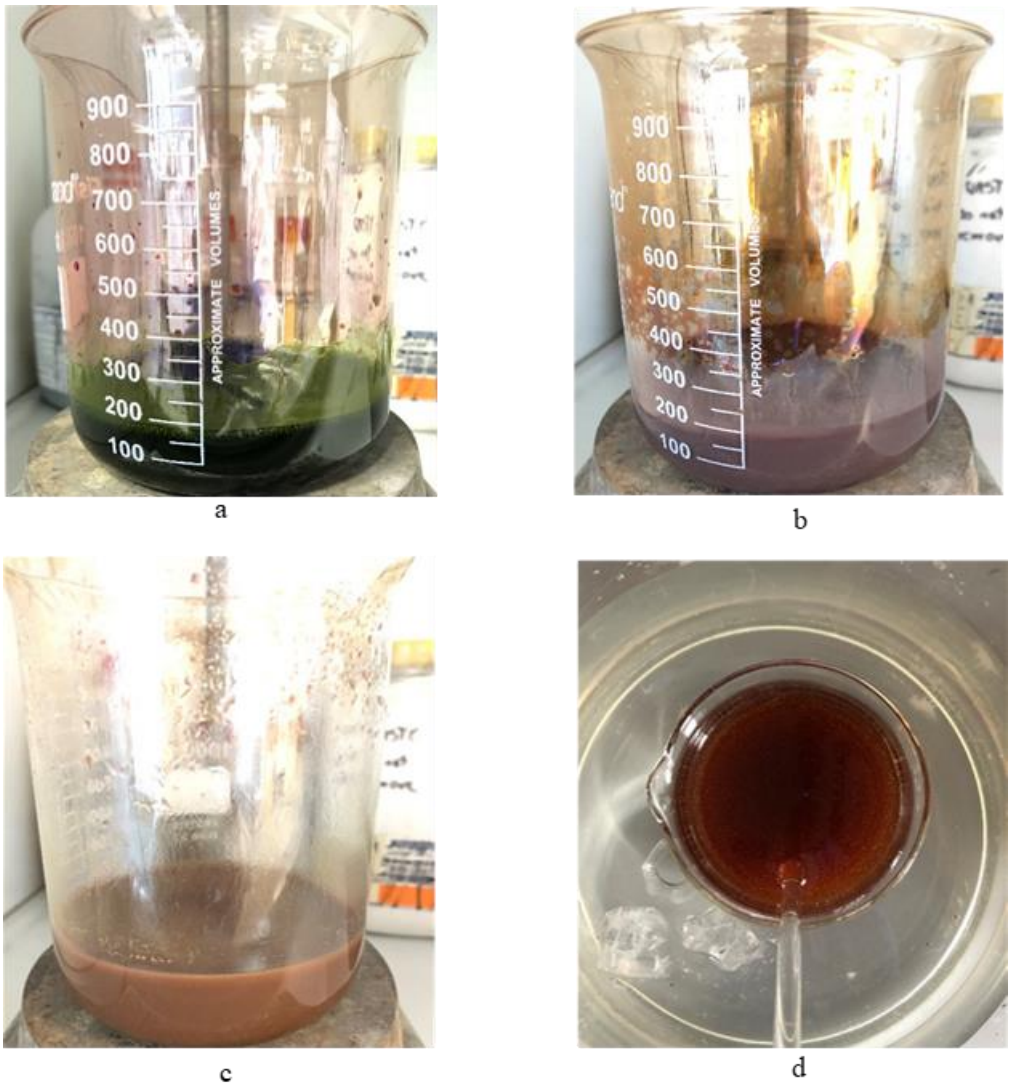


Figure 3.2.1 Images taken during reactions: (a) stage 1 of oxidation reaction; (b) stage 2 of oxidation reaction; (c) stage 3 of oxidation reaction; (d) after removed retained $KMnO_4$.

As reported in the literature [239,240], starting with 1 g of graphite powder typically yields about 1.3 g of graphene oxide, with the extra 0.3 g resulting from the incorporation of oxygen-containing functional groups during oxidation. Through the ultrasonic exfoliation process, it was possible to obtain graphene oxide sheets ranging from monolayers to a few layers thick, using a 150 W ultrasonic device for approximately 2-3 hours [20]. This careful procedure

ensures the production of high-quality graphene oxide, which is crucial for further applications.

Soluble graphene oxide powder supplied by Sigma Aldrich, Co., Ltd was also used in this research. 0.020 g GO powder was dispersed in 100 mL Cu acid brush plating solution then the mixture was suspended for 1 hour in ultrasonic bath (Ultrawave U2500H, 200 W) before plating [241].

3.3 Production of Composite Coating

Cu and GO/Cu coatings were generated by brush plating technique on 316 stainless steel and brass substrates. Brush plating process on 316 stainless steel was carried out with nano brush plating unit (NBP-100) developed by the Surface Engineering Research Institute, CMES, China (as depicted in Figure 3.3.1). The brush plating process consists of four main steps: electro-cleaning, electro-activating, nickel-strike and Cu or GO/Cu coating processes.

The 316 stainless steel substrates were securely fastened to the purposely fabricated working table, as illustrated in Figure 3.3.2a. The design of this working table ensures that all specimens are clamped under uniform conditions, thereby enhancing experimental repeatability and reliability. During the brush plating process, the stainless-steel rectangular plate is positioned at the upper left corner, as depicted in Figure 3.3.2b. To prevent substrate movement, four white bars are placed, each with a height of 2.5 mm ± 0.1 mm, ensuring consistent alignment with the substrate. Additionally, a clip on the opposite side further stabilizes the substrate. This setup allows for the production of samples under consistent conditions, ensuring the reproducibility of the experimental results.

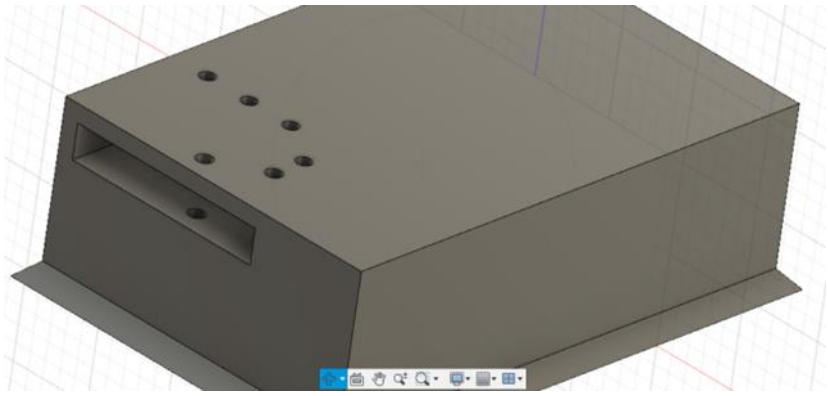


Figure 3.3.1 Image of electro-brush plating equipment.

Although the samples were grinded and cleaned and dried before electric brush plating, some oxides impurities might remain on the surface to be brush plated. Electrical cleaning process was used to remove surface impurities which cannot be removed by physical method. A passivation film normally formed on stainless steel surfaces, which leads to poor bonding strength of coating when it is applied directly by brush plating. Hence, electro-activating is applied to activate the surface by removing the passivation film and roughen substrate surface to increase the coating bonding strength. However, such electro-activating might be not enough for stainless steel substrate due to high electrochemical activity of chromium (Cr) and iron (Fe) within stainless steel. The most common used method is so-called ultra-thin nickel strike with special nickel electric plating solution (SIFCO Applied Surface Concepts (ASC)., Ltd). With this certain solution, an ultra-thin layer of special nickel layer would be produced. This Ni layer has relatively strong adhesive strength to stainless steel which would act as glue to bond stainless steel substrate and GO/Cu or Cu layer together strongly. At final plating step, GO of 0.2 g/L concentration would be blended into $CuSO_4$ plating solution with pure $CuSO_4$ solution

plated samples as control group. After each step of the plating procedure, the sample surfaces were rinsed under running water to remove any remaining plating solution, followed by rinsing with deionised water for 1 minute and dried using hot wind. The detailed parameters and process are summarised in Table 3.3.1.

(a)



(b)

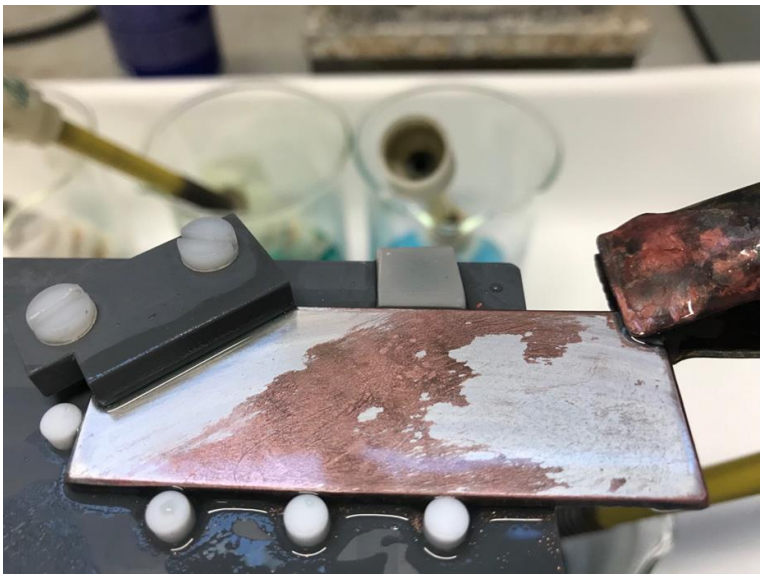


Figure 3.3.2 (a) 3D design model for the working table holding stainless steel specimens and (b) working picture.

Table 3.3.1 Electronic brush plating procedures for applying Cu coating and GO/Cu composite coatings on 316 stainless steel.

No.	Operation	Solution	Voltage/V	Time/min
1	Electrical clean	Cleaning solution	12	1
2	Electrical activate	Activating solution	12	2
3	Nickel strike	Special nickel solution	15	3
4	Final plating	Cu or GO/Cu solution	4, 6 and 8	30

Likewise, brush plating was also carried out with pulse brush plating unit provided by SPA Plating Co., Ltd. This unit could provide better finish than the previously stated unit. The brush plating experiments were employed to produce Cu and GO/Cu coatings on brass substrate, the process is demonstrated in Table 3.3.2. The plating process included three steps: active-cleaning, nickel strike and final copper-based plating. The active-clean and Cu plating solution were obtained from SPA Plating Co., Ltd. Nickel strike plating solution was supplied by SIFCO Applied Surface Concepts (ASC)., Ltd. For those solutions contains GO suspensions, the GO/Cu solutions were also ultrasonicated for more than 1 h within a water bath under a temperature of 40-50 ºC. After each step, specimens were cleaned with running water for around 60 seconds and dried with hot wind.

Table 3.3.2 Brush plating process for applying Cu coating and GO/Cu composite coating on brass.

No.	Operation	Solution	Voltage/V	Time/min
1	Active-cleaning	Active-cleaning solution	7	3
2	Nickel strike	Special nickel solution	7	3
4	Final plating	Cu or GO/Cu solution	2-6	30

3.4 General Characterisation

3.4.1 Raman Spectroscopy

A Renishaw inVia Reflex Raman spectroscope (Figure 3.4.1) was employed to obtain Raman spectra of graphite, GO powder, and GO/Cu coatings. The graphite and GO powders were placed on flat microscope slides measuring 76 × 26 mm with a thickness of 1.0 to 1.2 mm, provided by Thermo Scientific, Ltd. The GO/Cu coating samples were also placed on the same type of microscope slides and then positioned in the Raman chamber.

To locate the focus on the desired area for acquisition, a "20×" objective microscope was used, and the Raman scanning was performed at the centre of the field of view. Raman spectra were obtained using a 488 nm wavelength laser source, covering the range from 1000 to 3500 cm^{-1} to capture spectra of graphene, and from 100 to 900 cm^{-1} to gather information on copper oxides. The laser power was set to 50% of the 35 W laser source, with an exposure time of 10 seconds and three accumulations for each scan.

Data processing, including baseline removal, data smoothing, and noise reduction, was

conducted using WIRE software (version 4.2) developed by Renishaw. The Raman peaks were identified by referencing data from the literature.



Figure 3.4.1 Photo of the Raman spectroscopy used for graphene oxide and copper oxides measurement.

3.4.2 X-ray Diffraction (XRD)

The phase identification of the GO composite coating and the pure Cu control group on 316 stainless-steel substrates were carried out using Bruker D8 Advance x-ray diffractometer. Copper radiation tube was used to produce K_α resource (λ = 1.5405 Å). The XRD tests were performed from 40º to 100º of 2 theta position with 0.01º/s of steps. The phase structures of the GO composite coating and the pure Cu control group on brass substrates were investigated with Proto AXRD diffractometer (Figure 3.4.2). A copper line focus x-ray tube was used to produce

K_α resource (λ = 1.540593 Å) with 1.0 mm width of slits output to the sample. The input power was setting up at 30.0 kV and 20 mA. The XRD tests were performed from 20º to 100º of 2 theta position also with 0.01º/s scanning speed with 0.5 second of dwell time and 1/2 of snap. To index the peaks, identify the phases and calculate the crystalline size, the PANalytical X'Pert Highscore Plus software was utilised.

The crystalline size was calculated from the Scherrer's equation $D = k\lambda/\beta \cos\theta$, where the D represents the crystalline size from the direction perpendicular to coating surface, the λ is wavelength of X-ray resource (1.541864 Å), the θ is the Bragg's angle and the β is the full width at half maximum (FWHM) of the chosen peak [242]. The β could be influenced by the machine error resulting in FWHM expansion, and one of the methods to address this is to use the cadmium (Cd) standard sample to correct the FWHM expansion.



Figure 3.4.2 Photo of the Proto AXRD diffractometer utilised for pure Cu control group and GO/Cu composite coating surface.

3.4.3 Fourier Transform Infrared (FTIR) Spectroscopy

To study the graphite and graphene oxide powder, the ThermoFisher Scientific Nicolet 870 near-infrared spectrometer (UK) was employed. 2mg of sample powder to be measured was blended into 200 mg of potassium bromide (KBr) (≥ 99%, Sigma Aldrich, Co., Ltd). Compressed discs of 13 mm in diameter (Specac 3000, UK) were utilised to acquire FTIR spectra under transmission mode within the wavelength range of 4000 to 500 cm^{-1}, which is of 4 cm^{-1} resolution.

3.4.4 Surface Roughness Measurement

Ambios XP-200 stylus profilometer (tip radius 2 μm) was employed to measure the surface roughness and wear track profiles. For the roughness measurements, the stylus with a diamond tip scanned with a speed of 0.1 mm/s under a load of 8 mg for 10 mm in length. For the wear track measurement, the stylus scanned at a speed of 0.1 mm/s with 8mg of load in 1-2 mm length. All the measurements were repeated for at least three times and the average value was reported.

3.4.5 Scanning Electron Spectroscopy (SEM)

The feasibility study of GO/Cu composite coatings was conducted using a Philips XL-30 field emission scanning electron microscope (FESEM) to investigate surface morphology, layer structure, and the presence of graphene oxide within the coating. Images related to GO were captured under an accelerating voltage of 15 kV to prevent damage to the GO, while other images were taken at 20 kV. Additionally, a Joel 7000 field emission scanning electron microscope (FESEM) was used to analyse samples of brush-plated coatings on brass substrates at an accelerating voltage of 15 kV. This analysis aimed to reveal the presence of graphene oxide on the surface and within the layer structure of the GO/Cu composite coatings, as well as

the sample surfaces after wear and corrosion tests. An Apreo 2S HiVac scanning electron microscope (SEM) was utilised to obtain images of the surface morphology of typical worn tracks and their counterparts.

3.4.6 Energy Dispersive X-ray Spectroscopy (EDX)

For the Philips XL-30 FESEM, the INCA Energy system (Oxford Instruments) was used to obtain Energy Dispersive X-ray Spectroscopy (EDX) results. The in-situ elemental analysis was conducted within a few microns from the surface, with a spatial resolution of approximately 1-2 μm. The working distance, electron beam spot size, and other parameters were optimized to meet the specific requirements of the EDX analysis. Depending on the sample and type of analysis, different modes such as point, line-scan, and mapping were employed. For the Joel 7000 SEM, EDX (Oxford Instruments, Ultim Max 40) was utilised to detect the presence of graphene oxide on the surface and within the coating, as well as to observe elemental changes after wear and corrosion tests. Point EDX analyses were performed at the same accelerating voltage (15 kV) used for imaging, with each point analysed for 3 minutes. For corrosion tests, typical mappings were performed with a dwell time of 100 μs (0.1 ms) and a processing time of 1 second, resulting in a total scan time of approximately 5 minutes. Stack-layered EDX mappings were generated to reveal the elements on corrosion tested surfaces. Colour-chemical EDX on the Apreo 2S HiVac SEM was also employed to obtain colour mapping results of worn surfaces, worn counterparts, typical sample morphologies, crater bottoms, and layer structures.

3.4.7 Glow Discharge Optical Emission Spectroscopy (GDOES)

A glow-discharge optical emission spectrometer (GDOES, GDA Spectruma Analytic GmbH 650) was employed to measure and analyse the elemental depth profiles of brush-plated samples. The GDOES was also utilised to create craters with depths ranging from approximately 8 to 15 microns in the coating structures. These craters facilitated subsequent investigations of the newly exposed surfaces using Scanning Electron Microscopy (SEM) and Energy Dispersive X-ray Spectroscopy (EDX). During the Ar+ ion sputtering process, Cu and GO exhibited different sputtering rates, allowing GO sheets to preferentially remain at the bottom of the sputtering craters. The GDOES measurements were conducted with an excitation potential of 1000 V and a current of approximately 12 mA, producing craters with a diameter of 2.5 mm. These measurements were also used to determine the layer thickness of the coatings. To verify crater depth, a surface profilometer (Ambios XP-200) was employed following the GDOES analysis.

3.5 Mechanical and Tribological Property Assessments

3.5.1 Micro-hardness

Micro-hardness measurements were conducted using a Mitutoyo MVK-H1 micro-hardness tester, equipped with a Vickers indenter. The applied loads ranged from 10 to 1000 g. Prior to each set of measurements, the instrument was calibrated using a standard reference material (EP9716400, 757.3 $HMV_{0.3}$) to ensure accuracy. In this study, a load of 10 g was specifically chosen to maintain the indentation depth within 1/10th of the coating thickness. To ensure data reliability, each sample underwent a minimum of five indentations, with each indentation spaced more than three Vickers diagonal lengths apart.

3.5.2 Tribological tests

The reciprocating tribological tests of the substrate brass, Cu and GO/Cu coatings were conducted against ϕ8 mm 316 stainless steel balls (purchased from Spheric-Trafalgar Ltd,.) to evaluate the friction and wear performance under controlled conditions. The surface of samples was ultrasonicated (Ultrawave U2500H, 200 W) for at least 30 minutes before rinsed with deionised water, so that friction coefficient results could be more reliable. Those tests were performed under room temperature (around 18°C), around 47% humidity (MT-903, ATP Ltd.,) with a ball-on-plane tribometer (TE79 multi-axis, Phoenix Tribology Ltd., UK). The tests were carried out under 5N load at a speed of 5 mm/s under 0.5 Hz of frequency. Each test lasted for 30 minutes. Before the tribological test, the steel balls were cleaned with ultrasonic bath in soapy water and then with acetone to remove organic pollutants. The counterpart was replaced after each test, and new surface on counterpart was used in repeating tests (at least 3 times), to obtain relative reliable tribological data.

The samples were removed from the holder and further examined by a Surfcorder SE1700 profilometer to evaluate the wear performance of the coating samples and the uncoated brass. 2D worn ar along wear tracks were scanned no less than three positions (middle and two sides) and calculated. Then the worn area was multiplied by the wear track length of 5 mm to work out the wear volume loss. The worn track morphology, debris and worn surface were then examined by SEM and EDX.

3.6 Corrosion Property Evaluation

3.6.1 Preparation of Samples and Equipment

Samples of brass control group and with GO/Cu composite coatings were cleaned with soapy water under ultrasonic (Ultrawave U2500H, 200 W) for at least 30 minutes to remove grease on both sides, then under running water for around 2 minutes, and in deionised water for around 30 seconds before dried with hot air. As both sides would be connected to the test circuit, any impurities on the back of specimen were removed to ensure electric conductivity. All the glassware was also washed with soapy water, flushed under deionised water, and dried with hot wind, including beakers, glass rod, graduate cylinder (500.0 mL), volumetric flask (1000.00 mL) and standard funnel.

In this study, the corrosion tests were conducted in 3.5 wt.% of sodium chloride (NaCl) solution under ambient temperature (20 ºC). To prepare a 1000.00 mL solution, 35.00 g of NaCl powder (99.5% Sigma-Ardrich, Co. Ltd,.) was measured and pre-mixed with approximately 800 mL of deionised water in the beaker and filtered through analytical filter paper. The solution was transferred to volumetric flask through previous used filter paper on standard funnel and add deionised water to the curve of volumetric flask.

To perform corrosion tests, a Gamry Interface 100 instrument was employed. The accuracy of the instrument was relied on the regular signal calibration and 3-mintutes warm-up prior to every session. Figure 3.6.1 exhibits the configuration of the corrosion tester, which consisted of a counter electrode of platinum coated rod (ϕ6 mm), an Ag/AgCl reference electrode (Gamry Instruments) immersed in 3M of NaCl solution (99.5% Sigma-Ardrich, Co. Ltd,.) and samples fastened on the sample holder connected to the working electrode. The counter electrode, and

reference electrodes and reaction container were cleaned with running water and deionised water and rinsed with the 3.5 wt.% of NaCl solution before corrosion tests.

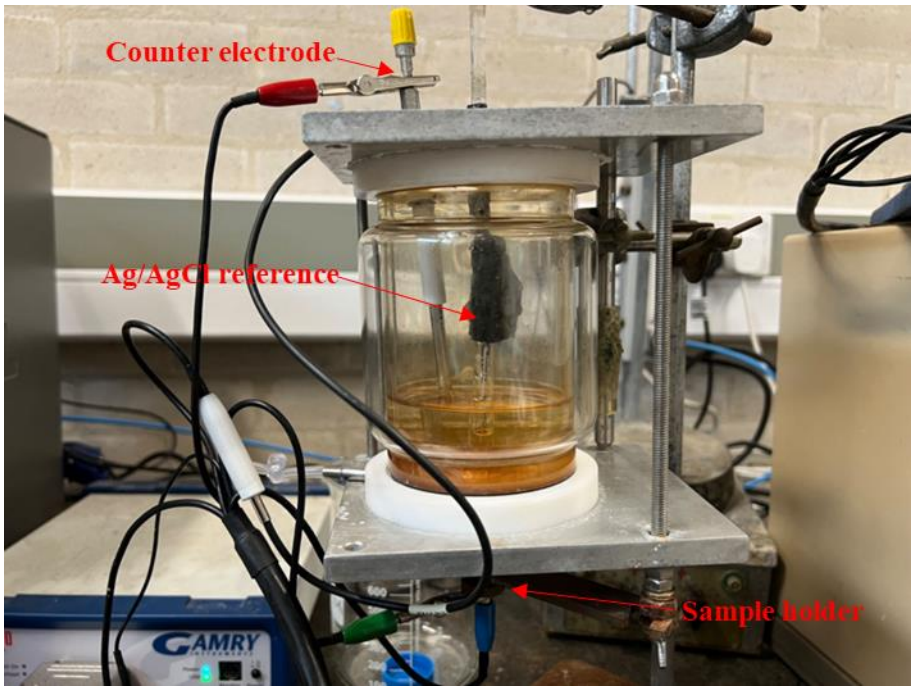


Figure 3.6.1 Electrochemical working station configuration.

3.6.2 Preformation of Open Circuit Potential (OCP)

Open circuit potential (OCP) measurements were performed as the initial stage of the electrochemical tests. In the absence of an external electric field, the potential difference between the reference electrode (Ag/AgCl electrode in this study) and the surface of the sample is defined as the OCP. The OCP values were continuously recorded for a fixed duration of 60 minutes. These OCP measurements were used to allow the sample surface to familiarise to the corrosion environment and to ensure the stability of the electrochemical interface for subsequent measurements.

3.6.3 Potentiodynamic Polarisation Test

Within the test sequence, the subsequent measurements started immediately when the previously stated OCP finished. From -0.5 to +1.5 V (versus the OCP), the potentiodynamic polarisation tests were carried out under 1 mV/s of scanning rate on the area (0.503 cm^2, round surface) immersed in 3.5 wt. % of NaCl electrolyte, to reveal both the cathodic and anodic polarisation of measured samples. Once the polarisation tests were finished, the external electric field was removed, and the sample was removed from the sample holder. The removed sample was flushed under tap water for at least 1 minute and rinsed with deionised water before dried with hot wind. The repeatability was ensured by at least two repeat measurements. The obtained potentiodynamic polarisation curves were analysed by the software provided also by Gamry Instruments (Echem Analyst) to perform Tafel fit to determine the corrosion potential (E_{corr}) and corrosion current density (I_{corr}).

3.7 Summary of Experimental

In this research, the fabrication and characterisation of copper-based self-lubricating and anti-corrosion coatings were systematically investigated. The experimental work began with the preparation of the raw substrate materials and graphene oxide (GO) precursors, providing the base for producing GO/Cu nanocomposite coatings (Sections 3.1 and 3.2). Then, an advanced fabrication process was developed using the brush plating technique to determine the optimal parameters for coating synthesis (Section 3.3).

Advanced characterisation techniques were employed to examine the microstructure of the coatings, providing insights into grain size distribution and the influence of processing parameters on the layered structures (Section 3.4). The mechanical properties, including wear

resistance and hardness, were evaluated using dedicated experimental methods (Section 3.5), while corrosion performance was assessed by electrochemical testing (Section 3.6). This experimental work provided a solid basis for the comprehensive understanding of the microstructures, material properties and the potential industrial applications of GO/Cu composite coatings.

Chapter 4 Results

4.1 Raw Materials

4.1.1 Graphene Oxide Produced

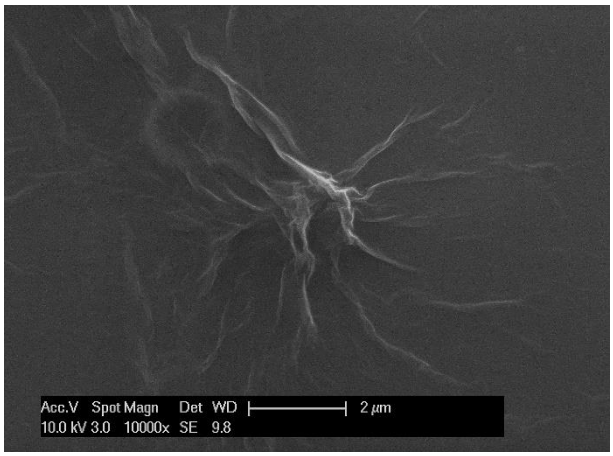


Figure 4.1.1 SEM image of graphene oxide produced by Hummer's method on silicon carbide (SiC) wafer.

In this study, two types of graphene oxide were employed as reinforcing phases in copper coatings, one synthesised using the Hummer's method, and the other obtained from industrial sources, as mentioned in the Experimental section. The essential properties of graphene oxide prior to its incorporation into the composite coating via electro-brush plating are elaborately discussed. Figure 4.1.1 illustrates the graphene oxide produced under modified Hummer's method with ripples and transparent to electrons.

Figure 4.1.2 exhibits a comparison of Raman spectra for graphite powder and graphene oxide flakes using 488 nm laser resource, as carbon molecules are sensitive to this wavelength of laser. The spectrum of graphite powder is shown by the red curve at the bottom of Figure 4.1.2. The

strongest Raman peaks around 1580 cm^{-1} is the G band, and the second strongest band is around 2700 cm^{-1} which is the 2D band. These two bands are the most representative bands for graphite. G band is there because of intrinsic bonding stretching of sp^2-hybridised carbon atoms. A weak D band is also shown in the Raman spectrum of graphite at around 1360 cm^{-1}, which is caused by defects and structural disorders in graphite.

The spectrum of graphene oxide depicted by dark curve at the top of Figure 4.1.2, and the fitting curves (Figure 4.1.3) and analysed results (Table 4.1.1) are also shown below. A narrow peak with a relatively high intensity at around 1596.74 cm^{-1} is denoted as G band and a band of comparable intensity at around 1355.49 cm^{-1} is the D band. There are two broad bands with a lower intensity at around 2685.37 cm^{-1} (2D band) and 2932.78 cm^{-1} (G+D band). The D to G intensity ratio (I_D/I_G) of graphene oxide was calculated by the fitted data listed at Table 4.1.1, which is 0.79. This relatively high I_D/I_G ratio results from the relatively high ratio of sp^3 carbon defects within the graphene oxide molecules.

Comparing the spectrum of graphite with that of the graphene oxide, the position of G or 2D bands is almost the same, whereas blue-shifting (right-shifting) occurred to the G band from 1580 cm^{-1} (graphite) to 1597 cm^{-1} (graphene oxide).

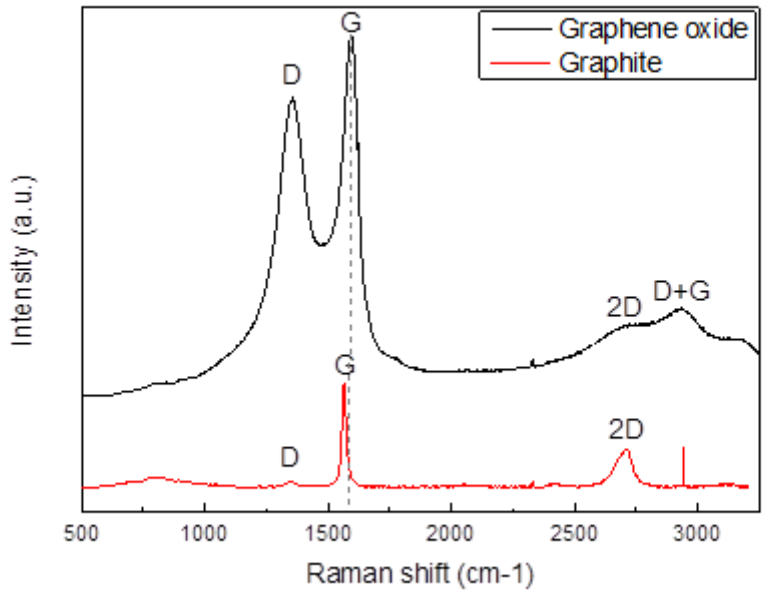


Figure 4.1.2 Raman spectrum of graphite powder and graphene oxide flakes.

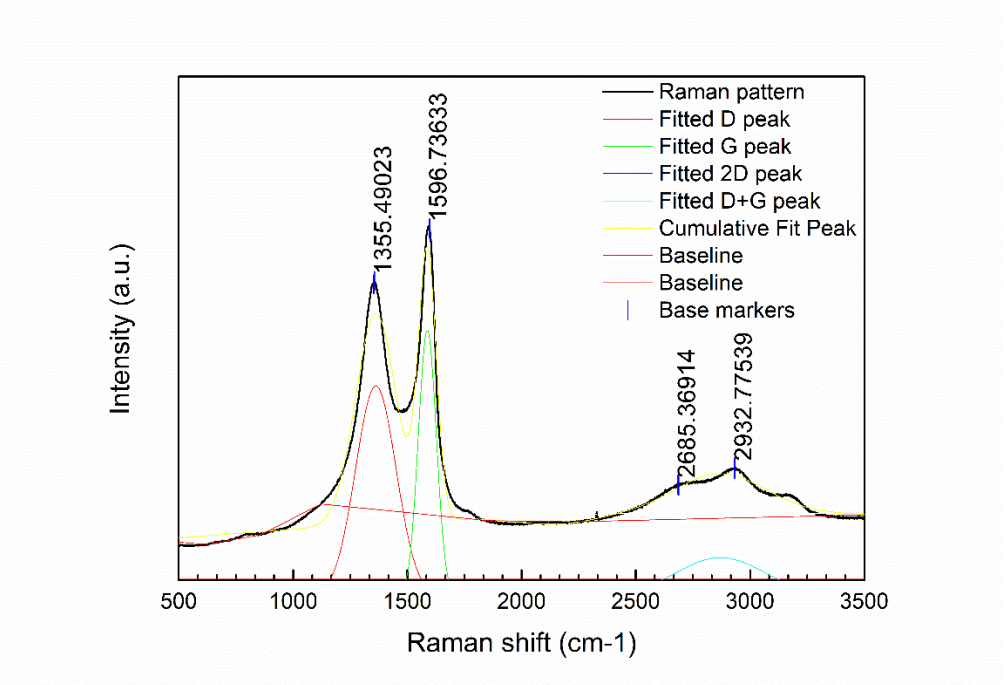


Figure 4.1.3 Raman spectrum and its fitted curves for graphene oxide flakes.

Table 4.1.1 Data of Raman pattern fitting of graphene oxide particle.

Fitted peaks	Height	Centre	FWHM
D peak	61911.69	1355.49	1354.06
G peak	78481.93	1596.74	1.39
2D peak	20517.68	2685.37	1.20
D+G peak	24210.17	2932.78	1.16

Figure 4.1.4 depicts the spectra of graphite powder and graphene oxide particles. As shown with red curve, the spectrum of graphene oxide is shown with contribution of hydroxyl (C-OH), carboxyl (COOH), epoxide (C-O-C) and ketonic species (C=O). The broadest band with high percentage of absorption (3382.12 cm^{-1}) is attributed to the stretching of hydroxyl (C-OH) group contributed by water, and oxidized graphene. And other two absorption bands located at 1054.27 cm^{-1} and 1732.59 cm^{-1} are also denoted as C-OH group, especially the vibration of C-OH at 1732.59 cm^{-1} band is from carboxy (COOH) group. The band at 853.55 cm^{-1} is assigned due to bending motion and asymmetric stretching (1223.61 cm^{-1}) of epoxide (C-O-C). As for band at 1621.71 cm^{-1}, it is due to vibration of carbonyl (C=O) [243].

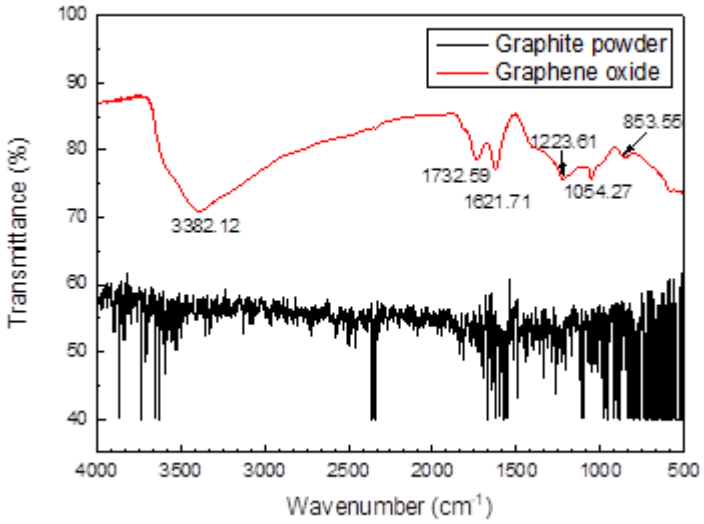


Figure 4.1.4 Comparison on FTIR spectra for graphite and graphene oxide.

As shown with the dark curve, there are many noise peaks with large absorption peaks. The possible reason for this phenomenon is that infrared cannot penetrate through the Gr/KBr transparent tablets [244]. As discussed before, graphene presents high light permeability so that it is easy for those infrared light travelling through to obtain usable information. However, graphite, as black substance, nearly all the light travelling through would be absorbed so that those intense absorption peaks are caused by graphite powder within KBr. To obtain usable FTIR spectrum, graphite powder could be produced to thin film on certain substrate, like silicon (Si) wafer. Then, this film can be tested under Attenuated Total Reflection - Fourier Transform Infrared Spectroscopy (ATR-FTIR).

4.2 GO/Cu Coatings on Stainless Steel 316 Substrate

With utilising the graphene oxide produced by Hummer's method stated before, the investigating of GO/Cu composite coating with certain voltage range is conducted. The feasibility of graphene oxide sheets blend into copper composite coating was investigated with 316 stainless steel substrates. The electro brush plating voltage range is expected to reveal the performance of GO/Cu composite coating by general characterisations. Hence, the voltages range could be discovered to improve the tribological properties could be ensured.

4.2.1 Influence of GO and Plating Voltages on GO/Cu Coatings

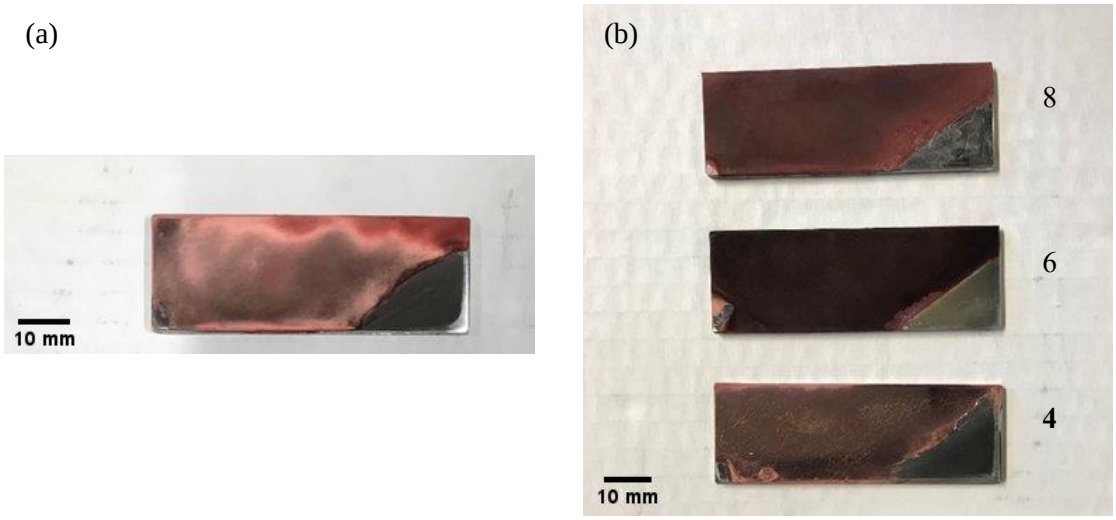


Figure 4.2.1 Pictures of post brush plating surface for (a) the Cu6 specimen and (b) the GO/Cu4-0.2, GO/Cu6-0.2 and GO/Cu8-0.2 specimens.

Figure 4.2.1 demonstrates the pictures of post brush plating procedure coating surfaces of pure Cu and GO/Cu samples with 0.2 g/L of GO concentration. Under 6 volts of potential, the pure copper coating on SUS 316 with special nickel interlayer was carried out, as shown in Figure 4.2.1a. This pure Cu coating sample presents relatively less uniform colour compared to samples with graphene oxide addition (Figure 4.2.1b). With 4 volts with brush plating, the

colour is the nearest to the colour of pure Cu control specimen, shown at the bottom of the Figure 4.2.1b. The GO/Cu6-0.2 demonstrates darker colour while GO/Cu8-0.2 exhibits red matte finish.

Figure 4.2.2b depicts the surface morphology of the GO/Cu coating obtained through brush plating at 4 volts, showing densely arranged fine spherical particles. Similarly, fine particles are distributed on the surface of the GO/Cu6 sample (Figure 4.2.2c), with some small dark areas or defects in the coating. A porous coating is shown on the surface of GO/Cu8 sample (as shown in Figure 4.2.2d). It exhibits many holes larger than 10 μm in diameter, and this porous structure might also extend into the main body of the coating.

As depicted in Figure 4.2.2, there are one pure Cu coated sample surface morphology, shown in Figure 4.2.2a, and three types of surface morphology for GO/Cu sample surface with GO within the coating structure, shown at Figure 4.2.2b, c and d. GO/Cu sample brush plated under 4 Volts shows small cauliflower structure and there are areas remain relatively flat and featureless morphology. Under 6 Volts of brush plating, relatively uniformly spread cauliflower like structure was shown at Figure 4.2.2c. In Figure 4.2.2d, the cauliflower structure expanded, and some porous area shown because of expansion, for GO/Cu8-0.2 samples. Comparing with pure Cu sample surface, samples contain GO within their coating shows different sizes of cauliflower structures. With uplifting voltage of brush plating, the featured cauliflower structure of brush plating is easier detected even under relatively low magnification. The Figure 4.2.2e and f illustrate the surface morphology under 15,000 magnification of Cu6 and GO/Cu4-0.2 samples. The pure copper coating deposited under 6V sample (Figure 4.2.2e) depicts quite standard cauliflower like structure which could be seen on those brush plated sample surface [245]. Figure 4.2.2f depicts the surface morphology with 15,000 magnification of GO/Cu4-0.2

coating revealed the graphene oxides at the surface denoted by red arrow. The graphene oxide is surrounded by the grain boundaries of the Cu grains.

Figure 4.2.3 summarises the surface roughness of the 316 stainless steel substrate and brush plated samples. It shows that the 316 stainless steel substrate and the Cu6 sample surfaces have comparable roughness. Compared with the surface of Cu6, the surface of the three GO/Cu composite plated samples are much rougher. Figure 4.2.2b-d show an increase in surface roughness of the GO/Cu composite plated samples with increasing plating potential (from 4V to 8V), which corresponds well with the roughness results. There is an abrupt increase in roughness for the GO/Cu8 sample surface, compared with the other two GO/Cu composite plated samples.

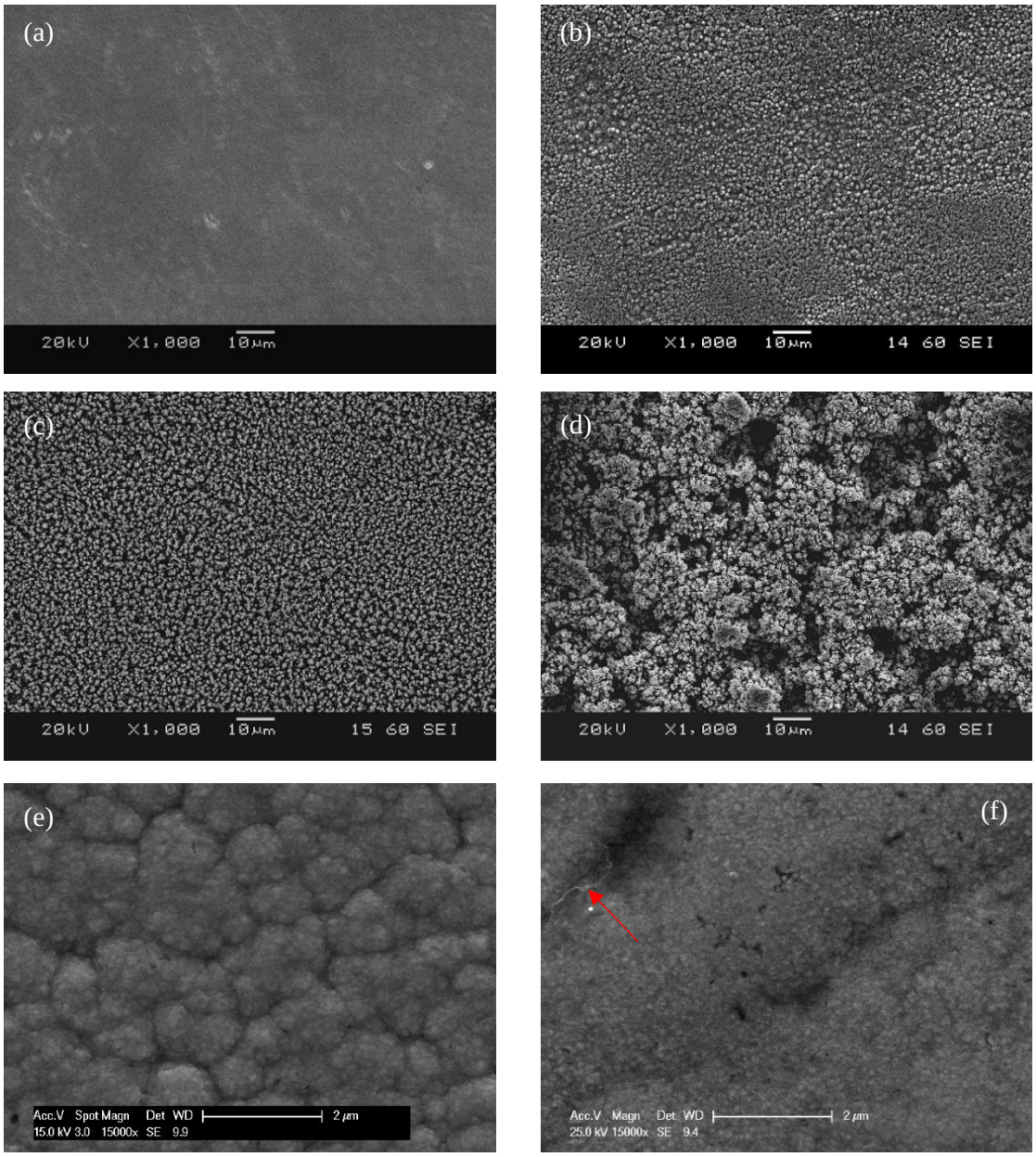


Figure 4.2.2 Surface morphology on GO/Cu plated samples: (a) Cu-6; (b) GO/Cu4-0.2; (c) GO/Cu6-0.2; (d) GO/Cu8-0.2; (e) higher magnification of Cu6 sample and (f) GO discovered under higher magnification for GO/Cu4-0.2.

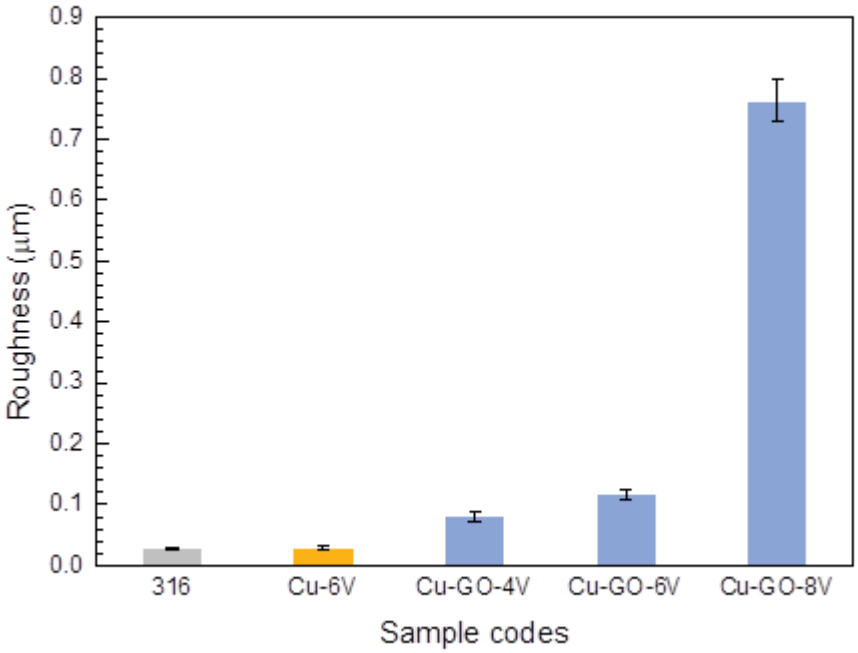


Figure 4.2.3 Surface roughness on grinded stainless steel and plated samples.

4.2.2 Cross-sectional Layer Structure for Cu6 and GO/Cu Sample Coatings

The cross-sectional SEM images in Figure 4.2.4 exhibit the coating layer structure produced by electro-brush plating. Figure 4.2.4a depicts the layer structure of Cu-6V sample and the coating thickness measured from the cross-sectional view is about 29.5 µm. Consistent with the top view shown in Figure 4.2.2a, the coating is one-layered and almost featureless. The GO/Cu composite coatings plated under 4 and 6 V are also one-layered (Figure 4.2.4b and c).

The GO/Cu composite coatings plated under 4 and 6 V are also one-layered, as shown in Figure 4.2.4b and c. The GO/Cu-4 sample surface (Figure 4.2.4b) is almost defect free with a thickness of about 12.5 µm. The thickness of the GO/Cu-6 coating is increased to about 54.3 µm and as shown in Figure 4.2.4c, there are some places near the surface region with laminate porous structure. The layer structure of the GO/Cu-8 coating could be divided into three parts: a highly

porous structure (about 16.0 μm in thickness) at the surface region followed by a low porous structure (about 30.1 μm in thickness) and finished by a very thin layer (about 1.9 μm in thickness) without obvious defects.

As described in Section 3, a thin Ni layer was plated on the substrate before starting the GO/Cu plating. Hence, a thin nickel layer is expected between the top copper-rich layer and the substrate. However, there is no visible boundary shown in Figure 4.2.4a to c. As it is only the cobalt (Co) in between the Fe and Ni layer in the periodic table of the elements. Hence, their atomic nucleus charges and electron arrangement are similar, so that they would show in similar brightness under SEM. The GO/Cu composite coating is structured with a Ni interlayer on 316 stainless steels, as illustrated in Figure 4.2.4d. The Ni interlayer, with a thickness of just 1.3 μm, is employed to enhance the bonding strength between the substrate and the composite coating. Corrosion occurred relatively severe on the coating structure, the coating is composed with Cu and graphene which would perform relatively severe cell reaction within the acidic etchant. Moreover, the stainless steel would be performed as cathode within the cell reaction which could be protected from oxidation reaction. However, the relatively severe corrosion would lead to chance to reveal the graphene oxide within the Cu plating coating structure on the cross-sectional view, as shown in the Figure 4.2.5.

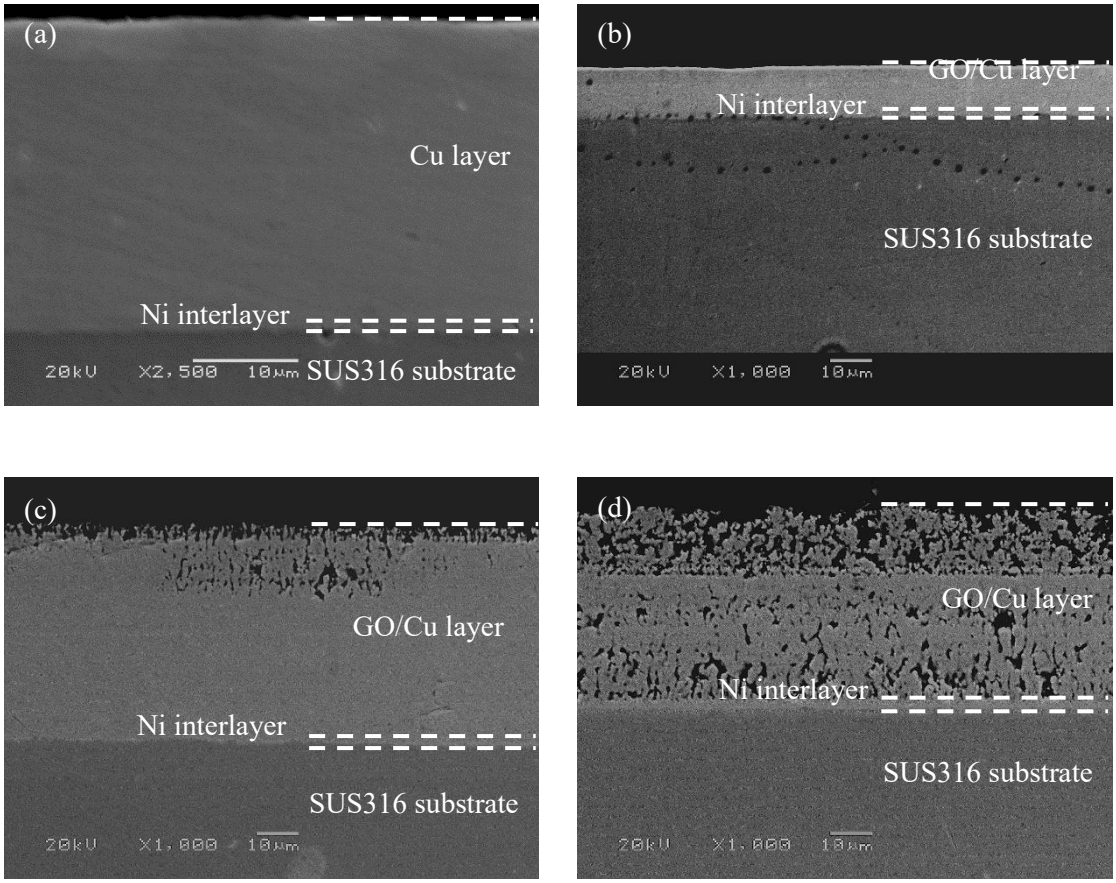


Figure 4.2.4 Cross-sectional images show coating structure of copper plated and GO/Cu composite plated samples: (a) Cu6-0.2; (b) GO/Cu4-0.2; (c) GO/Cu6-0.2; (d) GO/Cu8-0.2.

It is opportunity to investigate the graphene oxide structure at the cross-sectional direction. For GO/Cu4-0.2 sample, there is abrupt structure shown on Figure 4.2.5a which might be Cu plating structure protected by graphene oxide during etching. The detailed view of SEM image (Figure 4.2.5b) revealed the existence of GO sheets covered the Cu grains. The Cu grains illustrate relatively round structure with smooth boundary while the GO sheets are of lager size and sharp edge with different angles. Besides, the Cu grains exhibit relatively small size which less than 1 μm. Relative to GO/Cu4-0.2, structural pure graphene oxide structure was found on the etched GO/Cu6-0.2 sample, as shown in Figure 4.2.5c. As the GO/Cu6-0.2 depicts relatively less dense structure at the outmost region (Figure 4.2.4c), so the Cu structure could be depleted relatively completely. Figure 4.2.4c illustrates representative area of the etched area at the outermost area,

with remaining Cu structure shown at the bottom of this SEM image. The structure of graphene oxide structure could be noticed at Figure 4.2.5d, the featured ripple structure of graphene is shown. Moreover, the graphene oxide sheets are entangled, twisted, and stacked layer-by-layer at this cross-sectional view with some porous areas. Those areas could be areas of Cu metal structure dissolved within the etchant. As under this etchant, the austenite structure of SUS 316 could be revealed. Hence, it is possible that the Cu at the outmost area could be depleted and remained some graphene oxides. Graphene oxides could be found on GO/Cu8-0.2 for both outermost area (Figure 4.2.5e) and the area near to the Ni interlayer (Figure 4.2.5f). Similarly, there is porous structure of those attached graphene oxides sheets which could be seen on the as-polished SEM images shown in Figure 4.2.4d. The detailed SEM image of Cu6 sample is used to compare with the sample with graphene oxides, show in Figure 4.2.5g. Even under 50,000 of magnitude, no graphene oxides sheets are shown.

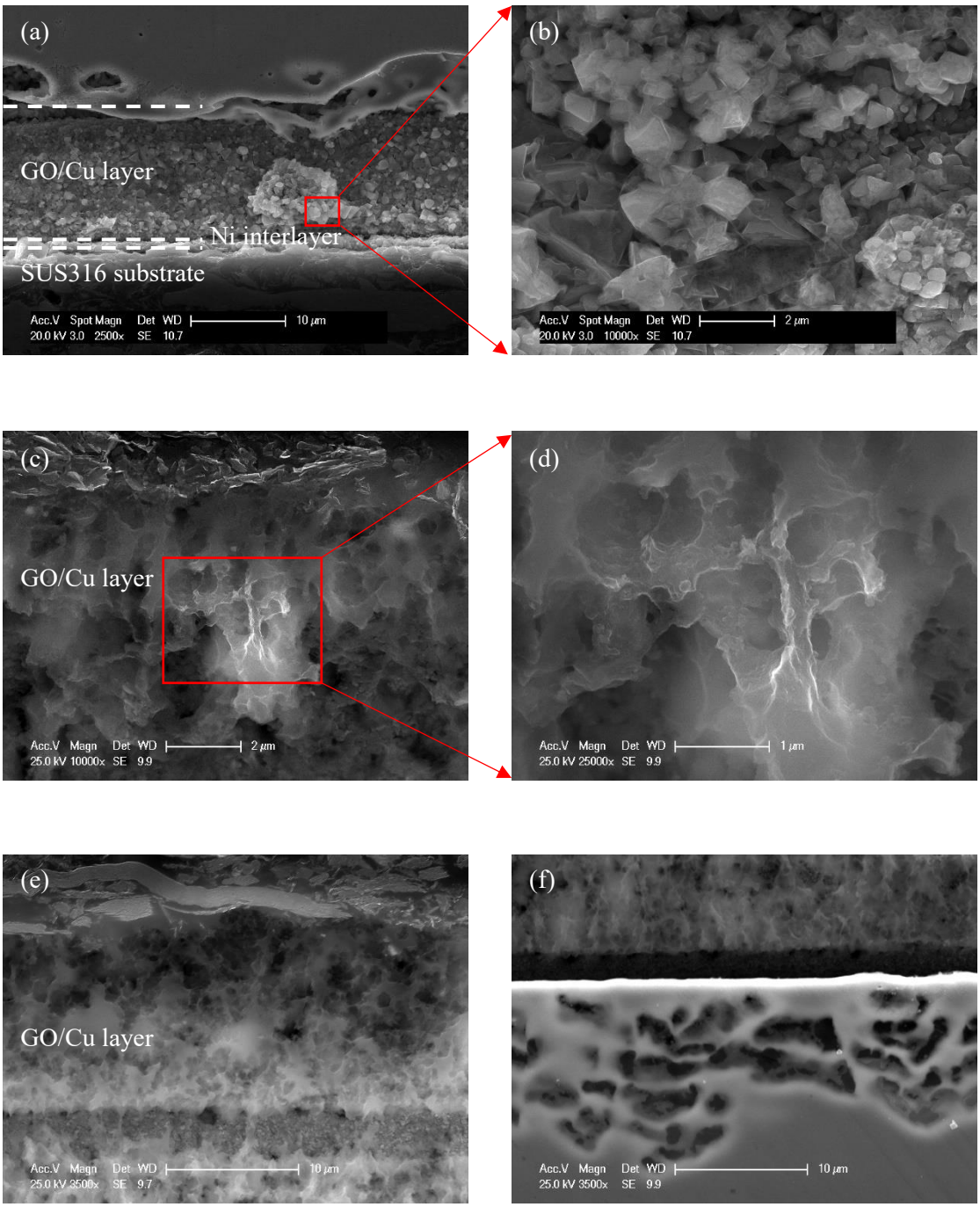


Figure 4.2.5 SEM images from cross-sectional view to discover the graphene oxides distribution: (a) general view of etched GO/Cu4-0.2 and (b) GO structure; (c) GO found with Cu plating structure and (d) detailed view of GO on GO/Cu6-0.2; (e) GO structure at the outermost area and (f) the bottom of coating structure of GO/Cu8-0.2.

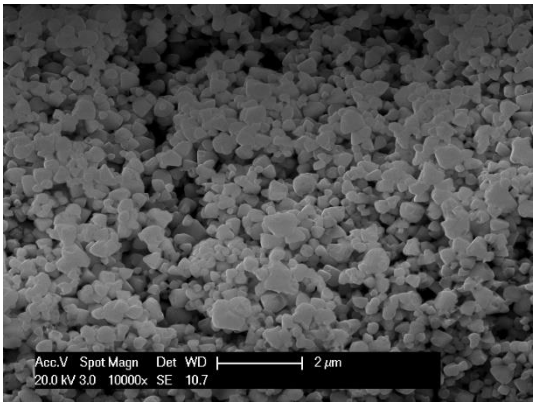


Figure 4.2.5 (continued) (g) detailed view of etched Cu6 control group.

4.2.3 Composition Depth Profile of GO/Cu Sample

Figure 4.2.6 illustrates the compositional profile of elements on the sputtered surface as a function of time during Ar^+ plasma sputtering. The left most part represents the GO/Cu particle composite coating area. It shows that the most majority of the coating consists of Cu, and it also shows the composition of oxygen and carbon. In this graph, the concentration of carbon and oxygen is one type of evidence of GO continuing existence within the GO/Cu composite coating system. Then, the Ni interlayer shows on the second part of the graph, which is relatively thin interlayer for stainless-steel substrate. The last part of the graph is from the substrate stainless-steel 316, and it is mainly composed of iron (Fe), nickel (Ni).

As mentioned at Experiment part, GDOES could analyse the excited atoms and ions layer by layer when the solid material was sputtered out by the argon plasma (Ar^+). So, if the test was stopped at the middle of a coating layer, it would exposure the coating structure feature on this new sputtered surface. Within this composite, Cu and GO as two different types of materials would show different sputtered speed, so it would be possible to reveal the GO inside the coating on this new surface. This surface was produced at new spot and this sputtering time was around 20 seconds. The surface SEM images were shown on Figure 4.2.7. It shows the crater

produced by Ar^+ plasma at Figure 4.2.7a, it could be seen at the middle of the circle that there are several dot-like structure. As mentioned before, the dot-like structures observed under SEM may result from the differing behaviours of Cu and GO during argon plasma sputtering. GO is possibly found around those dots, either on those dots or at the boundary of those dots. GO alike structure was found on Figure 4.2.7b, which shows semi-transparent features and relatively soft comparing with Cu grains. GO shows ripples structure under SEM as one of its features according to previous researches [246].

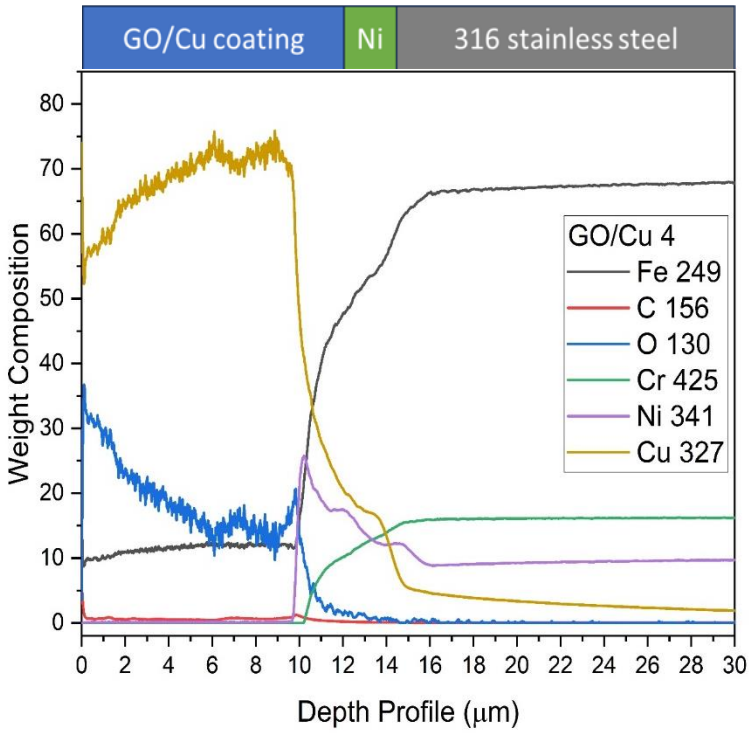


Figure 4.2.6 Glow discharge optical emission spectroscopy of GO/Cu4-SS316 sample.

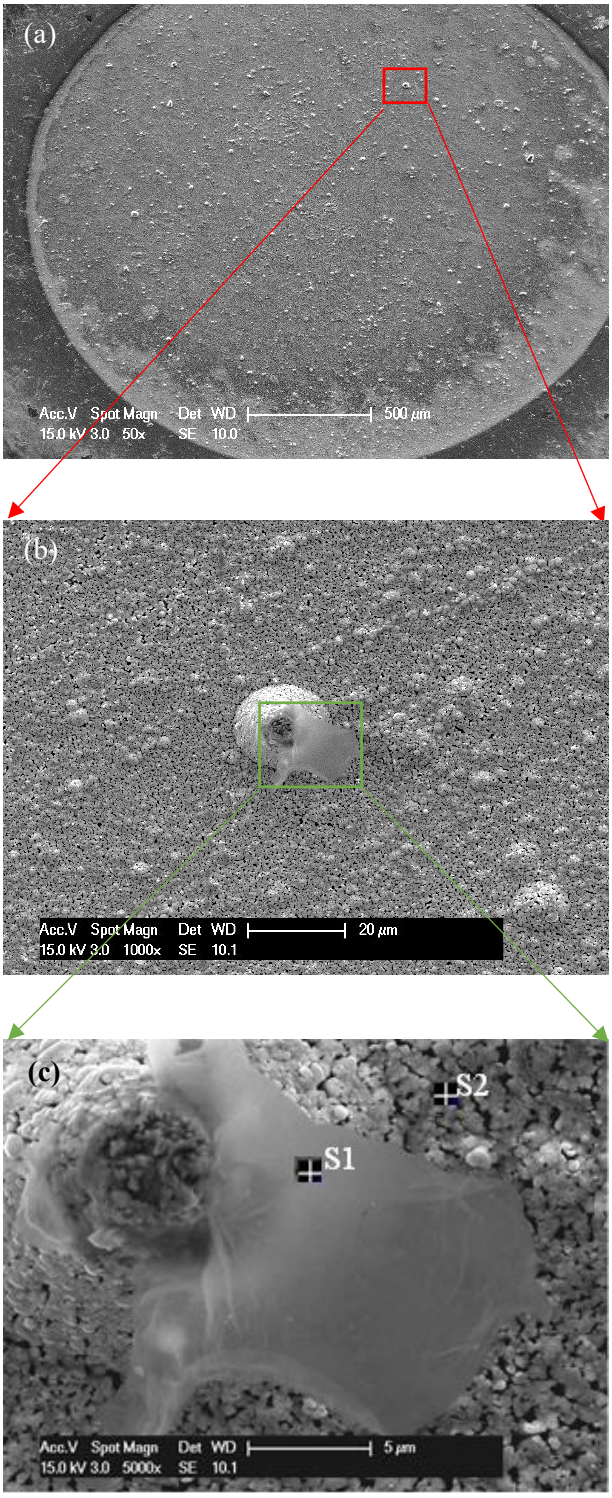


Figure 4.2.7 SEM images on argon produced crater bottom surface: (a) general observation of crater created around 20 seconds; (b) one special abrupt observed graphene like structure; (c) graphene oxides with ripples feature shown.

The remaining GO on the sputtered surface is possibly because part of this GO flake was twisted and enveloped Cu grains (Shown in Figure 4.2.7d), as the production process of this coating is co-depositing of Cu grains and GO flakes. During Ar^+ plasma sputtering process, GO acted as bounce, reflecting the plasma without loss of Cu or GO. Due to some area of GO remaining in the solid coating, so GO could still be seen even on the sputtered surface without reduction. The presence of these abrupt structures on the plasma created surface strongly indicates that GO was successfully incorporated into this composite coating system.

Table 4.2.1 EDX of GO like structure elements composition charts.

Spectra code	Weight constituents (wt%)		
	C	O	Cu
S1	36.88	7.36	55.76
S2	0	0	100

At Figure 4.2.7c, the EDX point scanning on Spectrum 1 (S1) and Spectrum 2 (S2) shows the weight constituents of elements detected by X-ray. The EDX results were carried out with AutoID mode, carbon (C), oxygen (O) and copper (Cu) weight constituents are depicted at Table 4.2.1. It is quite interesting to note that only 100% of Cu was detected at this spot, whereas 36.88% of C and 7.36% of O are exhibited at S1. This is one of most significant evidence to see and proof the GO like structure at Figure 4.2.7a is the GO within certain depth of GO/Cu composite coating structure.

4.2.4 Raman Results on GO/Cu Composite Coatings

Raman spectra of GO/Cu composite coatings and pure Cu coatings with a few microns of spatial resolution are shown in Figure 4.2.8. Among those three spectra there are two strong bands at around 1350 cm^{-1} and 1600 cm^{-1}. Band around 1600 cm^{-1} is denoted as G band which shows

intrinsic structure of sp^2-hybridised carbon atoms. In that case, the GO could be proved as blended into GO/Cu composite coating system from the outermost surface region. As the laser of Raman could detect the existence of GO at few microns from the surface. Structural defects and disorder in carbon honeycomb structure led to increase intensity of D band (around 1350 cm^{-1}). Hence, the level of graphene disorder can be indicated by the intensity ratio of D to G band (I_D/I_G).

The I_D/I_G ratios for GO/Cu4, GO/Cu6 and GO/Cu8 are 0.45, 0.82 and 4.52, respectively. The I_D/I_G ratio of graphene oxide as calculated before is 0.79, which is slightly lower than that of GO/Cu6, whereas the ratio of GO/Cu8 is much higher than graphene oxide. It is interesting to note that the I_D/I_G ratio of GO/Cu4 is even much lower than that of graphene oxide. One possible reason for this phenomenon is that GO may have been partially reduced to rGO by the constant negative potential provided by cathode during the brush plating [247,248].

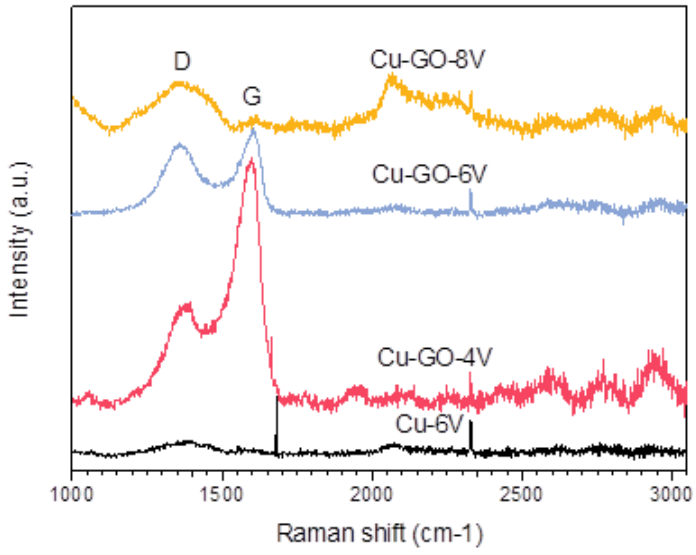


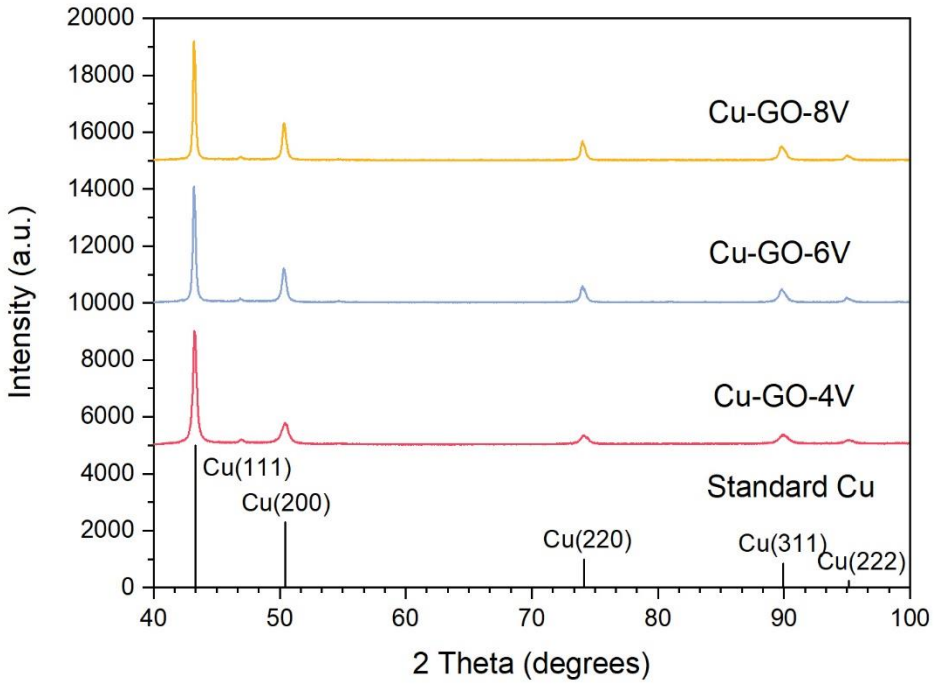
Figure 4.2.8 Comparing Raman spectra among GO/Cu plated under different working potentials.

4.2.5 Comparison of Surface Layer Phase Compositions

Figure 4.2.9a presents the standard copper XRD pattern test from ICSD (PDF 00-004-0836) and XRD patterns of GO/Cu composite plated samples. For standard copper, their (111) plane peak is near 43.298˚ (2θ) with an interplanar spacing of 0.209 nm. Moreover, other peaks of those three XRD patterns can also fit well with standard copper XRD pattern. Therefore, those peaks are denoted as copper peaks.

Comparing the three XRD peaks of plated samples, the width of XRD peaks is broader with lower electro-brush plating potential as shown in Figure 4.2.9b. As samples with smaller grain size show broader XRD peaks, this implies that the lower plating potential would have produced the coating with finer grain size. For GO/Cu plated samples, there are several small peaks between 40˚ and 65˚. XRD pattern of GO/Cu6 has been used as example to show detailed phase indexing, and Ni peaks of (111) and (200) along with Cu_2O peaks of (200) and (220) are identified (Figure 4.2.10). The Cu_2O could also be detected by Raman spectroscopy, and this would be discussed later at the friction test part.

(a)



(b)

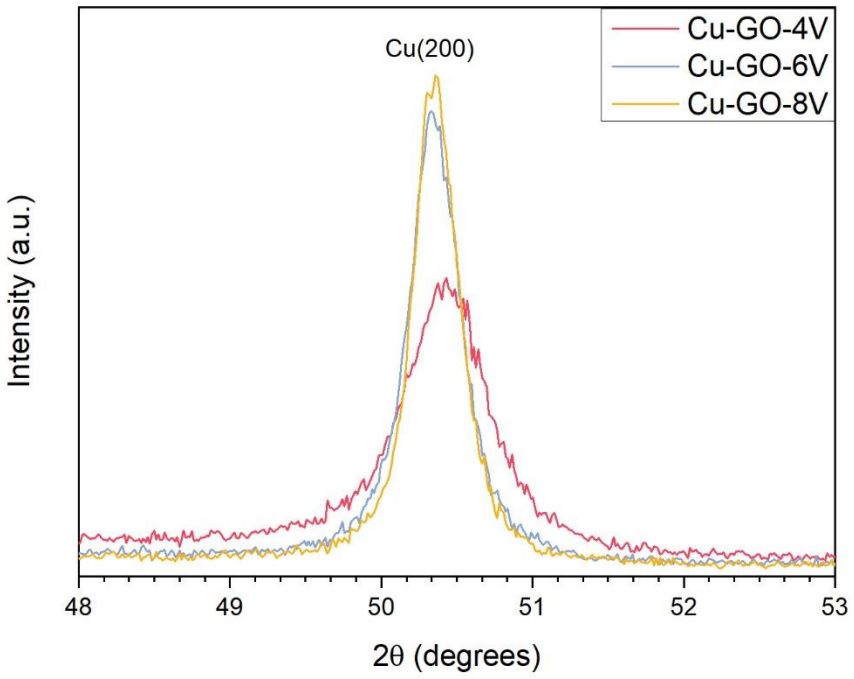


Figure 4.2.9 XRD patterns for GO/Cu composite plated sample surface and standard XRD peaks for pure copper.

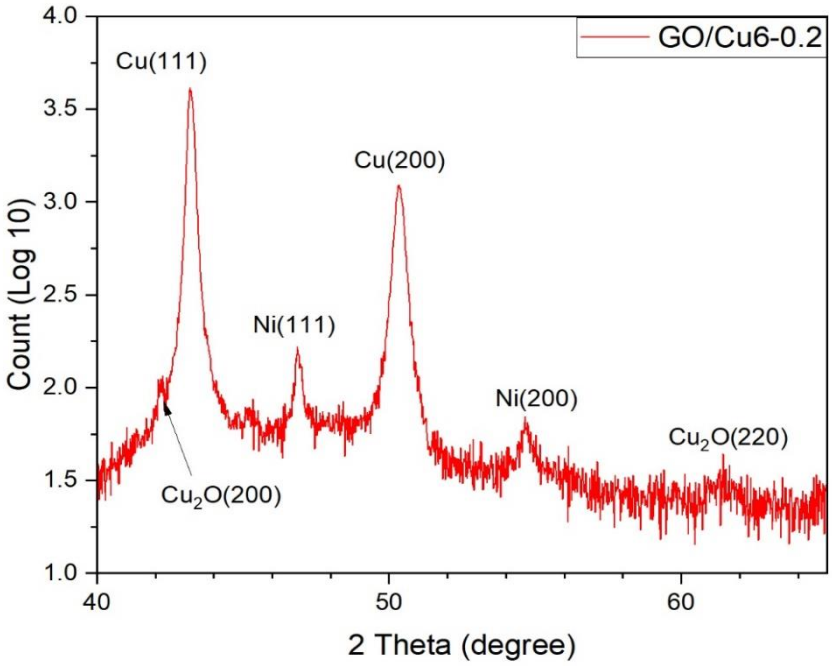


Figure 4.2.10 XRD pattern of GO/Cu6 with detailed phase indexing.

4.2.6 Surface Micro-hardness

Figure 4.2.11 shows the measured surface hardness of the pure copper and GO/Cu composite plated specimens. The micro-hardness of the neat-copper plated specimen is 192.0 $HV_{0.01}$, which has been improved after adding GO constituent into the coating system by electro-brush plating. It is interesting that the micro-hardness of the specimen surfaces decreased with increasing the plating potential from 4 to 8 volts. Especially, the micro-hardness decreased to 207.1 $HV_{0.01}$ for GO/Cu8. The reduced hardness should be related to the relatively highly porous structure observed in Figure 4.2.4d.

It has been reported that addition of graphene or graphene oxide onto copper sample surface can increase the micro-hardness to about 210 HV, which is corresponded well with aforementioned micro-hardness [249].

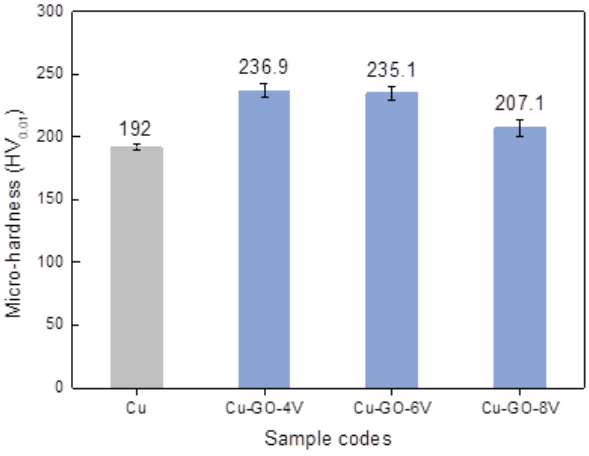


Figure 4.2.11 Comparing of micro-hardness for neat copper plated and GO/Cu composite plated specimens on their near surface region.

4.3 GO/Cu Coatings on Brass Substrate: Material Characteristics

In previous session, it is feasible to apply the GO/Cu composite coating on stainless steel 316 (SUS 316). Within the relatively large range of brush plating potential, the sample brush plating under 4 volts presents relatively better performance on the general characterisation. To investigate the application of GO/Cu composite coating on brass substrates, experiments were carried out with brush plating potentials as variant, regarding 4 volts as reference. The pure Cu control group was introduced to reveal the improvement with GO addition within the composite coating structure. Additionally, the influence of GO concentration would also be exhibited in this session. The optimal potential is expected to be discovered by general characterisations.

4.3.1 Brass Substrate GO/Cu Composite Coating System

Cu and GO/Cu on brass were produced by the brush plating method. The brush plating process was carried out with the MF Rectifier MK II (SPA Plating Co., Ltd.). It includes three main steps: active-cleaning, nickel-strike, and Cu or GO/Cu coating processes. The active-cleaning process was used to remove oxides on the brass surface. As for the nickel strike process, it is to improve the adhesive strength between the brass substrate and the coating layer. Between every step, the sample surface was put under running water to remove any remaining plating solution and rinsed with deionized water for 1 minute and dried with hot wind. The specific parameters and processes are outlined in detail in Table 4.3.1.

Table 4.3.1 Electric brush plating procedures for applying Cu coating and GO/Cu composite coatings on brass.

No.	Operation	Solution	Voltage/V	Time/min
1	Electrical active-clean	Active-cleaning solution	7	3
2	Nickel strike	Special nickel solution	7	3
3	Final plating	Cu or GO/Cu solution	2, 3,4, 5 and 6	30

4.3.2 Surface Morphology of Copper Control Group on Brass Substrate

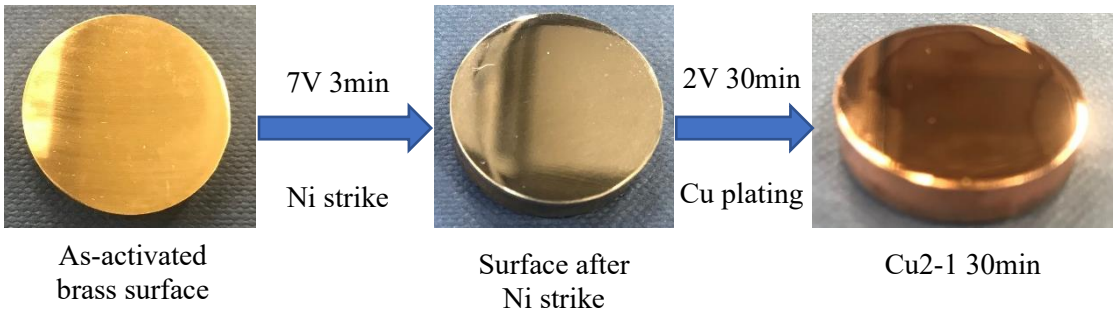


Figure 4.3.1 Surface changing with the brush plating procedure for pure Cu2 sample.

Figure 4.3.1 demonstrates the surface changing with the electric brush plating procedure. The brass substrate in yellow was grinded into #1200, then the activate procedure was introduced to remove the surface impurities and grease. The nickel (Ni) strike process is performed for 3 minutes, and the finish of this process is illustrated silver shade and mirror-like surface reduced visible grinding curves. After 30 minutes of brush plating under 2 volts, it exhibits with yellow tinted with red colour without depletion on mirror like finish.

To discover more information about the influence of GO on GO/Cu coatings under different brush plating voltages, a control group for each plating voltage was carried out and studied. Figure 4.3.2 shows how plating voltages influence the surface microstructure without the addition of GO. At lower plating voltages (2 volts and 3 volts), the surface morphology is relatively featureless except for the remaining grinding marks on Cu2 (Figure 4.3.2a). This might be due to the ultra-thin plating layer on the Cu2 samples, which is discussed later in the layer thickness section.

On Cu3 (Figure 4.3.2b), no notable defects were observed, resulting in a surface that is relatively featureless. The surface of the Cu4 sample (Figure 4.3.2c) still shows a morphology between featureless and cauliflower-like structures [245], with slightly more dark spots than those observed on the Cu3 surface, though they are not easily noticeable. Cu5 (Figure 4.3.2d) shows a more notable columnar structure with some granular structures. As for Cu6 (Figure 4.3.2e), it mainly consists of a cauliflower-like structure with some remaining granular structures at the boundaries.

As mentioned before, the cauliflower-like structure is one of the features of the brush-plated coating microstructure. This structure can be observed when the brush plating voltage is increased to 4 volts. The columnar structure exhibits a cauliflower-like morphology on the surface. With the increase in plating voltage, the growth rate of the columnar crystals also increases. Hence, this characteristic structure becomes more and more prominent and can be easily observed under SEM. Notably, the columnar boundaries become increasingly distinct with higher plating voltages, as shown in Figure 4.3.2c, d and e.

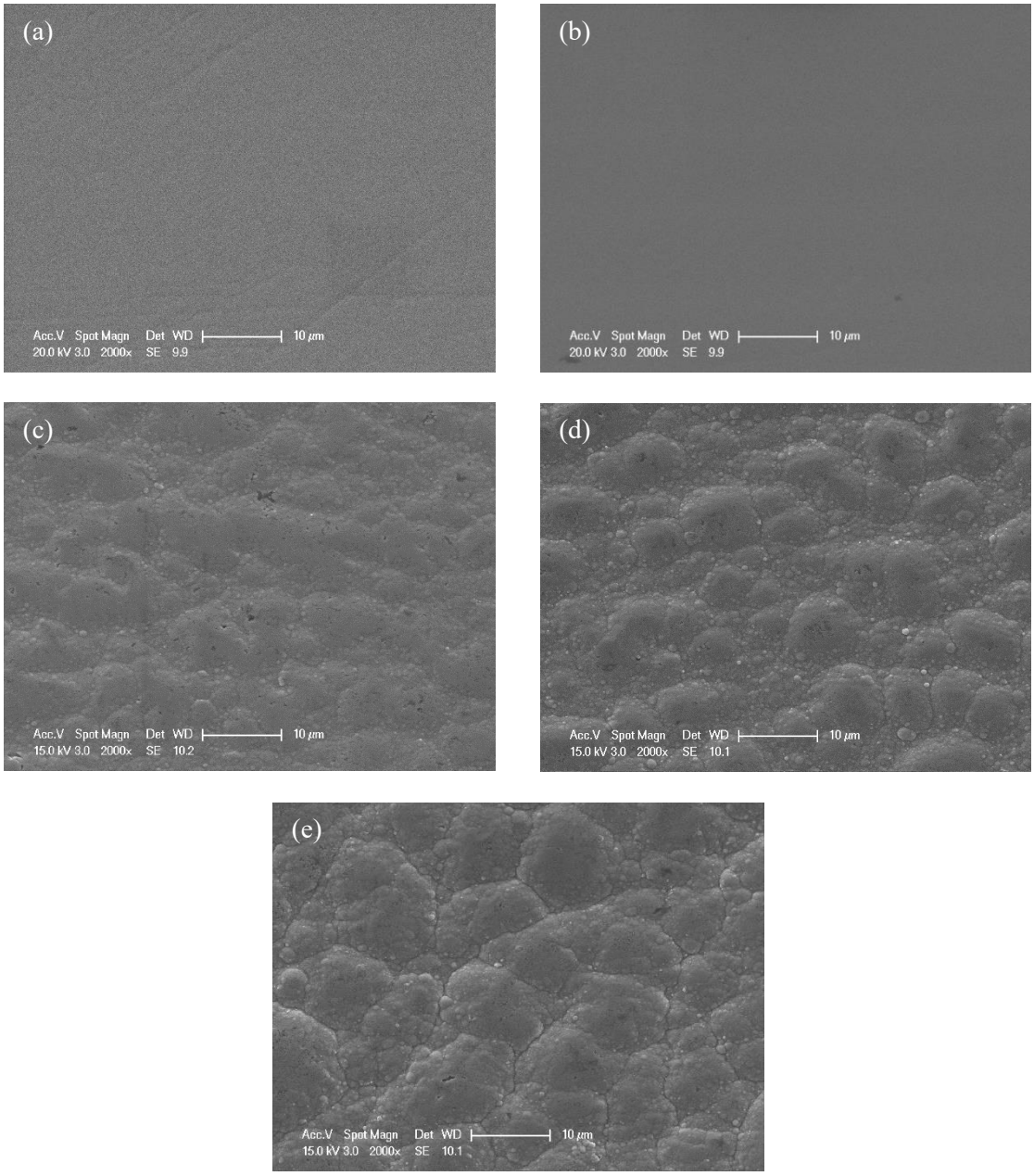


Figure 4.3.2 Surface microstructure for Cu coating samples: (a) Cu2-Brass; (b) Cu3-Brass; (c) Cu4-Brass; (d) Cu5-Brass and (e) Cu6-Brass.

4.3.3 Surface Morphology of GO/Cu Composite Coating with 0.2 g/L of GO

As depicted in Figure 4.3.3, it shows the surface morphology of GO/Cu composite coatings under different plating voltages with 0.2 g/L of GO concentration when brush plating. In Figure 4.3.3a, the surface microstructure of GO/Cu2 shows several grinding marks that could be seen, and some deeper colour shown around some of the grinding marks which are wider than the grinding marks themselves. These surface features could indicate an ultra-thin coating layer as mentioned at Cu2. Moreover, this layer might even be thinner than the Cu2 layers as sharp and small grinding curves could be seen on the surface. The grinding curves could also be seen on the GO/Cu3 sample surface (at Figure 4.3.3b), while the grinding curves are buried under several white dots like structures. Before certain thicknesses were grown on the substrate, new plating materials tended to accumulate at grinding curves. Then with more coatings growing, the surface could have a smooth and featureless finish.

As for the remaining three coatings plated under higher voltages, the surface cauliflower structure could also be noticed, which is the same as their pure Cu control group. While some differences could be noticed, the density of cauliflower structures is notably reduced compared with that of pure Cu coatings. As shown in Figure 4.3.3c, there are some relatively featureless areas that trap some cauliflower-like structure. To compare with its pure Cu control group, the Cu control group has a relatively continuous structure. This phenomenon could also be seen in GO/Cu coating samples plated under 5 and 6 volts. The size of the cauliflower structure is larger than that of the pure Cu control group at GO/Cu5 and 6 (Figure 4.3.3d and e) on brass. Figure 4.3.3f shows the line scan results of carbon elements on one of the cauliflower structures. From the results, the carbon constituents on the top area (with dark dots) are higher than other areas. This result is a great proof of the existence of graphene oxides at the outmost area GO/Cu coatings on cauliflower-like structure. The reason why this area can detect notable carbon

constituents would be discussed with micro-hardness data.

It is interesting to note that in the middle of the cauliflower-like structure, dark dots could be noticed, and the size of the cauliflower is bigger than that of their pure Cu control group. Those areas with darker colour might indicate an area accumulation of graphene oxides. As carbon is one of the light elements, there will be interference when detecting the existence of carbon, especially when carbon additives are not in a certain amount. So, the carbon existence would be shown at later Raman Spectroscopy results, which is one of the most professional detection methods for carbon elements.

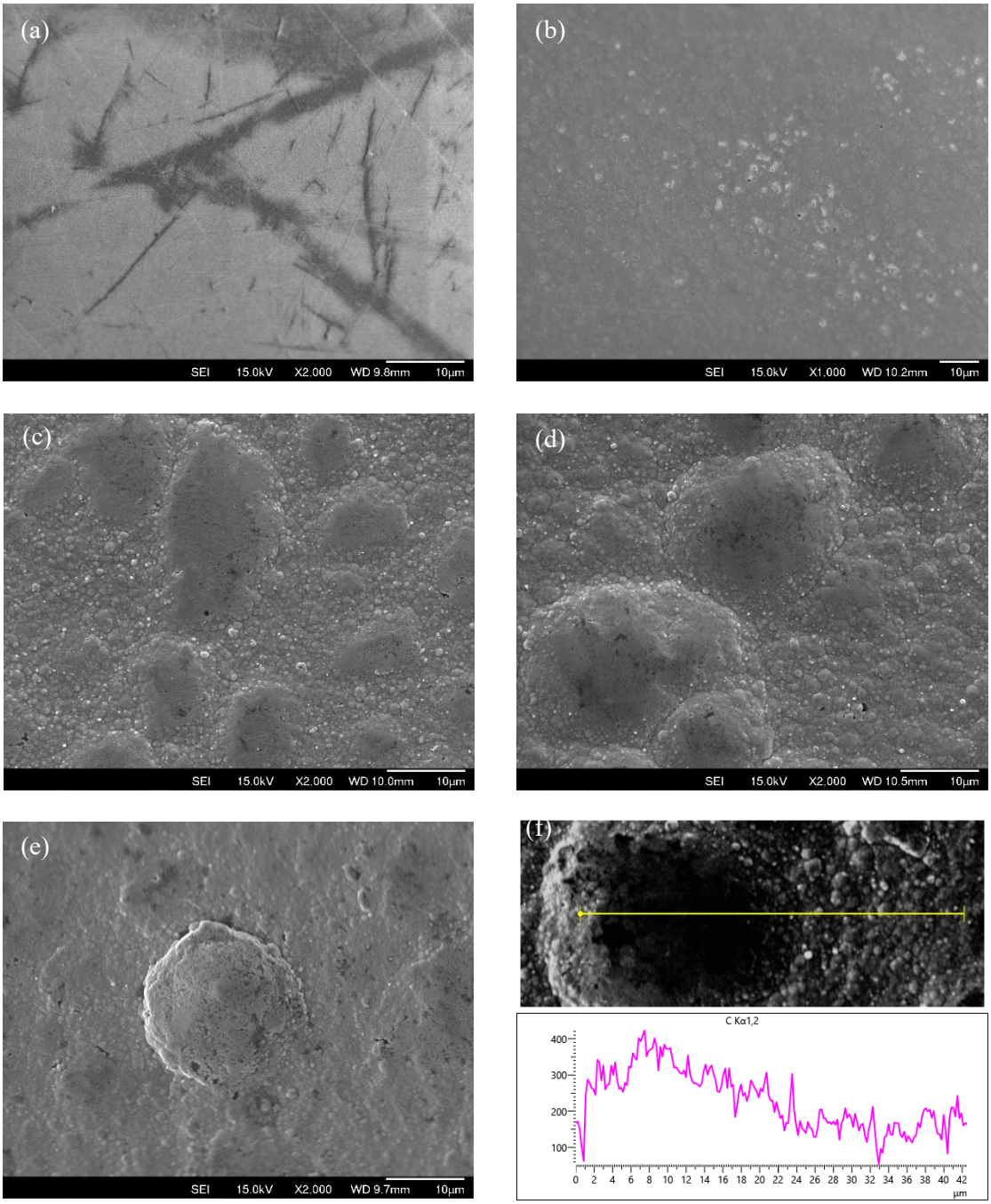


Figure 4.3.3 Surface morphology of GO/Cu composite coatings with 0.2 g/L of GO on the brass substrate: (a) GO/Cu2-Brass; (b) GO/Cu3-Brass; (c) GO/Cu4-Brass; (d) GO/Cu5-Brass, (e) GO/Cu6-Brass and (f) GO/Cu5-Brass EDX line scan on one of the cauliflower-like structure with dark area on the top and results.

4.3.4 Graphene Oxides at Surface Morphology under SEM and EDX

As depicted in Figure 4.3.4a, clear and featured graphene structure is shown on the surface morphology of GO/Cu3-Brass sample surface. It is easy to identify such featured graphene structure on the surface of GO/Cu3 because the surface morphology is featureless, making any distinct differences readily detectable. The EDX results (Figure 4.3.4b) was carried out with AutoID mode, only carbon and copper could be found at the area of Spectrum 1, even no oxygen was detected. On the Spectrum 2 area is the comparing group, only copper could be detected under AutoID mode. This is a great example of GO Found on the surface of GO/Cu sample coatings, as it was X-ray which is used during an EDX process, and it could penetrate several microns when detecting elements constituents. This is proof GO added on the surface of GO/Cu sample surface. That is because the SEM would work under certain sub-atmospheric pressure, impurities have less chance to be sticked on the sample surface. This GO detected under SEM is likely to be GO combined on the surface of the newly brush plated surface.

At Figure 4.3.4c, the upper position on SEM image shows the featured cauliflower like structure and the lower part of the SEM image shows the featured GO-like structure. Spectrum 5 located at the upper cauliflower like structure part and its EDX results show only pure Cu peaks was observed at the graph, exhibited at Figure 4.3.4d. A region with a GO-like structure was selected and analysed using X-ray detection, and relatively notable carbon and oxygen were found on the EDX graph results. These indicate that the GO like structure found in Figure 4.3.4b is GO brush plated on the coating surface. Those two representative examples show the existence of the GO on the outermost area of the GO/Cu composite coating. The further proofs of GO existence would be discussed later.

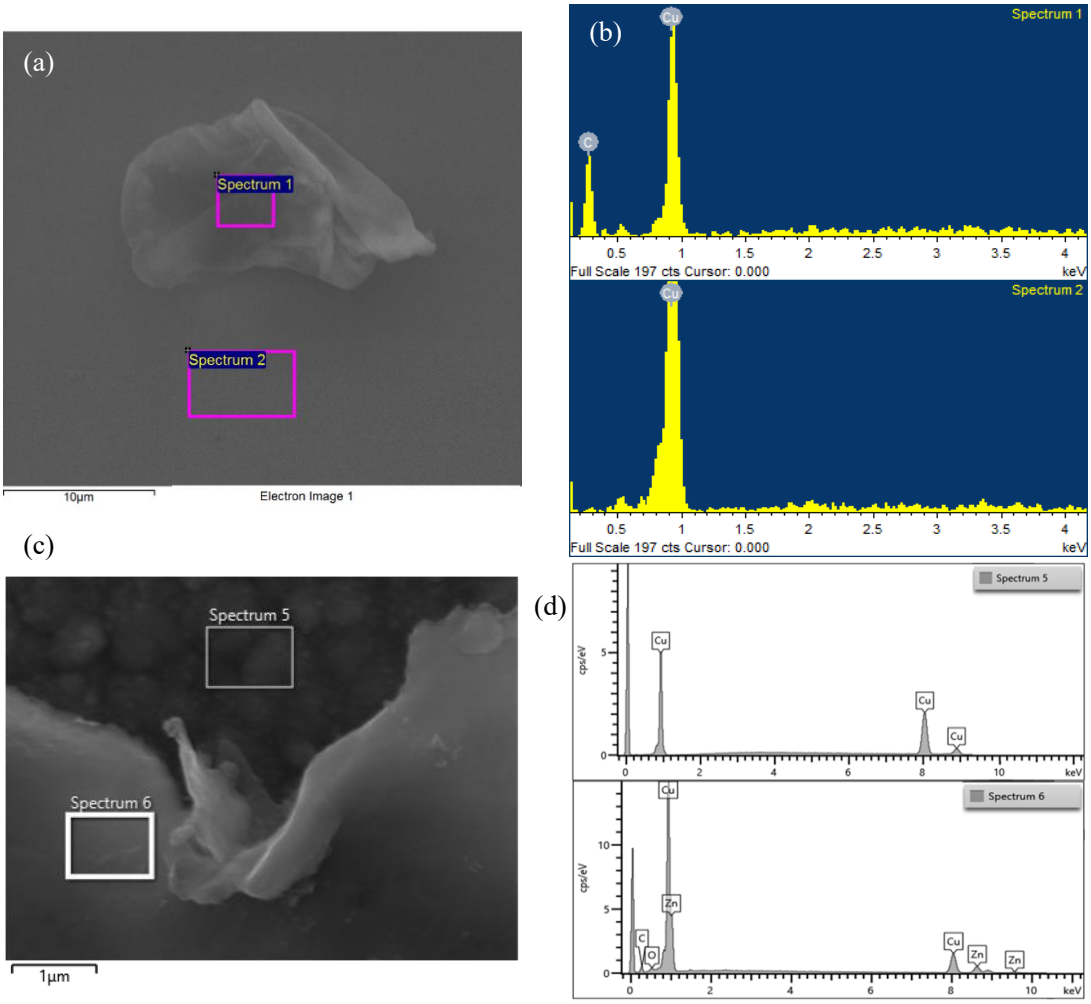


Figure 4.3.4 Graphene oxides found with SEM and EDX results: (a) SEM image for GO/Cu3-Brass and (b) two graphs of EDX results by AutoID mode; (c) SEM image for GO/Cu4-Brass and (d) graphs of Spectrum 5 and 6.

As mentioned before, the GO could be possible exposed on the surface around the top of cauliflower-like structures. Figure 4.3.5a depicts the colour-chemi images which show carbon rich area with red colour and those areas are mainly located at the middle area of cauliflower-like structure. Those carbon rich areas could also be found around the boundaries of cauliflower structures. This just means that the GO would be easier to expose at those areas as those areas are of relatively lower microhardness, so that those areas might to be of porous structure and X-ray information from those area would be of easier to be accumulated. At Figure 4.3.5b, the edge of the cauliflower like structure shows little depletion, GO could be detected as red area.

This is great proof of GO existence at near surface area of GO/Cu composite coatings.

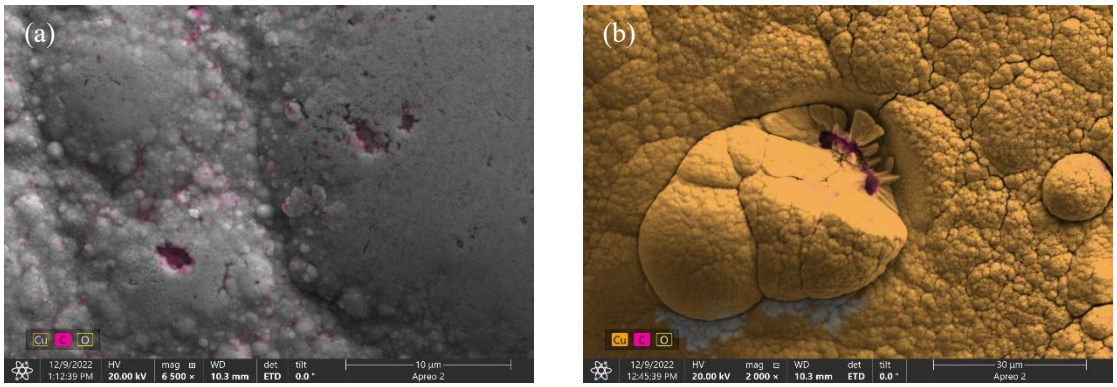


Figure 4.3.5 Carbon and copper with colour-chemi SEM images for GO/Cu5-Brass samples: (a) red shows carbon rich areas; (b) red and yellow show carbon and copper rich areas.

4.3.5 Surface Morphology of GO/Cu4 and GO/Cu5 Samples

Experiments were conducted on GO/Cu composite coatings to determine the influence of varying GO concentrations. Sample coatings plated under 4 and 5 volts were selected for this study. When compared with GO/Cu samples prepared with 0.2 g/L GO under 4 volts (Figure 4.3.3c), it was observed that additional GO tends to inhibit the growth of the cauliflower-like structure. Notably, the GO/Cu4-0.4 sample (Figure 4.3.6a) does not exhibit the characteristic cauliflower-like structure, and a laminated feature can even be observed on the surface view. This suggests that this sample may have better friction resistance than other coatings. The surface of the GO/Cu4-0.6 coating (Figure 4.3.6c) is relatively flat compared to GO/Cu4-0.4, and there are areas with darker shaded dots. However, the laminated structure is not as prominent as in GO/Cu4-0.4. Only the surface of the GO/Cu4-0.8 sample exhibits a cauliflower-like structure (Figure 4.3.6e), but these structures are trapped within granular structures. When comparing the size of the cauliflower structures, those in GO/Cu4-0.8 are smaller than those in the GO/Cu4-0.2 sample coatings.

Figure 4.3.6b, d, and f demonstrate that the surface morphology is influenced by GO concentrations when plated under 5 volts. A cauliflower structure can be observed on coatings conducted under 5 volts. Figure 4.3.6b presents GO/Cu5-0.4, where the cauliflower structure is smaller than that in GO/Cu5-0.2, while the granular area is larger than in GO/Cu5-0.2. As the GO concentration increases to 0.6 g/L (Figure 4.3.6d), the cauliflower structure slightly enlarges, and the granular area mildly reduces. When the GO concentration rises to 0.8 g/L, the cauliflower structure fills most of the area, but its size is smaller than that of the 0.2 g/L sample (Figure 4.3.3d). With an increase in GO concentrations from 0.4 g/L to 0.8 g/L, the granular structure shrinks in size and the cauliflower structure slightly grows, but these structures are smaller than those on the GO/Cu5-0.2 sample surface.

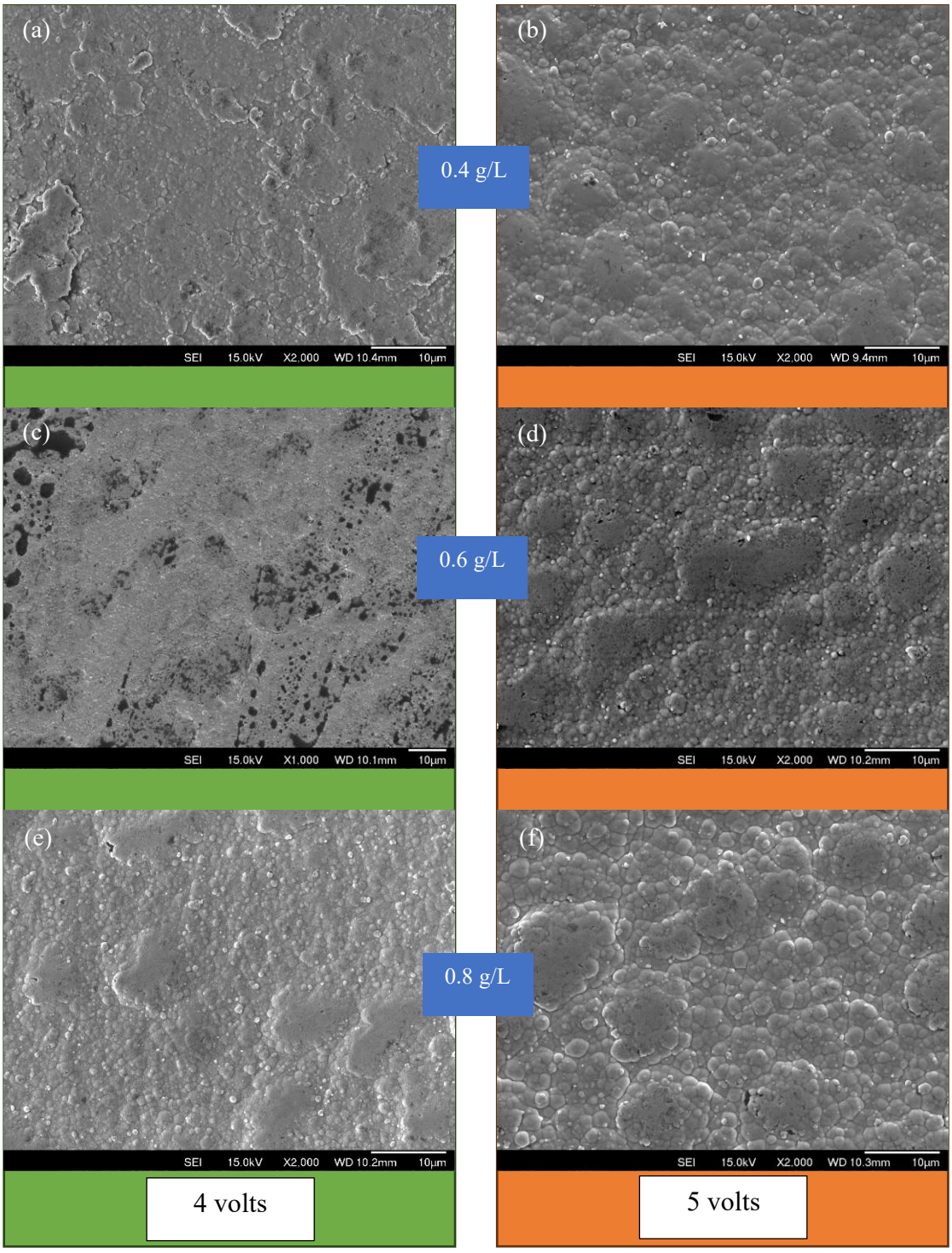


Figure 4.3.6 Surface morphology of GO/Cu4 and 5 samples deposited with 0.4, 0.6 and 0.8 g/L GO concentrations: (a) GO/Cu4-0.4; (b) GO/Cu5-0.4; (c) GO/Cu4-0.6; (d) GO/Cu5-0.6; (e) GO/Cu4-0.8 and (f) GO/Cu5-0.8.

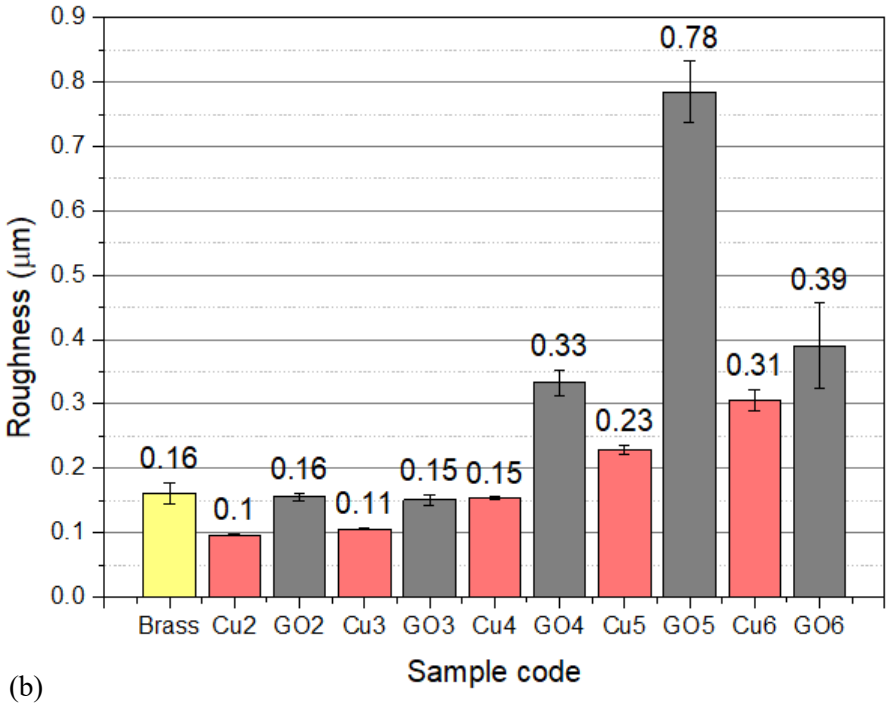
4.3.6 Roughness Comparison between Cu and GO/Cu Samples Coating Surfaces

At Figure 4.3.7a, the average roughness (Ra) of grinded brass substrate material is 0.16 μm before brush plating. The pure Cu control groups are of lower surface roughness compared to that of GO/Cu composite samples. This is the same trend showed at surface morphology SEM images (Figure 4.3.2). With rising of brush plating voltages, the roughness of pure Cu control group is gradually increased from 0.10 μm to 0.31 μm. The roughness of Cu2 (0.10 μm, Ra), Cu3 (0.11 μm, Ra) and Cu4 (0.15 μm, Ra) is smaller than grinded substrate brass which could be seen as nearly featureless SEM morphology. Cu5 (0.23 μm, Ra) and Cu6 (0.31 μm, Ra) shows obvious cauliflower structure under SEM and the surface roughness is larger than brass. GO/Cu samples are of greater average roughness than grinded brass. And it also shows a rising trend with increase of brush plating voltages. While GO/Cu5-Brass (0.78 μm, Ra) shows greatest roughness even than GO/Cu6-Brass (0.39 μm, Ra). This trend could also be seen at Figure 4.3.3. GO/Cu2-Brass and GO/Cu3-Brass shows comparable roughness to grinded substrate brass material, which are 0.16 μm and 0.15 μm respectively. Notably cauliflower structure was shown from brush plating voltage increased to 4 volts, so that the roughness of GO/Cu4-Brass (0.33 μm, Ra) is approximately two times higher than that under 3 volts.

To compare the average roughness of GO/Cu composite sample coatings under different GO concentrations, the bar chart was carried out at Figure 4.3.7b. The left half side shows the roughness of GO/Cu4 samples, and the right half part is GO/Cu5 samples of different GO concentration, ranging from 0.4, 0.6 and 0.8 g/L. It is interesting to note that GO/Cu samples of 0.4 g/L GO concentration has comparable roughness comparing with samples under 0.2g/L of GO. GO/Cu4-0.4 is of 0.32 μm average roughness as for GO/Cu4-0.2 is 0.33 μm. Likely, GO/Cu5-0.2 has 0.78 μm in average roughness and roughness slightly increased to 0.85 μm with 0.4 g/L GO addition. The roughness of higher GO concentration decreased which could

be possible. As GO is relatively flat 2D material and metal brush plated metal is of cauliflower-like structure, it is possible that with adding 2D material flatten the cauliflower structure of Cu. With 0.6 g/L GO concentration, GO/Cu samples are of comparable roughness with grinded substrate brass material which are 0.18 μm for GO/Cu4-0.6 and 0.17 μm for GO/Cu5-0.6. With the greatest roughness and relatively high GO concentration, the friction performance might be the best comparing with other GO/Cu composite samples with different parameters. GO/Cu4-0.8 (0.24 μm, Ra) and GO/Cu5-0.8 (0.23 μm, Ra) are of slightly higher roughness comparing with GO/Cu with 0.6 g/L. The relatively low roughness of 0.6 g/L and 0.8 g/L samples could be seen under SEM surface morphology images at Figure 4.3.7.

(a)



(b)

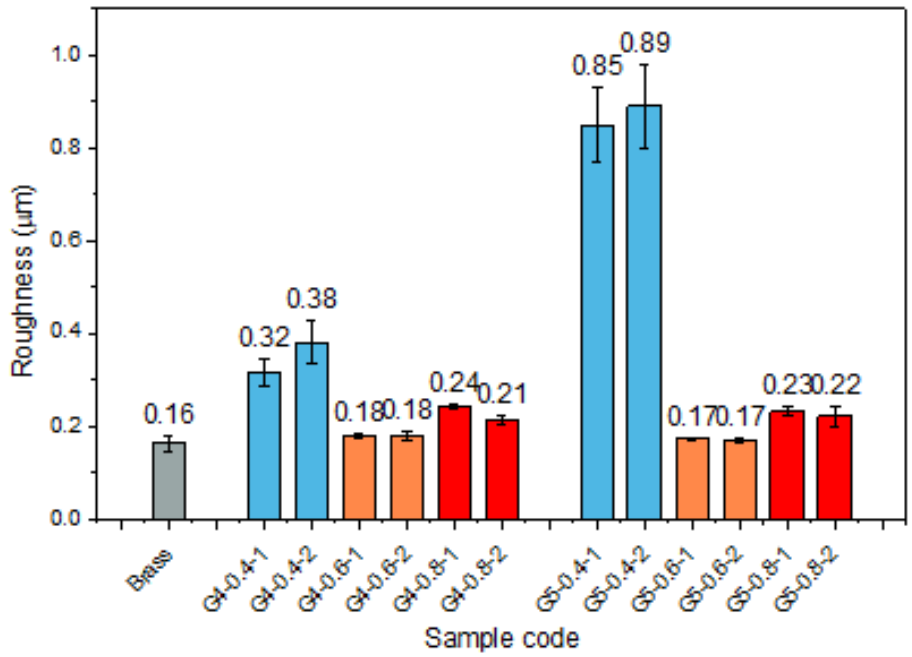


Figure 4.3.7 Bar charts for roughness comparisons for: (a) pure Cu and GO/Cu samples deposited with 0.2 g/L GO suspension; (b) GO/Cu samples deposited with 0.4, 0.6 and 0.8 g/L GO suspension.

4.3.7 Cross-sectional View SEM Images of Pure Cu Control Group

With the acidic ferric chloride ($FeCl_3$) etchant etching for around 30-60 seconds, the cross-sectional surface was shown under SEM. As depicted in Figure 4.3.8a, Cu2-Brass displays its layer structure from the top pure copper layer, then the nickel interlayer, to the copper-zinc (Cu-Zn) alloy substrate. The layer thickness of Cu2-Brass is only 2.8 μm, which could explain why Cu2-Brass still shows grinding curves on its surface morphology SEM image. Cu3-Brass, with a thickness of 8.5 μm, only exhibits a laminate structure produced with a layer-by-layer brush plating process. This can be easily seen in Figure 4.3.8b and could match the featureless surface morphology shown in Figure 4.3.2b. Cu4-Brass (Figure 4.3.8c) is composed of a laminate structure and column crystal structure, which can also be seen on surface morphology. The cauliflower structure also begins to appear on the Cu4-Brass surface. Figure 4.3.8d depicts the cross-sectional view of Cu5-Brass, which has a thickness of 39.1 μm. This abrupt increase in layer thickness can also be observed in previous experiments, but it results in a reduction of micro-hardness, which will be discussed later. Compared to Cu5-Brass, the layer thickness of Cu6-Brass (Figure 4.3.8e) only slightly increases to 44.0 μm. All in all, the pure Cu control group layer thickness rises with an increase in brush plating voltages. The cauliflower structure is column crystal shown at the cross-sectional view. At Figure 4.3.8f, the line scan of Cu4 shows the elements constituent near the interlayer Ni, the red curve shows Cu percentage, green curve shows Ni percentage and orange curve shows Zn percentage. There are three parts shown in the SEM image of line scan which are indicated in red a, b and c. The coating area a is composed of Cu and small constituents of Zn was detected, this might be because Zn transferred under $FeCl_3$ etchant. The area b is Ni interlayer and then the line scan shows nearly no element around the gap. The brass substrate area c shows Cu and Zn constituents on this area.

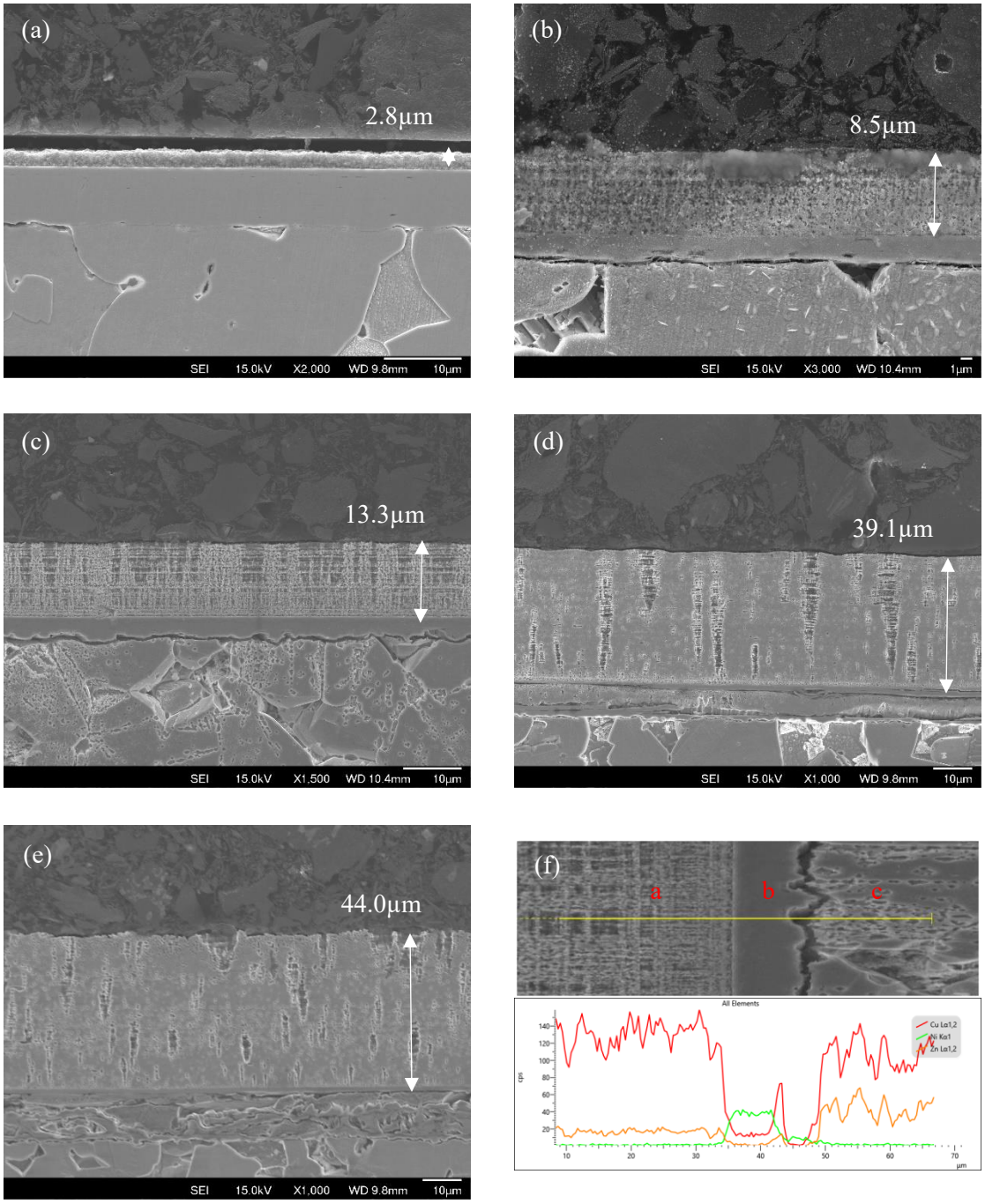


Figure 4.3.8 Cross-sectional view for pure Cu control group to investigate how the voltage would influence the layer structure of Cu brush plating coating: (a) Cu2-Brass; (b) Cu3-Brass; (c) Cu4-Brass; (d) Cu5-Brass; (e) Cu6-Brass and (f) Cu4-Brass-EDX.

4.3.8 Cross-sectional SEM Images of GO/Cu Composite Coating (0.2 g/L GO)

The cross-sectional view of GO/Cu2-Brass, shown in Figure 4.3.9a, reveals only a nickel layer approximately 2 μm thick and etched martensitic Cu-Zn (brass) crystals. From surface morphology SEM image of GO/Cu2-Brass as shown in Figure 4.3.3a, it shows clear thin grinding curves. From those two results, GO/Cu composite coating with 2 volts could only produce layer much thinner than 1 μm. As the limitation of layer thickness on some characterisation techniques, some of the results would not include results from this sample coating.

The layer thickness of GO/Cu composite coatings plated with 0.2 g/L shows an increasing trend with higher brush plating voltages, although the rate of increase varies. As shown in Figure 4.3.9b, the layer thickness of GO/Cu3-Brass is 3.0 μm, which is thinner than its control group (8.45 μm). For GO/Cu4-Brass (Figure 4.3.9c), the layer thickness is 19.4 μm, which is also thinner than that of its Cu control group. Additionally, columnar crystalline structures begin to appear under a brush plating voltage of 4 volts. These columnar structures exhibit a laminar pattern, and graphene-like features can also be observed in these areas, which will be discussed later.

The layer thickness increases significantly when the plating voltage is raised from 4 volts (19.4 μm) to 5 volts (Figure 4.3.9d, 36.6 μm), compared to the Cu control group. GO/Cu6-Brass (Figure 4.3.9e) further shows a slight increase in thickness to 41.3 μm compared to Cu6-Brass. Interestingly, the layer thickness of GO/Cu composite coatings is generally smaller than that of the pure Cu control group, except for GO/Cu4-Brass, whose layer is thicker than Cu4-Brass. The top of the columnar crystals exhibits an abrupt structure, corresponding to the inner features of the cauliflower-like morphology observed in the cross-sectional view.

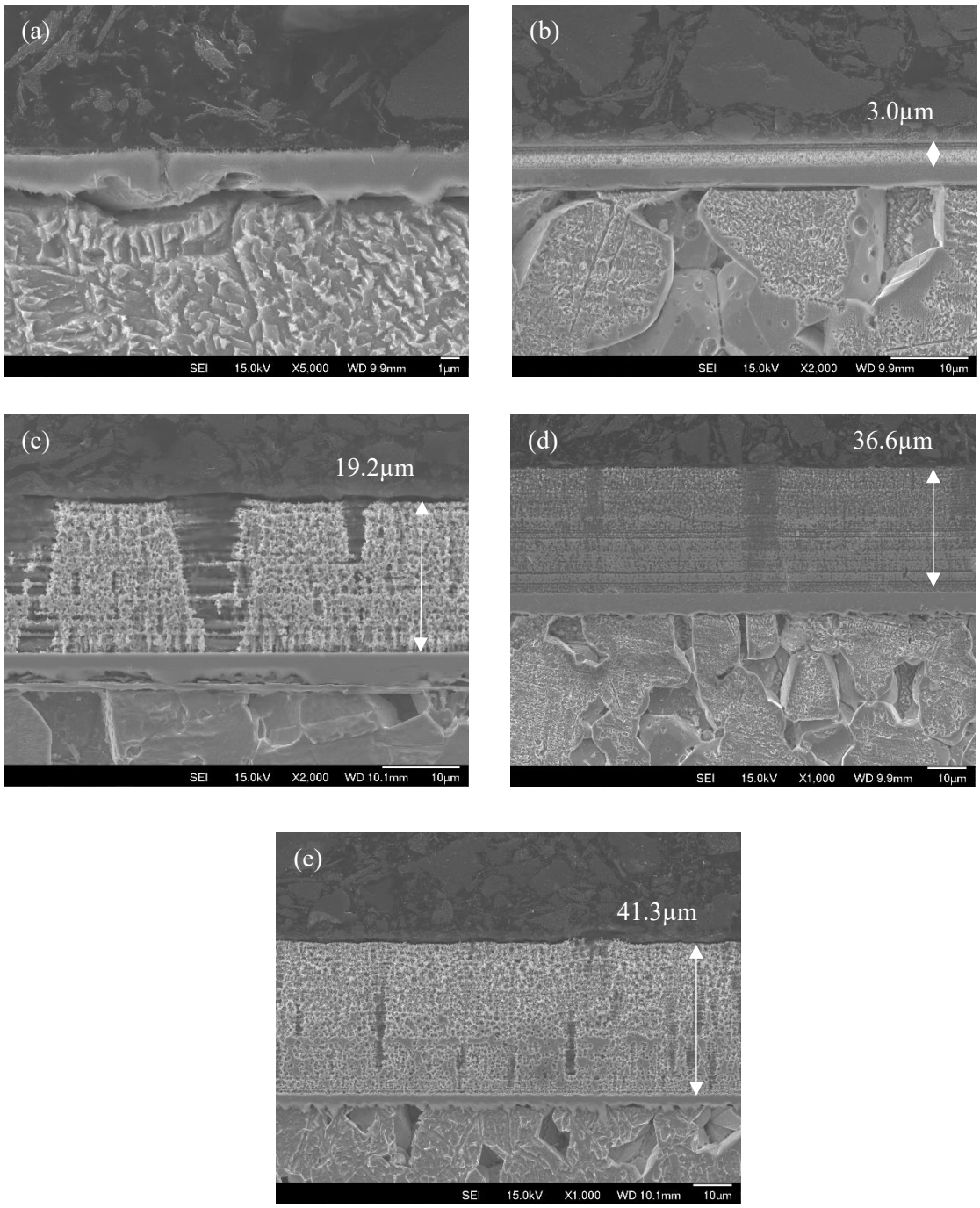


Figure 4.3.9 Cross-sectional view of GO/Cu brush plating coatings deposited with 0.2 g/L GO concentration: (a) GO/Cu2-Brass; (b) GO/Cu3-Brass; (c) GO/Cu4-Brass, (d) GO/Cu5-Brass and (e) GO/Cu6-Brass.

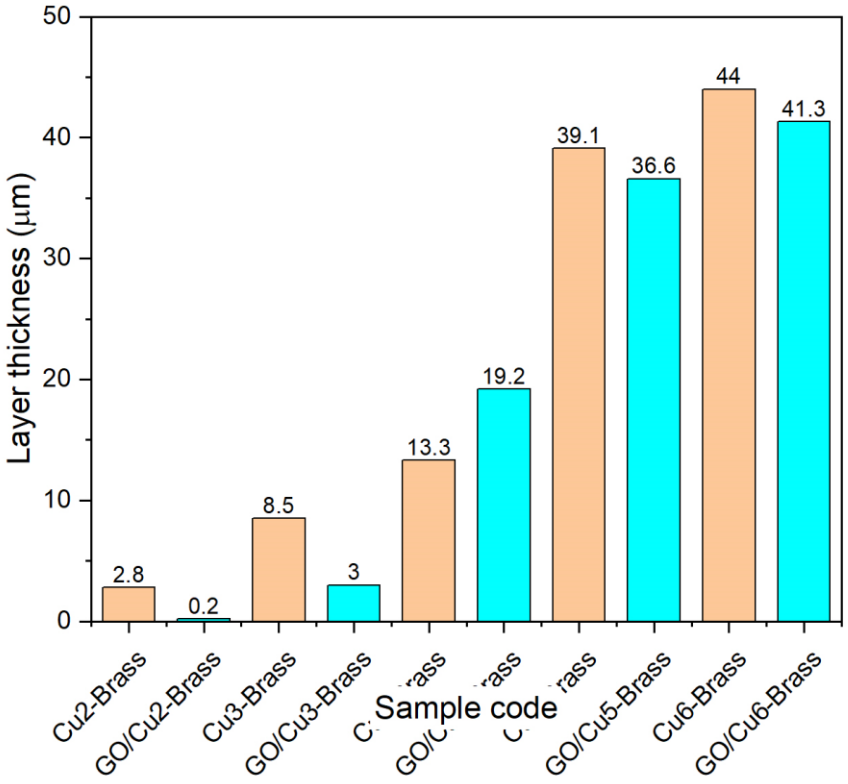


Figure 4.3.10 Comparison of layer thickness for pure Cu control group and GO/Cu-Brass samples.

It is shown in Figure 4.3.10 that the layer thickness influence of GO addition within the Cu based coating structure. Generally, it is notable that the growth of layer thickness would be impeded by the graphene oxide addition. While the layer thickness of GO/Cu4-Brass is slightly larger than that of Cu4-Brass. Under relatively low brush plating potential as 2 and 3 volts, the limited current density was applied to the sample surface. The additional GO suspension into the Cu plating solution could result in a significant reduction of growth in plating coating structure under 2 and 3 volts. The influence of GO suspension shows relatively smaller reduction under 5 and 6 volts.

4.3.9 Cross-sectional View of GO/Cu4-5 Samples with 0.4, 0.6 and 0.8 g/L GO

With increasing of GO concentrations, the GO/Cu4 sample coating thickness is gradually rising. The layer thickness of GO/Cu4-Brass (Figure 4.3.9c) is 19.2 μm and GO/Cu4-0.4 is 21.6 μm, which is slightly higher than that of GO/Cu4-Brass. Layer thicknesses of GO/Cu4-0.6 (Figure 4.3.11c) and GO/Cu4-0.8 (Figure 4.3.11e) are 20.7 μm and 22.4 μm respectively. The column structure of those two samples is not as notable as those of GO/Cu4-Brass, which shows similar trends as roughness results. There are still notable several laminate structures shown at Figure 4.3.11c and e. As acidic $FeCl_3$ would not result in corrodes on Ni interlayer, the area without corrosion is the Ni interlayer where the edge might corrode into crack. This could be caused by cell reactions occurred at this line on the brass substrate side.

Figure 4.3.12 exhibits the layer thickness of GO/Cu4 and GO/Cu5 samples under 0.2, 0.4, 0.6 and 0.8 g/L of GO concentrations. It is interesting to note that the GO concentrations show limited influence on the layer thickness for both GO/Cu4 samples. Although the GO/Cu4 samples illustrate fluctuation with uprising GO addition, the difference of the layer thickness is around only 2 μm. As for the GO/Cu5 samples, the layer thickness is notably decreased from 36.6 μm to 28.9 μm, with the GO concentration of 0.2 g/L increase to 0.4 g/L. While the differences in layer thickness are less than 2 μm as the GO concentration increases gradually from 0.4 g/L to 0.6 g/L and then to 0.8 g/L—measuring 28.9 μm, 27.8 μm, and 27.4 μm, respectively—this indicates that higher GO concentrations beyond 0.4 g/L have a diminishing effect on reducing the layer thickness of the GO/Cu5 samples.

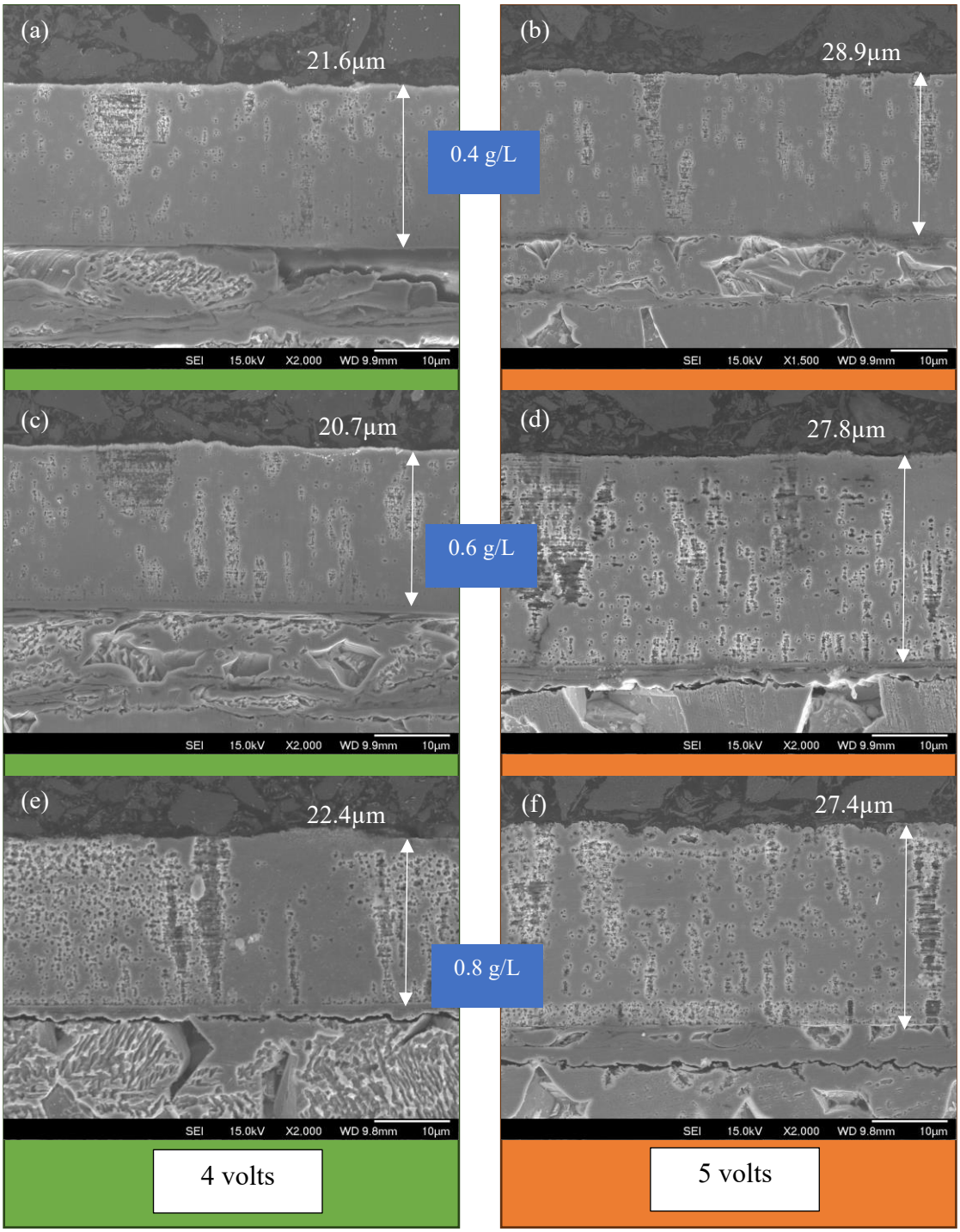


Figure 4.3.11 SEM images of cross-sectional view of GO/Cu4 and 5 samples deposited with 0.4, 0.6 and 0.8 g/L GO concentrations: (a) GO/Cu4-0.4; (b) GO/Cu5-0.4; (c) GO/Cu4-0.6; (d) GO/Cu5-0.6; (e) GO/Cu4-0.8 and (f) GO/Cu5-0.8.

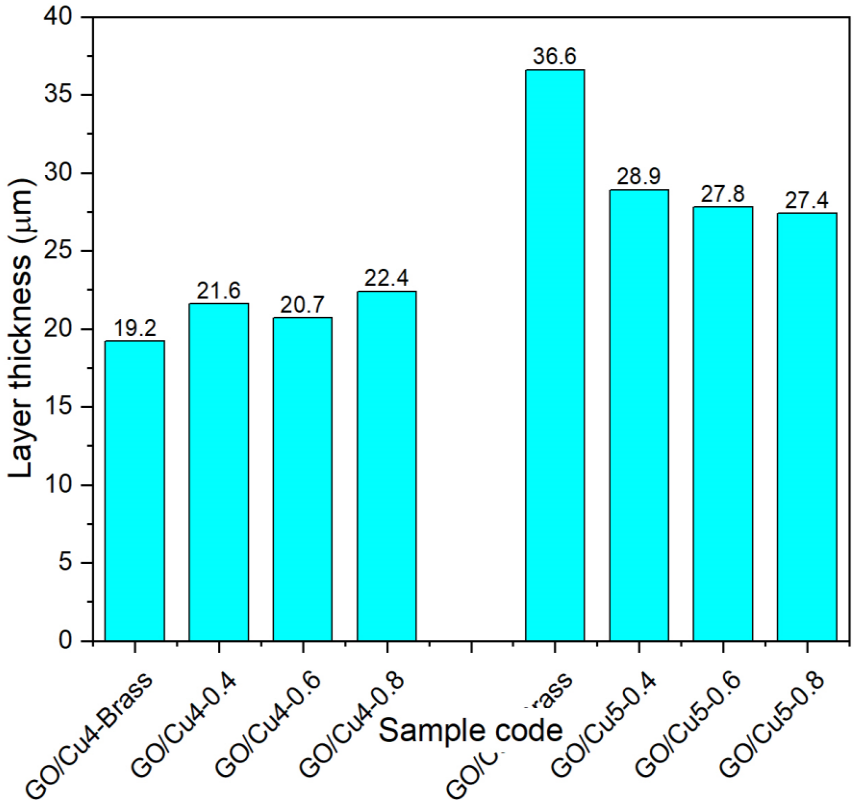


Figure 4.3.12 Comparing the layer thickness with GO differential GO concentrations under 4 volts and 5 volts.

The influence of GO concentration shows opposite trend on the GO/Cu5 samples. With rising on the GO concentration, the layer thickness decreased mildly. Similar situation also happened when the brush plating voltage were increased over 5 or 6 volts, the layer thickness shows decrease and voids and vacance increased. Compared with GO/Cu4-Brass sample (Figure 4.3.9c), less abrupt structure is shown on the outmost surface area and the laminate structures spread more uniformly.

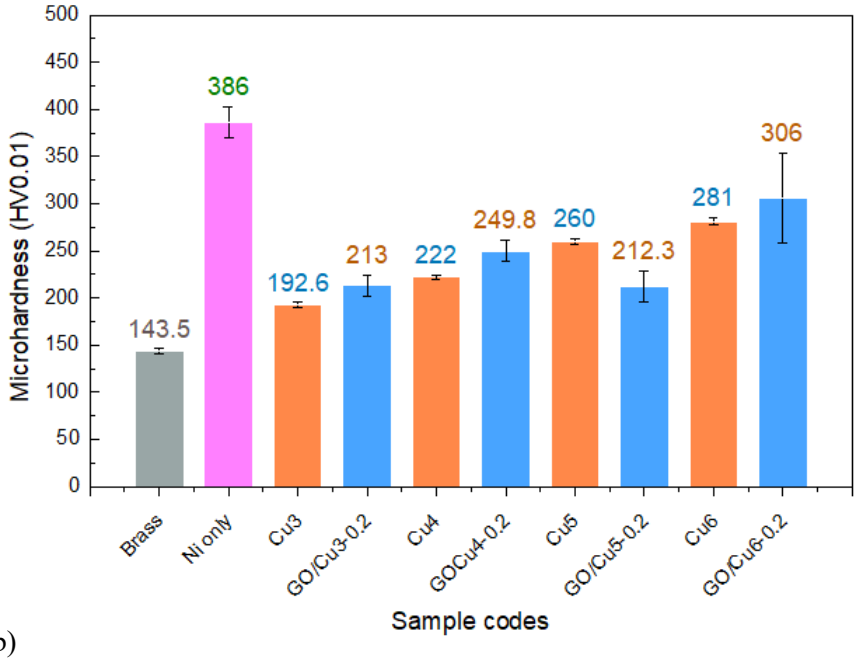
4.3.10 Microhardness Comparing with Sample with and without GO Addition

In Figure 4.3.13a, the orange vertical bars denote data to the pure copper control group, while the blue vertical bars depict the GO/Cu composite material coating. The hardness of the brass substrate is indicated by the grey vertical bars, which is registering at 143.5 $HV_{0.01}$. After the deposition of a special nickel intermediate layer, the hardness increases to 386 $HV_{0.01}$. The pure copper control group exhibits a nearly linear increase in hardness with the rising of electro-brush plating voltage from 192.6 $HV_{0.01}$ for Cu3 to 281.0 $HV_{0.01}$ for Cu6. However, Cu2 and GO/Cu2-Brass showed no detectable hardness, so there shows no data of those two samples in Figure 4.3.13a. Cu4 sample coating is of 222.0 $HV_{0.01}$ in hardness and Cu5 is of 260 $HV_{0.01}$. Likewise, the GO/Cu composite coating, with 0.2 g/L GO concentration, also demonstrates general increase in hardness with rising voltage from 213.0 $HV_{0.01}$ for GO/Cu3-Brass to 306.0 $HV_{0.01}$ for GO/Cu6-Brass. Whereas, in the case of the GO/Cu5-Brass sample, a notable reduction in hardness is observed with only 212.3 $HV_{0.01}$ which is comparable to the hardness of GO/Cu3-Brass. Those Cu control groups are of relatively smaller standard error compared with that of GO/Cu composite samples. This might be due to the GO addition causing the increase in cauliflower structures.

To investigate the impact of graphene oxide (GO) concentration on hardness, the analysis presented in Figure 4.3.13b was conducted. The gray vertical bars present the corresponding pure copper control group of 4 volts (222 $HV_{0.01}$) and 5 volts (260 $HV_{0.01}$), the GO addition makes the microhardness elevate slightly. As the relatively big errors and comparable hardness results among different parameters, so that the bar chart includes all hardness results are presented from two replicates. GO/Cu4-0.4-1 and 2 present relatively high microhardness (276.1 and 280.4 $HV_{0.01}$). GO/Cu5-0.4-1 and 2 depict higher microhardness compared to that of GO/Cu4-0.4 samples, which are 291.0 and 294.3 $HV_{0.01}$. After adding GO to 0.6g/L, the

microhardness decreased to 270.2 and 272.5 HV0.01 for GO/Cu4-0.6 and 285.5 and 282.6 $HV_{0.01}$ for GO/Cu5-0.6 samples. The hardness for GO/Cu4-0.8-1 and 2 slightly declined to 266.8 and 270.0 $HV_{0.01}$, compared with GO/Cu4-0.6 samples. As for GO/Cu5-0.8-1 and 2, the hardness of them is increased compared to GO/Cu4-0.8 to 286.7 and 276.4 $HV_{0.01}$. Comparing the hardness of samples with the same graphene oxide (GO) concentration, the overall trend indicates that the hardness of the 4V sample is slightly lower than that of the 5V sample. Although the addition of GO results in higher hardness compared to samples without GO, there is a gradual decline in sample hardness as the GO concentration increases.

(a)



(b)

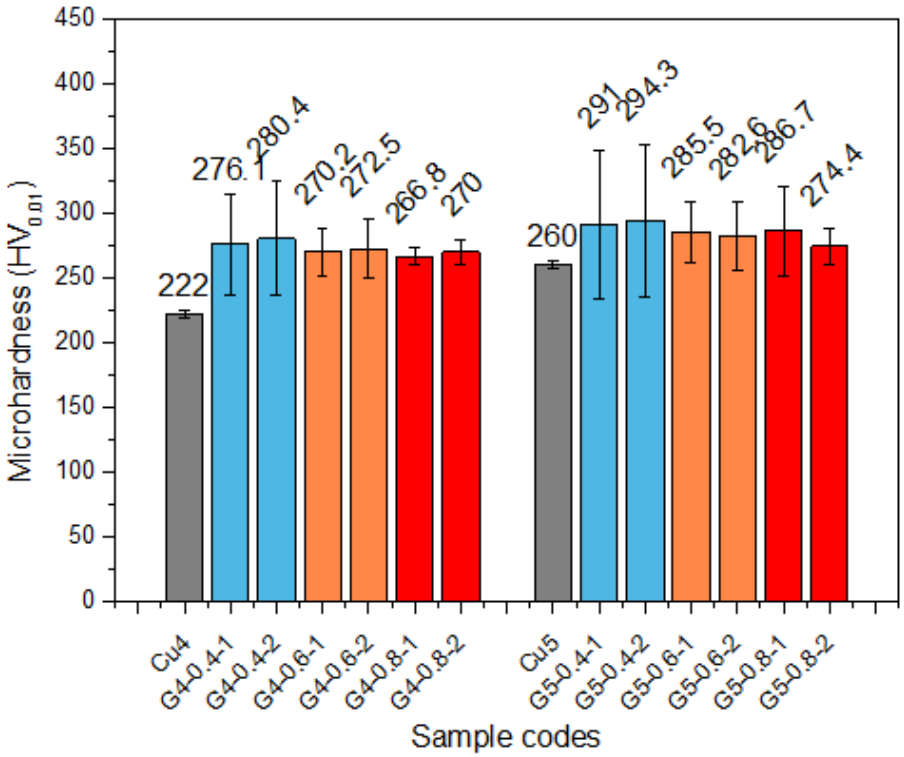
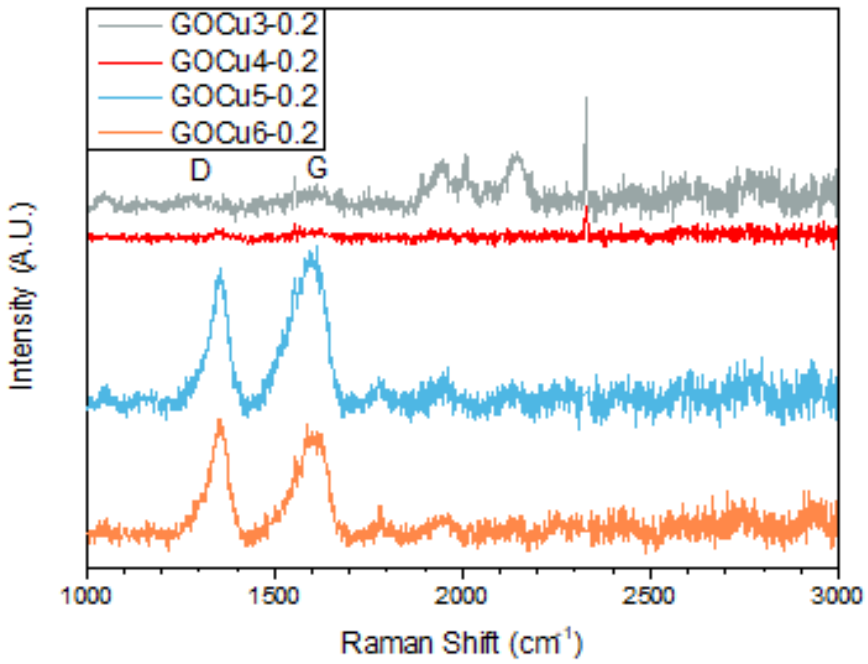


Figure 4.3.13 Microhardness comparison of GO/Cu samples with (a) different voltages and (b) different GO concentrations.

4.3.11 Raman Spectroscopy to Reveal GO on Outmost Coating Region

At Figure 4.3.14a, the graph illustrates the GO featured D and G peaks finding on specific locations on the GO/Cu sample surface. GO/Cu3-Brass exhibits D and G characteristic peaks, like the GO/Cu4-Brass sample. Those two Raman spectra present less notable D and G peaks, possibly due to limited exposure of GO to the air so it presents less signal captured by Raman detector. To investigate individually, the Raman spectra are notable. The D and G peaks for GO/Cu3 depict left shift (or blue shift), and the rest three spectra show similar D and G positions. As mentioned at SEM images session, the cauliflower like structure was shown with the plating voltage increasing to 4 volts. It is interesting to note that the intensity of D and G peaks can be easily identified in the Raman spectra of GO/Cu5-Brass and GO/Cu6-Brass samples. Moreover, 2D and D+G peaks could also be depicted on the Raman spectra. To reveal the GO, function within the composite coating, the I_D/I_G ratio is important. As mentioned before, the I_D/I_G ratio of GO power dissolved in the coating is tested as 0.79. Although the GO signal of GO/Cu3-Brass and GO/Cu4-Brass samples is relatively lower than the other two, the I_D/I_G ratio of them are 0.72 and 0.68 respectively. The I_D/I_G ratio is smaller than that of GO powder which might present better electrical property and tribological property. While the GO/Cu5-Brass presents 0.85 in I_D/I_G ratio which is slightly higher than GO powder. As for GO/Cu6-Brass, it depicts 1.06 I_D/I_G ratio which presents higher D peaks. With the Raman spectra, the GO/Cu4-Brass shows the best results which is only 0.68 and GO/Cu5-Brass also shows relatively great results. So, Raman spectra are one of the reasons the 4 and 5 volts were chosen in the test and further GO concentration parameter was discovered with those two volts.

(a)



(b)

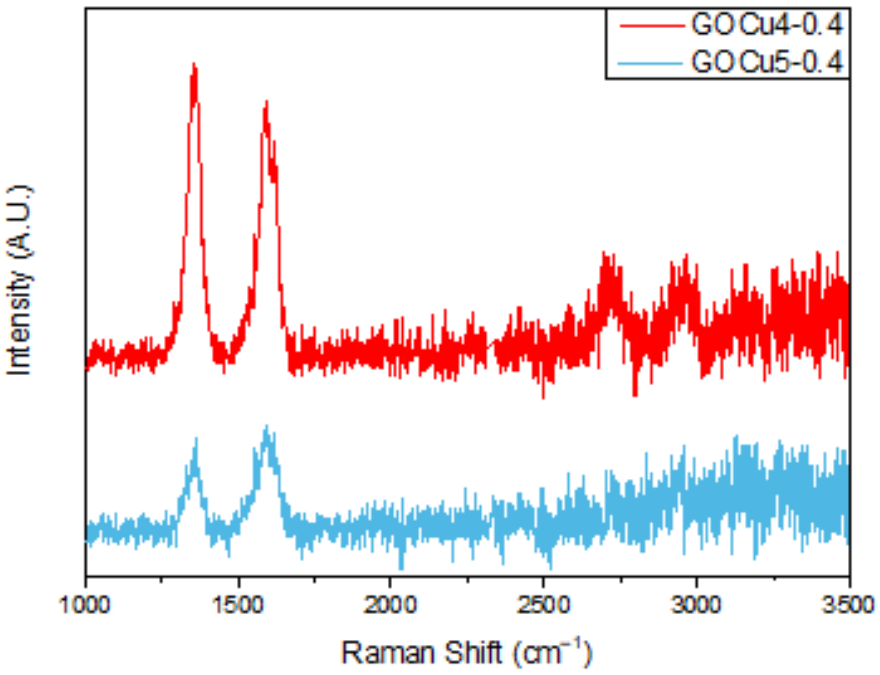


Figure 4.3.14 Raman spectroscopy for GO/Cu composite coating on Brass substrate deposited with different GO concentrations: (a) 0.2 g/L GO concentration and (b) 0.4 g/L GO concentration.

Figure 4.3.14b illustrates the Raman spectra of GO/Cu samples under 0.4 g/L of GO concentration with 4 and 5 volts of plating voltages. The Raman intensity could represent how the GO would influence the tribology results, as it presents the influence of GO on the surface region with limited penetration of laser resource of Raman. The intensity of GO/Cu4-0.4 D and G peaks is notably higher than that of GO/Cu5-0.4. Moreover, the 2D and D+G peaks could also be found at spectra of GO/Cu4-0.4. Hence, the tribological presentation of GO/Cu4-0.4 might be greater than that of GO/Cu5-0.4. Whereas the I_D/I_G ratio of them depicts opposite performance, the I_D/I_G ratio of GO/Cu4-0.4 and GO/Cu5-0.4 are 1.16 and 0.87 respectively. The I_D/I_G ratio of GO/Cu4-0.2 is only 0.68, the tribological performance would be discussed in later session.

4.3.12 X-ray Diffraction (XRD) Comparisons on Different Coatings

In Figure 4.3.15a, the pure copper control group consisting of Cu2 to Cu6 exhibits distinct patterns under identical scanning conditions. With different voltages, pure Cu control group coatings exhibit no position changes which could represent no lattice change along with the voltage difference. It is interesting to note that the XRD patterns of Cu2 exhibits relatively higher intensity $Cu_{0.64}Zn_{0.36}$ peaks (shown with red lines) along with relatively lower intensity Cu peaks (shown with red dashed lines). The intensity of $Cu_{0.64}Zn_{0.36}$ is declined with rising of brush plating voltages comprising 2, 3 and 4 volts. Cu (111) Cu (200) and (222) are the three Cu peaks could be found on Cu2 sample. As mentioned before, the layer thickness of Cu5 and Cu6 is 39.1 μm and 41.0 μm respectively, only pure Cu peaks could be found on its XRD and the Cu (111), Cu (200), Cu (220), Cu (311) and Cu (222) is denoted on the Figure 4.3.15a. Among those pure Cu XRD patterns, the peaks of brass (or $Cu_{0.64}Zn_{0.36}$), Nickel (Ni) and pure copper (Cu) are denoted with their directions. In Cu2, Cu3, and Cu4 sample coatings, $Cu_{0.64}Zn_{0.36}$ can be found and denoted on different positions at (111), (222), and (200).

Additionally, the interlayer Ni also could be detected and denoted as $Ni_{4.0}$ (111) and $Ni_{4.0}$ (022) on Cu2 to Cu4 sample surfaces. As mentioned before at SEM images of CS view for Cu4, the average thickness of Cu4 is 13.3 μm. As $Cu_{0.64}Zn_{0.36}$ is substrate beneath pure copper, so that X-ray could be penetrated over 13.3 μm for those Cu plated coatings.

As mentioned at Experimental part, using the Scherrer's equation, the crystalline size from the perpendicular direction of surface coating could be calculated out. Using the β (or FWHM) from Cu peaks exhibited on the patterns, the crystalline size of Cu in average were calculated with their standard errors. It is interesting to note that the calculated crystalline size of Cu in Cu3 is only 15 nm with 2 nm of standard error. And the crystalline size of Cu4, Cu5 and Cu6 exhibit gradual rising which are 17±1 nm, 19±2 nm and 21±2 nm, respectively. This is closely related to the increase of plating voltages.

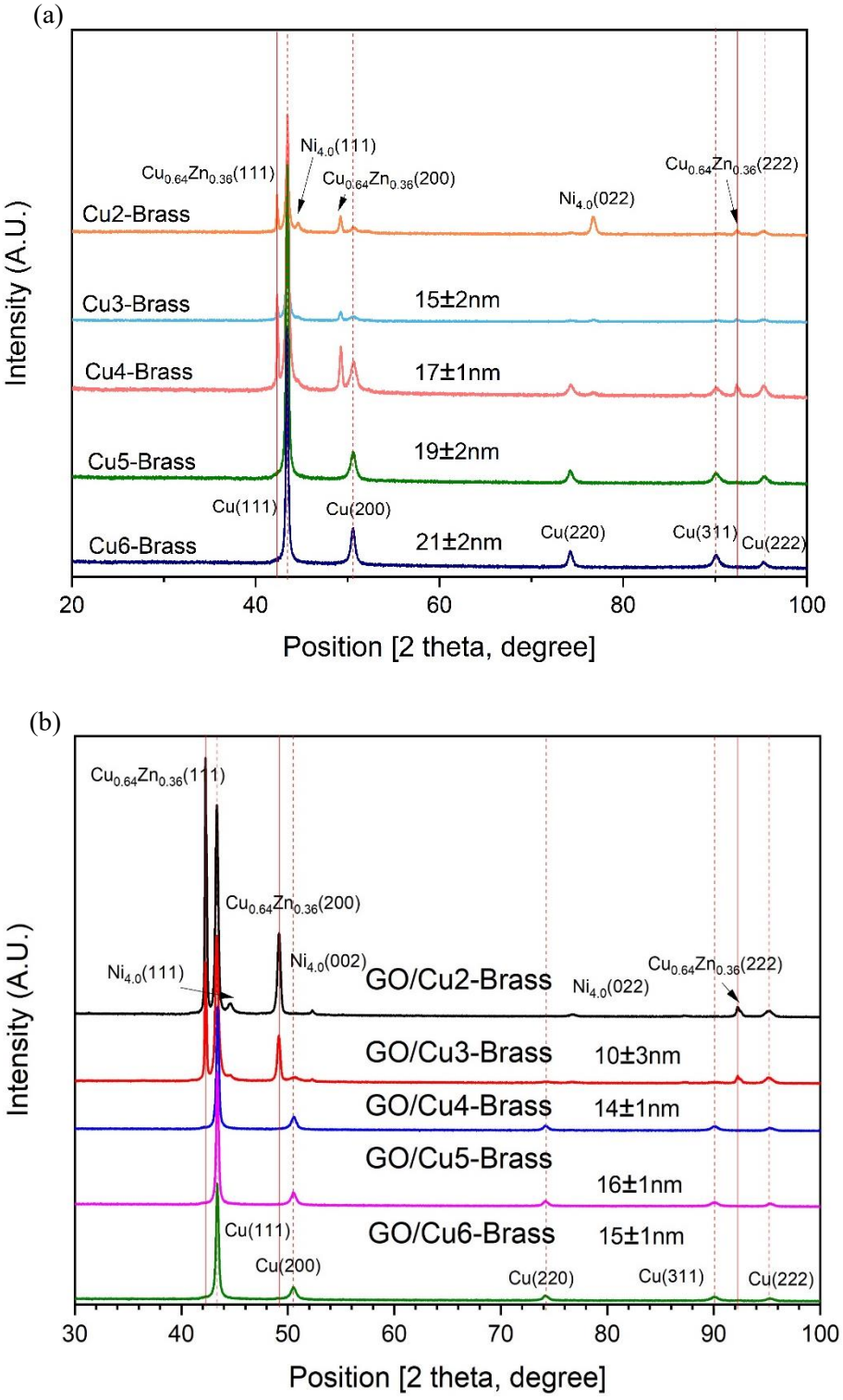


Figure 4.3.15 XRD patterns from coating surface of (a) Cu control group and (b) GO/Cu-Brass materials.

Figure 4.3.15b exhibits the XRD patterns of GO/Cu samples on brass substrate with 0.2 g/L of GO concentrations. To compare with Cu control group, the $Cu_{0.64}Zn_{0.36}$ peaks (shown with red lines) and Ni peaks only depict on the GO/Cu2-Brass and GO/Cu3-Brass which denoted as $Ni_{4.0}$ (111) and $Ni_{4.0}$ (022). There only shows Cu peaks (shown with red dashed lines) on the GO/Cu4-Brass, GO/Cu5-Brass and GO/Cu6-Brass. The layer thickness of GO/Cu4-Brass is 19.2 μm, so that it is possible that the XRD from perpendicular angle could be penetrate through 13.3 μm of Cu coating but 19.2 μm of GO/Cu composite coating. The brush plating voltages also show no influence in the XRD peak positions for GO/Cu composite coating materials. As for the crystallite size calculation from perpendicular direction of coating surface, the GO/Cu3-Brass shows the smallest crystallite size which is only 10±3 nm. Whereas crystallite size of GO/Cu3-Brass is slightly larger than that of Cu3's. For GO/Cu4-Brass, GO/Cu5-Brass and GO/Cu6-Brass samples, the crystallite size of them exhibits comparable calculation results which are 14 ±1 nm, 16±1 nm and 15±1 nm, respectively.

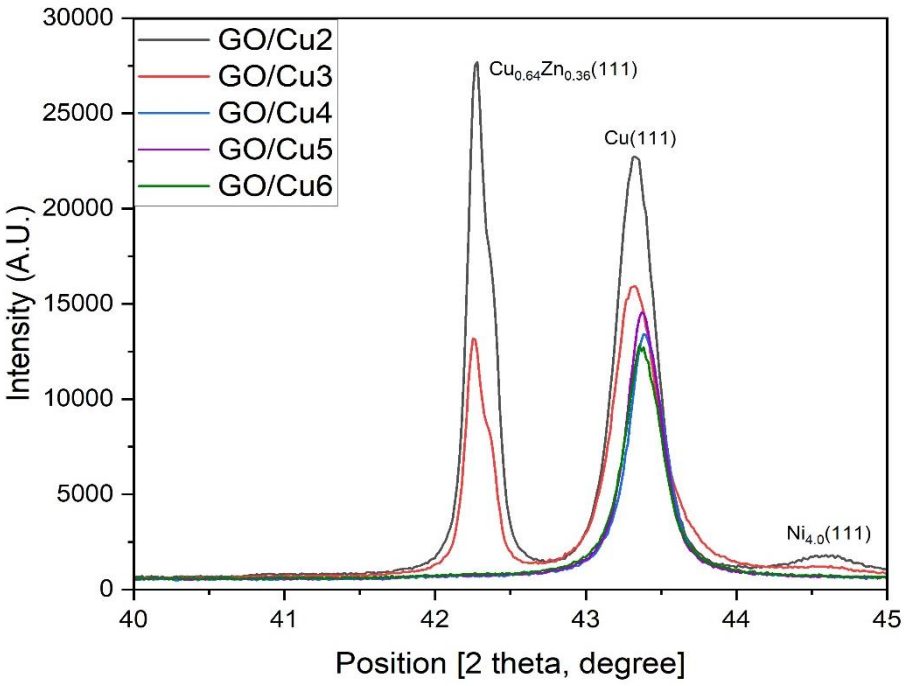


Figure 4.3.16 Detailed XRD patterns of GO/Cu samples at lower positions.

The Figure 4.3.16 illustrates the XRD patterns of GO/Cu samples with 40-45 in 2 theta position. As mentioned before, the XRD analysis enclosed the presence of $Cu_{0.64}Zn_{0.36}$ (111) and Ni (111) on the GO/Cu2-Brass and GO/Cu3-Brass samples. While the remaining samples only exhibit the Cu (111) peak within the previous state range. Notably, the Cu (111) peak from GO/Cu2-Brass sample demonstrate relatively broader width among those samples shown in the Figure 4.3.16. The Cu (111) peak of GO/Cu3-Brass depicts narrower comparing with that of GO/Cu2-Brass. It is interesting to note that the Cu (111) peaks in the GO/Cu4-Brass, GO/Cu5-Brass and GO/Cu6 specimens are almost coincide, demonstrating weaker and narrower peaks than the other two specimens.

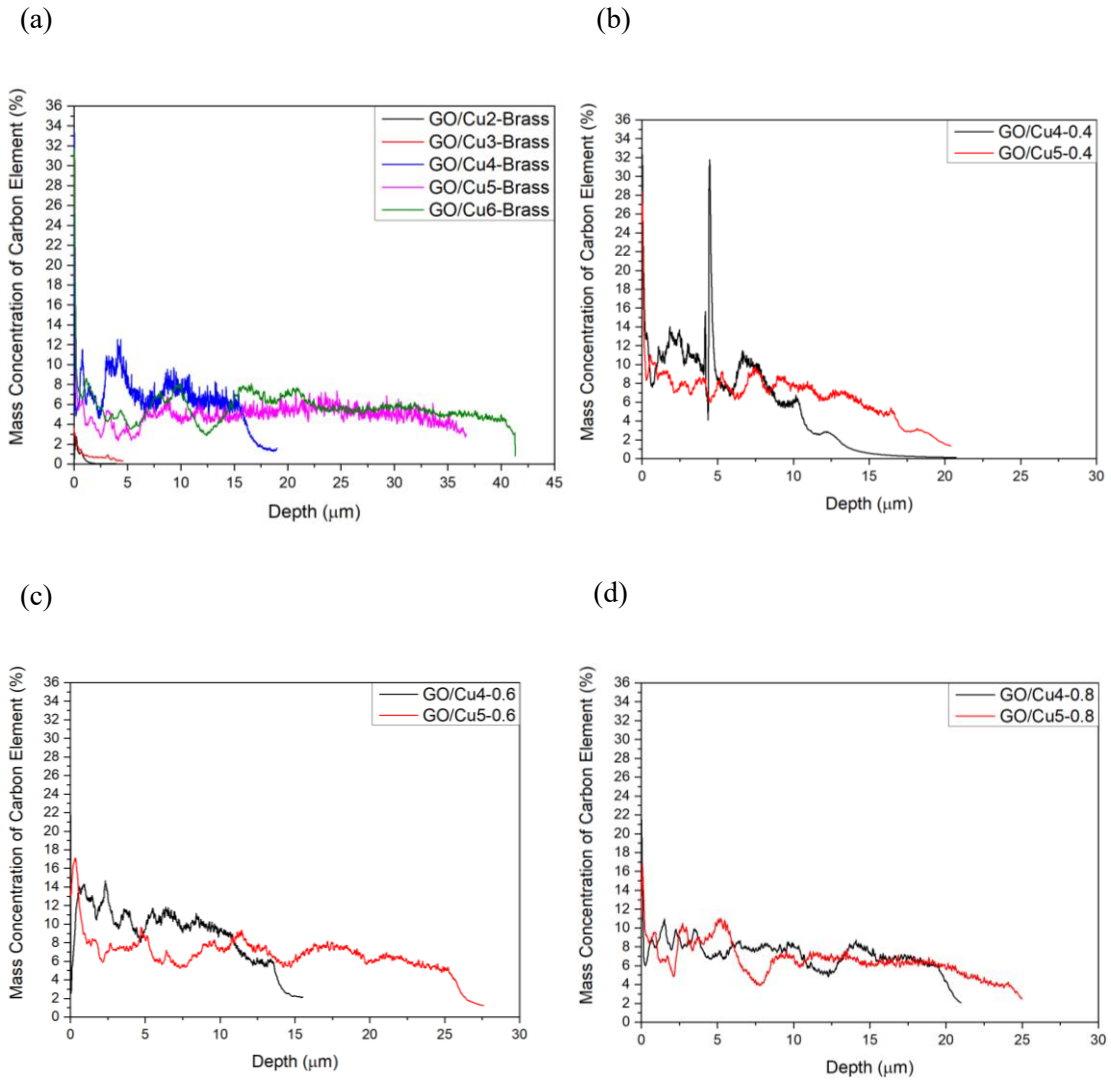


Figure 4.3.17 GDOES results of carbon concentrations for samples deposited with different GO additions: (a) 0.2 g/L; (b) 0.4 g/L; (c) 0.6 g/L and (d) 0.8 g/L.

4.3.13 GDOES Results of Carbon Concentration

Figure 4.3.17a exhibits the comparison of the carbon (C) weight concentrations under different brush plating voltages with 0.2 g/L of GO concentrations. There is no carbon component contained in the brass substrate, so that the depth of carbon content could represent the depth of GO/Cu coating with 0.2 g/L of GO concentrations. The depth or layer thickness is uprising with increase of brush plating voltages which depicts similar the layer thickness increasing trend shown in SEM images result at 4.3.6. The depth of GO/Cu2-Brass sample is only less

than 2 μm and the mass concentration could be better not to use in this circumstance, as there are few microns of not applicable data on GDOES result. It only depicts around 1% of carbon constituents in the GO/Cu3-Brass coating, but the existence of carbon is continuous in its coating structure. It is interesting to note that the carbon composition of GO/Cu4-Brass is slightly higher than other samples which is around 9%. The carbon composition of GO/Cu5-Brass is slightly lower than that of GO/Cu6-Brass which are approximately 5% and 7% respectively.

Figure 4.3.17b-d shows carbon composition profile contained within GO/Cu4 and 5 sample coatings with comprising 0.4 g/L to 0.8 g/L of GO concentrations. Similar to GO/Cu4-Brass and GO/Cu5-Brass (shown in Figure 4.3.17b), the GO/Cu5-0.4 exhibits slightly lower C content than that of GO/Cu4-0.4, with respective values at around 8% and 12%. On the same time, the carbon mass concentration profile of GO/Cu4-0.4 is relatively fluctuated, compared with that of GO/Cu5-0.4. With 0.6 g/L of GO solution (shown at Figure 4.3.17c), the carbon composition of samples plated under 4 volts is generally larger than that of samples plated under 5 volts which are 11% and 8% respectively. As for GO/Cu4-0.8 and GO/Cu5-0.8, their carbon concentrations of them are approximately the same, at around 8%.

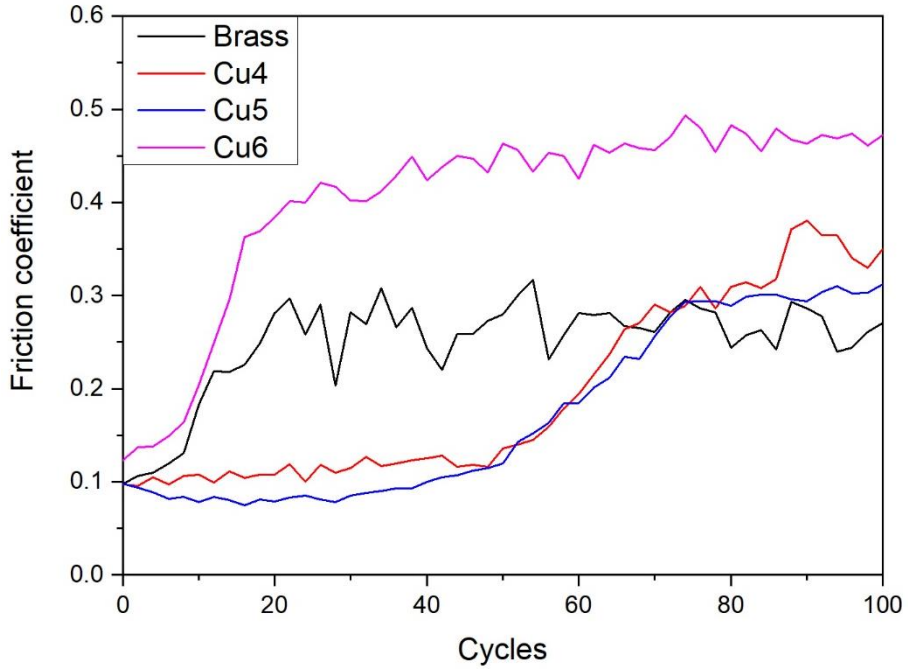
4.4 Tribological Properties

4.4.1 Tribological Comparison of Pure Cu and GO/Cu-Brass Samples

4.4.1.1 The Friction Coefficient for Pure Cu and GO/Cu-Brass Coatings

As depicted in Figure 4.4.1a and b, the friction coefficient (COF) changes with tribo-test cycles are depicted for Cu control group and grinded brass under ambient atmospheric conditions using a dry sliding mode. For Cu4, 5 and 6 samples, with increasing of sliding cycles, the friction coefficient increased from around 0.1 to a relatively stable platform. In the initial around 100 cycles (Figure 4.4.1a), Cu6 shows the fastest COF increasing which is comparable to grinded brass and stabled on the relatively highest platform. The increase speed of Cu4 and Cu5 is similar to each other, while the Cu6 shows faster increasing, at the initial 100 cycles. Brass exhibits abrupt increase and then stabilises at a COF approximately 0.28 for the rest of the test cycles. As shown in Figure 4.4.1c and d, the COF of non-plated brass material is 0.28 which is smaller than the plated samples probably due to the increased roughness of the Cu and GO/Cu brush plated surfaces (Figure 4.3.7a). The Cu brush plating samples exhibits different behaviours. And the COF of those pure Cu plating samples climbed to relatively stable levels ranging from 0.4 to 0.6 within the 2000 cycles (Figure 4.4.1b). It is relatively clear that the COF of Cu samples gradually increased with the increasing of brush plating voltage from 4 to 6 volts.

(a)



(b)

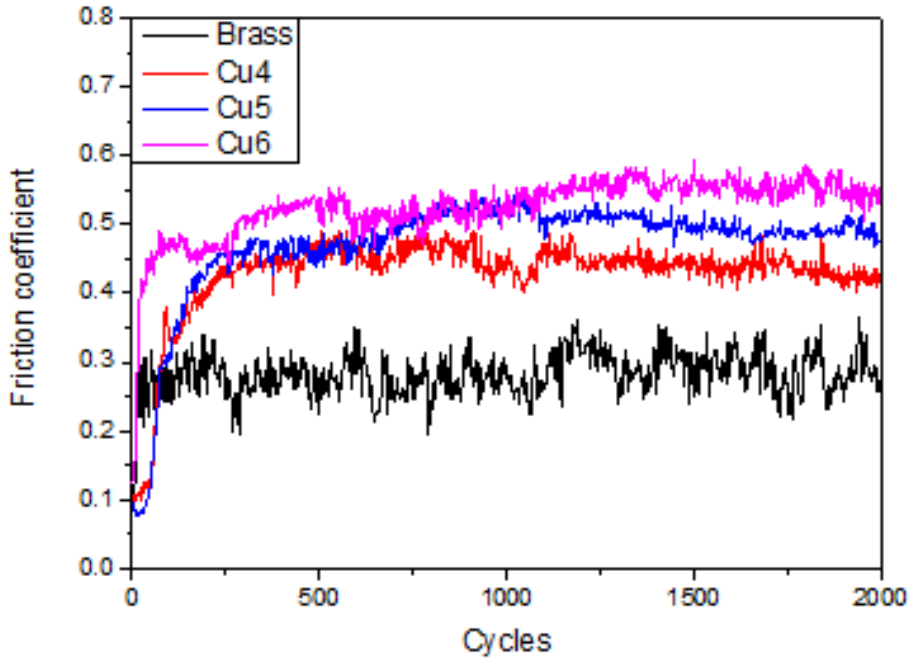
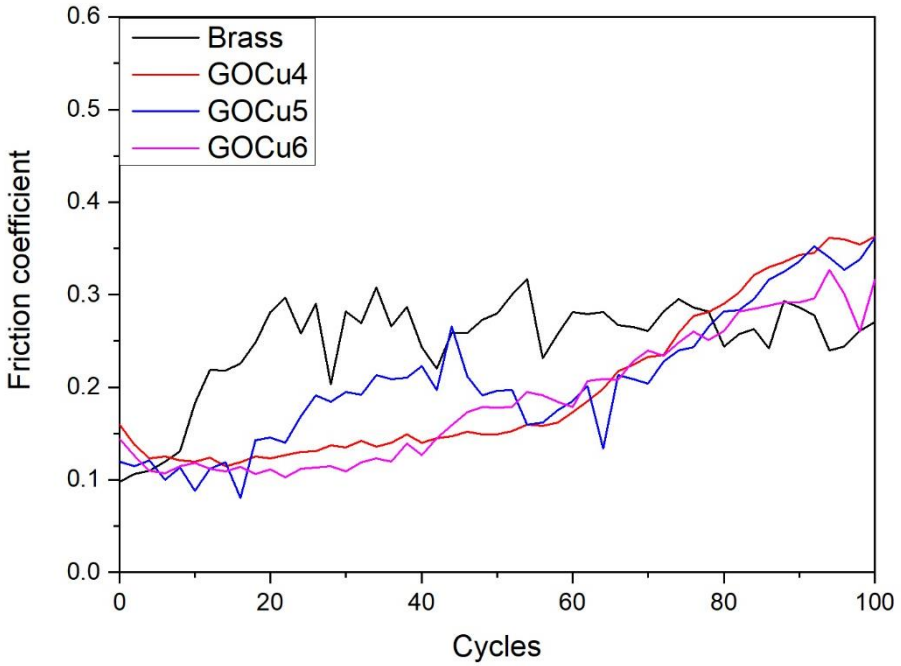


Figure 4.4.1 (a-b) Friction coefficient curves comparing among grinded brass and pure Cu control group: (a) within initial 100 cycles and (b) 2000 cycles.

(c)



(d)

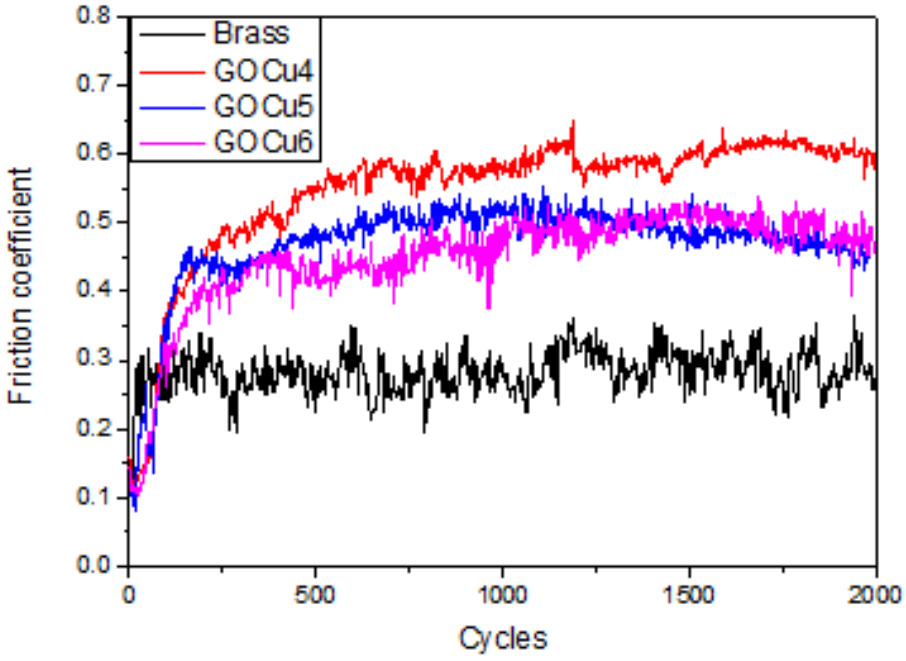


Figure 4.1.1 (continued) Friction coefficient curves comparing within: (c) 100 cycles and (d) 2000 cycles for grinded brass and GO/Cu-Brass samples.

As limited coating thickness of GO/Cu2 and 3-Brass as mentioned before, the tribology tests were carried on GO/Cu4-Brass, GO/Cu5-Brass and GO/Cu6-Brass coated surfaces (exhibited at Figure 4.4.1c and d). Comparing to the GO/Cu samples, the increase of friction coefficient (COF) of grinded brass is relatively greater, at the initial around 100 cycles (Figure 4.4.1c). Whereas the COF of GO/Cu samples gradually stabled at a higher COF range than that of the grinded brass. The addition of graphene oxide (GO) changed the relationship between the friction coefficient and the brush plating voltage, which is different from the trend indicated in the pure Cu control group. As mentioned before, the COF of pure Cu control group exhibits an uprising trend with increasing of the brush plating voltage (Figure 4.4.1b). If the GO/Cu composite coating samples demonstrate similar trend of Cu control group, the GO/Cu4 might show the lowest COF. However, GO/Cu4-Brass presents the highest COF (Figure 4.4.1d) among the GO/Cu composite coating samples with 0.2 g/L of GO concentration, which is approximately 0.6. It is interesting to note that the COF for GO/Cu5 and GO/Cu6 were comparable to each other and lower than that of GO/Cu4. And the GO/Cu5 shows slightly lower average COF than that of GO/Cu6. The GO/Cu5 might be the optimised voltage in GO/Cu composite coating.

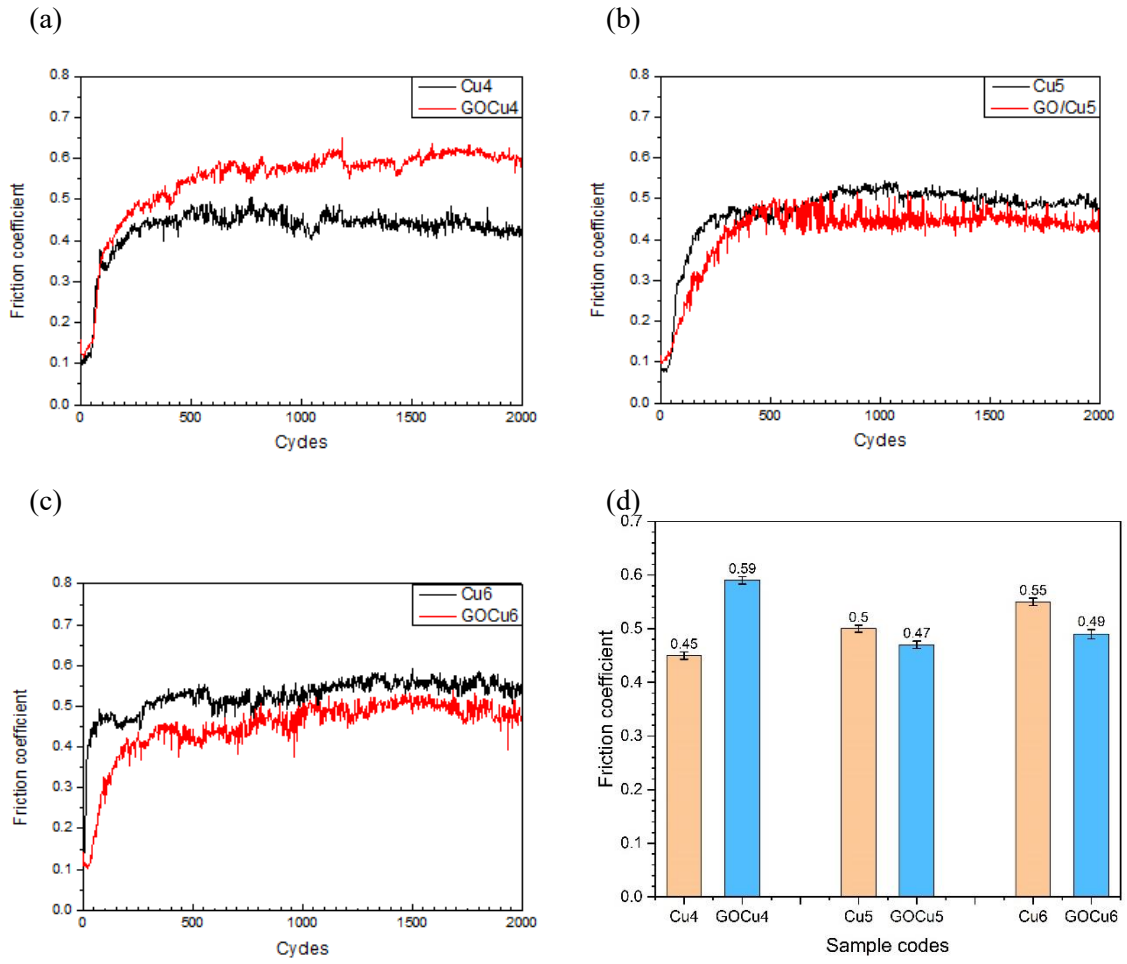


Figure 4.4.2 The influence of GO addition on the friction coefficient: (a) plated under 4 volts; (b) plated under 5 volts; (c) plated under 6 volts and (d) summarised friction coefficient results.

At Figure 4.4.2a to c, it presents the comparison of friction coefficient (COF) among the pure Cu coating and GO/Cu composite coating where the black curves represent the COF of pure Cu and red curves represent that of GO/Cu composite coating samples. The COF of GO/Cu4 is higher than that of Cu4 (Figure 4.4.2a), this might be due to the increase of surface roughness after GO addition. The COF of GO/Cu5 is smaller than that of Cu5 (Figure 4.4.2b). Similarly, the COF of GO/Cu6 is smaller than that of Cu6 (Figure 4.4.2c). As exhibited at Figure 4.4.2d, the bar chart shows the average COF analysed results. The blue bars depict the Cu coating COF results, and the yellow bars depict the GO/Cu composite coating COF results. The COF of GO/Cu4 is the highest among those Cu and GO/Cu samples which is 0.59. It is significant to

note that the COF of GO/Cu5 (0.45) and GO/Cu6 (0.55) is lower than the corresponding Cu5 (0.50) and Cu6 (0.55) respectively even if the surface of the GO/Cu5 and GO/Cu6 is rougher than Cu5 and Cu6 counterparts. Therefore, it can be deduced that the addition of GO can effectively reduce the COF of Cu.

4.4.1.2 The Wear of Cu and GO/Cu Coating Samples

As report at section 4.4.1, although the friction coefficient of brass is the smallest, its wear is significantly larger than Cu or GO/Cu coated samples (Figure 4.4.3a). As Cu nano-particles are able to be used as anti-friction particles, it is possible that the Cu particles produced by wearing test on the brass reduced the friction by consuming itself [16,250,251]. At Figure 4.4.3b to c, the black curves exhibit the 2D worn tracks of Cu4, Cu5 and Cu6, and the GO/Cu4 to 5 2D worn tracks are shown with red curves. As shown in Figure 4.4.3b, the Cu4 wear track shows clear and relatively deep galling tracks comparing with GO/Cu4's. As for GO/Cu5 and Cu5 (Figure 4.4.3c), the 2D wear tracks are comparable while the galling curves of Cu5 is relatively more notable than GO enhanced GO/Cu5. The comparison of the wear track profiles of Cu6 and GO/Cu6 in Figure 4.4.3d shows the influence of GO. The wear area of Cu6 is higher than that on GO/Cu6. Moreover, it shows deep galling on the 2D worn track scanning of Cu6 which is with the similar to that of entire worn track of Cu6. In contrast, there is no such galling on GO/Cu6 composite coating. With adding of GO, the galling on the worn track was successfully prevented.

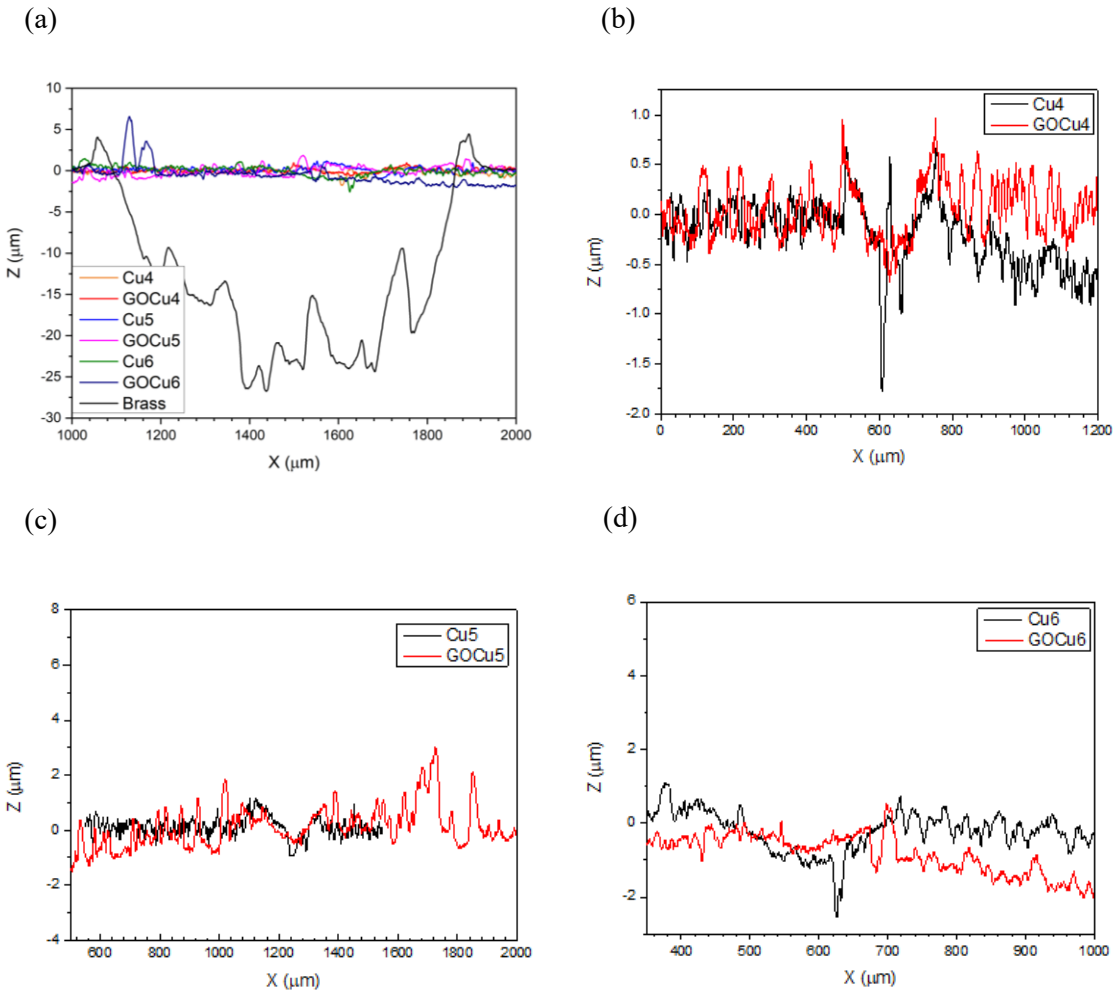


Figure 4.4.3 (a) 2D scan comparison of worn track on brass, Cu control group and GO/Cu sample under 0.2 g/L of GO; comparing of Cu coating and GO/Cu coating samples: (b) Cu4 and GO/Cu4-Brass; (c) Cu5 and GO/Cu5-Brass and (d) Cu6 and GO/Cu6-Brass.

To quantify the wear volume, Figure 4.4.4 was carried out to exhibit the numeric results of wear volume in the bar chart. In this graph, the wear volume of the pure Cu control group is represented by orange bars as for GO/Cu samples are by blue bars. The wear volume of brass is 712.10 × 10^{-4} mm^3 which is larger by two orders of magnitude than other samples with Cu based coatings. As compared with the pure Cu control group, all the three GO containing samples showed reduced wear. The wear volume of GO/Cu6 (4.21 ×10^{-4} mm^3) is slightly bigger than that of GO/Cu4 (3.20 ×10^{-4} mm^3). And the GO/Cu5 has the smallest wear volume which is only 2.30 ×10^{-4} mm^3. Among the GO/Cu coated samples, the 5V plated samples showed the

smallest wear volume and the relatively low COF. Therefore, 5V is the optimal voltage for the improvement of tribological performance under 0.2 g/L of GO concentration.

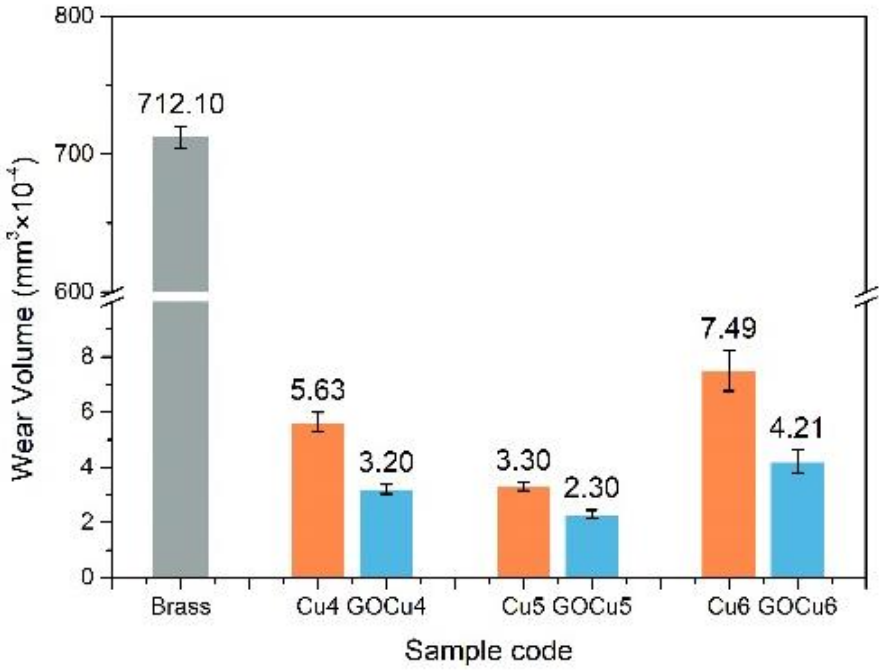


Figure 4.4.4 The comparison of wear volume among brass, pure Cu control group and GO/Cu composite coatings.

4.4.1.3 SEM and Elements Analysis of Wear Tracks of Cu and GO/Cu Coatings

The SEM images of wear tracks for Cu5-Brass and GO/Cu5-Brass samples were obtained under 100 magnifications, as exhibited in Figure 4.4.5a and b. Cu5-Brass and GO/Cu5 were dry-sliding under 5N load with 2000 cycles using 316 stainless steel as the counter ball. The wear track of Cu5-Brass shows a relatively obvious wear track with a certain width compared to that of GO/Cu5-Brass. In addition, the worn debris of Cu5-Brass is more than that on the wear track of GO/Cu5-Brass. Post tribo-test, a painting brush was used to remove the debris of Cu5-Brass as the sample surface produced a relatively large amount of debris. However, it was found that and the debris near the wear track is compacted onto the samples surface which could not be brushed out post-test with the painting brush, on the total view of wear track (Figure 4.4.5a). Moreover, there are two notable spots in the middle of the Cu5-Brass wear track that indicate adhesive wear on the pure Cu control group. While there is no obvious adhesive wear and relatively less notable abrasive grooves on the GO/Cu5-Brass, this might be due to the addition of GO, which reduced the adhesive strength and, as a solid lubricant, also reduced the formation of debris.

Figure 4.4.5c shows the worn 316 stainless steel counter ball of Cu5-Brass and its closer view of the colour-chemical image (Figure 4.4.5d) indicate the distribution of copper (Cu), iron (Fe), chromium (Cr) and nickel (Ni). There are abrasive grooves in the middle of the worn counter ball and the debris is exhibited at the edge of the counter ball, shown in Figure 4.4.3c. On the debris of Cu5-Brass counterpart, it even shows some grooves on the debris, which might indicate that the debris was compressed and participated in the wear test during the 2000 cycles. Moreover, there shows some particles, pointed out by green arrow line, with certain size on the worn counter ball. At the colour-chemical result of Cu5-Brass (shown in Figure 4.4.5d), the main worn body of counter ball is significantly consisted of Fe along with some Cu was sticked

on its surface. Besides, one of the particles mentioned previously is Cu particle which is denoted by yellow arrow. The green coloured spots denoted by green arrows between the abrasive grooves (Figure 4.4.5d) and debris indicates the existence of oxides. This could be caused by the oxidation wear occurred during the wear test process and it would be discussed later at worn surface Raman results. It is interesting to note that as harder material compared to Cu coating, the Cu was transferred to the stainless-steel counter ball, as shown in Figure 4.4.5d. Hence, it is possible that Cu was worn under abrasive and adhesive wear as relatively soft tribological test plane, and certain Cu debris was produced, incorporated into the wear process, and stuck onto the counter ball.

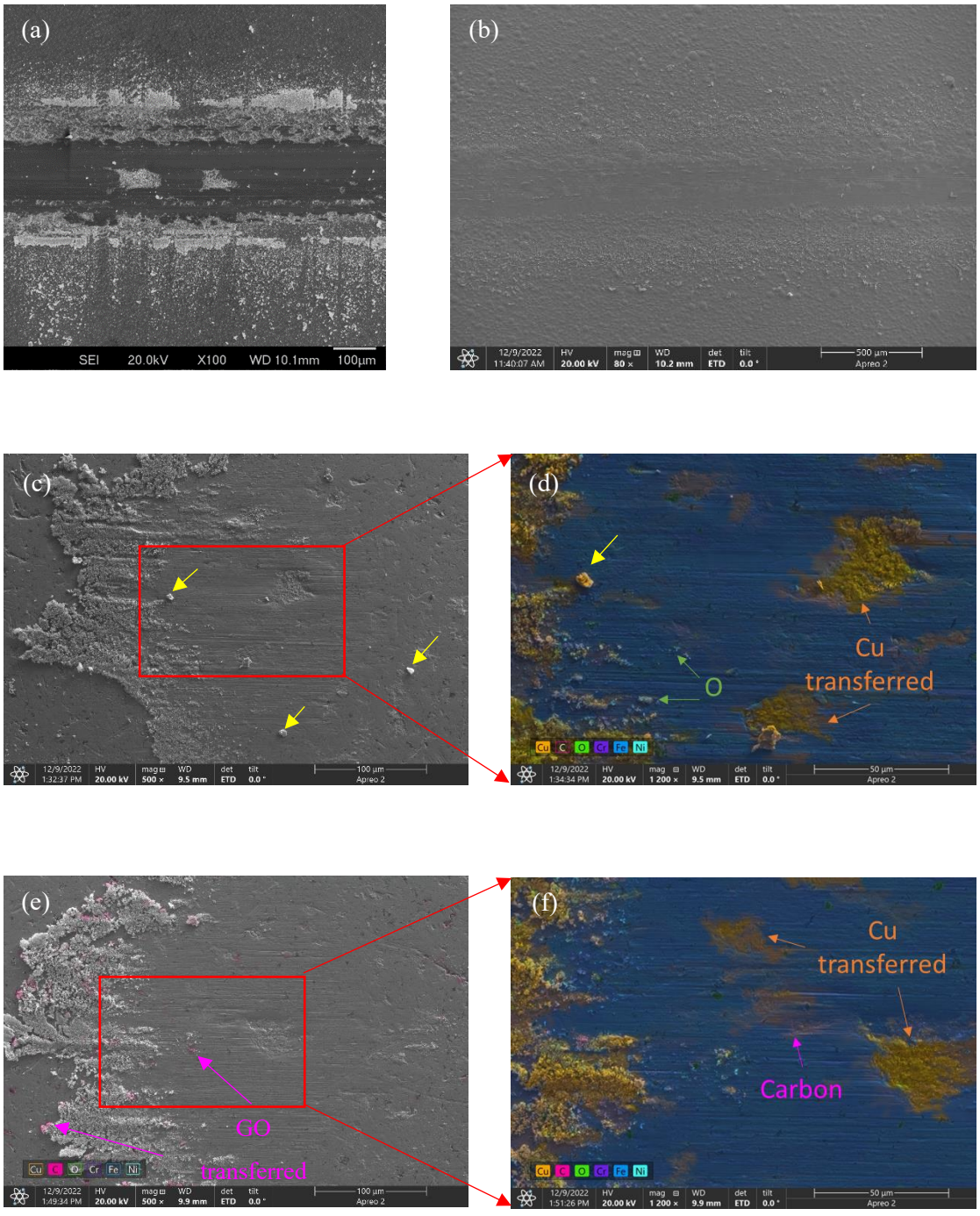


Figure 4.4.5 Comparison of SEM and colour-chemical results for wear track and wear counter ball on GO/Cu5 and Cu5: (a) Cu5-Brass wear track; (b) GO/Cu5-Brass wear track; (c) Cu5-Brass wear counterpart; (d) colour-chemical image of Cu5-Brass counter ball; (e) GO/Cu5-Brass wear counter ball to reveal the carbon component; (f) colour-chemical image of GO/Cu5-Brass counter ball.

Figure 4.4.5e exhibits the colour-chemical image on the worn counterpart of GO/Cu5-Brass, showing the SEM image along with carbon contribution (shown in red colour denoted by purple arrows) on this area. As demonstrated at Figure 4.4.5f, the carbon rich areas or GO transferred example areas were pointed out by purple arrows. The GO found on the debris is quite reasonable as GO as light matters could be easily transported to the two edges of the worn track on both counter ball and wear track. The remaining GO on the abrasive grooves could be one piece of evidence to reveal the GO performed as solid lubricant during the wear test of GO/Cu composite samples. To compare with the worn counter ball of Cu5-Brass, the surface is not showing as large particles as found on Cu5-Brass counter ball. The addition of GO within the coating might be reduced the formation of Cu based debris, on both numeric and particle size. The debris on worn counter ball of GO/Cu5-Brass shows relatively looser structure and abrasive grooves could not be seen, compared with that of Cu5-Brass. Full elements colour-chemical scan of on the red rectangular area of Figure 4.4.5e for GO/Cu5-Brass sample is exhibited at Figure 4.4.5d. Similarly, there also are Fe with abrasive grooves in blue and Cu debris along with Cu transferred at the middle of worn counter ball, as the worn counter ball of Cu5-Brass. The presence of GO, marked in red, was clearly observed on the worn surface of the GO/Cu5-Brass counter ball, in contrast to its absence or minimal presence on the Cu5-Brass counter ball.

The wear tracks of Cu5-Brass are exhibited at Figure 4.4.6a and b showing the general view and detailed view of the wear track. There is vast debris surrounding the wear tack of Cu5-Brass (Figure 4.4.6a), the width of the debris area is almost the same as the width of wear track itself. Moreover, there is severe adhesive wear shown on this side of the wear track of relatively large in size which is one third of the width for the wear track and over 500 μm of length. In addition to the adhsive wear found at Figure 4.4.5a, adhesive wear is severer than that on GO/Cu5-Brass. Under higher magnification (shown in Figure 4.4.6b), more wear mechanisms

could be revealed. There are areas of galling exhbited on both the uppper side and the bottom side of the image. In the meantime, the area of plastic deformation is indicated at the upper side. It is interesting that there is an area at the middle region of this image, there are plenty of cracks mostly perpendicular to the sliding direction. They are most likely to be fatigue cracks caused by the cyclic work of 2000 cycles of wear test. To conclude, the pure Cu coating without GO as lubricant presents relatively severe gallings occurred.

As shown in the Figure 4.4.6c, one of the two sides of the wear track for GO/Cu5-Brass is shown in this image which exhibits the wear and debris at the left hand side along with the unworn coating surface at the right hand side. The orange coloured region represents the Cu element rich region and the yellow coloured region is for oxygen (O) rich region, as for the blue region is for the C rich region. Might due to relatively low magnification and finite size of GO, there is not notable blue region that could be seen on the Figure 4.4.6c. The right hand side of this image is the unworn surface region which is in orange colour shows relatively greater Cu compositions. And the left hand side is of yellow colour, these is one piece of eveidence shows oxidant wear occurred during this 2000 cycles of wear test. In addition, there still are abrasive grooves depicted on the debris and also relatively loose strucuture of wear debris. Those debris is compressed by the cyclic wear of 316 stainless steel counter ball, and take part in the wear process.

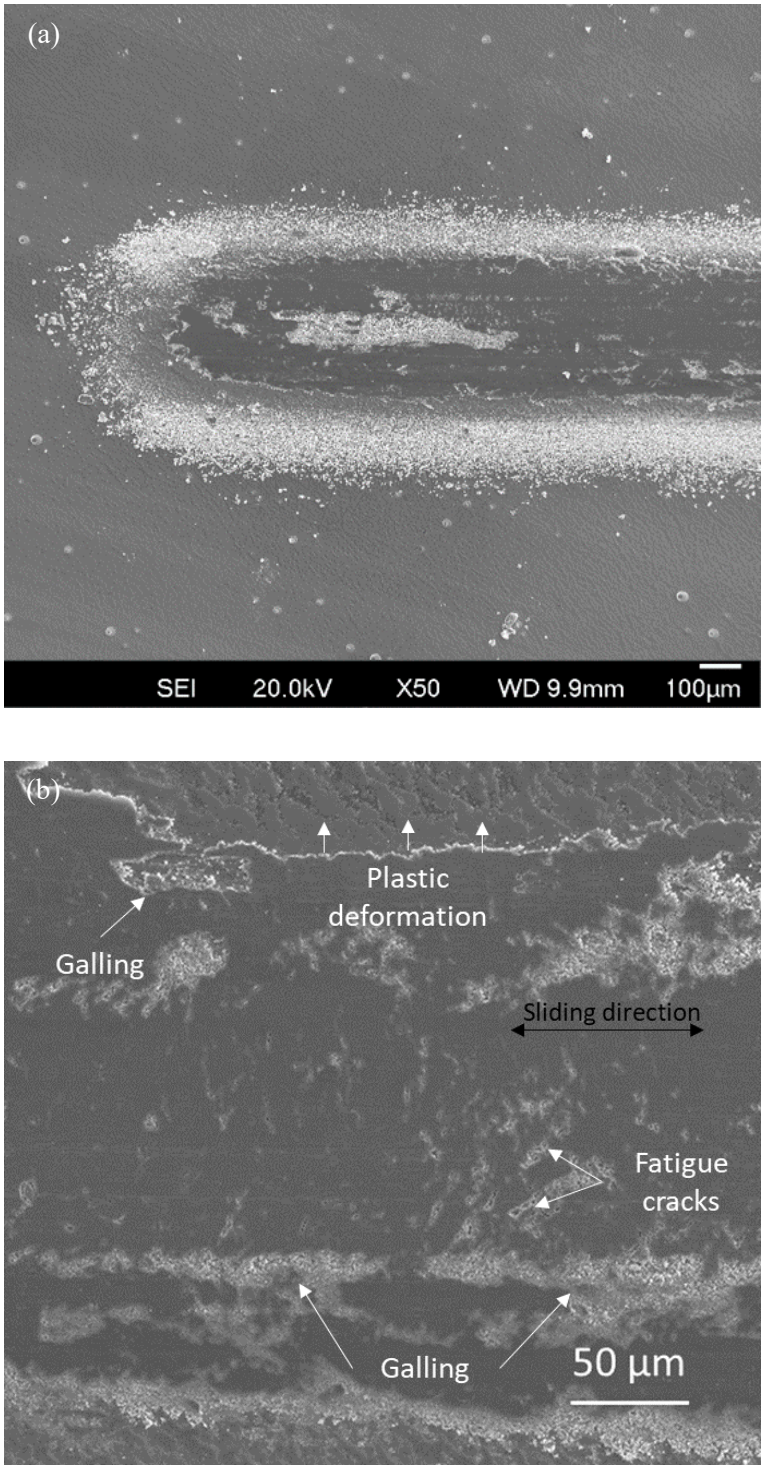


Figure 4.4.6 (a-b) SEM images of worn track of Cu5-Brass plated coating under 316 stainless steel counter ball in air under 5N load.

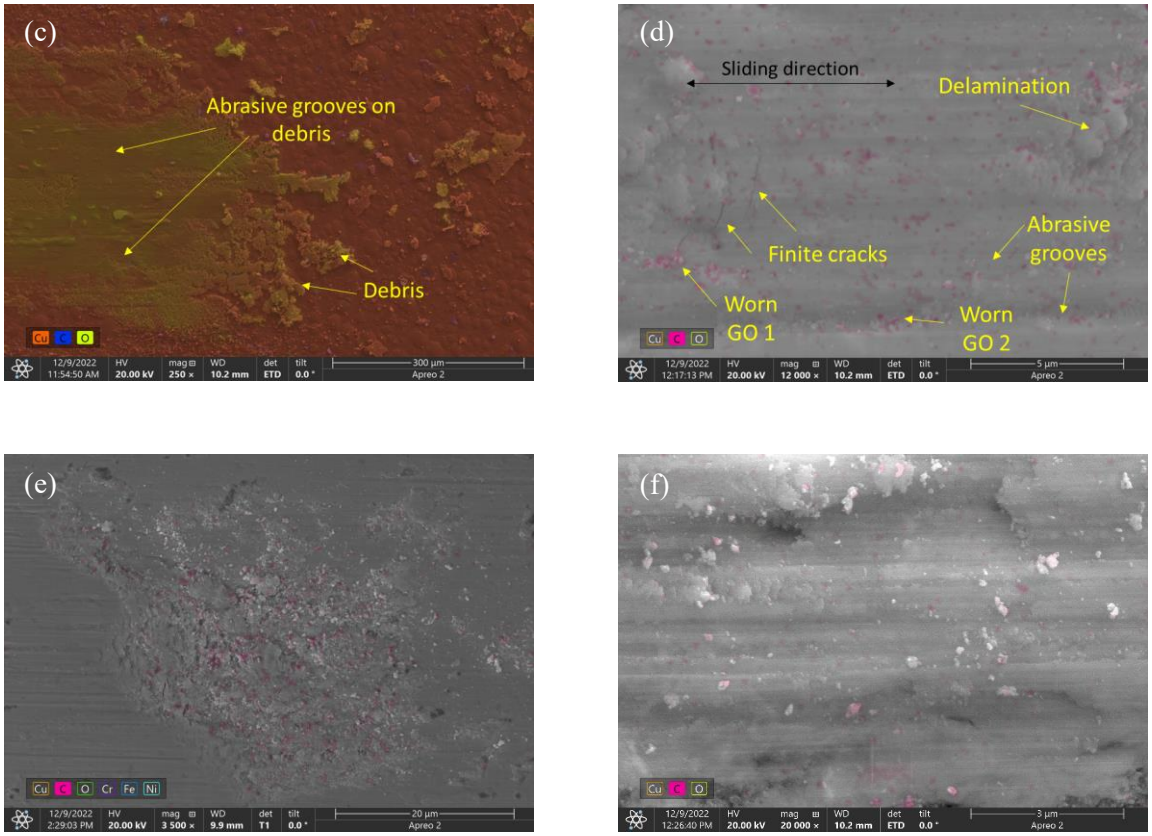


Figure 4.4.6 (continued) (c-f) Colour-chemical images for the GO/Cu5-Brass sliding against 316 stainless steel counter ball under 5N loads: (c) general view on wear track edge, (d) site 1, (e) site 2 and (f) site 3.

At Site 1 in wear track of GO/Cu5-Brass (Shown in Figure 4.4.6d), this image shows some representative mechanism influenced the wear process within the wear track region. The carbon distribution could be seen with red colour using colour-chemical function. It is not quite easy to notice that there are several parallel abrasive grooves at the sliding direction in this image. Delamination on the worn surface could be noticed, which might be developed to adhesive wear if the wear test was continued. The Cu transferred to its counter ball could be expained as the delamination process and other relatively smaller adhesive wear occurred on GO/Cu5-Brass than that on the worn Cu5-Brass. It could be noted that finite cracks initiate and slightly propagate perpendicular to the sliding direction under 12,000 of magnification. With cyclic wear test under certain loads, fatigue cracks could grow along perpendicular direction to the

sliding direction [252]. The initiate of this finite crack could due to the delamination process produced several “notches” on the wear interface, then finite crack initiate through the edge of delamination [253,254].

Worn GO area could be note at Figure 4.4.6d as red coloured spots, there are two relatively representative spots denoted as “Worn GO 1” and “Worn GO 2”. The “Worn GO 1” spot is near to end of the finite crack as mentioned above, which is possibly stopped the propagating of the crack, at the perpandicular direction. This is an area accumulated several GO spots, this could be caused by accumulated of Cu fine particles accumulation in this area. As shown in the Figure 4.4.6e, this is Site 2 area accumulated with Cu fine particles and GO exhibited with red colour. The “Worn GO 2” spot shows the GO (red coloured) on the abrasive grooves, where GO could significantly reduce the wear and friction coeffient. The carbon scan on Figure 4.4.6f (site 3) presents the carbon found (red in colour) at the abrasive groove region on worn counter ball of GO/Cu5-Brass which is the carbon could be involved in the wear test as solid lubricant. This image provides relatively detailed view on GO on the abrasive grooves compared with Figure 4.4.6d. Some of the particles are covered with red colour and some of the particles are not. Those particles exhibit as red colour indicated the GO rich region and those GO would reduce deep galling as discussed at last session. As the GO concentration in the brush plating solution increases, it is possible that the red-colored particles, or GO, will also increase. Consequently, the tribological properties may improve compared to the GO/Cu composite coating with a 0.2 g/L GO concentration [255].

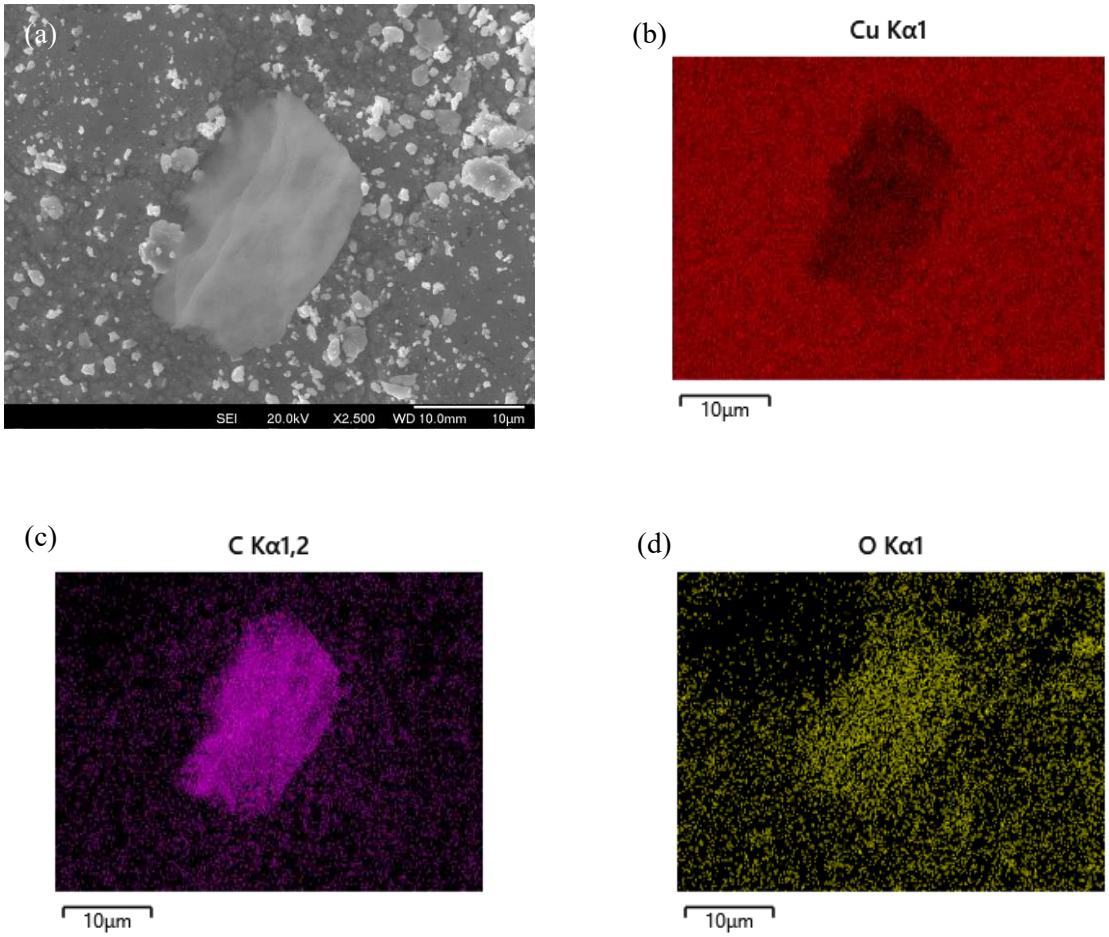


Figure 4.4.7 SEM images and EDX mapping results on worn surface of GO/Cu5-Brass sample.

Although GO could be seen under colour-chemical SEM images, there is not more effective proof that could directly show the GO after wear test. As shown in previous images, GO could be found combined relatively well within the cauliflower like structure. Hence, the GO-like structure found at the Figure 4.4.7a is of highly possibility that is caused by wear process. This image was taken at the relatively loose debris region. Around the GO-like area, there are many particle debris and flake debris. Those particles are relatively small which is around 2 to 3 µm in diameter and those flakes could possibly be worn GO flakes from the worn track. At Figure 4.4.7b, the area of GO-like structure shown lower Cu composition which shape could roughly match the edge of GO-like structure. Although it would not be accurate if quantify light elements like C and O, clear region of C rich and O rich region reveal the GO-like structure is

consisted of C and O. In this way, this GO-like structure is GO flake found at debris region. This is another proof to the GO operating as solid lubricant in the wear test process.

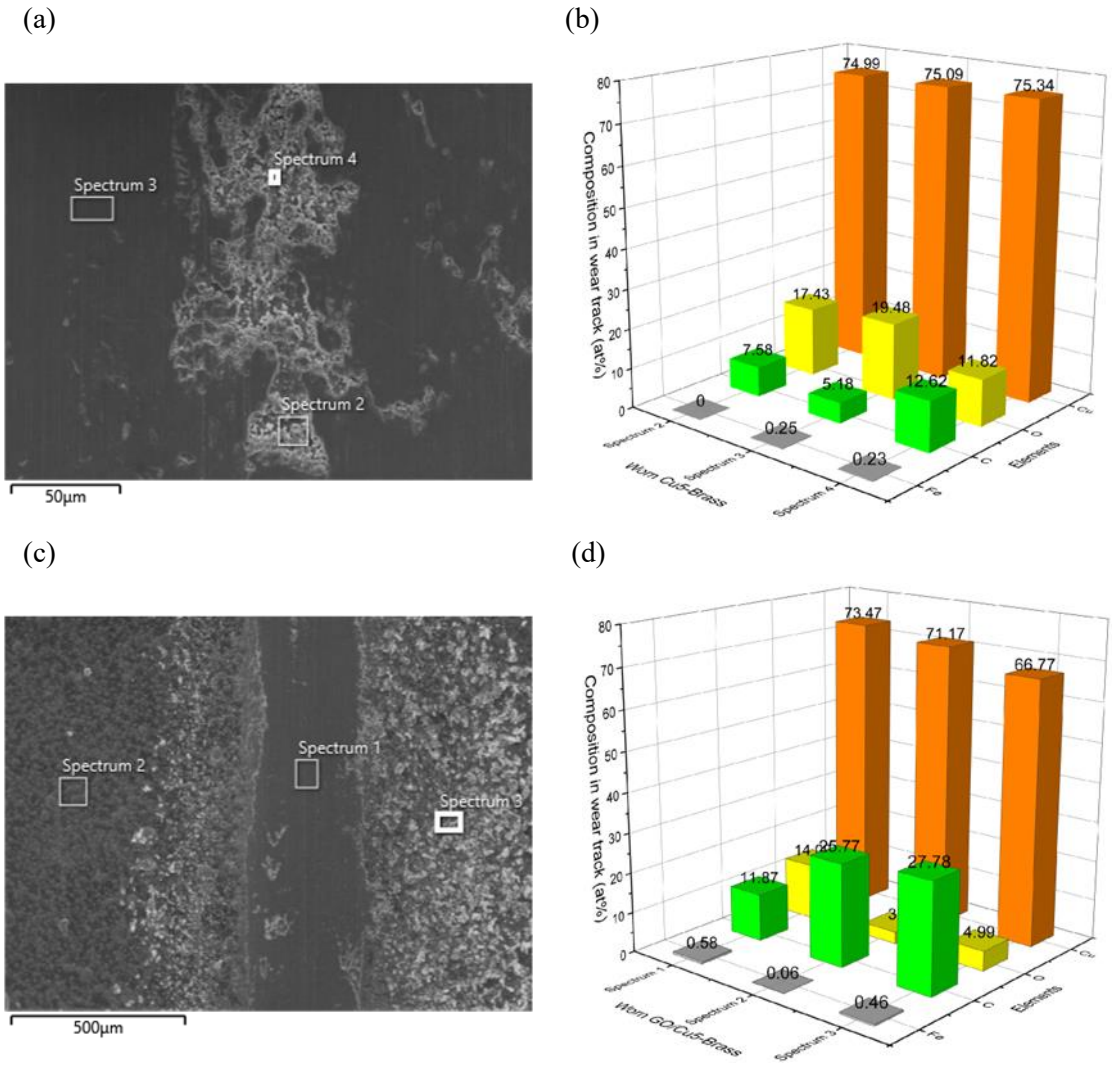


Figure 4.4.8 EDX results in 3D bar chart for the on the wear track of Cu and GO/Cu5: (a) Cu5-wear track; (b) Cu5-EDX; (c) GO/Cu5-wear track and (d) GO/Cu5-EDX.

Figure 4.4.8 demonstrates the EDX quantitative results on worn surface of Cu5 and GO/Cu5 coatings on certain areas with their 3D bar chart. At Figure 4.4.8a, the Spectra 2 and 4 are on the place of adhesive wear as for Spectrum 3 is located on the abrasive wear area. The 3D quantified Energy Dispersive X-ray Spectroscopy (EDX) of Cu5-Brass and GO/Cu5-Brass are shown respectively at Figure 4.4.8b and d. The horizontal axis represents the three different

spectra, while the vertical axis lists the elements detected, which are iron (Fe), oxygen (O), carbon (C), and copper (Cu). As for the depth axis show the composition in atomic percentage with numbers shown on top. At Spectra 2-4 (shown in Figure 4.4.8b), the carbon composition is of 7.58 at%, 5.18 at% and 12.62 at%, respectively. As shown in Figure 4.4.6c, the wear track region is of relatively high O composition. The oxygen composition is also necessary to investigate the oxides production after wear test. There are 17.43 at%, 19.48 at% and 11.82 at% of O composition for Spectra 2-4 of worn Cu5-Brass. As the counter ball is stainless steel, so Fe composition is to determine whether Fe could be transferred on to wear track or not. Only finite percentage of Fe was detected on the Cu5-Brass which is less than 0.3 at%.

As shown in Figure 4.4.8c, this is the image shows the general view of GO/Cu5-Brass wear track. Although there seems to be galling area, it is relatively smaller than that on Cu5-Brass shown before. Spectrum 1 is located around the middle of the wear track of Go/Cu5-Brass, Spectrum 2 is on the unworn surface and Spectrum 3 is on the wear debris area at one side of the wear track. The carbon composition of worn Cu5-Brass is utilised to compare with the carbon composition of worn GO/Cu5-Brass at Figure 4.4.8d, so that the carbon composition is influenced by GO addition could be noticed. It is interesting that the carbon compositions on those Spectra 1-3 of worn GO/Cu5-Brass are 11.87 at%, 25.77 at% and 27.78 at% which could be noticed these are generally larger than that of worn Cu5-Brass. Increasing on carbon composition indicates that the GO is performed a role in the wear test on GO/Cu composite coatings. As for the oxygen composition, the Spectrum 1 exhibits the highest composition compared with the other two spectra which is 14.09 at%. There are only 3.00 at% and 4.99 at% of O% for Spectra 2 and 3 which are the on unworn and debris. Hence, there is oxidative wear occurred on the wear tracks of GO/Cu5-Brass and Cu5-Brass. Spectrum 1 on worn GO/Cu5-Brass (middle row on x axis) exhibits the lowest carbon composition with 11.87 at%. It is

possible as the abrasive wear along the sliding direction might sweep away the particles contains GO, and remaining GO might be too small to be detected under relatively low magnification. To conclude, the GO addition might reduce the oxidative wear, and it was performed as solid lubricant during wear test.

Under optical images, Cu oxidation could be directly noticed by the colour changes on wear tracks. Two nearby sites of worn GO/Cu5-Brass are taken both optical images and Raman spectra. The Cu5-p1(shown in Figure 4.4.9a) was taken at relatively middle of the wear track, it could be noted that the significant part of the site is with green colour under the yellow bulb placed in the Raman chamber. Those green coloured area might indicate the existence of Cu oxides this would be discussed by Raman spectroscopy results. As for the area in black colour, it could be caused by two possible reasons. Firstly, the Copper (II) oxide (or CuO) is of black colour. Secondly, the cracks or galling could also present in this colour. The CuO could be discovered by Raman spectroscopy, cracks would be clearer under SEM as discussed before. At the edge of worn surface for Cu5-p2 (Figure 4.4.9b), it presents much brighter yellow colour compared to the area in the middle and the green area could also be seen. Galling occurred at the edge of green coloured area, as the original bright yellow colour of Cu is revealed after galling. In between the green zone and unworn surface, the abrasive groove on this area is in relatively darker colour than the fresh galling area. This might be because the Cu (I) oxide (or Cu_2O) is in red colour which makes the bright yellow turn darker.

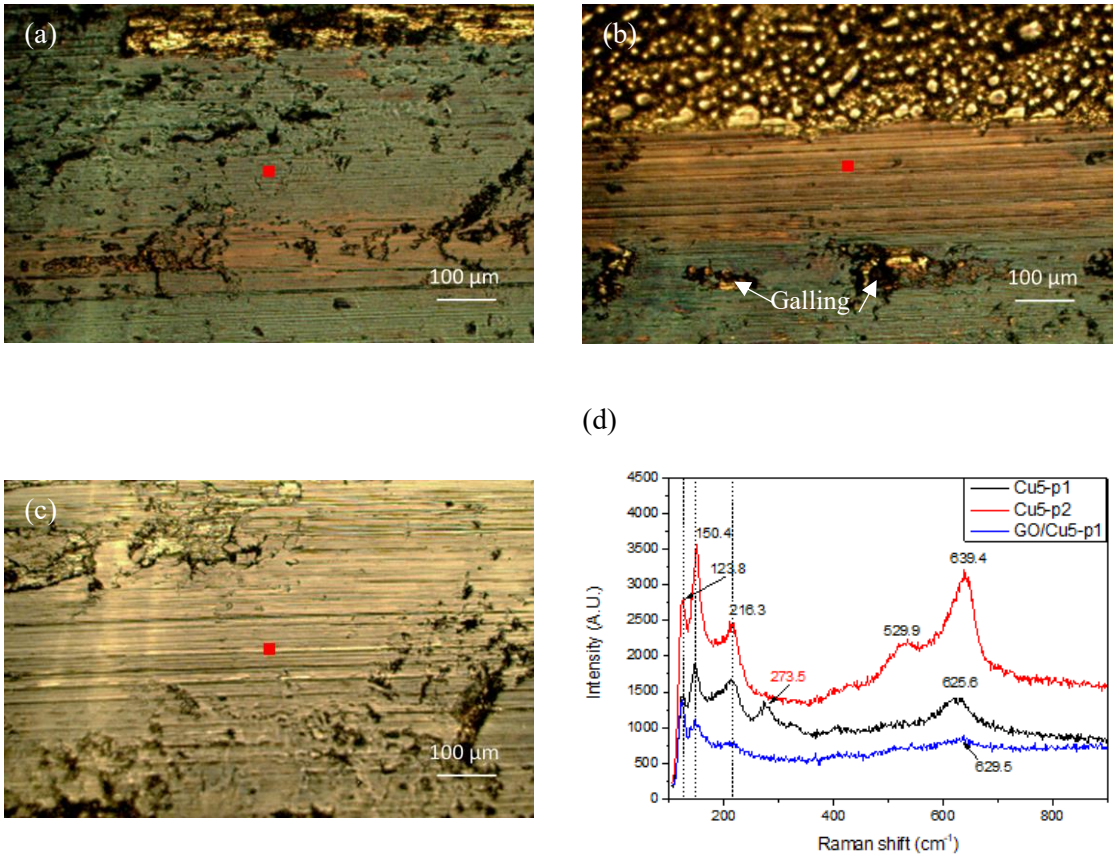


Figure 4.4.9 Raman spectroscopy of worn tracks of Cu5-Brass and GO/Cu5-Brass and their optical images: (a) Cu5-p1, (b) Cu5-p2, (c) GO/Cu5-p1 and (d) Raman spectroscopy of pointed out position.

The GO/Cu5-p1 is at the middle of the worn GO/Cu5-Brass (shown in Figure 4.4.9c), it depicts abrasive groove over yellow colour and some areas of black colour. Those areas could be resulted by cupric oxides or GO flakes. Compared to Cu5-p1 and 2, GO/Cu5-p1 is of less colour which could indicate less Cu oxides on the GO/Cu worn coatings and less severe the oxidation reaction occurred. The answer to this question shown in the Raman shift result seen in Figure 4.4.9d. The red dots, shown in Figure 4.4.9a-c, are the area taken the Raman tests. The black curve and red curve are the Raman spectra on green area and yellow area on worn Cu5-Brass. According to other research, the Raman peak at around 273.5 cm-1 could be denoted as featured peak for cupric oxide (CuO), which is oxidised severer than cuprous oxide (Cu_2O) [256]. And Raman peaks around 529.9 and 638.4 cm-1 could be indicated as Cu2O. Hence, the green

coloured area on Cu5-p1 (black curve) has not only CuO but also Cu_2O, and darker yellow area on Cu5-p2 only shows Cu_2O although is of the highest intensity. It is significant to note that the intensity of Cu oxide Raman spectra is the smallest for the GO/Cu5-p1, comparing with the Cu5-p1 and Cu5-p2. The GO addition is of high possible that has weakened the oxidative wear. Besides, it only shows the Cu_2O featured peaks. All in all, the GO/Cu5-Brass presents less intensity in Cu oxide and Cu only oxidised to Cu_2O, as for Cu5 samples, the intensity of Cu oxides is relatively greater and both CuO and Cu_2O could be found on its surface.

4.4.2 Comparison of the GO/Cu Samples under Different GO Concentrations

4.4.2.1 Friction Coefficient of GO/Cu Samples with Different GO concentrations

The COF influenced by GO concentrations under 4 and 5 volts is demonstrated at Figure 4.4.10a and b. At those two graphs, the black curves represent the 0.2g/L of GO/Cu4 and 5, the 0.4 g/L, 0.6 g/L and 0.8 g/L are utilised the red, blue, and purple colours, respectively. Under 4 volts of brush plating, the COF changes with GO concentrations is shown in Figure 4.4.10a. Those COF curves of GO/Cu4 series samples are initiate from 0.1 and increased with different speed then stabled at certain area. The increase of COF for GO/Cu4-0.8 is the fastest comparing to other GO concentrations, at the first approximately 200 cycles. The next fastest is the GO/Cu4-Brass sample with 0.2 g/L of GO, while the slowest two are the GO/Cu4-0.4 and GO/Cu4-0.6 samples, which exhibit a similar rate of increase. With rising of GO concentrations from 0.2 g/L, the COF values of GO/Cu4-0.4 to 0.8 are significantly reduced to around 0.25. The COF values of GO/Cu4-0.4, GO/Cu4-0.6 and GO/Cu4-0.8 are stabled at comparable locations comparing with each other.

As for COF of GO/Cu5 series coatings (Figure 4.4.10b), the influence of different GO additions is of different COF performance. Those COF are also grown from 0.1 then to stable platform.

The COF growth during the first 200 cycles for GO/Cu5-Brass, GO/Cu5-0.6, and GO/Cu5-0.8 is comparable, whereas the COF growth for GO/Cu5-0.4 is noticeably smaller. Similar to GO/Cu4-Brass, GO/Cu5-Brass shows the highest COF compared to samples with other GO concentrations. It is interesting to note that the GO/Cu5-0.4 possessed the smallest COF. The friction performance of GO/Cu5-0.4 is relatively better than other concentrations under 5 volts of brush plating. The COF of GO/Cu-0.8 is slightly greater than that of GO/Cu5-0.4, and the COF of GO/Cu-0.6 is greater than that of GO/Cu5-0.8. As the Micro-hardness of GO/Cu4 and GO/Cu5 samples of different GO concentrations is comparable to each other, the GO performance during friction coefficient tests might be the main reason for those samples.

Figure 4.4.10c depicts the numeric friction coefficient of GO/Cu4 and GO/Cu5 under different GO concentrations respectively with blue and orange colour of bars. The COF of GO/Cu5-Brass (0.2 g/L GO) is 0.47 which is larger than those with higher GO concentrations, as shown in Figure 4.4.10c. Although the COF of GO/Cu5-0.6 is 0.39, which is higher than the values for 0.4 g/L and 0.8 g/L GO concentrations (0.26 and 0.31, respectively), it is significantly lower than that of GO/Cu5-Brass. The COF of GO/Cu4-Brass is 0.59 which is the largest COF in GO/Cu4 series of samples. The other GO/Cu4 samples with 0.4 g/L, 0.6 g/L and 0.8 g/L of GO concentrations are of COF at 0.26, 0.29 and 0.28, respectively.

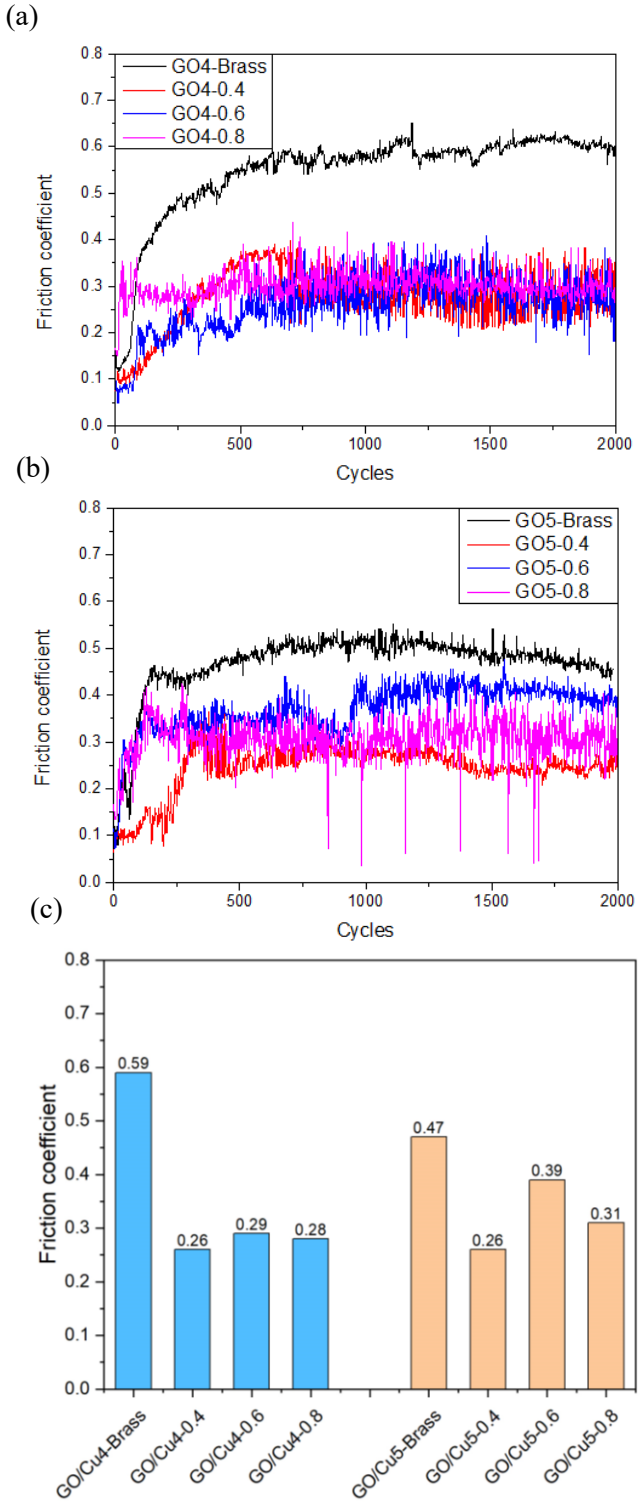


Figure 4.4.10 The friction coefficient comparing among the GO/Cu4 and GO/Cu5 samples deposited with different GO concentrations including 0.2, 0.4, 0.6 and 0.8 g/L: (a) GO/Cu4 samples and (b) GO/Cu5 samples under different GO concentrations; (c) COF for GO/Cu4 and 5 samples.

4.4.2.2 The Wear of GO/Cu Samples with Diverse GO Concentrations

The GO/Cu samples brush plating under 4 volts is illustrated in the Figure 4.4.11a showing the 2D wear tracks. GO/Cu4-0.2 and 0.4 illustrate comparable wear at their 2D scans. Although the friction of GO/Cu4-0.4 is notably reduced (Figure 4.4.10a), the wear did not improve significantly. It is interesting to note an abrupt feature on one side of the 2D wear scar, indicating debris from the worn GO/Cu4-0.6 surface, which may contain GO and contribute to improved frictional properties. The GO/Cu5-0.8 demonstrates relatively higher debris height than the others wear debris, this might be due to the debris produced by the wear process is more likely to accumulated at the sides rather than involved in the wear test. As the wear track scan of GO/Cu5-0.8 shown a sharp galling track compared to GO/Cu4-0.4 samples (Figure 4.4.11c), this area might be the start area for wear afterwards. GO/Cu4-0.6 demonstrates the deepest wear scar at this 2D scan, besides the COF of it is also slightly higher than samples of 0.4 and 0.8 g/L GO concentrations. As mentioned before, the COF of GO/Cu4 samples is relatively similar, then the wear tracks discussed before are also of comparable wear scars shown in cross-sectional scan.

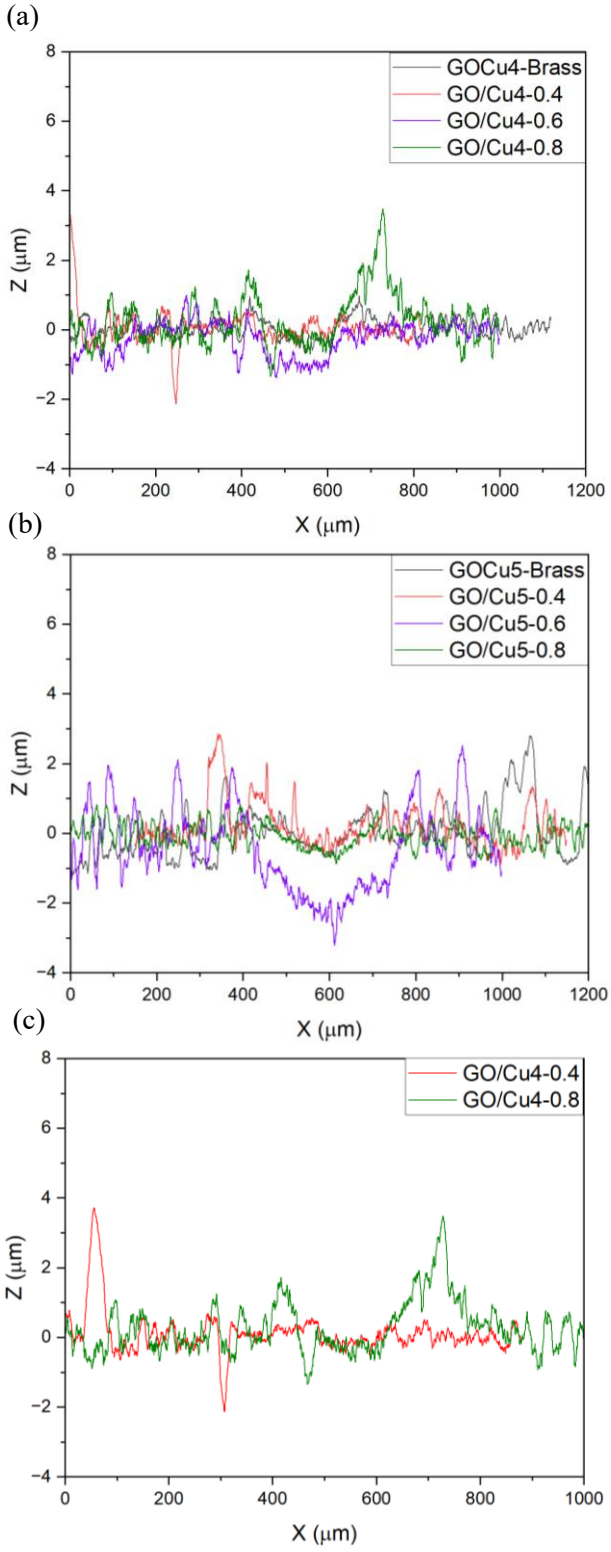


Figure 4.4.11 Comparison of 2D wear scar scans for (a) GO/Cu4 and (b) GO/Cu5 samples deposited with 0.2-0.8 g/L of GO concentrations using profilometer along with (c) comparing GO/Cu4-0.4 and 0.8.

For GO/Cu5 samples with different GO concentrations, their 2D wear scars scans are presented in the Figure 4.4.11b. It is interesting that the 2D wear scar of GO/Cu5-0.6 is notably wider and deeper than the others. Moreover, galling-like structures caused by adhesive wear can be observed, which might be attributed to the relatively higher COF compared to the other GO/Cu samples. For the other GO/Cu5 samples, they exhibited much smaller wear scars than the GO/Cu5-0.6. The wear scar of GO/Cu5-0.8 is slightly larger than that of GO/Cu5-0.4. Additionally, GO/Cu5-0.4 exhibited areas that are slightly higher above the average height of the sample surface. Those area could be GO related or Cu oxides related which would be discussed later. The 2D wear scars scanned for GO/Cu5-Brass and GO/Cu5-0.8 exhibit comparable results, although the COF for GO/Cu5-0.8 presents an improvement by comparison.

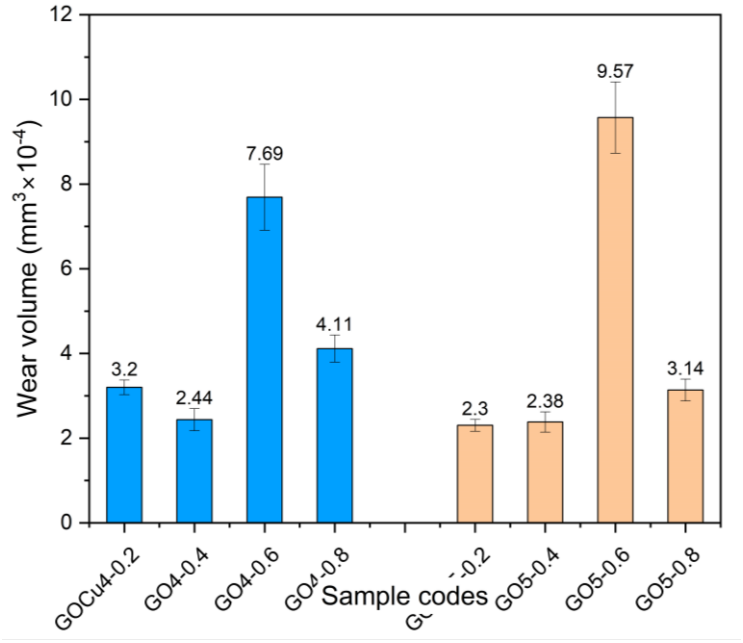


Figure 4.4.12 Bar chart of wear volume for GO/Cu4 and 5 samples deposited with different GO concentrations.

The wear volume is calculated and exhibited with bars at the Figure 4.4.12, the blue bars present

the wear volume of GO/Cu4 samples and orange bars are for the GO/Cu5 samples with different GO concentrations. GO/Cu4-0.4 and GO/Cu5-0.4 are of better wear resistance than other GO concentrations. GO/Cu4-0.4 exhibits a wear volume of 2.44×10^{-4} mm^3, while GO/Cu5-0.4 shows a slightly higher value of 2.38×10^{-4} mm^3. It is observed that the highest wear volumes in GO/Cu4-0.6 and GO/Cu5-0.6 are caused by the detection of deep galling in their 2D wear scan, measuring 7.69×10^{-4} mm^3 and 9.57×10^{-4} mm^3 respectively. With relatively higher GO concentration than other parameters, the GO/Cu4-0.8 is not of the smallest wear volume possessed 4.11×10^{-4} mm^3 which is slightly larger than that of GO/Cu4-0.4. This might be due to the galling shown in previous 2D wear scars of GO/Cu4-0.8. The wear volume of GO/Cu with a concentration of 0.8 g/L is quite interesting as the wear volume is relatively small than GO/Cu samples under 0.6 g/L of GO and higher than the samples of 0.4 g/L of GO.

4.4.2.3 SEM and Elements Analysis of Worn GO/Cu Samples

As shown in Figure 4.4.13, the optical image of worn counter ball for GO/Cu4 and 5 samples with 0.4 to 0.6 g/L of GO concentrations are exhibited with circled their wear elliptical shape area with red colour. Those images were taken just after the wear test, so the debris condition could be used to discover the debris accumulated on their related counter ball. GO/Cu samples with same GO concentration are essentially similar debris conditions on optical images. There are relatively small districts of debris agglomeration near to wear area of counter ball for GO/Cu4-0.4 (Figure 4.4.13a) and GO/Cu5-0.4 (Figure 4.4.13b). As for the debris on GO/Cu4-0.6 and GO/Cu5-0.6 worn counter ball, relatively larger districts of debris agglomeration also are exhibited around the edges of worn surface, compared to samples with 0.4 g/L of GO. The worn counter ball surface of GO/Cu4-0.8 and GO/Cu5-0.8 is relatively neat comparing with other concentrations, only dot like debris could be found on their worn surface. The debris colour is black under optical microscopy, this might be due to the oxidative wear and the colour

of GO.

It could be note that the GO/Cu of 0.6 GO concentration possessed not only the largest COF and the largest worn surface area on counter ball at Figure 4.4.13c and d. It could be noted that the worn counter ball for GO/Cu4-0.8 exhibits the relatively smaller worn area compared to that of GO/Cu4-0.4. While the worn counter ball area of GO/Cu5-0.8 illustrates slightly larger worn area on its counter ball. The numeric ellipse area was calculated by $A = \pi a * b$ and the unit is transferred from μm^2 to mm^2, exhibited in Figure 4.4.14.

Those blue bars represent the wear surface area on counter ball for GO/Cu4 samples and orange bars are that of GO/Cu5 samples. The worn areas on counter ball for 0.6 g/L are relatively the largest which are 4.84×10^{-2} mm^2 for GO/Cu4-0.6 and 5.25×10^{-2} mm^2 for GO/Cu5-0.6. The 2D wear track area of those two samples are also the largest as discussed in previous section. Relatively severe wear occurred on both the coating and counter ball sides on GO/Cu samples with 0.6 g/L of GO concentration. Wear area on worn counter ball for GO/Cu4-0.4 is 3.95×10^{-2} mm^2 while that for GO/Cu5-0.8 is 2.33×10^{-2} mm^2. As stated before, the wear surface on GO/Cu4-0.8 was just showing depletion on the cauliflower like structure. The surface conditions on wear counter ball explain the reason why the 2D wear tracks of GO/Cu-0.8 is higher than the surface of unworn coating. As shown in orange bars, the wear surface area on counter ball of GO/Cu5-0.4 is 2.87×10^{-2} mm^2 and that of GO/Cu5-0.8 is 3.74×10^{-2} mm^2 which is slightly larger area than that on GO/Cu5-0.4. The COF of GO/Cu5-0.4 is also smaller than that of GO/Cu5-0.8.

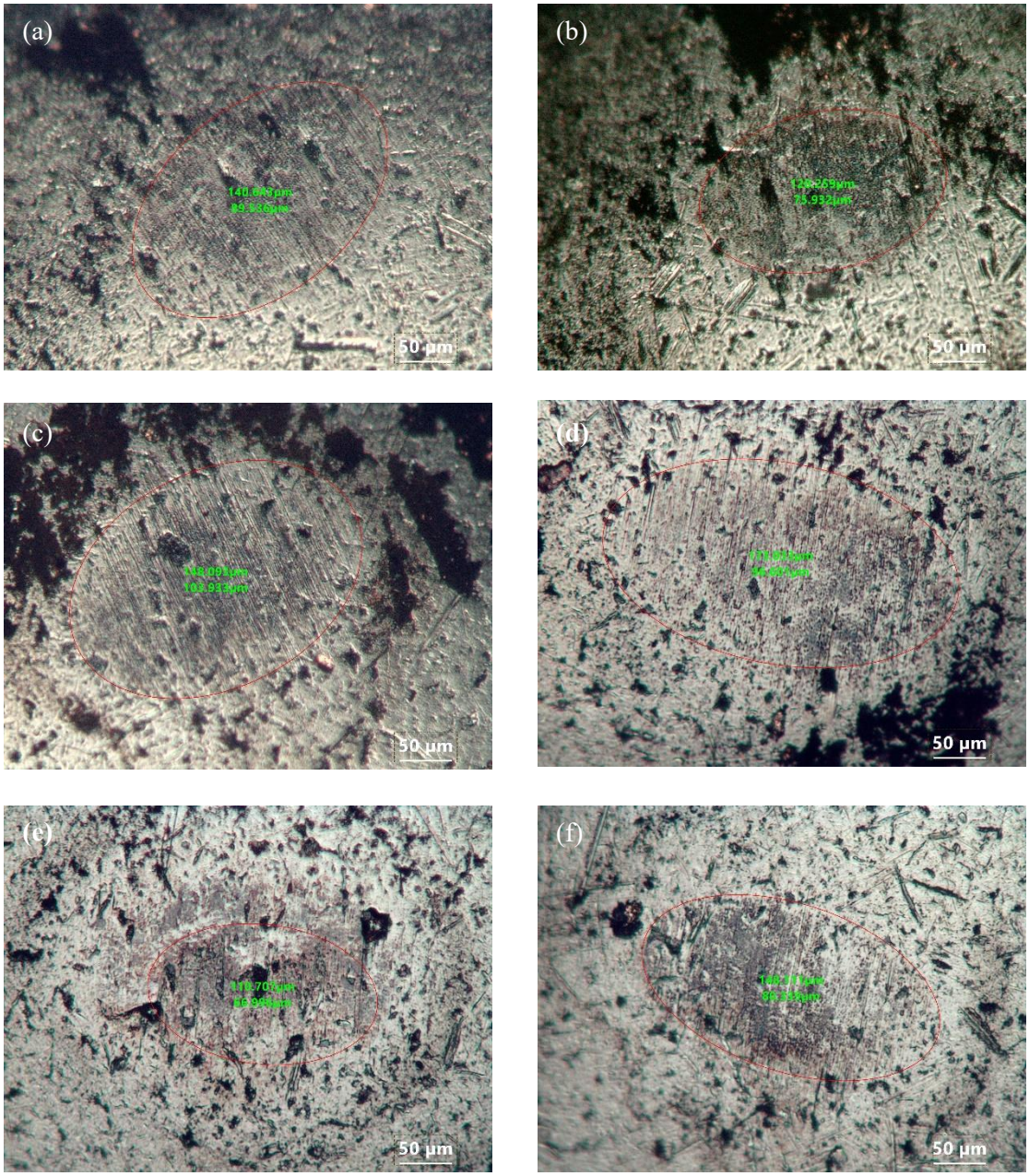


Figure 4.4.13 Optical images of worn counter ball for GO/Cu4 and GO/Cu5 samples deposited with 0.4-0.8 g/L GO concentrations: (a) GO/Cu4-0.4, (b) GO/Cu5-0.4, (c) GO/Cu4-0.6, (d) GO/Cu5-0.6, (e) GO/Cu4-0.8 and (f) GO/Cu5-0.8.

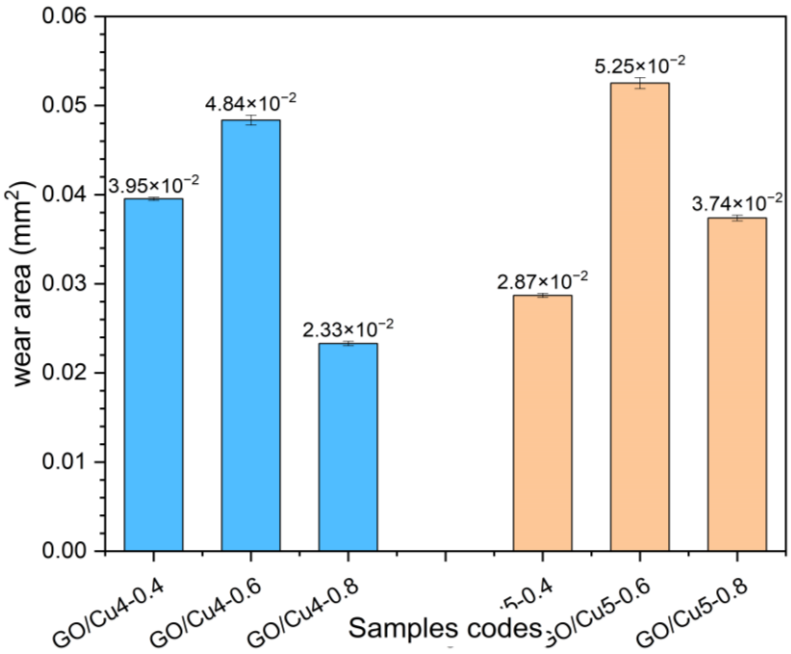


Figure 4.4.14 Wear area estimated on counter ball by ellipse area calculated.

The SEM images providing an overview of the wear tracks for GO/Cu4 and GO/Cu5 samples at GO concentrations ranging from 0.2 to 0.8 g/L are presented in Figure 4.4.15a to h. To compare the wear track of GO/Cu4-Brass and GO/Cu5-Brass, GO/Cu4-Brass demonstrates more material transferring on the surface. SEM images of wear tracks on GO/Cu samples under 0.4 - 0.8 g/L of GO concentrations were taken under same magnifications. As the length of those wear tracks are fixed at 5 mm, the width of those wear tracks could be used to reveal some results.

GO/Cu4-0.4 possessed (Figure 4.4.15c) relatively better friction and wear properties, according to previous sections. The width of the GO/Cu4-0.4 is thinner than GO/Cu4-0.6 and 0.8 (shown in Figure 4.4.15e and g). It is interesting that the darker area at the SEM of worn GO/Cu4-0.4 could be GO involved in the cyclic wear process. The GO induced in the wear tests might be the reason to the great tribological performance. The EDX results for this wear track would be discussed later. As for GO/Cu5-0.6 (Figure 4.4.15f), it is significant that its width is the largest,

which may explain the greater wear area observed on the wear counter ball. The wear tracks of GO/Cu5-0.4 and GO/Cu5-0.8 demonstrate a comparable width on their wear tracks, the GO/Cu5-0.4 is slightly wider than the other. It could be noted that the GO/Cu4 samples are more likely to suffer from adhesive wear than the GO/Cu5 series of samples. As mentioned at microhardness part, the hardness of GO/Cu5 samples possessed relatively higher hardness than the GO/Cu4 samples.

As discussed before, the wear performance of GO/Cu5-0.6 seems the worst and the GO/Cu4-0.4 exhibits the relatively great wear performance than other samples. Hence, the EDX of those two samples is demonstrated at Figure 4.4.16, to find out some reason to explain those phenomena. The S1 and S3 rectangular areas are on wear track of GO/Cu5-0.6 (Figure 4.4.16a) which are on abrasive groove and abrasive like area, respectively. As for S2, EDX was operated at certain distance to the wear track. It is interesting to note that the carbon (C) composition of S2 is larger than S1 and S2 on GO/Cu5-0.6, as shown in Figure 4.4.16b. Hence, the unworn area possessed higher carbon concentration then the areas on the wear track on GO/Cu5-0.6. The lack participation of GO within the 2000 cycles of wear test may have resulted in severe dry sliding lack of lubrication. Then, it results in the increase of friction and wear rate of GO/Cu5-0.6. Besides, the oxygen (O) composition of S2 is only 2.51 at% which is much smaller than that on S1 and S3 (23.04 at% and 23.44 at%, respectively). Both S1 and S2 detected the existence of iron (Fe) with 0.57 at% and 0.41 at%, while no Fe was detected on S2.

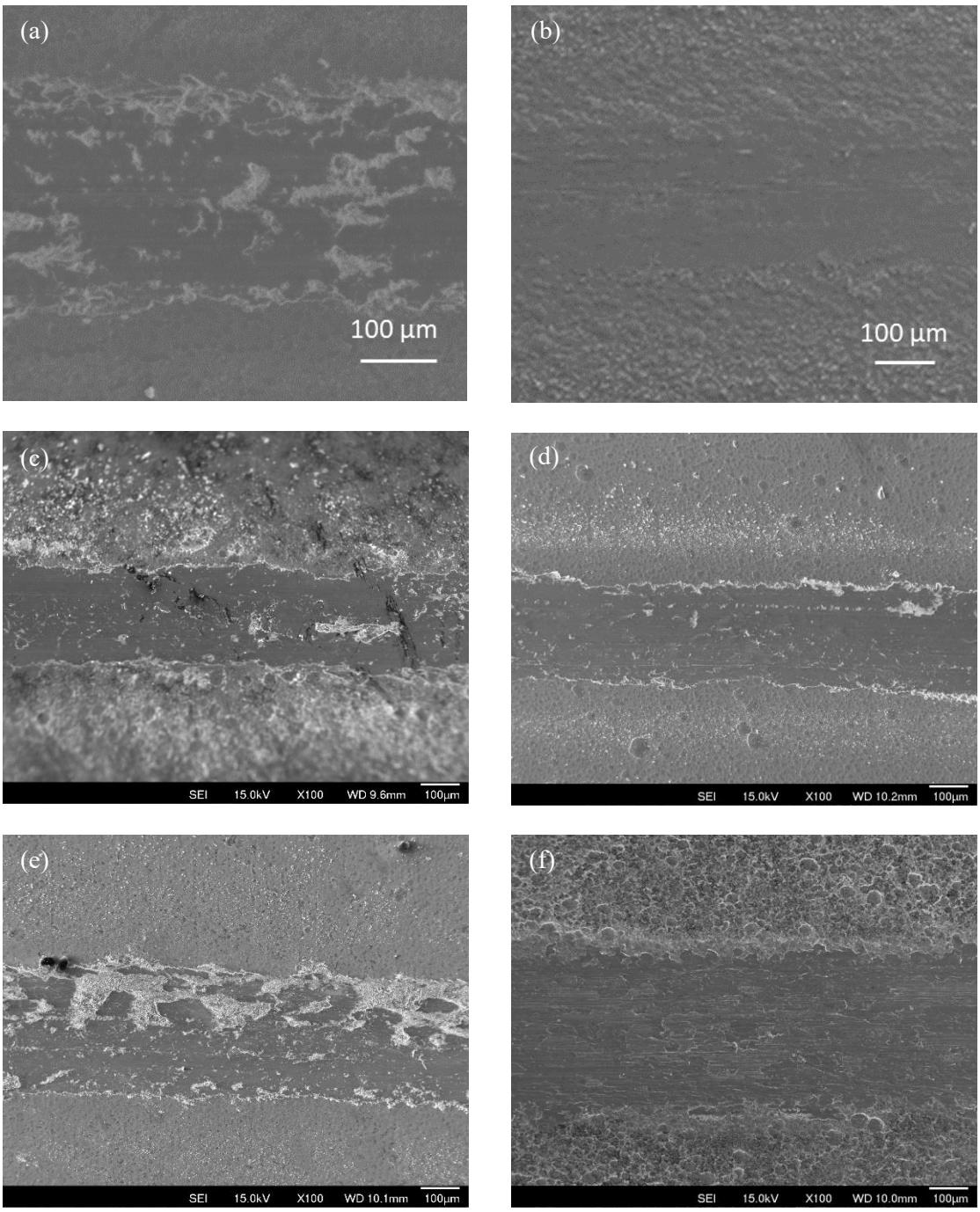


Figure 4.4.15(a-f) Comparisons for wear tracks of GO/Cu4 and 5 samples deposited with different GO concentrations of 0.2, 0.4, 0.6 and 0.8 g/L: (a) GO/Cu4-0.2, (b) GO/Cu5-0.2, (c) GO/Cu4-0.4, (d) GO/Cu5-0.4, (e) GO/Cu4-0.6 and (f) GO/Cu5-0.6.

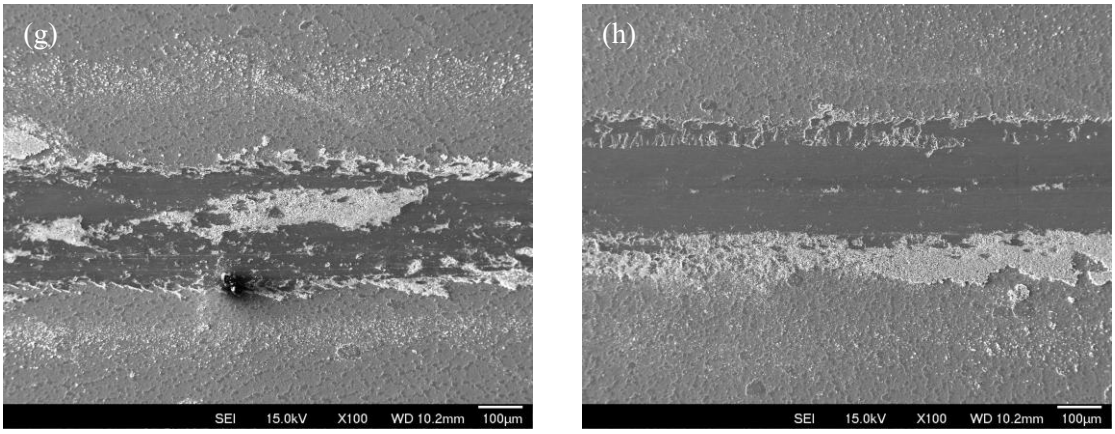


Figure 4.4.15 (continued) (g-h) Wear track of (e) GO/Cu4-0.8 and (f) GO/Cu5-0.8 sample coatings.

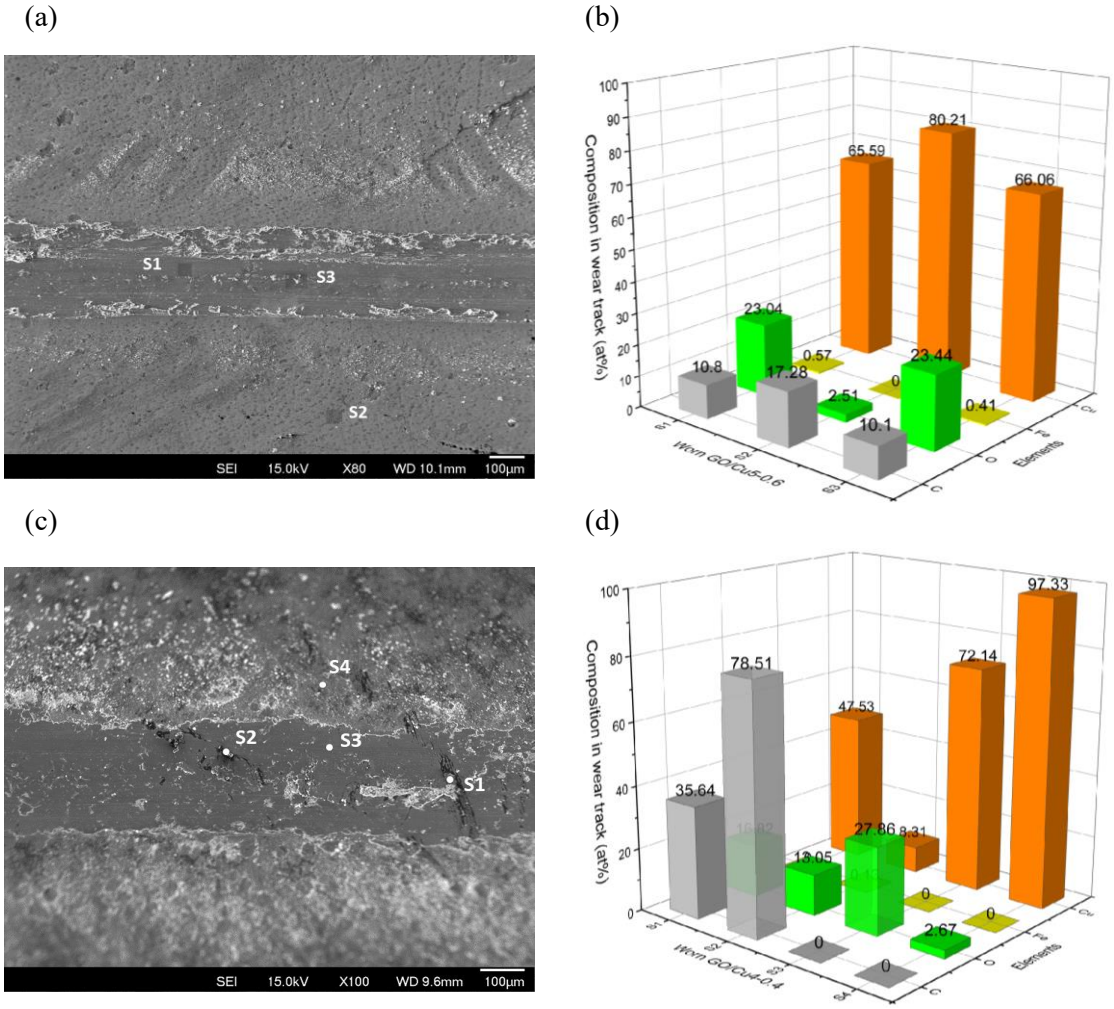


Figure 4.4.16 SEM after EDX tests for (a) worn GO/Cu5-0.6 and (b) its EDX results; (c) GO/Cu4-0.4 SEM image denoted spectra and (d) its EDX 3D bar charts.

As shown in the Figure 4.4.16c, there are 4 spectra exhibited on the SEM image showing the spots tested by EDX. The S1 and S2 spots are located on the black coloured structure exhibiting on the wear track. S3 and S4 are utilised as control group to compare with the area of GO, S3 is within the wear track on abrasive groove and S4 is near to the wear track without notable debris. Their EDX results of GO/Cu4-0.4 were summarised with 3D bar chart, as shown in Figure 4.4.16d. The S4 of GO/Cu4-0.4 represents the unworn coating surface and could be used to compare with the wear track areas. There are 97.33 at% of Cu and only 2.67 at% of O detected on S4, so that the O composition over S4's would be due to oxidative reaction during the wear process and carbon composition could be GO on the wear track. The S3 of GO/Cu4-0.4 is used to compare with the area which possess those black colour area, there are also only of Cu and O constituents with 72.14 at% and 27.86 at% composition, respectively.

It is notably that the S1 and S2 are of extremely high atomic percentage of C which are 35.64 % and 78.51 % in atomic composition. While the S3 and S4 demonstrate no carbon composition by AutoID mode of EDX. Hence, those black areas on worn GO/Cu4-0.4 would contain GO with different compositions. The S1 and S2 is also possess O composition under EDX test, with 16.82 at% and 13.05 at% respectively. It is quite interesting that the GO/Cu4-0.4 is of less GO within its coating, compared to GO/Cu5-0.6, but the GO participate more while dry sliding test under air. Then, the wear performance of GO/Cu4-0.4 is much better than GO/Cu5-0.6.

As discussed at the EDX results, the carbon composition on wear track of GO/Cu4-0.4 is relatively larger than that of GO/Cu5-0.6. To prove those area high in carbon composition is the GO flakes, Raman spectroscopy would be much reliable than EDX. Depicted in Figure 4.4.17a is optical images taken before Raman tests, as denoted with red squares are three spectra (S1, S2 and S3) that were subjected to Raman spectroscopy. S1 and S2 are on the flake-like structure

and S3 is on one of the black coloured areas. Compared to the Raman photos taken with GO/Cu5-Brass, the images of GO/Cu4-0.4 is relatively brighter than the GO/Cu5-Brass samples. Moreover, the red, black, or green coloured of Cu oxides is not shown on its wear track, both on Figure 4.4.17a and c. Besides, galling could not be found on Raman optical images of GO/Cu4-0.4. Those indicate relatively less loss of materials after wear tests on GO/Cu4-0.4. Several Raman spectra were conducted on worn GO/Cu4-0.4 (Figure 4.4.17b), those spectra all present relatively obvious D and G peaks which represent the existence of GO at S1 to S3 shown in Figure 4.4.17a. The S1 and S3 present relatively higher intensity in D and G peaks, while relatively low intensity of D and G peaks is found on S2. S1 and S3 are at the inner area of wear track while the S3 is on the outer area of wear track. This might indicate that the GO more likely remains within the wear track rather than repelled to the unworn areas. To compare the GO on wear track to lower GO concentrations, the Raman spectrum of GO/Cu4-Brass is illustrated at the bottom of the Figure 4.4.17b. It was found on the wear debris on worn GO/Cu4-0.4 surface while no such peaks could be found on the wear tracks of this specimen. The reason for better COF on GO/Cu4-0.4 than that on GO/Cu4-Brass could be revealed.

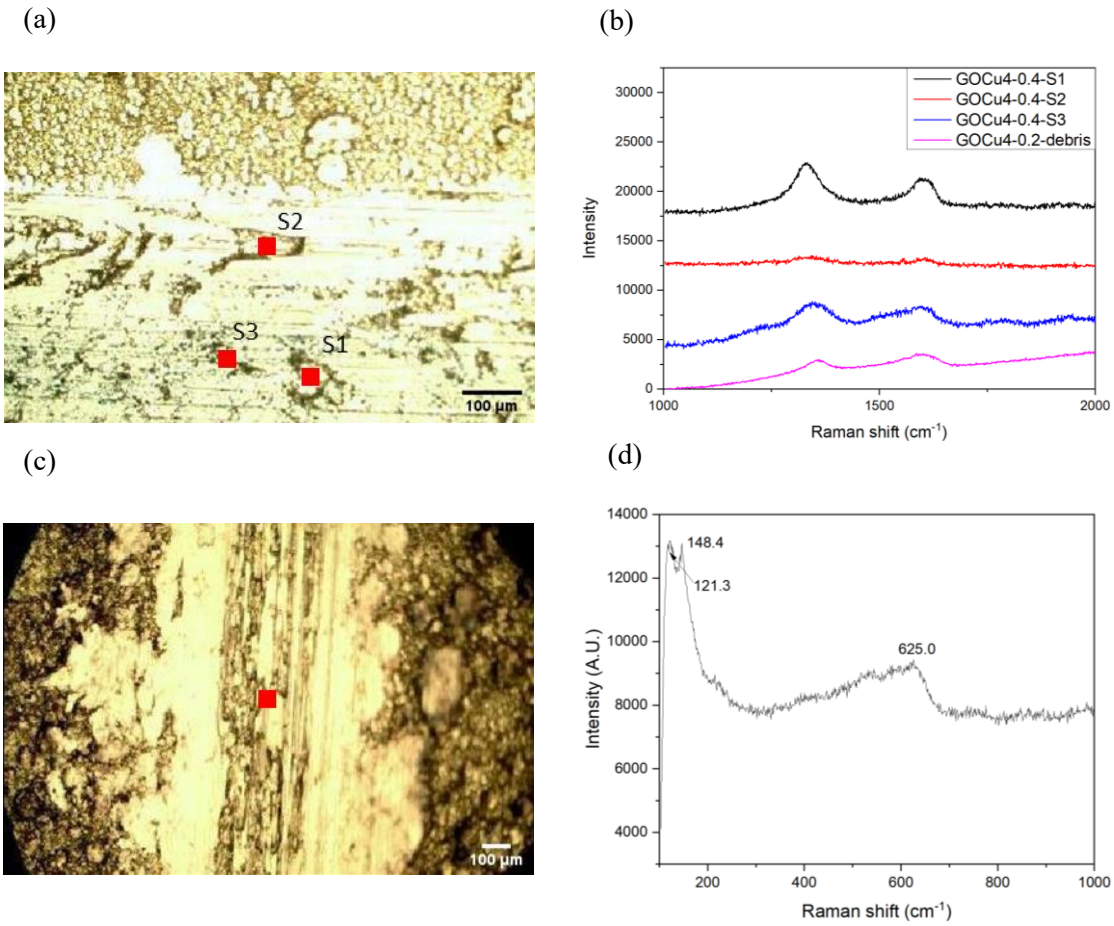


Figure 4.4.17 Raman spectroscopy on different areas of wear surface of GO/Cu4-0.4 to reveal the GO and oxides: (a) GO/Cu4-0.4 worn area with possible graphene spots and (b) the Raman spectra of spectra 1 to 3; (c) GO/Cu4-0.4 worn area with possible oxides and (d) its Raman spectrum

Figure 4.4.17c presents optical microscope images corresponding to the Raman data for copper oxides identification, so that the oxidative wear could be noticed. In this depiction, the wear track exhibits a notably brighter colour compared to the unworn area, indicative of the degree of oxidative wear resulting from the wear process. Raman spectrum as depicted in Figure 4.4.17d, reveals peaks at 121.3 cm^{-1}, 146.4 cm^{-1} and 625.0 cm^{-1}. The 625.0 cm^{-1} could be characterised to Cu_2O. The absence of another characteristic peak of Cu_2O suggests only a relatively mild oxidation occurred at the red square point on the wear track of GO/Cu4-0.4. The darker area on the Figure 4.4.17c was because it is of smaller magnification, so it was involved the unworn area showing relatively general view of worn surface on GO/Cu4-0.4. The irregular

edges of the wear track could indicate the debris near the wear track which is also with bright yellow colour. The oxidation of this sample would be less severe than that on GO/Cu5-Brass.

4.5 Electrochemical Corrosion Properties

To explore the electrochemical corrosion behaviour, a series of potentiodynamic polarisation experiments were carried out with the bare brass and GO/Cu composite coating samples with different GO concentrations. As mentioned in Section 4.3 and 4.4, the GO/Cu samples produced with 4 and 5 volts possess superior general and tribological properties. Hence, these two brush plating potentials were selected for assessing corrosion resistance. The experiments were conducted on the GO/Cu4 and GO/Cu5 series of samples to investigate the effects of different GO concentrations (0.2, 0.4, 0.6 and 0.8 g/L) on their corrosion properties.

4.5.1 Potentiodynamic Polarisation of GO/Cu and Brass at Varying GO

The corrosion performance of GO/Cu coatings was evaluated by potentiodynamic polarisation in an inhibitor of simulated seawater (3.5 wt.% NaCl). Figure 4.5.1 demonstrates the exampled repeat tests of GO/Cu samples under 0.4 g/L of GO concentration. It is interesting to note that the repeatability of the polarisation curve for GO/Cu4-0.6 is excellent from the beginning of corrosion potential to the passivation time and the corrosion current density at the final stage of corrosion. The repeatability of GO/Cu5-0.6 is also great, except for around 0.03V of difference in the corrosion start potential. With GO sheets addition within the laminate Cu coating structure, the uniformity of the coating surface under electrochemical corrosion evaluation is excellent.

Figure 4.5.2 exhibits the polarisation curve comparisons between GO/Cu samples and bare

brass after an OCP test for 1 h. With an uprising of potential from -1.0 V, the brass sample starts corrosion at the lowest potential compared to samples with GO/Cu coatings. With continuous increase potential at the anodic polarisation area, the corrosion illustrates the metastable stage [257,258]. After that stage, the corrosion becomes severer with rising potential. Then, it shows slight passivation, and the current density remains relatively stable with increase of potential. To compare the bare brass, the corrosion potential of GO/Cu coating samples possesses a clear positive shift. Hence, the GO/Cu composite coatings have significant improvement on the corrosion potential.

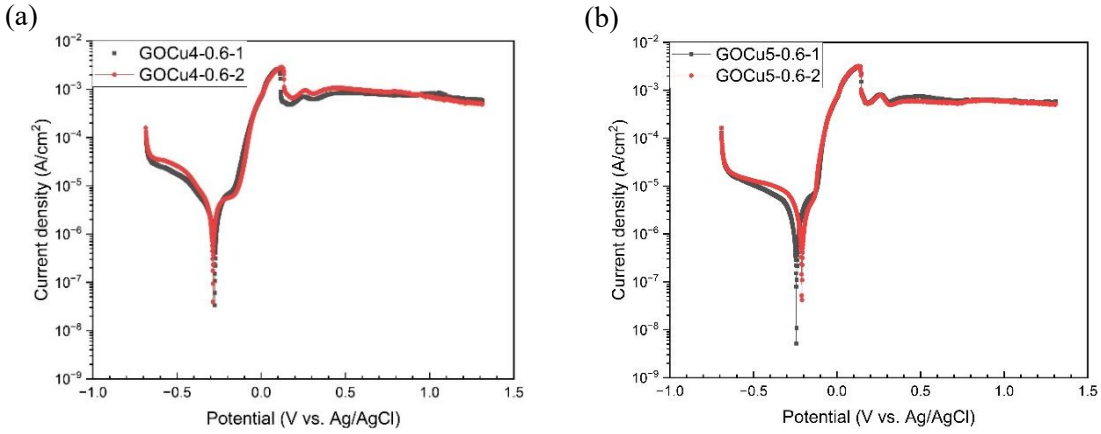


Figure 4.5.1 Potentiodynamic polarisation curves for (a) GO/Cu4-0.6 and (b) GO/Cu5-0.6 samples showing the repeatability.

The potentiodynamic polarisation curves of GO/Cu4 series samples compared with the brass are shown in Figure 4.5.2a. With the uprising of GO concentration, the corrosion potential of GO/Cu4 samples generally depicts an increased tendency. While GO/Cu4-0.4 exhibits a slightly more positive shift than GO/Cu4-0.6. The GO/Cu4-0.2 corrodes earliest compared with other GO/Cu4 samples, and the corrosion potential of GO/Cu4-0.8 depicts the largest corrosion potential. As mentioned in Section 4.2.2 and Section 4.3.3, with GO addition, the coating structure of GO/Cu samples tends to perform a porous structure. The porous structure would

reduce corrosion resistance. It could be noticed that the GO/Cu4 samples show passivation around the 0-0.2 V region and the current density dropped lower than that of brass samples. The corrosion status generally stabled after the potential increased to 0.5 V. Under higher current density, it leads to severe corrosion.

As for the GO/Cu5 samples (Figure 4.5.2b), the start corrosion potentials of GO/Cu5 samples also present much higher than that of substrate brass. To compare the GO/Cu4 samples, the GO/Cu5 samples presents certain regulations with GO concentration change. The potential of corrosion start of GO/Cu5 series presents an uprising tendency with the increase of GO concentrations. While corrosion start potential of GO/Cu5-0.6 is just a slightly more positive shift than that of GO/Cu5-0.4. To explore the regulation of corrosion potential and current density, Tafel fitting was carried out by the Origins software and the results showing at the Table 4.5.1.

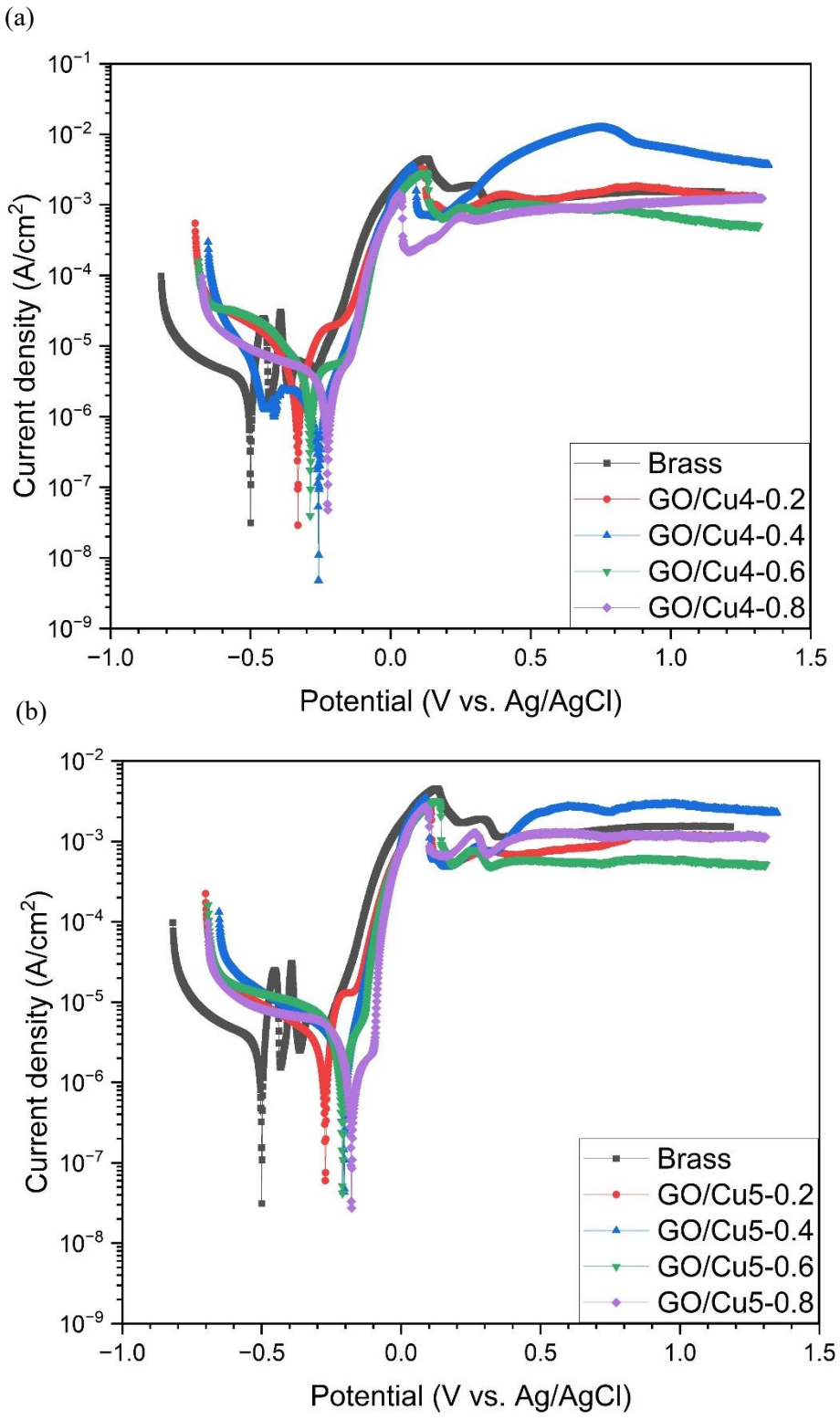


Figure 4.5.2 The comparisons of potentiodynamic polarisation curves for samples deposited with various GO concentrations in (a) GO/Cu4 and (b) GO/Cu5 series versus brass substrate.

Table 4.5.1 Tafel fitting data from potentiodynamic polarisation curves of bare brass, GO/Cu4 and GO/Cu5 samples of different GO concentrations.

Samples		E_{corr} (V)	I_{corr} ($\mu A/cm^{-2}$)
Brass		-5×10^{-1}	18.9
GO/Cu-0.2	GO/Cu4-0.2	-3.38×10^{-1}	4.55
	GO/Cu5-0.2	-2.81×10^{-1}	3.89
GO/Cu-0.4	GO/Cu4-0.4	-2.53×10^{-1}	2.84
	GO/Cu5-0.4	-2.04×10^{-1}	2.46
GO/Cu-0.6	GO/Cu4-0.6	-2.71×10^{-1}	2.52
	GO/Cu5-0.6	-2.10×10^{-1}	2.13
GO/Cu-0.8	GO/Cu4-0.8	-2.11×10^{-1}	2.41
	GO/Cu5-0.8	-1.67×10^{-1}	1.07

The corrosion potential (E_{corr}) of brass is -5.0×10^{-1} volts (V), which is lower than all the GO/Cu samples. Among the GO/Cu series, the GO/Cu4-0.2 sample has a corrosion potential of -3.38×10^{-1} V, indicating it is of the lowest corrosion potential. The corrosion potentials of GO/Cu4-0.4 (-2.53×10^{-1} V) and GO/Cu4-0.6 (-2.71×10^{-1} V) are near to each other which is both larger than that of GO/Cu4-0.2. The largest corrosion potential of GO/Cu4 samples is -2.11×10^{-1} V which possess best corrosion potential in corrosion prevention. The GO/Cu5 samples also present an uprising tendency with increase of GO concentrations, from -2.81×10^{-1} V for GO/Cu5-0.2 to -1.67×10^{-1} V for GO/Cu5-0.8. The GO/Cu5-0.4 (-2.04×10^{-1} V) and GO/Cu5-0.6 (-2.10×10^{-1} V) samples possess similar corrosion potential. It is interesting to note that the GO/Cu5-0.8 possesses the highest corrosion potential (-1.67×10^{-1} V) which exhibits the best corrosion potential among presented parameters.

The corrosion current density (I_{corr}) of the substrate brass is 18.9 μA, which is an order of magnitude higher than that of both the GO/Cu4 and GO/Cu5 series samples. Among GO/Cu4

and GO/Cu5 series, the GO/Cu4-0.2 possesses the highest corrosion current density of 4.55 $\mu A/cm^{-2}$. The I_{corr} of GO/Cu4 samples demonstrates descending trend with increase of GO, from 4.55 $\mu A/cm^{-2}$ for GO/Cu4-0.2 to 2.41 $\mu A/cm^{-2}$ for GO/Cu4-0.8 samples. The I_{corr} of GO/Cu4-0.4 (2.84 $\mu A/cm^{-2}$) is slightly larger than that of GO/Cu4-0.6 (2.53 $\mu A/cm^{-2}$). The I_{corr} of GO/Cu5 series also decrease with increase of GO concentrations, from 3.89 $\mu A/cm^{-2}$ for GO/Cu5-0.2 to 1.07 $\mu A/cm^{-2}$ for GO/Cu5-0.8. The I_{corr} of GO/Cu5-0.4 (2.46 $\mu A/cm^{-2}$) is also slightly larger than the GO/Cu-0.6's (2.13 $\mu A/cm^{-2}$). The I_{corr} optimal is also from GO/Cu5-0.8 likewise to the optimal E_{corr}.

4.5.2 The SEM and Elements Analysis on Corroded Sample Surface

4.5.2.1 Corroded substrate material brass

As the substrate, the brass is evaluated to discover whether the GO/Cu coating is improved, the SEM images of corroded brass are shown in Figure 4.5.3. The general view of the corroded brass as depicted in Figure 4.5.3a, it presents the corroded brass surface at the left region and uncorroded at the right. The brass was ground with 1200 grit before the corrosion test, as illustrated on the right; however, no grinding marks are present on the corroded surface. At the boundary, some pits are visible, as indicated by the yellow arrows, which were caused by crevice corrosion. Figure 4.5.3b demonstrates the corroded surface from the relatively middle region of corrosion. It presents quite severe galvanic corrosion between zinc and copper which could not reveal the original grindings, as well as pits at the granular boundaries. Moreover, it exhibits severe crevice corrosion at the boundary, as there are several pits illustrates on both sides.

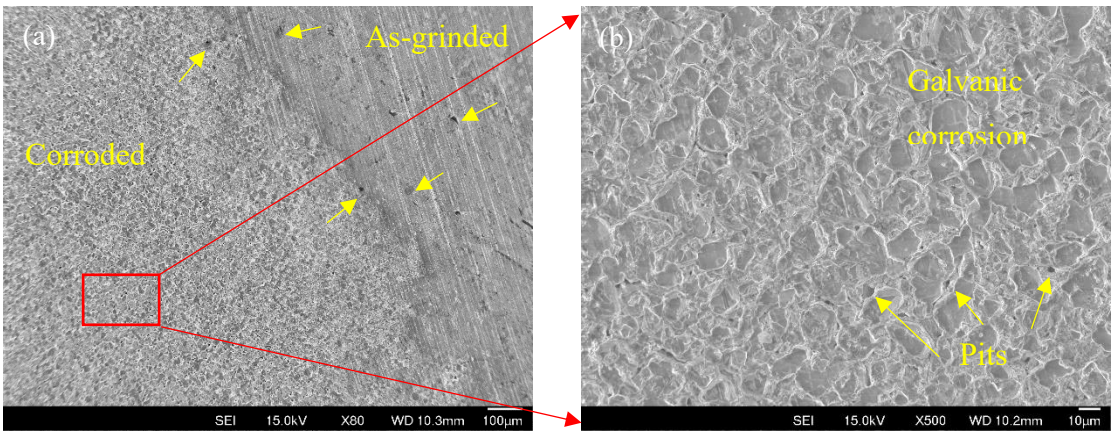


Figure 4.5.3 The corroded surface of bare brass: (a) the edge of corrosion and (b) a detailed view of the corrosion region.

There are pits-like areas around the grain boundaries of brass on the corroded surface of the brass. Figure 4.5.4a demonstrates one of the SEM examples found at the grain boundaries. After Cu EDX mapping (Figure 4.5.4b) carried out by X-ray, it exhibits an area of low mapping signal at the pit-like area. As a high-frequency radiated signal, characteristic X-ray is likely to be trapped rather than captured by the sensor, especially in the pitting corrosion area. Hence, this is pitting found on the corroded surface. It is interesting to note that there is oxygen (O) (Figure 4.5.4c) and carbon-rich (C-rich) (Figure 4.5.4d) areas at the edge of the pit. It could indicate the existence of the corrosion products. There are two possible types of corrosion products for Cu with 3.5 wt.% of NaCl solution inhibitor which is copper hydroxide chloride (Cu(OH)Cl) and basic copper carbonate ($Cu_2(OH)_2CO_3$). Without the chloride (Cl) element revealed by the EDX, $Cu_2(OH)_2CO_3$ is possibly produced after the corrosion test.

As illustrated in Figure 4.5.4e, the remaining zinc with low composition was exhibited at the area near to the copper peaks. This is might due to the dezincification of brass, caused by the dissolving of zinc under this lower electrochemical activity of copper than zinc [259–262]. To conclude, pitting corrosion, galvanic corrosion and dezincification could be noticed on the

corroded brass surface.

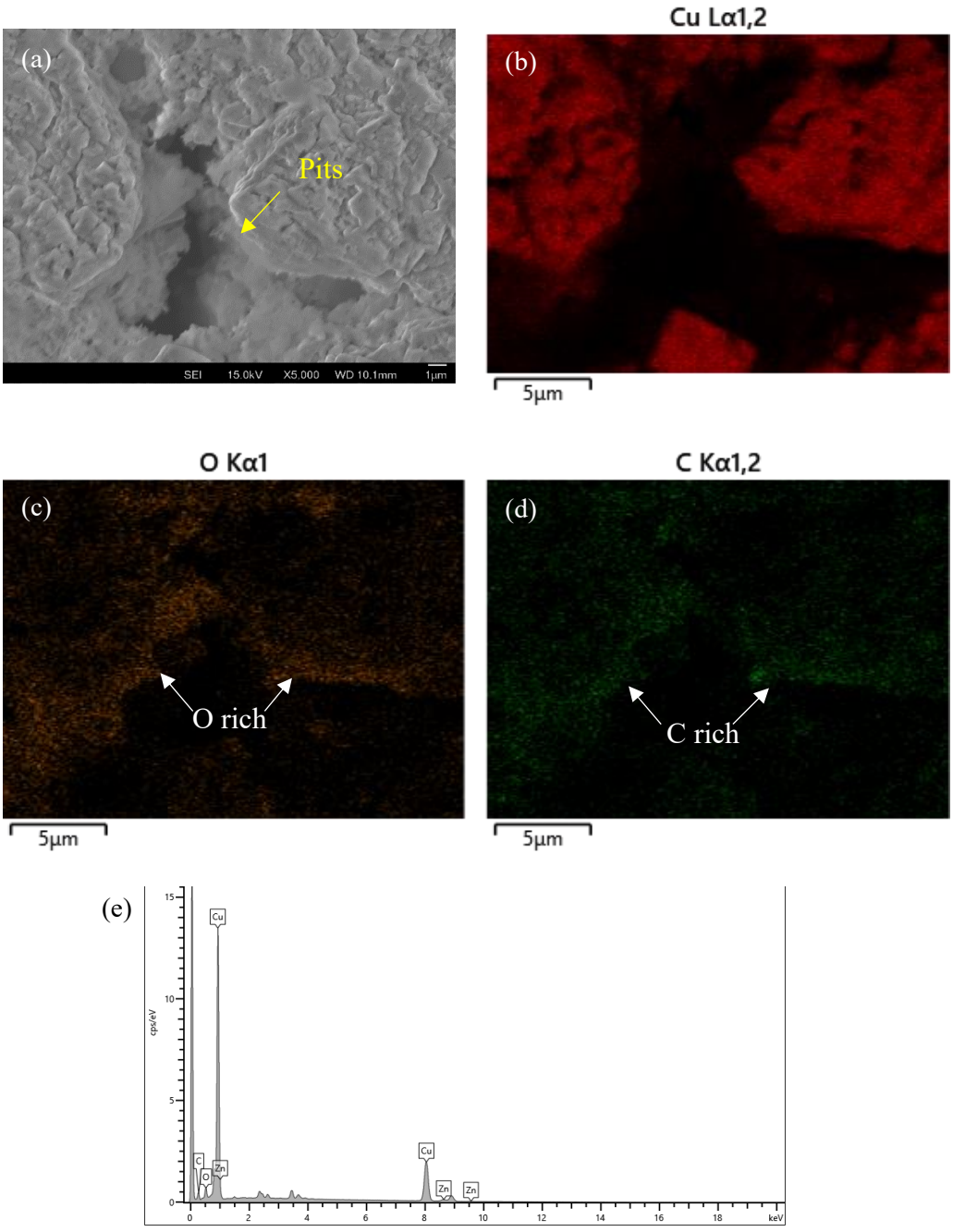


Figure 4.5.4 EDX mappings on (a) the corroded brass surface with (b) Cu, (c) O and (d) C elements and (e) elements summarised results.

4.5.2.2 Corroded surface on the GO/Cu composite coating surface

The corrosion behaviour of the GO/Cu4 series with varying GO concentrations is illustrated in Figure 4.5.5. Figure 4.5.5a, c, e, and g display the extent of corrosion at the test boundaries. Specifically, the sample GO/Cu4-0.2 (Figure 4.5.5a) experienced significant crevice corrosion at the boundaries with a GO concentration of 0.2 g/L. In contrast, the corroded surface of the GO/Cu4-0.4 sample (Figure 4.5.5c) shows substantial deviations from the uncorroded surface, highlighting the impact of increased GO concentration. However, the surfaces of samples GO/Cu4-0.6 and GO/Cu4-0.8 (Figure 4.5.5e and g, respectively) exhibit less pronounced changes post-corrosion, indicating a possible mitigation of corrosion with higher GO concentrations.

Figure 4.5.5b, d, f, and h depict the influence of GO concentrations on the GO/Cu4 series samples. It is significant that the corroded surface of GO/Cu4-0.2 (Figure 4.5.5b) depicts quite severe uniform corrosion, compared to other samples. Moreover, relatively great amounts of pits could be found on this surface. The corroded surface of the GO/Cu4-0.4 sample also possesses some pits, as shown in Figure 4.5.5d. In the meantime, uniform corrosion could also be seen on this corroded sample, where some of the areas have been corroded down with a certain depth. The uniform corrosion of GO/Cu4-0.6 (Figure 4.5.5f) is relatively less severe than that of GO/Cu4-0.4, and there are no obvious pits exhibiting on the corroded surface. It is interesting to note that intergranular corrosion is illustrated on the GO/Cu4-0.8 corroded surface along with uniform corrosion, as depicted in Figure 4.5.5h. The GO/Cu4-0.6 depicts the best corrosion resistance among the GO/Cu4 samples under SEM.

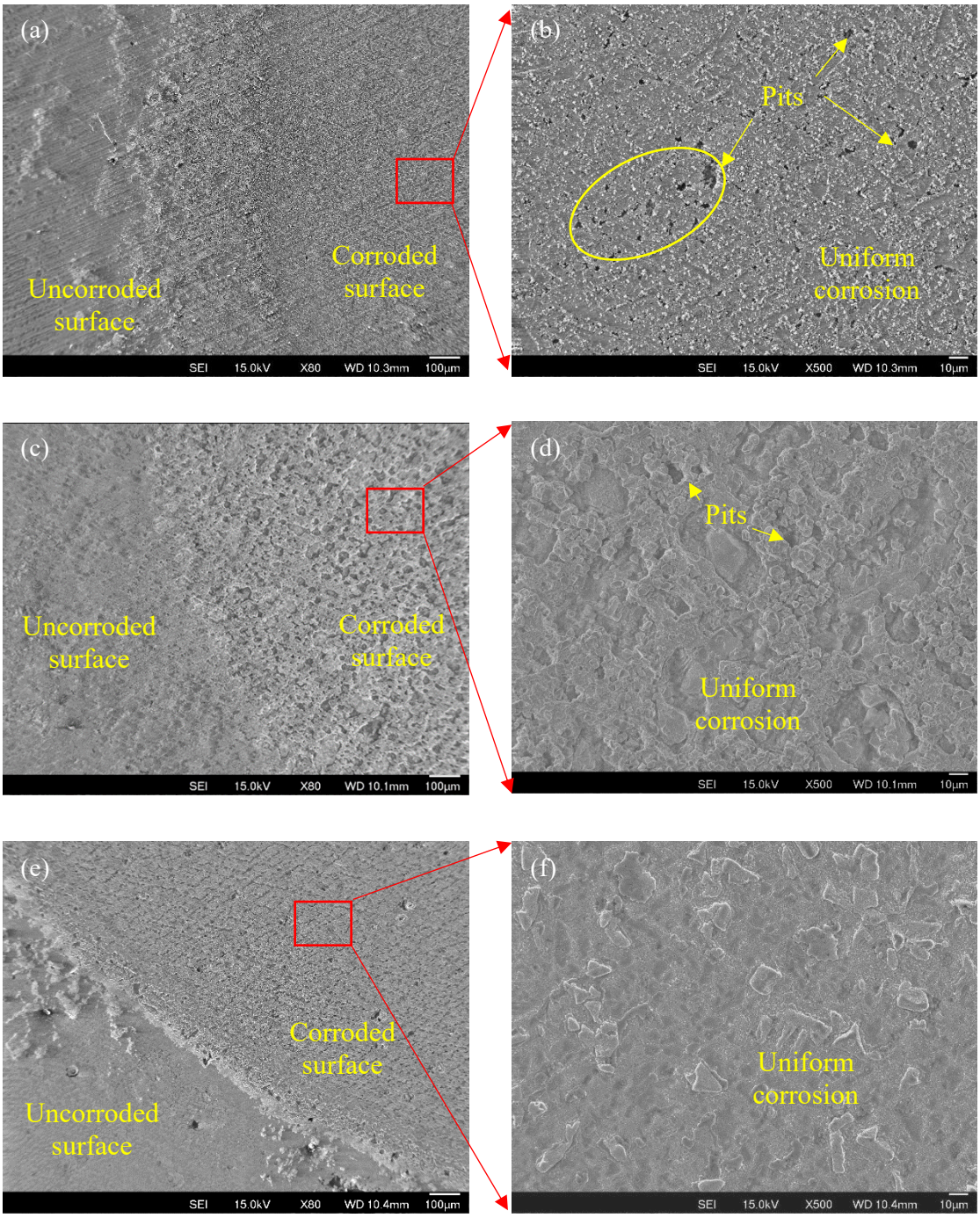


Figure 4.5.5(a-f) The SEM images of corroded surfaces for GO/Cu4 series of samples: (a, b) GO/Cu4-0.2; (c, d) GO/Cu4-0.4; and (e, f) GO/Cu4-0.6.

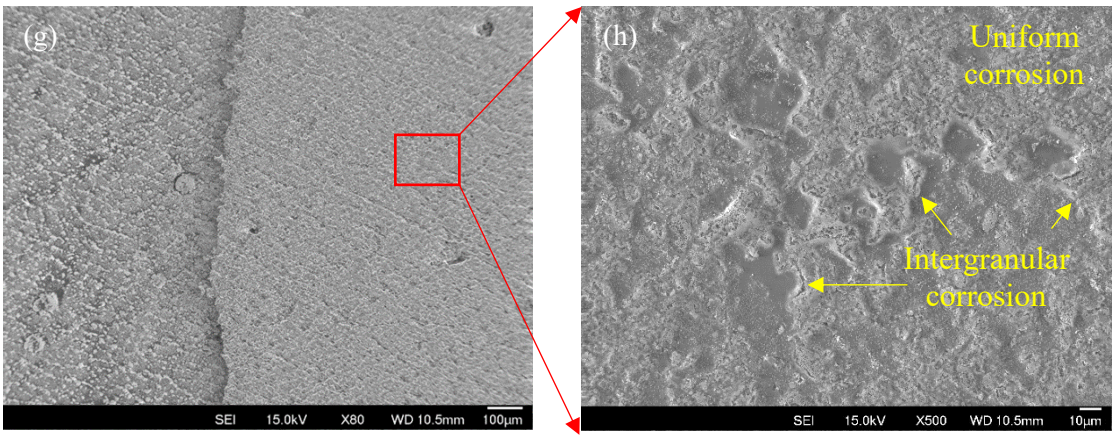


Figure 4.5.5 (continued) (g-h) corroded surfaces of GO/Cu4-0.8 sample.

Similar to the GO/Cu4 samples, the GO/Cu5 series also demonstrates varying corrosion performance at different GO concentrations, as depicted in Figure 4.5.6. Examination of the corroded surfaces (Figure 4.5.6a, c, e, and g) reveals the presence of crevice corrosion at the edges, alongside pitting corrosion. With increasing concentrations of GO, there is a noticeable reduction in the number of pits. The most pronounced crevice corrosion occurs in the GO/Cu5-0.4 sample, which corresponds to the highest corrosion current density observed during the final stages of corrosion, as illustrated in Figure 4.5.2b.

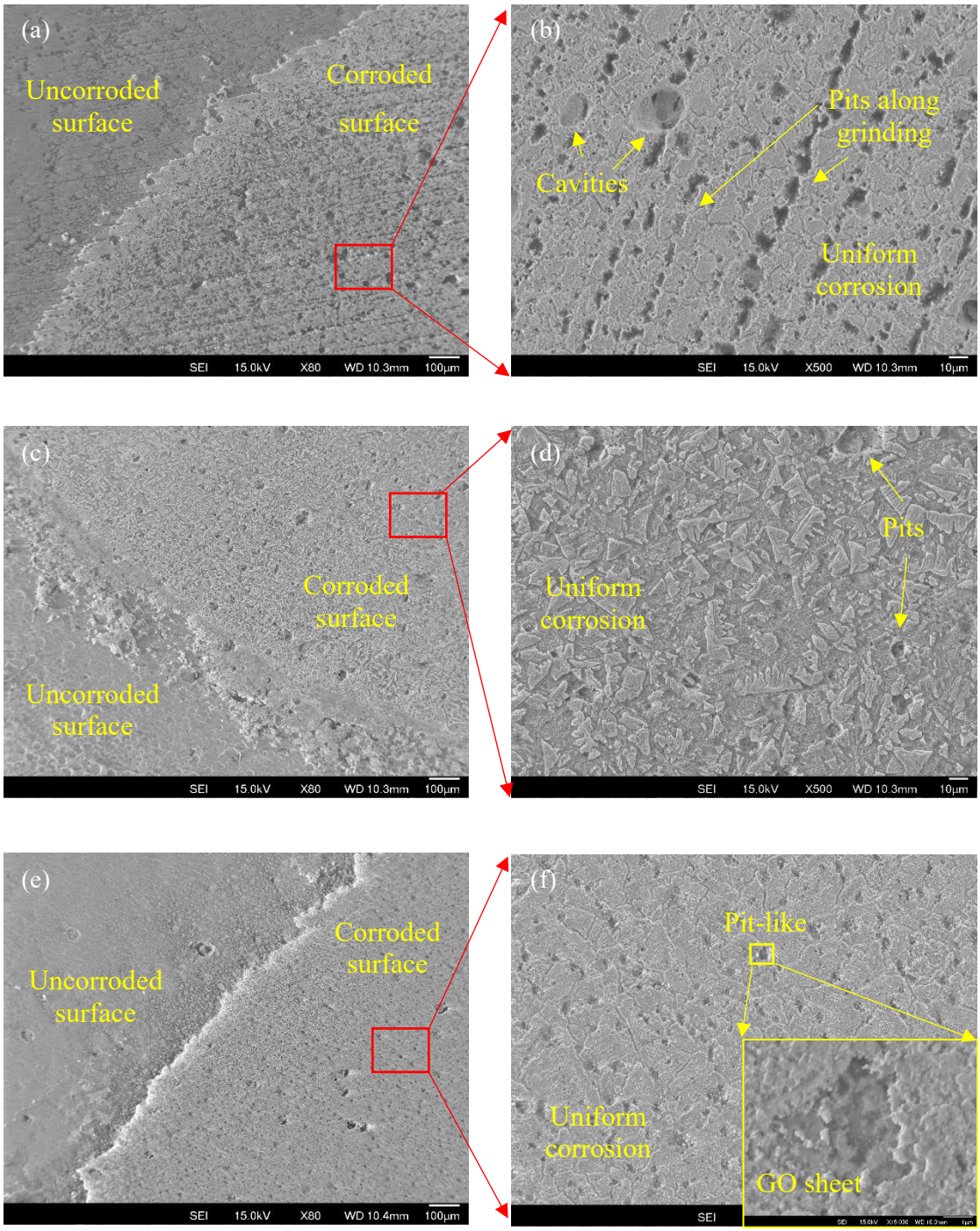


Figure 4.5.6(a-f) The SEM images of corroded surface for GO/Cu5 series of samples: (a, b) GO/Cu5-0.2; (c, d) GO/Cu5-0.4; and (e, f) GO/Cu5-0.6.

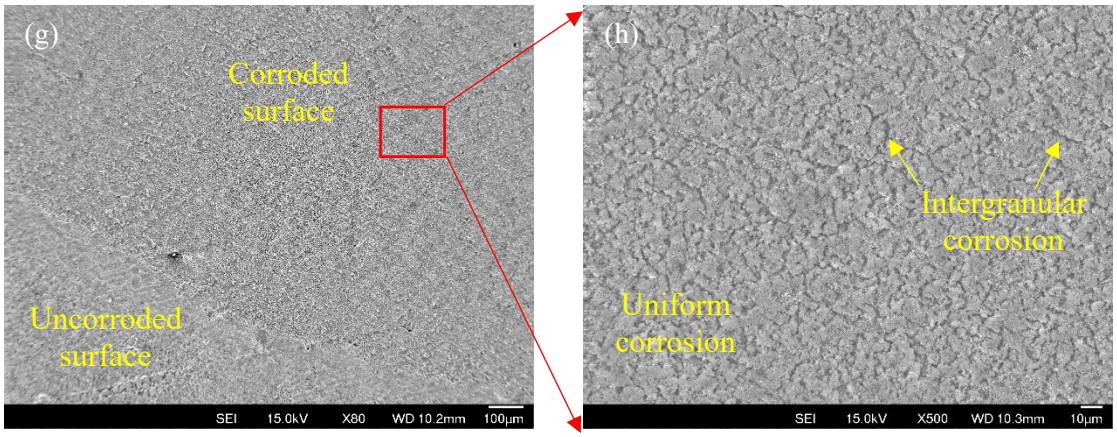


Figure 4.5.6 (continued) (g-h) Corroded surface of GO/Cu5-0.8 sample.

Figure 4.5.6b, d, f and h illustrate the corroded surface at "500×" magnifications, revealing the impact of GO concentrations on those GO/Cu5 samples. It could be seen on the corroded GO/Cu5-0.2 surface (Figure 4.5.6b) that relatively severe pitting corrosion was occurred, leading to several cavities and pitting areas are arranged as dot-line formation. It is possible that the pitting occurred along the grinding direction. Meanwhile, relatively severe uniform corrosion also happened which reveals the boundary of Cu crystal. Similarly, severe uniform corrosion could also be noticed on the corroded GO/Cu5-0.4 surface (Figure 4.5.6d) which also revealed the grain boundary of Cu. And pitting corrosion also occurred as form of several pits without cavity. The GO/Cu5-0.6 sample demonstrates pit-like area with certain numbers, as depicted in Figure 4.5.6f, figuring out under higher magnification that the corrosion was stopped by the graphene oxide sheet beneath the corroded area, preventing the potential pitting penetration. And the uniform corrosion of GO/Cu5-0.6 is relatively less severe than the former two samples. Pitting corrosion was also not found under 500 magnifications on the corroded GO/Cu5-0.8, as shown in Figure 4.5.6h. The uniform corrosion is severer than that GO/Cu5-0.6, intergranular corrosion might occur on the grain boundaries which would be further discussed at the Discussions session.

It is clear that with increasing of GO concentrations, the number of pits areas are also gradually reduced. Both GO/Cu5-0.6 and GO/Cu5-0.8 samples exhibit no pitting, moreover, the GO/Cu5-0.6 presents better corrosion surface. Therefore, GO/Cu5-0.6 is considered the optimal parameters for corrosion prevention application.

4.5.2.3 Corrosion Products of GO/Cu sample

It presents a typical example from GO/Cu4-0.4 sample in Figure 4.5.7 revealing the corrosion products on GO/Cu samples. This corrosion test makes some GO sheets exposure to air as seen in the carbon composition shown in Figure 4.5.7d. Figure 4.5.7a exhibits corrosion products at the boundary of corroded and uncorroded area. This area is consistent with relatively higher level of oxygen (O) and chloride (Cl), as respectively shown in Figure 4.5.7c and e. As mentioned in Section 4.5.2.1, copper hydroxide chloride (Cu(OH)Cl) and basic copper carbonate ($Cu_2(OH)_2CO_3$) are two possible corrosion products after corrosion test with 3.5 wt.% of NaCl. It is more likely that Cu(OH)Cl is produced at the spot of crevice corrosion.

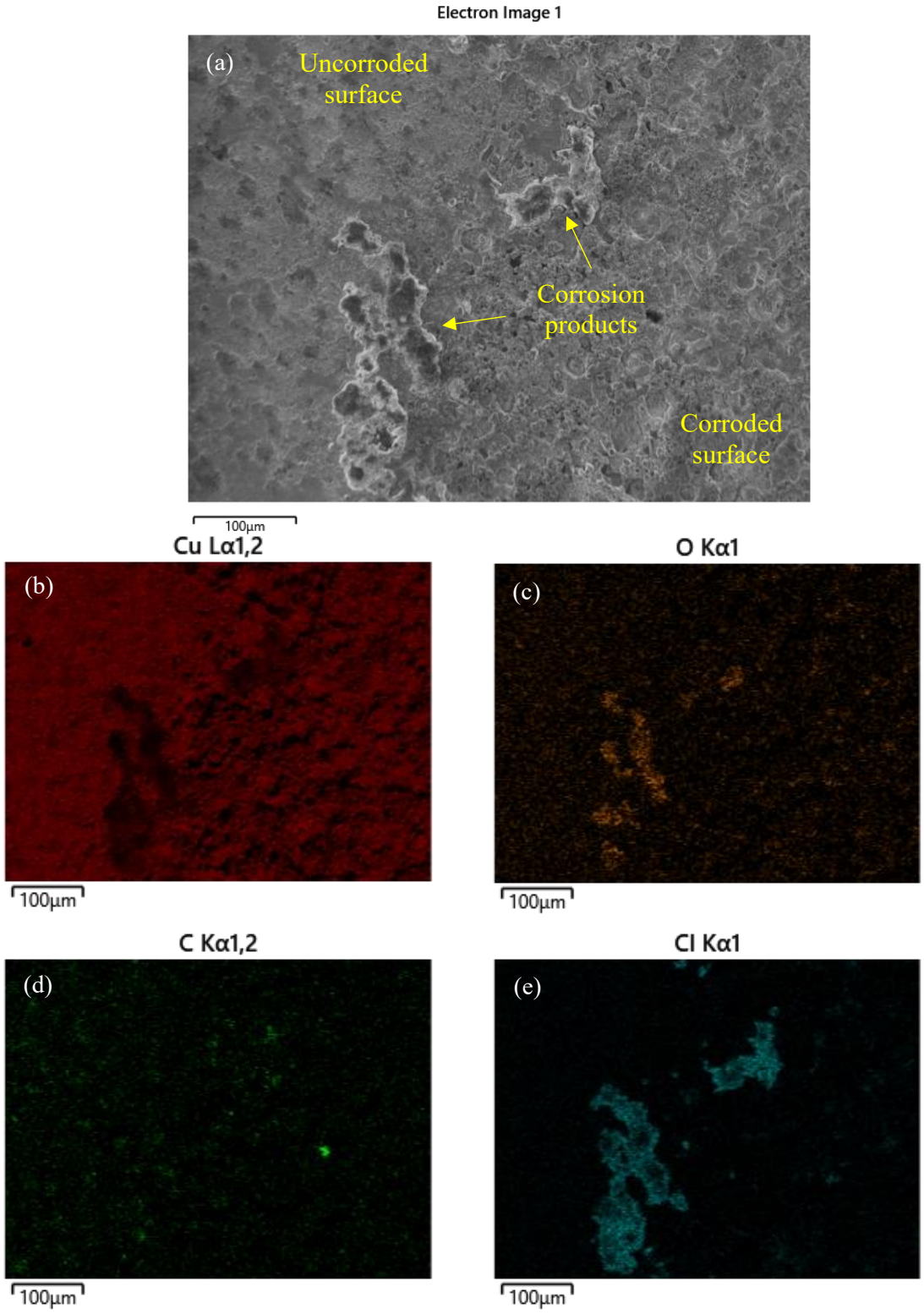


Figure 4.5.7 EDX mapping on corroded GO/Cu4-0.4 sample showing the (a) SEM image and mapping with (b) Cu, (c) O, (d) C and (e) Cl elements.

4.6 Summary of Results

The major experimental results are presented in this chapter in order of the microstructure development, tribological property improvements and electrochemical performance enhancement. GO reinforcement components were produced with required chemical performance (Section 4.1). Microstructural analysis (Sections 4.2 and 4.3) confirmed the uniform dispersion of GO within the copper matrix, resulting in significant grain refinement and enhanced layer uniformity. Furthermore, the optimisation of brush plating parameters led to the development of the GO/Cu coatings with superior tribological performance (Section 4.4), as evidenced by a reduced coefficient of friction and minimal wear under dry sliding conditions. These findings underpin the potential of the fabricated GO/Cu coatings for industrial applications requiring refined microstructure and good tribological performance.

Corrosion studies (Section 4.5) also indicated that the GO/Cu coatings provided significantly improved resistance to pitting and crevice corrosion in sodium chloride (NaCl) environments, compared to uncoated substrates. These findings clearly indicate that the aims and objectives of the research have been achieved.

Chapter 5 Discussion

5.1 Incorporation of Graphene Oxide into Copper Based Coating

5.1.1 Comparison of GO Incorporation Mechanisms in Bath and Brush Plating

As mentioned in the Literature Review section, comparing with conventional bath plating, brush plating could facilitate the incorporation of GO into metal matrix to form homogeneous composites due to the repeated brush movement during the brush plating process.

During conventional bath plating, the free energy of reaction between electrodes would decide the GO/Cu coating on certain metallic substrates, and here 316 stainless steel substrate and iron anode are used as example for discussion. As reported in Chapter 4, some functional groups were identified by FTIR (Figure 4.1.4) on the surface of graphene oxides (GO) particles, and the important component was found to be the carboxyl specie (COOH) as hydrophilic structure within GO structures [263]. It is widely reported that the GO sheets could be dissolved in polar solvent due to the hydrophilic oxidised functional group on the honeycomb structure of GO, especially the COOH group as mentioned before [264]. Within aqueous acidic electrolyte, COOH would be dissociate into COO^- and H^+. Then the GO would be deposited to the substate by electrophoretic mobility. Possible electro-chemical reactions under acidic conditions were observed on both electrodes are as follows [265,266]:

$$Anode \quad Fe = Fe^{2+} + 2e^{-} \tag{5.1.1}$$

$$2RCOO^{-} + 2H^{+} \rightleftharpoons 2RCOOH \tag{5.1.2}$$

$$Cathode \quad Cu^{2+} + 2e^{-} = Cu \tag{5.1.3}$$

$$2H^{+} + 2e^{-} = H_2(g) \tag{5.1.4}$$

With the anode reaction Equation 5.1.2, it could be seen that the negatively charged GO ($RCOO^{-}$) sheet was re-protonated and the repulsion between GO sheets were reduced, thus leading to deposition and aggregation of GO sheets at the anode. With co-deposition of Cu and GO, there would be risk of aggregation of GO sheets within and/or on the surface of the composite coating.

As described in Chapter 3 Experimental, nickel strike was conducted before final coating, the structure of the coating system formed on the 316 stainless steel should consist of a nickel strike (or nickel special) interlayer underneath the GO/Cu composite coating layer, as shown in Figure 5.1.1. The Ni strike interlayer is induced for enhancing the adhesion strength of Cu based coating on 316 stainless steels. This is because the stainless steel surface can develop a thin, dense and self-healing passivation oxides layer (Cr_2O_3), and as metal oxide, it will reduce the electrical conductivity on reaction surface [267,268]. With this Ni interlayer, the following Cu brush plating would be under better electrical conductivity. The "pill off" of Cu would not occur, compared to the Cu coating plating without Ni trike. Moreover, the key constituents of Ni strike electrolyte solution are nickel ion (Ni^{2+}) and chloride ion (Cl^{-}). The chloride ion would deplete the passivation film on the stainless steel, so that the Cu could be then brush plated on top of this Ni interlayer [1].

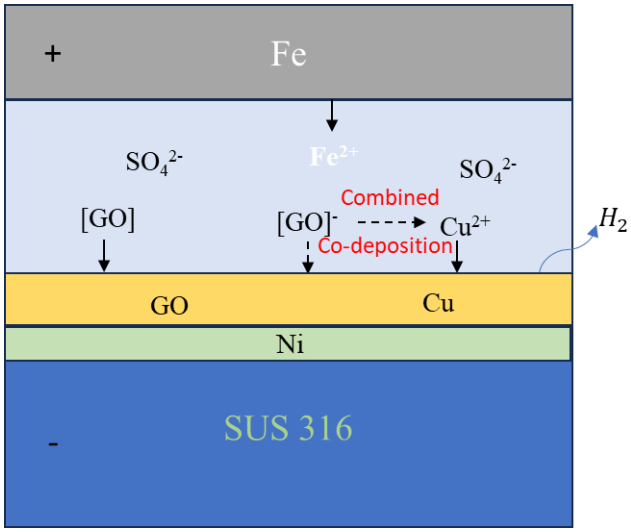


Figure 5.1.1 Electro-chemical reaction schematics on the conventional GO/Cu co-plating process with Ni interlayer.

In principle, the electrode reactions of conventional bath plating and brush plating should be the same as the electrochemical conditions are quate similar. The brush plating would normally be conducted by saturated plating solution compared to conventional bath plating. A graphene oxide sheet readily exhibits negative charges in polar solvents like water. Hence, it is likely that the copper cation would attract the $[GO]^-$, and both of them could be plated on the substrate layer-by-layer. Therefore, the GO could be brush-plated along with Cu to produce homogenous GO/Cu composite coating.

The brush plating is performed with only very small gap between the anode -the wrap sobbed with plating solution and the cathode- the substrate. Moreover, apart from the electric force, the brush plating is performed with a certain force and continuous relative movement on the brush plating surface. Comparing with conventional electro-plating, the relatively close distance between the cathode and anode would lead to less distance for the Cu and GO ions migration from the plating solution to the cathode. The movement of the brush during the brush plating process applies mechanical force, which facilitates the separation and alignment of GO sheets

as Cu is plated onto the cathode surface.

5.1.2 Successfully GO Introduction into Cu Coating on 316 Stainless Steel

In the current study, graphene oxide (GO) enhanced copper composite coating in nano scale was produced by electro brush plating on stainless steel with Ni strike interlayer. The GO was identified in the surface layer by Raman spectroscopy (Figure 4.2.8 and Figure 4.3.14), SEM and EDX (Figure 4.2.7 and Figure 4.3.4). Besides, the successful incorporated graphene oxide throughout the GO/Cu composite coating has been proved by GDOES depth profiling as indicated by the continuous existence of carbon throughout the coating (Figure 4.2.6 and Figure 4.3.17). This is further evidenced by direct observation of GO by SEM assisted by EDX at the bottom of plasma sputtered crater produced by GDOES at around 15 μm distance to the outermost surface of GO/Cu composite coating, as demonstrated in Figure 4.2.5 and Figure 4.2.6.

GO, as carbon-based matters, possesses a relatively high flexibility which would allow the GO sheets to fit into the particle boundaries of copper (Figure 4.2.5d). The GO sheets found at the GDOES crater under SEM were covered and trapped into the Cu grains. Hence, some area of GO remained in the solid composite coating on the crated surface even after plasma sputtering. As there are loads of abrupt structures on the created surface, this is one of the best pieces of evidence of successful GO incorporation into this composite coating system.

It is interesting to note that the GO sheets exposed out of the surface seem to possess several layers of GO sheets, as depicted in Figure 4.2.7c. The observations under SEM revealed that more than one layer of GO sheets was exhibited on the crater produced by argon cation (Ar^+) plasma collision. It could be observed that the GO sheets were entangled and twisted together

before they were sputtered off by the argon cation (Ar^+) plasma. It might be possible that the GO would form in the plating process as 3D networks with the nucleation, growth, and combination of copper grains. Moreover, the GO sheets found on several layers on the Cu laminate structure might suggest that the GO sheets are not just blended in some laminate of this layer-by-layer structure but could be found within each layer.

According to the literature, it is feasible that GO can be reduced by electrochemical methods to form reduced graphene oxide (rGO). It could reduce GO under an applied negative potential field [270,271], by linear sweep voltammetry (LSV) or cyclic voltammetry (CV) [272–275], or by electrophoretic deposition [276,277] as well as electroplating [278,279]. In this study on stainless steel, 4, 6 and 8 volts were inducted. The reduction of GO was identified by Raman spectroscopy on 4 volts composite coating surface, as shown in Figure 4.2.7, evidenced by reduced I_D/I_G ratio from 0.79 to 0.45. This is because with increased voltages, the reduction of GO is not as significant as the coating plated under 4 volts. For example, it has been reported that the applied potential on cathode of 0 to -0.5 V would initiate the reduction reaction of hydroxyl groups (OH), the potential between -1.0 V and -1.4 V would induce complete reduce of carboxyl groups to carbonyl groups and the final reduction would occurred under -1.6 V to -1.8 V [280,281]. However, it should be indicated that the threshold values would vary with different techniques used, and the results from this study demonstrated that the 4 volts resulted in reduction of GO to rGO. With relatively low potential, the GO is possibly reduced and applied onto the cathode stainless steel substrate.

5.1.3 The Influence of Graphene Oxide Concentration

As reported in Figure 4.2.1, featureless grey shades are exhibited in the SEM images of the pure copper control group while the GO/Cu composite coating samples present darker areas which could be caused by the incorporation of graphene oxide.

It can be seen from the calculated XRD results that the crystallite size of the brush plated coatings is influenced by the brush plating voltages and graphene oxide addition, as depicted in Figure 5.1.2. It is noted that compared with the crystallite size of the pure Cu coating the GO addition can reduce the crystallite size of the brush plated coatings. It is also interesting to note that whist for the pure Cu coating, the crystallite size increased monotonically with the plating voltage, the crystallite size of the GO/Cu coatings increased firstly when increasing the plating voltage from 3 to 5 V and then marginally decreased or flattened out when further increasing plating voltage to 6 V.

It is known from physical metallurgy theory and formation of crystalline materials that the final the crystalline size depends both on nucleation and growth, and the nucleation and crystalline growth processes are competitive interplay [282]. Therefore, the reduction of the crystalline size should be related to the effect of GO as well as the plating voltages on the nucleation and growth of the coatings.

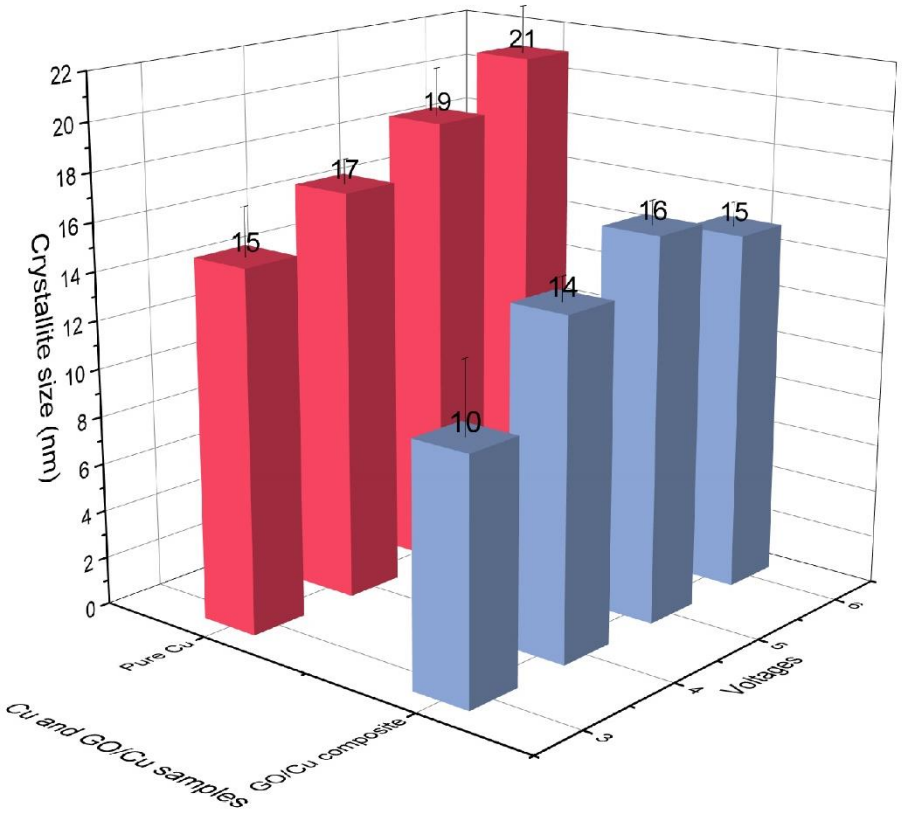


Figure 5.1.2 3D bar charts showing the effects of GO addition and brush plating voltage on the crystalline size calculated from XRD results.

The reasons for reduction in size could be attributed to three possible reasons: the nucleation promotion effect GO, the pinning effect of GO as physical barrier for the growth of Cu grains and the electrochemical effect of GO during brush plating. In the context of electrochemical deposition processes, nucleation and crystal growth are competitive processes. Specifically, a higher nucleation rate tends to result in smaller crystal formations [282–285]. Additionally, scanning electron microscopy (SEM) has provided further insights (as shown in Figure 5.1.3b), showing that Cu grains formed on the GO sheets. While the pure Cu coating control group shows no such Cu grain (Figure 5.1.3a). The GO sheet intersects the clusters of copper, and the intersection disrupts the normal growth of copper crystals and serves as a nucleation sites for the formation of new grains [286–288]. SEM observations revealed GO sheets covered on and embed in the clusters of copper, which is effectively hindered the growth of Cu crystal (Figure

5.1.3b). Hence, the concentration of GO sheets within the brush plating solution would also affect the microstructure of the plated coatings [289]. With higher GO concentration, Cu grain is refined under similar magnification as shown in Figure 5.1.3b and c because the existence of GO sheet on the plated layer would reduce the plating speed for the next layer because of the reduced electric conductivity required for the brush plating. Most probably, all these effects collectively have led to the observed refinement in grain size of the plated coatings.

Refinement of grain size is one of the mechanisms for material hardening, and hence the incorporation of GO led to increased microhardness (Figure 4.3.13). This is because GO sheets entangled with Cu grains would result in hindered movement of dislocations when they intersect those GO entangled grains. Accordingly, the coating structure and hardness are improved by the incorporation of GO phase. However, it should be pointed out that the hardness of the coatings could be influenced by some other variants; the addition of too much GO would also hinder the improvement of hardness due to the formation of a porous microstructure.

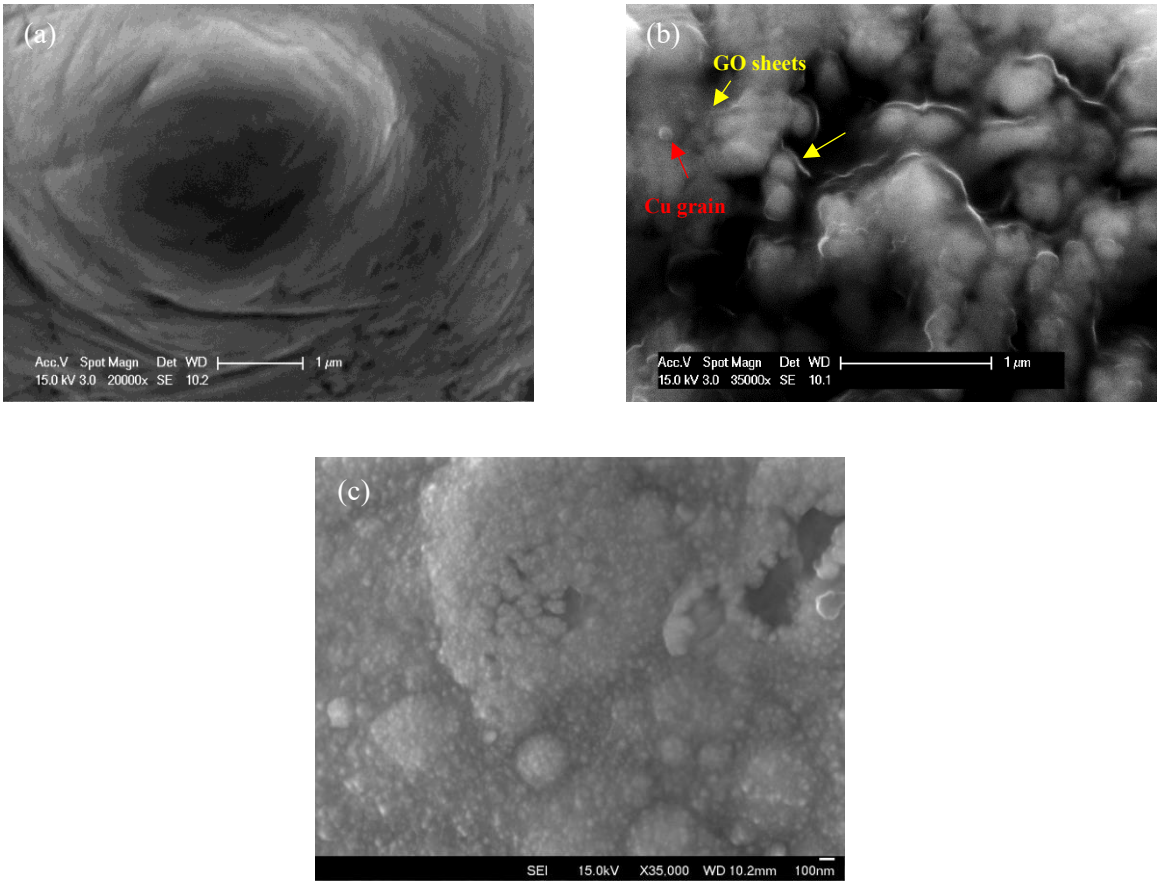


Figure 5.1.3 Surfaces of two different coating showing (a) Pure Cu coating surface, (b) GO/Cu coating with lower GO and (c) GO/Cu sample with higher GO.

5.2 Improved Tribological Properties

Tribological properties in terms of coefficient of friction (COF) and wear resistance are very important for the performance and life of Cu-based sliding bearings. Therefore, in this study, the tribological performance the GO enhanced copper composite coating obtained by electric brush plating was evaluated using a tribometer sliding against a stainless-steel ball in air. In the meantime, the corresponding pure copper control groups were also tested for a comparison. In this section, the effects of brush plating voltages and the GO concentrations on the tribological performance of the GO/Cu coatings are discussed.

5.2.1 The GO Impact on Friction Coefficient

As reported in Section 4.4, the GO/Cu composite coating developed from this research exhibited a lower coefficient of friction (COF) as compared to that for their pure Cu counterparts, as illustrated in Figure 4.4.10. With an increase in GO concentration, there is a notable reduction in the COF, especially when compared with the GO/Cu samples containing 0.2 g/L (GO4-Brass and GO5-Brass). The COF can decrease to as low as 0.26 (GO/Cu4-0.4 and GO/Cu5-0.4), in contrast to the Cu control group where the COF values are 0.45 for Cu4 and 0.5 for Cu5, nearly half that of the pure Cu samples. However, the brass substrate, an alloy of copper (Cu) and zinc (Zn) with lead (Pb) additives, demonstrates a superior COF compared to both the Cu and GO/Cu samples. This may be attributed to the addition of Pb, which, despite reducing the COF, is toxic to both animals and humans [290]. Furthermore, the wear resistance of brass is significantly inferior to that of GO/Cu coating samples, a topic that will be discussed in the next section (Section 5.2.2).

In the GO/Cu composite coating system, the effects of GO on the COF are concentration dependent. While GO confers the self-lubricating properties of the coating, it also influences the structural characteristics and surface roughness of the coating itself. As previously discussed, too much increase in GO concentration would lead to the formation of a porous structure of the coating, as depicted in Figure 4.2.4. This structural change contributed to a reduction in surface hardness, an increase in surface roughness, and then an increases in the COF [291–293]. Consequently, the addition of GO impacts the coating in two significant ways: it not only confers the self-lubricating properties but also affects the surface hardness and roughness of the copper coatings. As more GO is added, the coating becomes increasingly lubricious, although this is accompanied by a mild decrease in surface hardness (Figure 4.3.13). Hence, the best COF is not present at the highest GO concentrations in this study. The GO/Cu4-0.4 sample

presents the lowest COF. This could be owing to the exposure of GO on the surface of this sample, as the peaks on Raman spectra for GO/Cu4-0.4 are larger than that for GO/Cu4-0.2 (Figure 5.2.1).

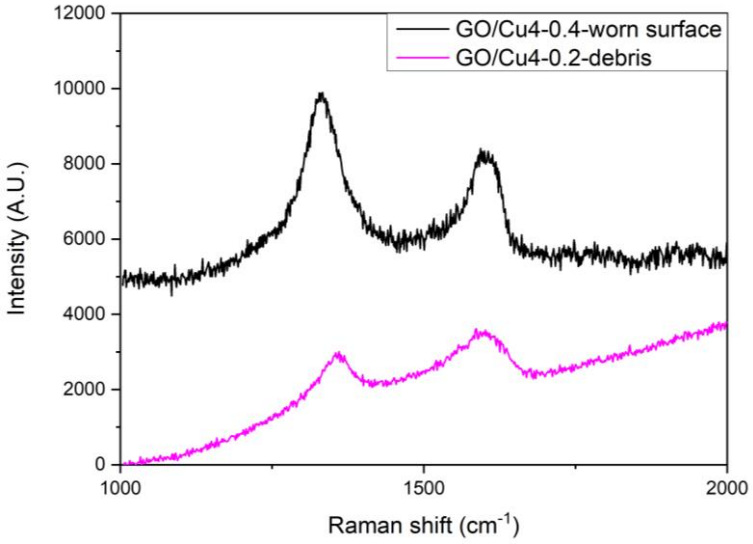


Figure 5.2.1 Raman spectroscopy on the worn track of GO/Cu4-0.4 and wear debris of GO/Cu4-0.2.

5.2.2 The Improvement of Wear

As has been reported in Section 4.4, the GO-incorporated GO/Cu samples have shown significantly improved wear resistance by 2 orders of magnitude as compared with that for the brass samples (Figure 4.4.3). Firstly, this strong improvement in the wear behaviour could be associated with the different character of plastic deformation for Cu and brass. It was reported that plastic deformation of Cu during wear is localised in thin surface layers about a few microns, while it is close to 20 μm for brass [294]. As evidenced in Figure 5.2.2a, the worn surface of brass is characterised by severe plastic deformation, which is attributed to the low stacking faults energy (14mJ/m^2) of the brass [295], and such severe plastic deformation led to the formation of thick and large wear particles, accompanied with sticking and re-adhering, and therefore to a high wear rate.

On the other hand, for the GO/Cu coatings, very shallow abrasive grooves were observed with no perceptible adhesive wear resistance features (Figure 5.2.2b). It is the thinner plastic deformation layer of the Cu than brass, combined with the nano-crystalline structure and increased harness of the Cu coatings might have contributed to the significantly improved wear resistance of the coating samples. During the sliding, when the plastic deformation concentrated within the surface layer, deformation hardening could occur within the deformed thin layer and the nanocrystalline structure served abnormal dislocation and twin originates, which made the hardening effect further and provided low wear [296]. This assumption is supported by the research of Meshs [296], who found that the friction of Cu is accompanied with a localised deformation at thin surface. This resulted in the formation of a nano-crystalline structure with an improved surface hardness and provided low wear of Cu samples.

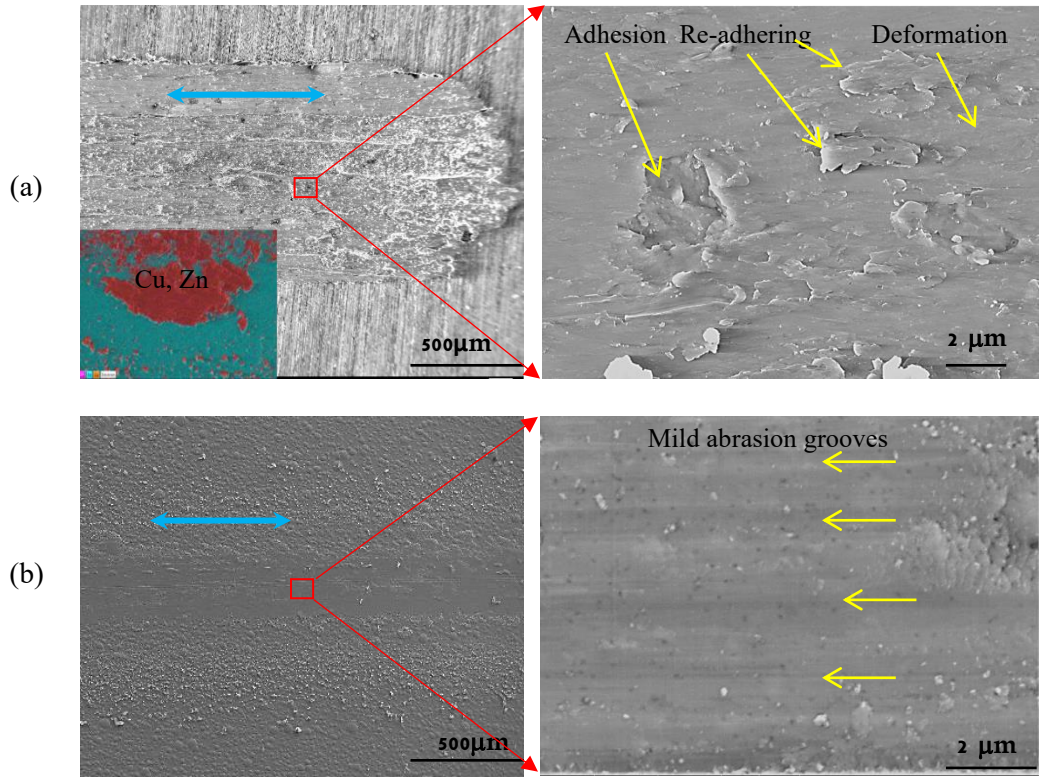


Figure 5.2.2 Typical wear tracks of brass and coating samples: (a) Brass (in insertion, EDX mapping showing brass transferred to the count-part stainless steel ball surface); (b) coating GO/Cu5. Sliding direction is shown by arrows.

Comparing the wear properties of the coating samples, the GO embedded (0.2-0.4 g/L) GO/Cu samples performed better wear resistance than the Cu coating samples (Figure 4.4.12) up to the extent of 2 times. This improvement could be attributed to the GO sheets introduced. Firstly, GO films can act as a lubricant film to partially separate the counterparts contact at the tribological testing zone and to decrease the occurrence of the adhesive wear. This is evidenced by the higher carbon content of GO/Cu5 sample than Cu5 sample in both the wear track and the wear debris areas (Figure 5.2.3a-c). This is further supported by the lower COF of most GO/Cu coatings than the corresponding Cu samples (Figure 4.4.2d and Figure 4.4.10c). Secondly, embedded GO sheets changed oxidation behaviour, or oxidative wear of the coatings during sliding. Surface morphology images coupled with chemical element analysis, as shown in Figure 5.2.3a-c, indicated lower oxygen content detected from the GO/Cu5 sample than from

the Cu5 sample, both in the wear track and in the debris areas. Raman analysis confirmed the formation of cupric oxide CuO and cuprous oxide Cu_2O [297] both in the wear track and in the debris areas of the Cu coating samples. In contrast, only low intensity peaks of cuprous oxide Cu_2O were detected for the GO/Cu5 sample (Figure 5.2.3d). This reduced oxidation behaviour of GO/Cu sample is believed to be resulted from GO films, which reduced the coefficient of friction and thus reduced the friction heat on the surface. Less oxides within the wear debris further reduced the wear loss of the GO/Cu samples.

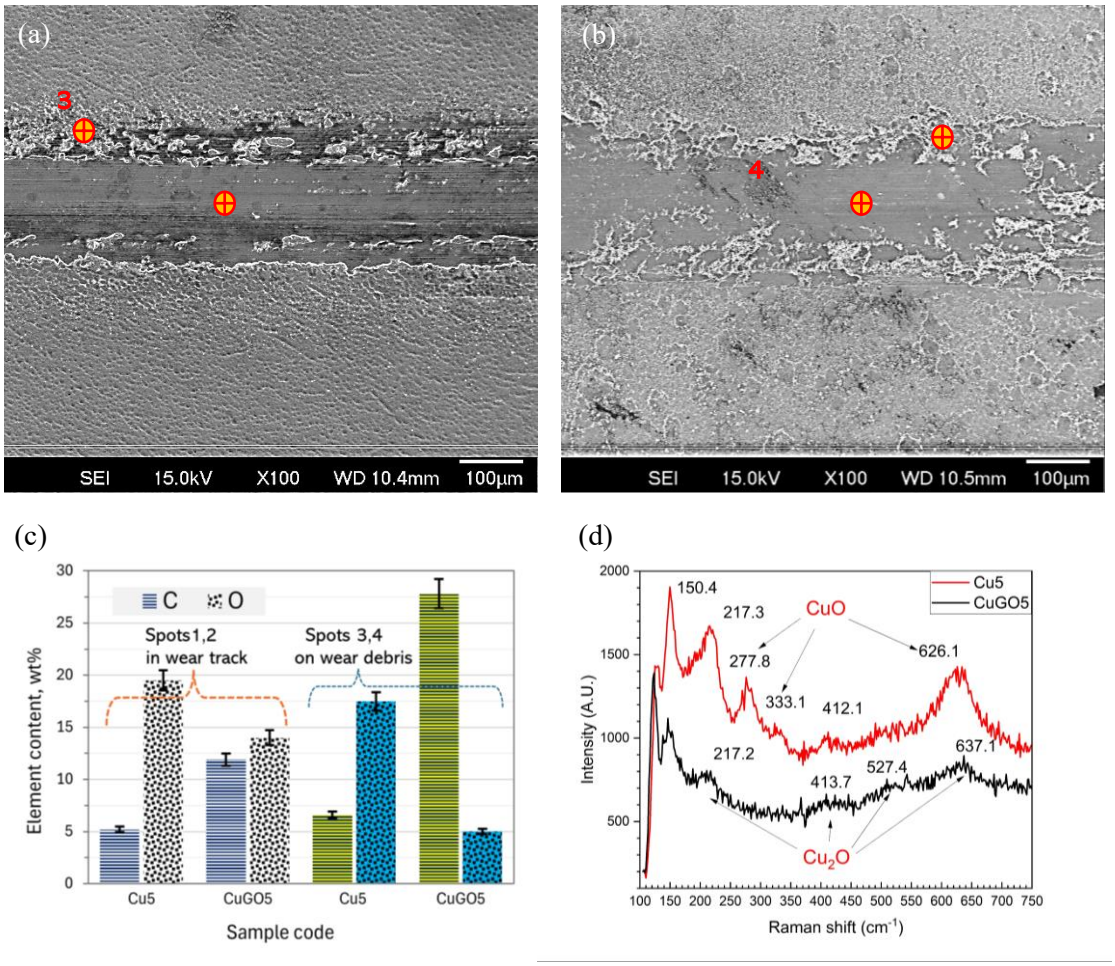


Figure 5.2.3 SEM images of wear tracks from (a) Cu5 and (b) GO/Cu5 samples. (c) EDX composition (carbon and oxygen only) analysis from wear tracks (denoted as 1, 2 in (a), (b)) and wear debris (denoted as 3, 4 in (a), (b)), and Raman spectra from wear tracks of Cu and GO/Cu5 samples.

5.2.3 Optimal Brush Plating Conditions for Wear Resistant Coatings

Wear performance refers to a material's ability to resist wear, which includes resistance to surface damage, abrasion, and the loss of material due to friction during use. It is clear from Chapter 4 that the wear performance of Cu and GO/Cu coatings produced by brush plating well performed on the brass material.

It is clear from Chapter 4 that the wear performance of Cu and GO/Cu coatings produced by brush plating well outperformed the brass material. For the GO/Cu coatings, their wear performance is related to the brush plating voltage and the amount of GO additions in the Cu plating solution. From processing voltage point of view, the 5 V processed coatings plated with 0.2 g/L GO solution possess the lowest wear volume loss (Figure4.4.4). When GO/Cu coatings are produced under this optimal processing voltage of 5 V, the wear performance of the coatings is related to the GO quantity in the coatings. A low quantity (0.2-0.4g/L) of GO addition to Cu coatings can enhance their wear performance. Further increase of the GO to above 0.4g/l in Cu solution leads to reduced wear resistance (Figure 4.4.12). This may be related to the quality of the coatings. As the GO sheets are embedded within the lamellar layers (Figure 5.2.4), when too many GO films are introduced, the bounding between the GO films is loosely connected, which will reduce the integrity of the coatings, resulting in severe wear loss. To sum up, for the best wear resistant Cu coatings, the optimum brush plating conditions are at 5V with GO addition at the concentration of 0.2-0.4g/L in the plating solution.

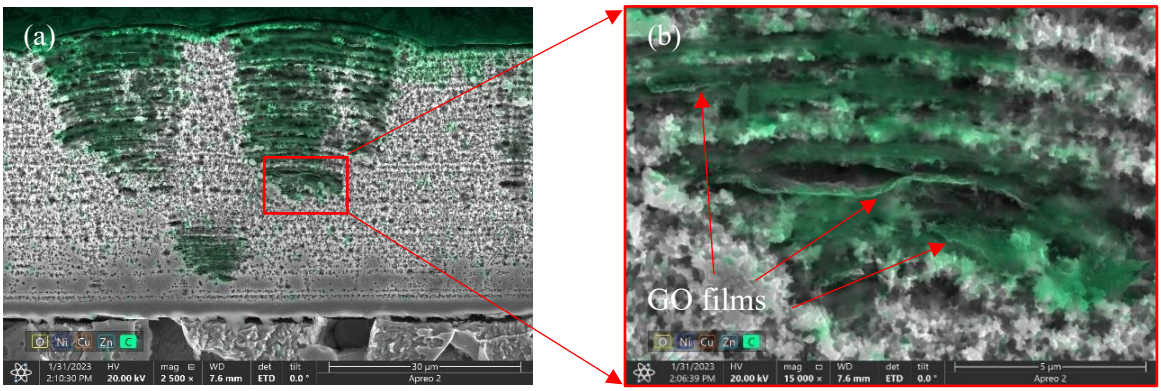


Figure 5.2.4 Typical SEM images of (a) well-developed columnar structures of GO/Cu samples showing (b) GO within the lamellar layers.

5.2.4 Wear Mechanisms

As discussed in Chapter 2, few-layers graphene (Gr) and graphene oxide (GO) are reported as having self-lubricate properties, owing to the laminate honeycomb structure with Lorentz force [298–302]. It has been reported that graphene addition to steel [298] and Ni [146] can reduce their friction and e wear. This study has demonstrated that the addition of a small amount of graphene oxide to Cu can improve the tribological properties of Cu-based coatings and potential friction and wear reduction mechanisms are discussed in this section.

As evidenced in Figure 5.2.5, GO sheets were embedded in copper oxide particles produced by the sliding of 316 stainless steel counter ball. These GO sheets could act as a friction-reducing shield due to their self-lubricate properties, thus minimizing the friction between the 316 stainless steel counter ball and the coating surface. In addition, the GO induced effective friction reduction (Figure 4.4.10) would simultaneously lower the local temperature of the asperities on the wear track because of the reduced friction-induced heat. Consequently, the oxidation of Cu is reduced in the GO/Cu samples, as indicated by the Raman spectra taken from the worn Cu5 and GO/Cu5 samples (Figure 5.2.3d). The spectra revealed that only cuprous oxide (Cu_2O) is produced on the worn GO/Cu5 samples, whilst cupric oxide (CuO) was identified from the

worn Cu5 track surface.

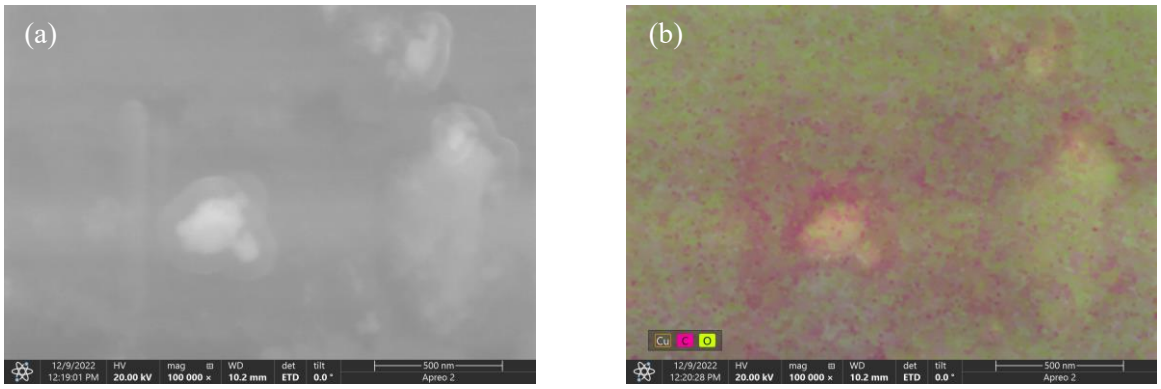


Figure 5.2.5 The graphene oxide performed as lubricants on the middle of the wear track on GO/Cu5-0.2.

Based on the discuss above, the wear mechanisms for pour Cu coating and GO enhanced CU composite coating are proposed schematically in Figure 5.2.6. As shown in Figure 5.2.6a, the Cu coating consists of laminated Cu layers, typical feature of brush plated coatings. The sliding of the austenitic stainless ball will introduce huge amount of frictional heat and as illustrated in Figure 5.2.6b due to the high flash temperature at the asperities in real contact with the counterpart ball the pure Cu control group samples would suffer aggressive oxidation to form a CuO surface film. Irregular CuO particles would be formed (Figure 5.2.6c) as the wear test continues. Those particles would perform as abrasives, to cut into the wear track through the laminar structured Cu forming severe three-body abrasive wear (Figure 5.2.6a).

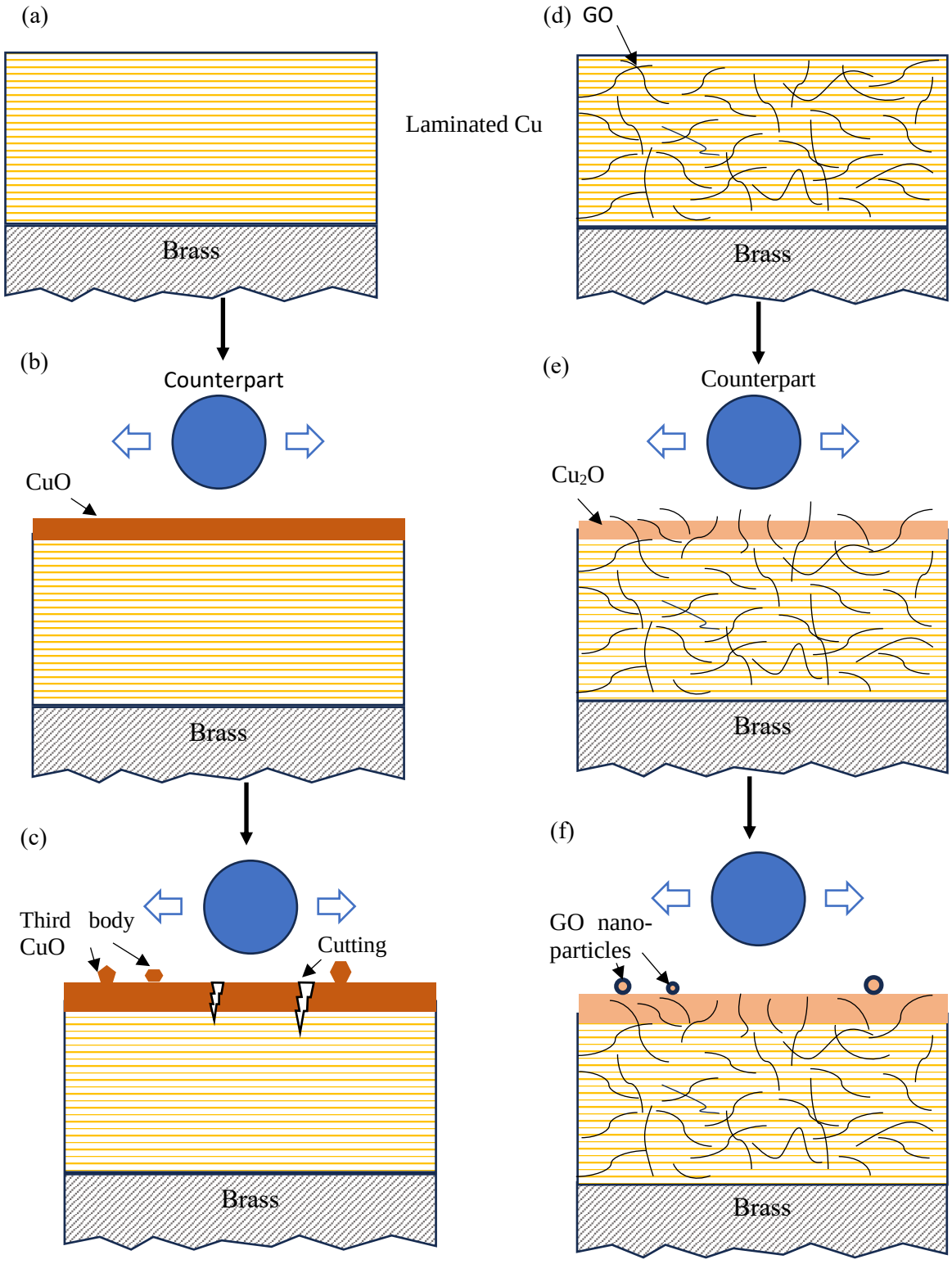


Figure 5.2.6 Schematics of wear mechanisms on (a-c) pure Cu coating and (d-f) GO enhanced Cu composite coating.

On the other hand, the GO sheets within the GO/Cu composite coating are mostly entangled and twisted within the laminated Cu coating (Figure 5.2.6d). As revealed by Raman study, Cu2O was formed in the wear track in GO/Cu sample and the formation of a c Cu_2O film (Figure 5.2.6e) would benefit the friction and wear by reducing the metal-metal direct contact [303,304]. With continuing sliding, the previously mentioned GO shielding for the outmost area, along with the thickening of Cu_2O layer (Figure 5.2.6f) can protect the surface of GO/CU sample from wear. This is supported by the observation of the wear track where a black tribo-layer was formed (Figure 4.4.15). Hence, the friction and wear of GO/Cu composite coatings can be significantly reduced as compared with pure Cu coating.

5.3 Corrosion Protection

As reported in Section 4.5, the GO/Cu composite coatings present better corrosion resistance than brass substrate. This would benefit from the excellent impermeability of graphene and graphene oxide on their perpendicular direction [305–307]. As proved before, the GO sheets are mainly arranged along the laminar structure of Cu. Hence, the GO sheets in Cu matrix could be beneficial for corrosion protection of Cu-based materials.

5.3.1 GO concentrations Impact on Corrosion Behaviour

As shown in Section 4.5, the GO/Cu coatings present outstanding corrosion protection properties in terms of much more positive corrosion potentials and decreased corrosion current densities (Table 4.5.1), compared with bare brass. In contrast, t severe pitting corrosion and galvanic corrosion occurred to brass surface in 3.5 wt.% of NaCl solution, as depicted in Figure 5.3.1a as evidenced by several pits and larger corrosion holes possibly penetrated into the subsurface. The etching-like finish of galvanic corrosion is mainly due to the cell reactions

between Cu and Zn components during the corrosion test [308].

As schematically shown in Figure 5.2.6, the GO/Cu composite coatings consist of individual small GO sheets, the influences of small GO sheets on corrosion would differ from continuous GO film. The GO/Cu composite coatings developed from this research can still exhibit localised corrosion, penetrating into certain areas to specific depths because the surface does not fully cover with a continuous GO film. GO sheets oriented perpendicular to the direction of corrosion could prevent or retard further penetration of the NaCl solution, thereby hindering the progression of corrosion in the GO/Cu coating due to the well-documented impermeability of graphene.

For instance, the GO/Cu5-0.4 sample does not exhibit pits; instead, a protective film prevents the penetration of the corrosion inhibitor, as shown in Figure 5.3.1b. The GO sheets are observed (as indicated by the red arrows) due to the characteristic GO featured ripple structure whereas severe localised corrosion at the edge of GO sheets occurred. The GO concentration would impact the corrosion resistance. Firstly, the lack of sufficient amount of GO component cannot ultimately protect the coating from pitting. Therefore, the corrosion protection would initially increase with GO concentration. Then, the largest addition of GO does not necessarily provide the best corrosion protect, as evidenced by small pitting shown in Figure 5.3.1c. This is probably because layer-by-layer stacking of GO sheets can lead to a lack of adhesive strength in the coating structure, resulting in the formation of porous structures. The remaining corrosion inhibitor would penetrate through those pores. Specifically, pores near the edges of GO sheets can create a Cu/graphene galvanic cell, leading to severe localised corrosion.

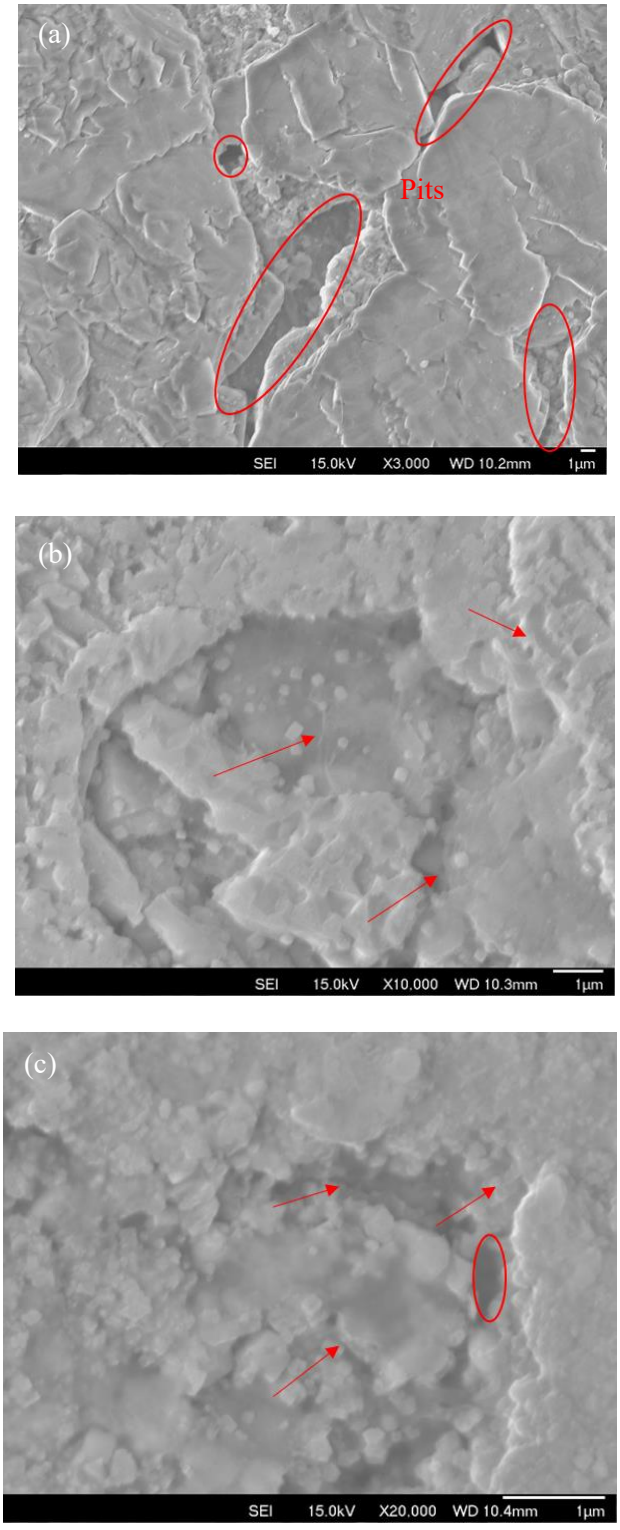


Figure 5.3.1 Corrosion situation of (a) brass substrate, (b) GO/Cu composite coating of GO/Cu5-0.4 and (c) GO/Cu5-0.8 sample.

5.3.2 Influence of Brush Plating Voltage on Corrosion

As mentioned above, the GO/Cu samples with a GO concentration of 0.6 g/L exhibit the greatest corrosion prevention ability, as observed under SEM. Therefore, this concentration is selected to discuss the influence of brush plating voltage on the corrosion resistance between the GO/Cu4 and GO/Cu5 samples (Figure 5.3.2a). It is evident from the potentiodynamic curves that the GO/Cu5 sample is positioned at a slightly higher potential and demonstrates a significantly lower current density, approximately one order of magnitude smaller. Furthermore, the corrosion potential of GO/Cu5-0.6 is slightly higher, and its corrosion current density is lower compared to GO/Cu4-0.6. Notably, the current density of GO/Cu5-0.6 remains lower at the final stage of corrosion, indicating better corrosion resistance.

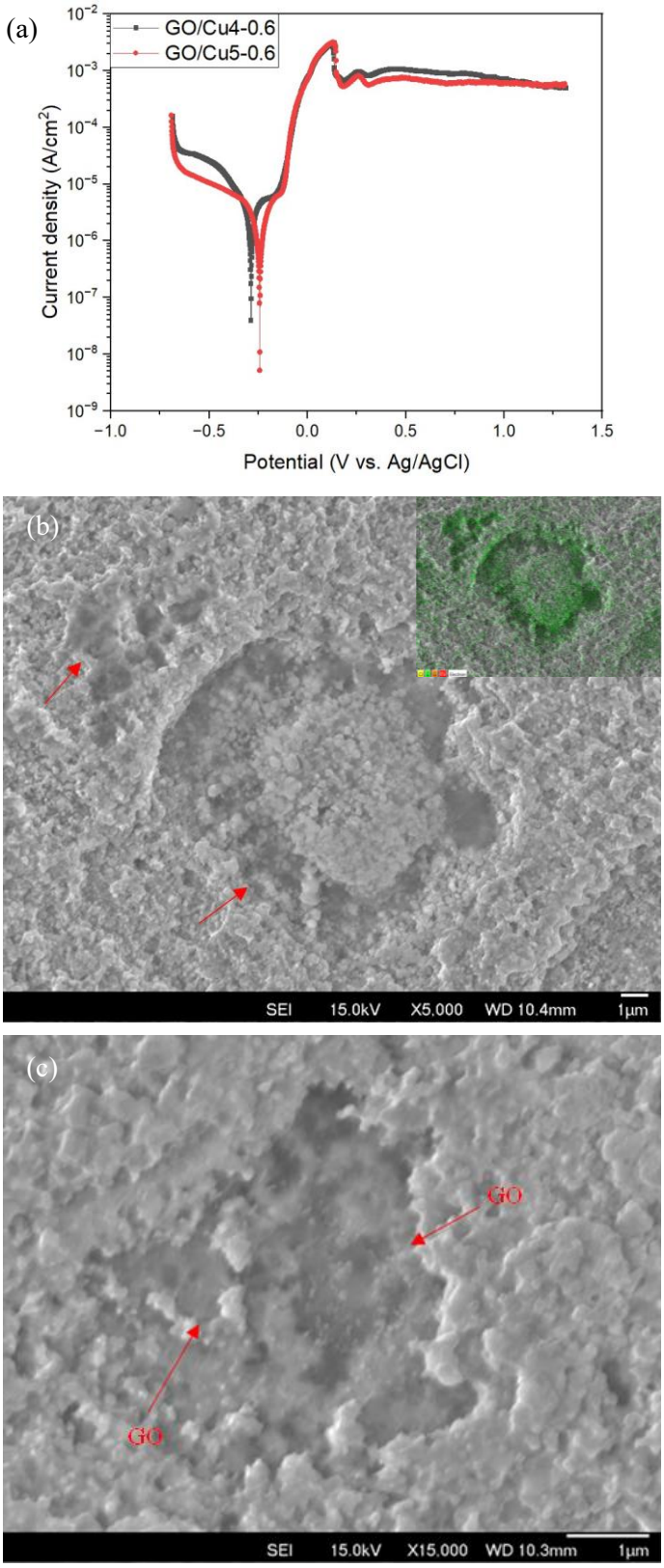


Figure 5.3.2 (a) Potentiodynamic polarisation curves of GO/Cu samples deposited with 0.6 g/L GO concentrations and corroded surface of (b) GO/Cu4-0.6 and (c) GO/Cu5-0.6.

Figure 5.3.2b and c illustrate the sample surface of GO/Cu4-0.6 and GO/Cu5-0.6 after corrosion tests. GO sheets are indicated in red arrows at the middle of those two SEM images, which is further proved by carbon rich region indicated in green at the right corner of Figure 4.3.2b for GO/Cu4-0.6. It is possible that the GO sheets exposed by corrosion process would have hindered the further corroding of the coating. To compare, the GO sheets exposure of GO/Cu4-0.6 is much larger than that of GO/Cu5-0.6. Besides, the corrosion surface of GO/Cu4-0.6 seems much severe than that on the corroded GO/Cu5-0.6 surface.

It is evident that the corrosion resistance of the GO/Cu4 and GO/Cu5 samples is significantly better than that of brass. Within the GO/Cu coatings, their corrosion resistance is influenced by the brush plating voltage and the GO concentration in the Cu plating solution. Considering the processing voltage, samples plated at 5 V exhibit higher corrosion potential and lower current density (Table 4.5.1), as well as less corrosion observed under SEM (Figure 5.3.2). When the processing voltage is fixed at the optimal level, the corrosion performance varies with GO concentrations (0.2-0.8 g/L). The GO/Cu5-0.8 sample shows the highest corrosion potential and the lowest current density, indicating optimal performance. However, GO/Cu5-0.6 demonstrates the lowest current density at the final stage of corrosion. Additionally, SEM images (shown in the Results section) indicate that the best results are achieved with 0.6 g/L GO. This may be related to the porous surface structure produced when excessive GO sheets are introduced. The weaker connections between GO sheets, compared to Cu bonds, can create voids and vacancies. These voids may lead to severe localized corrosion in the composite coating. Overall, the optimal brush plating condition for corrosion resistance is achieved with the GO/Cu5-0.6 sample.

5.3.3 Corrosion Mechanisms for GO/Cu Composite Coating

Based on discussion mentioned above, different corrosion mechanisms for brass and graphene oxide sample are proposed as schematically shown in Figure 5.3.3. Owing to the extreme thin nature of GO, GO sheets could be fitted within the laminar of layered Cu. The alignment of GO sheets could confer corrosion protection. In addition to previously stated GO impermeability, it is possible that GO could be helpful for surface corrosion prevention.

Figure 5.3.3a depicts the schematic of corrosion of brass. As described in Chapter 3, the brass is consisted of Cu, Zn and small amount of Pb. When immersing the brass into solution contained Cl^-, Zn would be dissolved into inhibitor. Hence, there would be oxidation reaction occurring near the Cu component and OH^- would be produced. Hence, there would be Cu^{2+}, Zn^{2+}, Cl^- and OH^- that participated in the corrosion product produced during corrosion. According to the EDX mapping results of corrosion products (Figure 4.5.4), it is highly possible that copper hydroxide chloride (Cu(OH)Cl) was produced. The depletion of Zn would leave a hole where Zn had once existed, and pitting would initiate from those areas (Figure 5.3.3a).

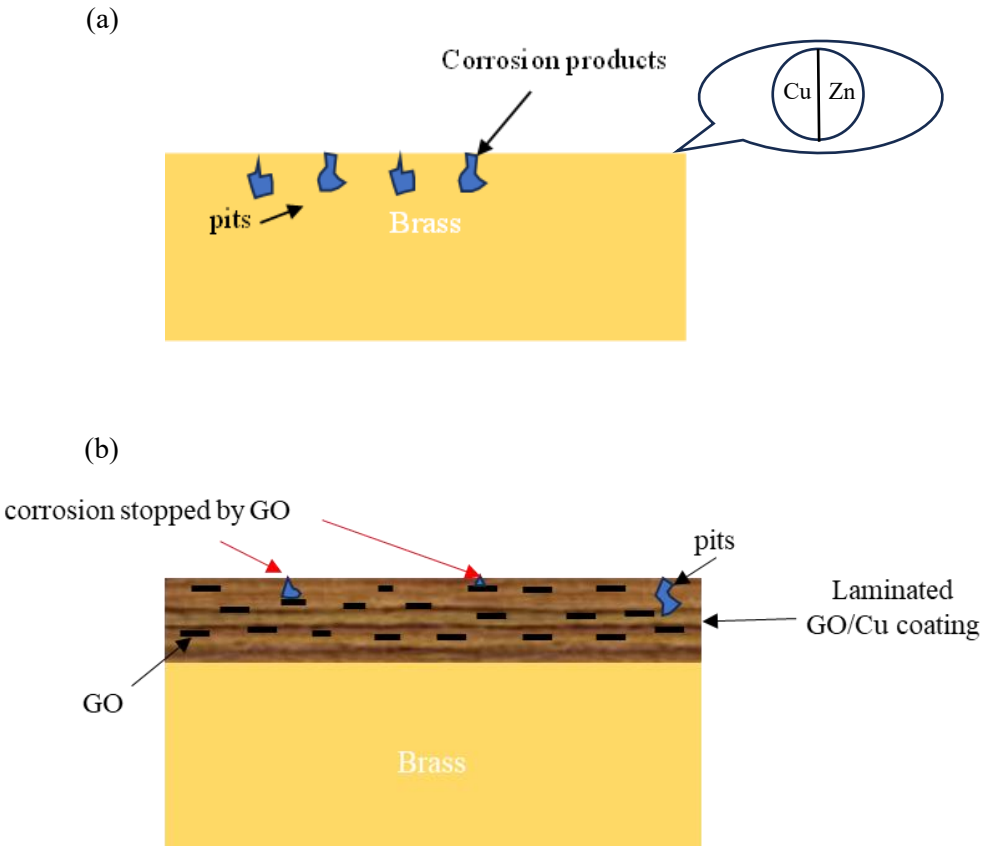


Figure 5.3.3 Schematics of the corrosion mechanism for (a) brass and (b) GO/Cu composite coating.

The GO sheets, acting as an impermeable component, tend to align parallel with the Cu layers (Figure 5.3.3b). On the surface of the GO/Cu composite coating, only the pure Cu component is susceptible to uniform corrosion. With relatively small amounts of GO sheets, the corrosion solution can still penetrate through and continue corroding if it does not encounter with GO sheets at the outermost region (Figure 5.3.4a), leading to potential pitting. However, with the addition of GO, the likelihood of pitting decreases due to the protective barrier provided by the GO sheets. Hence, it seems reasonable to assume that the more GO added, the less the pitting to occur. Nevertheless, there is an optimal amount of GO that can be beneficial. Indeed, excessive GO can lead to the formation of a porous structure (Figure 5.3.4b), which can also facilitate pitting through these porous regions. Therefore, while the addition of GO can enhance corrosion resistance, the amount of GO must be carefully controlled to avoid compromising the

integrity of the composite coating.

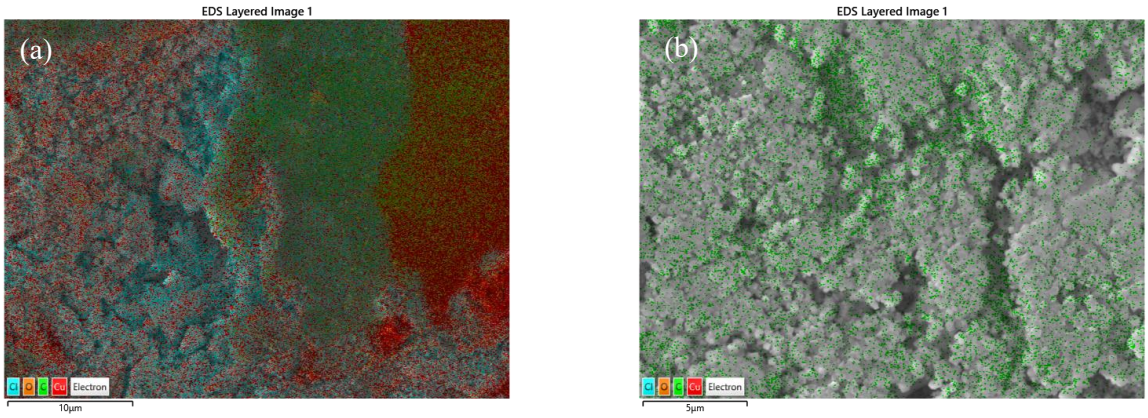


Figure 5.3.4 Corroded surface of GO/Cu samples with colour-chem image with (a) 0.2 g/L and (b) 0.8 g/L of GO.

5.4 Summary of Discussion

In this chapter, the synthesis of the main findings related to the fabrication, performance, and potential mechanisms of GO reinforcement in tribological, and corrosion performance are discussed to advance scientific understanding. The preparation of coatings, the possible electrochemical reactions and the reasons that led to the successful incorporation of GO into the composite system were discussed first (Section 5.1). This is followed by the discussion of improved tribological properties in terms of the impact of GO on COF and wear reduction mainly due to GO promoted self-lubrication mechanisms (Section 5.2). Additionally, the mechanism of corrosion protection for GO/Cu composite coatings is also explored (Section 5.3).

Chapter 6 Conclusions and Future Work

6.1 Conclusions

In this study, a cost-effective and scalable GO-based composite coating system has been successfully developed using the electro-brush plating (EBP) technique on stainless steel and brass substrates. Comprehensive microstructural characterisation and analysis of properties was conducted using a wide range of materials research methods. The mechanical, tribological and corrosion properties of the GO/Cu composite coatings were evaluated; and the mechanisms involved have been investigated. The key findings derived from the results and discussion are summarised as follows:

Part I – Feasibility and Fabrication of GO/Cu Composite Coatings

1. It is feasible to introduce GO into copper to develop novel GO/Cu composite coatings using cost-effective and highly flexible electro-brush plating (EBP) technique on both 316 stainless steel and brass substrates.

Part II – Microstructure and Mechanical Properties

2. Graphene oxide (GO) can be uniformly incorporated into the copper matrix, forming the GO/Cu composite coating. The electro-brush plating (EBP) technique has been proved effective in producing thick and compact coatings, with the ability to adjust the GO content through varying ratios of additions.
3. The presence of graphene oxide (GO) on the outermost surface and at various depths

within the GO/Cu coating was confirmed through a range of characterisation techniques, which provided insights into the surface structure, internal composition, and distribution of graphene within the coating.

4. The average crystalline size of the nano-scaled copper matrix was reduced under most of the applied parameters. This refinement of the copper matrix resulted in enhanced mechanical strength, attributed to the grain refinement and the pinning effects by the graphene sheets.
5. The fabrication of GO/Cu coatings with consistent and reliable thickness as well as relatively strong bonding to the substrate can be achieved by optimising the deposition parameters. For practical applications, the thickness of high-quality GO/Cu composite coatings can exceed 19.2 μm.

Part III – Enhanced Tribological Properties

6. The GO/Cu composite coatings produced under 5V (GO/Cu5) and 6V (GO/Cu6) can improve the friction property of copper mainly due to the self-lubricating of the GO added into the coatings. The wear of GO/Cu coatings can effectively reduce by two orders of magnitude as compared with brass.
7. The GO concentrations ranging from 0.2 g/L to 0.8 g/L led to variations in both the layer thickness and porosity of the coatings. Among these concentrations, 0.4 g/L and 0.6 g/L demonstrated more favourable structural characteristics, providing an optimal balance between coating thickness and quality.
8. The incorporation of GO reinforcements altered the wear mechanism from plasticity-dominated severe adhesive wear and galling to oxidation-dominated mild wear. Hence, the novel GO/Cu coatings are possibly utilised as self-lubricating and wear resistant

coatings for tribological applications.

Part IV – Improved Corrosion Performance

9. The GO/Cu composite coating significantly enhanced the corrosion resistance of the brass substrate, resulting in a reduction of corrosion current by over 90% and an improvement in corrosion potential by approximately 60%.
10. The incorporation of graphene forms a discontinuous impermeable membrane within the GO/Cu composite coating, effectively repelling corrosive solutions from penetrating the main body of the coating. However, as the GO fraction increases, the coating becomes less dense, and the resulting porosity can lead to pitting in these areas. The GO/Cu5-0.6 composition demonstrated the optimal corrosion resistance, striking a balance between the protective graphene membrane and the porosity induced by higher graphene content.

6.2 Proposed Future Work

This study has successfully established the feasibility of fabricating GO/Cu coatings on metallic surfaces through cost-effective EBP technique. Additionally, the research has provided important insights into how graphene enhances material properties, including its role in strengthening and improving tribological properties and corrosion resistance. The GO/Cu composite coating produced by the EBP technique is optimised by tailored brush plating voltages and GO concentrations. Building on the findings and insights gained from these results, the following two areas are proposed for further investigation:

Evaluation of further potential applications:

In this study, the tribological and corrosion properties of the GO/Cu composite coating have been investigated. However, beyond these tribological applications discussed, the GO/Cu composite coatings are expected to have significant potential in electrochemical applications, including high-voltage power transmission and electric-thermal applications. Further exploration of these areas could realise the full potential for wider applicability of the GO/Cu coatings developed.

Further exploration on ceramic reinforced component of GO composite coating systems:

In this study, the feasibility of the brush plating technique has been demonstrated for the deposition of electrically conductive and semi-conductive components onto electrically conductive substrates. Graphene oxide (GO) was explored as a reinforcement in this process, and further investigations could extend to other semi-conductive reinforcements. For instance, ceramics such as Al_2O_3 [309], which can be produced via electrochemical oxidation reactions,

show potential for co-deposition with GO. Exploring the synergistic effects of such combinations on the mechanical, chemical and tribological performance of the composites coatings would be a valuable avenue for future research.

Reference

[1] K.S. Novoselov, S.V. Morozov, T.M.G. Mohinddin, L.A. Ponomarenko, D.C. Elias, R. Yang, I.I. Barbolina, P. Blake, T.J. Booth, D. Jiang, J. Giesbers, E.W. Hill, A.K. Geim, Electronic properties of graphene, Phys. Status Solidi B 244 (2007) 4106–4111. https://doi.org/10.1002/pssb.200776208.

[2] K.S. Novoselov, V.I. Fal′ko, L. Colombo, P.R. Gellert, M.G. Schwab, K. Kim, A roadmap for graphene, Nature 490 (2012) 192–200. https://doi.org/10.1038/nature11458.

[3] S.-E. Zhu, S. Yuan, G.C.A.M. Janssen, Optical transmittance of multilayer graphene, Europhys. Lett. 108 (2014) 17007. https://doi.org/10.1209/0295-5075/108/17007.

[4] C. Lee, X. Wei, J.W. Kysar, J. Hone, Measurement of the Elastic Properties and Intrinsic Strength of Monolayer Graphene, Science 321 (2008) 385–388. https://doi.org/10.1126/science.1157996.

[5] M.A. Giambra, V. Mišeikis, S. Pezzini, S. Marconi, A. Montanaro, F. Fabbri, V. Sorianello, A.C. Ferrari, C. Coletti, M. Romagnoli, Wafer-Scale Integration of Graphene-Based Photonic Devices, ACS Nano 15 (2021) 3171–3187. https://doi.org/10.1021/acsnano.0c09758.

[6] I. Fakih, O. Durnan, F. Mahvash, I. Napal, A. Centeno, A. Zurutuza, V. Yargeau, T. Szkopek, Selective ion sensing with high resolution large area graphene field effect transistor arrays, Nat. Commun. 11 (2020) 3226. https://doi.org/10.1038/s41467-020-16979-y.

[7] J. Sengupta, C.M. Hussain, Graphene-based field-effect transistor biosensors for the rapid detection and analysis of viruses: A perspective in view of COVID-19, Carbon Trends 2 (2021) 100011. https://doi.org/10.1016/j.cartre.2020.100011.

[8] M. Dadashbeik, D. Fathi, M. Eskandari, Design and simulation of perovskite solar cells based on graphene and TiO2/graphene nanocomposite as electron transport layer, Sol. Energy 207 (2020) 917–924. https://doi.org/10.1016/j.solener.2020.06.102.

[9] D. Berman, A. Erdemir, A.V. Sumant, Graphene: a new emerging lubricant, Mater. Today 17 (2014) 31–42.

[10] M. Boopathi, S. Shankar, S. Manikandakumar, R. Ramesh, Experimental Investigation of Friction Drilling on Brass, Aluminium and Stainless Steel, Procedia Eng. 64 (2013)

1219–1226. https://doi.org/10.1016/j.proeng.2013.09.201.

[11] P.K. Rohatgi, S. Ray, Y. Liu, Tribological properties of metal matrix-graphite particle composites, Int. Mater. Rev. 37 (1992) 129–152. https://doi.org/10.1179/imr.1992.37.1.129.

[12] H. Liang, J.-M. Martin, R. Lee, Influence of oxides on friction during Cu CMP, J. Electron. Mater. 30 (2001) 391–395. https://doi.org/10.1007/s11664-001-0049-4.

[13] S. Shahnazar, S. Bagheri, S.B. Abd Hamid, Enhancing lubricant properties by nanoparticle additives, Int. J. Hydrog. Energy 41 (2016) 3153–3170. https://doi.org/10.1016/j.ijhydene.2015.12.040.

[14] M. Asrul, N.W.M. Zulkifli, H.H. Masjuki, M.A. Kalam, Tribological Properties and Lubricant Mechanism of Nanoparticle in Engine Oil, Procedia Eng. 68 (2013) 320–325. https://doi.org/10.1016/j.proeng.2013.12.186.

[15] W. Dai, B. Kheireddin, H. Gao, H. Liang, Roles of nanoparticles in oil lubrication, Tribol. Int. 102 (2016) 88–98. https://doi.org/10.1016/j.triboint.2016.05.020.

[16] H. Tan, Y. Guo, D. Wang, Y. Cui, The development of a Cu@Graphite solid lubricant with excellent anti-friction and wear resistant performances in dry condition, Wear 488–489 (2022) 204181. https://doi.org/10.1016/j.wear.2021.204181.

[17] Y. Liu, Application of graphene oxide in water treatment, in: IOP Conf. Ser. Earth Environ. Sci., IOP Publishing, 2017: p. 012060.

[18] Y. Raghupathy, A. Kamboj, M.Y. Rekha, N.N. Rao, C. Srivastava, Copper-graphene oxide composite coatings for corrosion protection of mild steel in 3.5% NaCl, Thin Solid Films 636 (2017) 107–115.

[19] A.K. Behera, A. Mallik, Ultrasound assisted electroplating of nano-composite thin film of Cu matrix with electrochemically in-house synthesized few layer graphene nano-sheets as reinforcement, J. Alloys Compd. 750 (2018) 587–598.

[20] S. Qi, X. Li, Z. Zhang, H. Dong, Fabrication and characterisation of electro-brush plated nickel-graphene oxide nano-composite coatings, Thin Solid Films 644 (2017) 106–114.

[21] K.S. Novoselov, A.K. Geim, S.V. Morozov, D. Jiang, Y. Zhang, S.V. Dubonos, I.V. Grigorieva, A.A. Firsov, Electric Field Effect in Atomically Thin Carbon Films, Science 306 (2004) 666–669. https://doi.org/10.1126/science.1102896.

[22] P.R. Wallace, The Band Theory of Graphite, Phys. Rev. 71 (1947) 622–634. https://doi.org/10.1103/PhysRev.71.622.

[23] M.I. Katsnelson, Graphene: carbon in two dimensions, Mater. Today 10 (2007) 20–27. https://doi.org/10.1016/S1369-7021(06)71788-6.

[24] N.D. Mermin, Crystalline Order in Two Dimensions, Phys. Rev. 176 (1968) 250–254. https://doi.org/10.1103/PhysRev.176.250.

[25] SITNFlash, Graphene: The coolest material that shouldn't exist, Sci. News (2011). https://sitn.hms.harvard.edu/flash/2011/graphene-the-coolest-material-that-shouldnt-exist/ (accessed July 19, 2024).

[26] N.D. Mermin, Crystalline Order in Two Dimensions, Phys. Rev. 176 (1968) 250–254. https://doi.org/10.1103/PhysRev.176.250.

[27] H.P. Boehm, A. Clauss, U. Hofmann, GRAPHITE OXIDE AND ITS MEMBRANE PROPERTIES, J. Chim. Phys. Fr. Merged Rev Gen Colloides Form J Chim Phys Rev Gen Colloides Vol: 58 (1961). https://www.osti.gov/biblio/4061342 (accessed July 29, 2024).

[28] H.-P. Boehm, Graphene—How a Laboratory Curiosity Suddenly Became Extremely Interesting, Angew. Chem. Int. Ed. 49 (2010) 9332–9335. https://doi.org/10.1002/anie.201004096.

[29] Z. Liu, X. Zhou, Graphene: Energy Storage and Conversion Applications, CRC Press, 2014.

[30] H.P. Boehm, R. Setton, E. Stumpp, Nomenclature and terminology of graphite intercalation compounds, Carbon 24 (1986) 241–245. https://doi.org/10.1016/0008-6223(86)90126-0.

[31] D.R. Dreyer, R.S. Ruoff, C.W. Bielawski, From Conception to Realization: An Historial Account of Graphene and Some Perspectives for Its Future, Angew. Chem. Int. Ed. 49 (2010) 9336–9344. https://doi.org/10.1002/anie.201003024.

[32] H.-P. Boehm, E. Stumpp, Citation errors concerning the first report on exfoliated graphite, Carbon 45 (2007) 1381–1383. https://doi.org/10.1016/j.carbon.2006.12.016.

[33] M. Noel, R. Santhanam, Electrochemistry of graphite intercalation compounds, J. Power Sources 72 (1998) 53–65. https://doi.org/10.1016/S0378-7753(97)02675-X.

[34] K.S. Novoselov, A.K. Geim, S.V. Morozov, D. Jiang, Y. Zhang, S.V. Dubonos, I.V. Grigorieva, A.A. Firsov, Electric Field Effect in Atomically Thin Carbon Films, Science 306 (2004) 666–669. https://doi.org/10.1126/science.1102896.

[35] J.C. Meyer, A.K. Geim, M.I. Katsnelson, K.S. Novoselov, T.J. Booth, S. Roth, The structure of suspended graphene sheets, Nature 446 (2007) 60–63. https://doi.org/10.1038/nature05545.

[36] M.J. Allen, V.C. Tung, R.B. Kaner, Honeycomb Carbon: A Review of Graphene, Chem. Rev. 110 (2010) 132–145. https://doi.org/10.1021/cr900070d.

[37] Y. Bleu, F. Bourquard, T. Tite, A.-S. Loir, C. Maddi, C. Donnet, F. Garrelie, Review of Graphene Growth From a Solid Carbon Source by Pulsed Laser Deposition (PLD), Front. Chem. 6 (2018). https://doi.org/10.3389/fchem.2018.00572.

[38] L.E.F.F. Torres, S. Roche, J.-C. Charlier, Introduction to Graphene-Based Nanomaterials: From Electronic Structure to Quantum Transport, Cambridge University Press, 2014.

[39] D.R. Cooper, B. D'Anjou, N. Ghattamaneni, B. Harack, M. Hilke, A. Horth, N. Majlis, M. Massicotte, L. Vandsburger, E. Whiteway, V. Yu, Experimental Review of Graphene, Int. Sch. Res. Not. 2012 (2012) 501686. https://doi.org/10.5402/2012/501686.

[40] G. Yang, L. Li, W.B. Lee, M.C. Ng, Structure of graphene and its disorders: a review, Sci. Technol. Adv. Mater. 19 (2018) 613–648. https://doi.org/10.1080/14686996.2018.1494493.

[41] A.R. Urade, I. Lahiri, K.S. Suresh, Graphene Properties, Synthesis and Applications: A Review, JOM 75 (2023) 614–630. https://doi.org/10.1007/s11837-022-05505-8.

[42] J.H. Warner, F. Schaffel, M. Rummeli, A. Bachmatiuk, Graphene: Fundamentals and Emergent Applications, Newnes, 2012.

[43] Y. Kim, J. Lee, M.S. Yeom, J.W. Shin, H. Kim, Y. Cui, J.W. Kysar, J. Hone, Y. Jung, S. Jeon, S.M. Han, Strengthening effect of single-atomic-layer graphene in metal–graphene nanolayered composites, Nat. Commun. 4 (2013) 2114. https://doi.org/10.1038/ncomms3114.

[44] G.M. Rutter, N.P. Guisinger, J.N. Crain, P.N. First, J.A. Stroscio, Edge structure of epitaxial graphene islands, Phys. Rev. B 81 (2010) 245408. https://doi.org/10.1103/PhysRevB.81.245408.

[45] R. Sharma, J.H. Baik, C.J. Perera, M.S. Strano, Anomalously Large Reactivity of Single Graphene Layers and Edges toward Electron Transfer Chemistries, Nano Lett. 10 (2010) 398–405. https://doi.org/10.1021/nl902741x.

[46] A.K. Geim, K.S. Novoselov, The rise of graphene, Nat. Mater. 6 (2007) 183–191. https://doi.org/10.1038/nmat1849.

[47] M.J.B. Moura, M. Marder, Tearing of free-standing graphene, Phys. Rev. E 88 (2013) 032405. https://doi.org/10.1103/PhysRevE.88.032405.

[48] J. Shi, W. Yu, C. Hu, H. Duan, J. Ji, Y. Kang, K. Cai, Effects of Tearing Conditions on the Crack Propagation in a Monolayer Graphene Sheet, Int. J. Mol. Sci. 23 (2022) 6471. https://doi.org/10.3390/ijms23126471.

[49] D. Sen, K.S. Novoselov, P.M. Reis, M.J. Buehler, Tearing Graphene Sheets From Adhesive Substrates Produces Tapered Nanoribbons, Small 6 (2010) 1108–1116. https://doi.org/10.1002/smll.201000097.

[50] Even with Defects, Graphene Is Strongest Material in the World, Columbia Eng. (2017). https://www.engineering.columbia.edu/news/even-defects-graphene-strongest-material-world (accessed August 1, 2024).

[51] C. Lee, X. Wei, J.W. Kysar, J. Hone, Measurement of the Elastic Properties and Intrinsic Strength of Monolayer Graphene, Science 321 (2008) 385–388. https://doi.org/10.1126/science.1157996.

[52] A. Zandiatashbar, G.-H. Lee, S.J. An, S. Lee, N. Mathew, M. Terrones, T. Hayashi, C.R. Picu, J. Hone, N. Koratkar, Effect of defects on the intrinsic strength and stiffness of graphene, Nat. Commun. 5 (2014) 3186. https://doi.org/10.1038/ncomms4186.

[53] Engineers Prove Graphene is the Strongest Material, (n.d.). https://phys.org/news/2008-07-graphene-strongest-material.html (accessed August 1, 2024).

[54] G.-H. Lee, R.C. Cooper, S.J. An, S. Lee, A. van der Zande, N. Petrone, A.G. Hammerberg, C. Lee, B. Crawford, W. Oliver, J.W. Kysar, J. Hone, High-Strength Chemical-Vapor–Deposited Graphene and Grain Boundaries, Science 340 (2013) 1073–1076. https://doi.org/10.1126/science.1235126.

[55] A. Zandiatashbar, G.-H. Lee, S.J. An, S. Lee, N. Mathew, M. Terrones, T. Hayashi, C.R. Picu, J. Hone, N. Koratkar, Effect of defects on the intrinsic strength and stiffness of graphene, Nat. Commun. 5 (2014) 3186. https://doi.org/10.1038/ncomms4186.

[56] A. C. Ferrari, F. Bonaccorso, V. Fal'ko, K. S. Novoselov, S. Roche, P. Bøggild, S. Borini, F.H. L. Koppens, V. Palermo, N. Pugno, J. A. Garrido, R. Sordan, A. Bianco, L. Ballerini, M. Prato, E. Lidorikis, J. Kivioja, C. Marinelli, T. Ryhänen, A. Morpurgo, J. N. Coleman, V. Nicolosi, L. Colombo, A. Fert, M. Garcia-Hernandez, A. Bachtold, G. F. Schneider, F. Guinea, C. Dekker, M. Barbone, Z. Sun, C. Galiotis, A. N. Grigorenko, G. Konstantatos, A. Kis, M. Katsnelson, L. Vandersypen, A. Loiseau, V. Morandi, D. Neumaier, E. Treossi, V. Pellegrini, M. Polini, A. Tredicucci, G. M. Williams, B.H. Hong, J.-H. Ahn, J.M. Kim, H. Zirath, B.J. van Wees, H. van der Zant, L. Occhipinti, A.D. Matteo, I. A. Kinloch, T. Seyller, E. Quesnel, X. Feng, K. Teo, N. Rupesinghe, P. Hakonen, S.R. T. Neil, Q. Tannock, T. Löfwander, J. Kinaret, Science and technology roadmap for graphene, related two-dimensional crystals, and hybrid systems, Nanoscale 7 (2015) 4598–4810. https://doi.org/10.1039/C4NR01600A.

[57] Atomic Structure of Graphene on SiO2 | Nano Letters, (n.d.). https://pubs.acs.org/doi/full/10.1021/nl070613a (accessed June 23, 2024).

[58] D. Berman, A. Erdemir, A.V. Sumant, Graphene: a new emerging lubricant, Mater. Today 17 (2014) 31–42. https://doi.org/10.1016/j.mattod.2013.12.003.

[59] S. Chen, L. Brown, M. Levendorf, W. Cai, S.-Y. Ju, J. Edgeworth, X. Li, C.W. Magnuson, A. Velamakanni, R.D. Piner, J. Kang, J. Park, R.S. Ruoff, Oxidation Resistance of Graphene-Coated Cu and Cu/Ni Alloy, ACS Nano 5 (2011) 1321–1327. https://doi.org/10.1021/nn103028d.

[60] S. Wang, P.K. Ang, Z. Wang, A.L.L. Tang, J.T.L. Thong, K.P. Loh, High Mobility, Printable, and Solution-Processed Graphene Electronics, Nano Lett. 10 (2010) 92–98. https://doi.org/10.1021/nl9028736.

[61] K. Takei, R. Kapadia, H. Fang, E. Plis, S. Krishna, A. Javey, High quality interfaces of InAs-on-insulator field-effect transistors with ZrO2 gate dielectrics, Appl. Phys. Lett. 102 (2013) 153513. https://doi.org/10.1063/1.4802779.

[62] Y. Zhang, Y.-W. Tan, H.L. Stormer, P. Kim, Experimental observation of the quantum Hall effect and Berry's phase in graphene, Nature 438 (2005) 201–204. https://doi.org/10.1038/nature04235.

[63] K.S. Novoselov, A.K. Geim, S.V. Morozov, D. Jiang, M.I. Katsnelson, I.V. Grigorieva, S.V. Dubonos, A.A. Firsov, Two-dimensional gas of massless Dirac fermions in graphene, Nature 438 (2005) 197–200. https://doi.org/10.1038/nature04233.

[64] Z. Xu, 4 - Fundamental Properties of Graphene, in: H. Zhu, Z. Xu, D. Xie, Y. Fang (Eds.), Graphene, Academic Press, 2018: pp. 73–102. https://doi.org/10.1016/B978-0-12-812651-6.00004-5.

[65] X. Zhang, S. Wan, J. Pu, L. Wang, X. Liu, Highly hydrophobic and adhesive performance of graphene films, J. Mater. Chem. 21 (2011) 12251–12258. https://doi.org/10.1039/C1JM12087E.

[66] G.F. Schneider, Q. Xu, S. Hage, S. Luik, J.N.H. Spoor, S. Malladi, H. Zandbergen, C. Dekker, Tailoring the hydrophobicity of graphene for its use as nanopores for DNA translocation, Nat. Commun. 4 (2013) 2619. https://doi.org/10.1038/ncomms3619.

[67] L.A. Belyaeva, G.F. Schneider, Wettability of graphene, Surf. Sci. Rep. 75 (2020) 100482. https://doi.org/10.1016/j.surfrep.2020.100482.

[68] C.N.R. Rao, K. Gopalakrishnan, A. Govindaraj, Synthesis, properties and applications of graphene doped with boron, nitrogen and other elements, Nano Today 9 (2014) 324–343. https://doi.org/10.1016/j.nantod.2014.04.010.

[69] V. Jain, B. Kandasubramanian, Functionalized graphene materials for hydrogen storage, J. Mater. Sci. 55 (2020) 1865–1903. https://doi.org/10.1007/s10853-019-04150-y.

[70] T. Granzier-Nakajima, K. Fujisawa, V. Anil, M. Terrones, Y.-T. Yeh, Controlling Nitrogen Doping in Graphene with Atomic Precision: Synthesis and Characterization, Nanomaterials 9 (2019) 425. https://doi.org/10.3390/nano9030425.

[71] I.-Y. Jeon, H.-J. Noh, J.-B. Baek, Nitrogen-Doped Carbon Nanomaterials: Synthesis, Characteristics and Applications, Chem. – Asian J. 15 (2020) 2282–2293. https://doi.org/10.1002/asia.201901318.

[72] C. Bie, H. Yu, B. Cheng, W. Ho, J. Fan, J. Yu, Design, Fabrication, and Mechanism of Nitrogen-Doped Graphene-Based Photocatalyst, Adv. Mater. 33 (2021) 2003521. https://doi.org/10.1002/adma.202003521.

[73] L. Feng, Z. Qin, Y. Huang, K. Peng, F. Wang, Y. Yan, Y. Chen, Boron-, sulfur-, and phosphorus-doped graphene for environmental applications, Sci. Total Environ. 698 (2020) 134239. https://doi.org/10.1016/j.scitotenv.2019.134239.

[74] Y. Zhao, Y. Xie, Y. Yu Hui, L. Tang, W. Jie, Y. Jiang, L. Xu, S. Ping Lau, Y. Chai, Highly impermeable and transparent graphene as an ultra-thin protection barrier for Ag thin films, J. Mater. Chem. C 1 (2013) 4956–4961. https://doi.org/10.1039/C3TC30743C.

[75] Y. Su, V.G. Kravets, S.L. Wong, J. Waters, A.K. Geim, R.R. Nair, Impermeable barrier films and protective coatings based on reduced graphene oxide, Nat. Commun. 5 (2014) 4843. https://doi.org/10.1038/ncomms5843.

[76] V. Berry, Impermeability of graphene and its applications, Carbon 62 (2013) 1–10. https://doi.org/10.1016/j.carbon.2013.05.052.

[77] P.Z. Sun, Q. Yang, W.J. Kuang, Y.V. Stebunov, W.Q. Xiong, J. Yu, R.R. Nair, M.I. Katsnelson, S.J. Yuan, I.V. Grigorieva, M. Lozada-Hidalgo, F.C. Wang, A.K. Geim, Limits on gas impermeability of graphene, Nature 579 (2020) 229–232. https://doi.org/10.1038/s41586-020-2070-x.

[78] F. Li, L. Long, Y. Weng, A Review on the Contemporary Development of Composite Materials Comprising Graphene/Graphene Derivatives, Adv. Mater. Sci. Eng. 2020 (2020) 7915641. https://doi.org/10.1155/2020/7915641.

[79] Y. Xiao, Y.X. Pang, Y. Yan, P. Qian, H. Zhao, S. Manickam, T. Wu, C.H. Pang, Synthesis and Functionalization of Graphene Materials for Biomedical Applications: Recent Advances, Challenges, and Perspectives, Adv. Sci. 10 (2023) 2205292. https://doi.org/10.1002/advs.202205292.

[80] R. Goodrum, H. Weldekidan, H. Li, A.K. Mohanty, M. Misra, Graphene-based nanostructures from green processes and their applications in biomedical sensors, Adv. Ind. Eng. Polym. Res. 7 (2024) 37–53. https://doi.org/10.1016/j.aiepr.2023.03.001.

[81] K. Uzdrowska, N. Knap, J. Gulczynski, A. Kuban-Jankowska, W. Struck-Lewicka, M.J. Markuszewski, T. Bączek, E. Izycka-Swieszewska, M. Gorska-Ponikowska, Chasing Graphene-Based Anticancer Drugs: Where are We Now on the Biomedical Graphene Roadmap?, Int. J. Nanomedicine 19 (2024) 3973–3989. https://doi.org/10.2147/IJN.S447397.

[82] G.E. Fenoy, W.A. Marmisollé, O. Azzaroni, W. Knoll, Acetylcholine biosensor based on the electrochemical functionalization of graphene field-effect transistors, Biosens. Bioelectron. 148 (2020) 111796. https://doi.org/10.1016/j.bios.2019.111796.

[83] S. Shahriari, M. Sastry, S. Panjikar, R.K. Singh Raman, Graphene and Graphene Oxide as a Support for Biomolecules in the Development of Biosensors, Nanotechnol. Sci. Appl. 14 (2021) 197–220. https://doi.org/10.2147/NSA.S334487.

[84] S. Brosel-Oliu, G. Rius, A. Aviñó, N. Nakatsuka, X. Illa, E. del Corro, M. Delgà-Fernández, E. Masvidal-Codina, N. Rodríguez, J.P. Merino, A. Criado, M. Prato, R. Tkatchenko, R. Eritja, P. Godignon, J.A. Garrido, R. Villa, A. Guimerà, E. Prats-Alfonso, Single-Step Functionalization Strategy of Graphene Microtransistor Array with Chemically Modified Aptamers for Biosensing Applications, Small 20 (2024) 2308857. https://doi.org/10.1002/smll.202308857.

[85] H. Aghamohammadi, R. Eslami-Farsani, M. Torabian, N. Amousa, Recent advances in

one-pot functionalization of graphene using electrochemical exfoliation of graphite: A review study, Synth. Met. 269 (2020) 116549. https://doi.org/10.1016/j.synthmet.2020.116549.

[86] A. Zhao, J. She, D. Manoj, T. Wang, Y. Sun, Y. Zhang, F. Xiao, Functionalized graphene fiber modified by dual nanoenzyme: Towards high-performance flexible nanohybrid microelectrode for electrochemical sensing in live cancer cells, Sens. Actuators B Chem. 310 (2020) 127861. https://doi.org/10.1016/j.snb.2020.127861.

[87] O.A. Oyetade, Y. Wang, S. He, H.R.M. Margavio, S.R. Bottum, C.L. Rooney, H. Wang, C.L. Donley, G.N. Parsons, T. Cohen-Karni, J.F. Cahoon, Covalent Functionalization of Silicon with Plasma-Grown "Fuzzy" Graphene: Robust Aqueous Photoelectrodes for CO2 Reduction by Molecular Catalysts, ACS Appl. Mater. Interfaces 16 (2024) 37885–37895. https://doi.org/10.1021/acsami.4c04691.

[88] H. Zhang, E. Bekyarova, J.-W. Huang, Z. Zhao, W. Bao, F. Wang, R.C. Haddon, C.N. Lau, Aryl Functionalization as a Route to Band Gap Engineering in Single Layer Graphene Devices, Nano Lett. 11 (2011) 4047–4051. https://doi.org/10.1021/nl200803q.

[89] H.Y. Mao, Y.H. Lu, J.D. Lin, S. Zhong, A.T.S. Wee, W. Chen, Manipulating the electronic and chemical properties of graphene via molecular functionalization, Prog. Surf. Sci. 88 (2013) 132–159. https://doi.org/10.1016/j.progsurf.2013.02.001.

[90] M.H.N. Akashah, M.R. Sahudin, R.A. Rani, P.J. Scully, S.R. Makhsin, Chapter 3 - Chemical properties of graphene, in: Y. Al-Douri (Ed.), Graphene Nanotub. Quantum Dots-Based Nanotechnol., Woodhead Publishing, 2022: pp. 43–67. https://doi.org/10.1016/B978-0-323-85457-3.00023-2.

[91] S. Priyadarsini, S. Mohanty, S. Mukherjee, S. Basu, M. Mishra, Graphene and graphene oxide as nanomaterials for medicine and biology application, J. Nanostructure Chem. 8 (2018) 123–137. https://doi.org/10.1007/s40097-018-0265-6.

[92] M. Acik, G. Lee, C. Mattevi, M. Chhowalla, K. Cho, Y.J. Chabal, Unusual infrared-absorption mechanism in thermally reduced graphene oxide, Nat. Mater. 9 (2010) 840–845. https://doi.org/10.1038/nmat2858.

[93] H. Liu, Y. Liu, D. Zhu, Chemical doping of graphene, J. Mater. Chem. 21 (2011) 3335–3345. https://doi.org/10.1039/C0JM02922J.

[94] G. Giovannetti, P.A. Khomyakov, G. Brocks, V.M. Karpan, J. van den Brink, P.J. Kelly, Doping Graphene with Metal Contacts, Phys. Rev. Lett. 101 (2008) 026803. https://doi.org/10.1103/PhysRevLett.101.026803.

[95] Y. Shao, S. Zhang, M. H. Engelhard, G. Li, G. Shao, Y. Wang, J. Liu, I. A. Aksay, Y. Lin, Nitrogen -doped graphene and its electrochemical applications, J. Mater. Chem. 20 (2010) 7491–7496. https://doi.org/10.1039/C0JM00782J.

[96] Review on Recent Progress in Nitrogen-Doped Graphene: Synthesis, Characterization, and Its Potential Applications | ACS Catalysis, (n.d.). https://pubs.acs.org/doi/full/10.1021/cs200652y (accessed August 5, 2024).

[97] H.M. Cobb, The History of Stainless Steel, ASM International, 2010.

[98] C.R.C. and lngemar Olefjord, Passivity of Austenitic Stainless Steels, in: Corros. Mech. Theory Pract., 3rd ed., CRC Press, 2011.

[99] J.R. Davis, Stainless Steels, ASM International, 1994.

[100] M.F. McGuire, Stainless Steels for Design Engineers, ASM International, 2008.

[101] B. Al-Mangour, Powder metallurgy of stainless steel: State-of-the art, challenges, and development, in: 2015: pp. 37–80.

[102] S. Nishimura, T. Yamane, T. Kondo, High-strength brass alloy for sliding members, and sliding members, US9322085B2, 2016. https://patents.google.com/patent/US9322085B2/en (accessed June 23, 2024).

[103] C.-E. Manufacturing, Copper Alloy Bearings, Copp. Dev. Assoc. CDA Publ. TN45–1971–44 P (1971).

[104] K. Rajkumar, S. Aravindan, Microwave sintering of copper–graphite composites, J. Mater. Process. Technol. 209 (2009) 5601–5605. https://doi.org/10.1016/j.jmatprotec.2009.05.017.

[105] J. Wang, R. Zhang, J. Xu, C. Wu, P. Chen, Effect of the content of ball-milled expanded graphite on the bending and tribological properties of copper–graphite composites, Mater. Des. 47 (2013) 667–671. https://doi.org/10.1016/j.matdes.2013.01.008.

[106] H. Yue, L. Yao, X. Gao, S. Zhang, E. Guo, H. Zhang, X. Lin, B. Wang, Effect of ball-milling and graphene contents on the mechanical properties and fracture mechanisms of graphene nanosheets reinforced copper matrix composites, J. Alloys Compd. 691 (2017) 755–762. https://doi.org/10.1016/j.jallcom.2016.08.303.

[107] J. Li, L. Zhang, J. Xiao, K. Zhou, Sliding wear behavior of copper-based composites

reinforced with graphene nanosheets and graphite, Trans. Nonferrous Met. Soc. China 25 (2015) 3354–3362. https://doi.org/10.1016/S1003-6326(15)63970-X.

[108] A.K. Behera, A. Mallik, Ultrasound assisted electroplating of nano-composite thin film of Cu matrix with electrochemically in-house synthesized few layer graphene nano-sheets as reinforcement, J. Alloys Compd. 750 (2018) 587–598. https://doi.org/10.1016/j.jallcom.2018.03.264.

[109] Y.L. Zhong, Z. Tian, G.P. Simon, D. Li, Scalable production of graphene via wet chemistry: progress and challenges, Mater. Today 18 (2015) 73–78. https://doi.org/10.1016/j.mattod.2014.08.019.

[110] Y. Liu, Application of graphene oxide in water treatment, IOP Conf. Ser. Earth Environ. Sci. 94 (2017) 012060. https://doi.org/10.1088/1755-1315/94/1/012060.

[111] G. Eda, G. Fanchini, M. Chhowalla, Large-area ultrathin films of reduced graphene oxide as a transparent and flexible electronic material, Nat. Nanotechnol. 3 (2008) 270–274. https://doi.org/10.1038/nnano.2008.83.

[112] S. Gilje, S. Han, M. Wang, K.L. Wang, R.B. Kaner, A Chemical Route to Graphene for Device Applications, Nano Lett. 7 (2007) 3394–3398. https://doi.org/10.1021/nl0717715.

[113] E. Kymakis, E. Stratakis, M.M. Stylianakis, E. Koudoumas, C. Fotakis, Spin coated graphene films as the transparent electrode in organic photovoltaic devices, Thin Solid Films 520 (2011) 1238–1241. https://doi.org/10.1016/j.tsf.2011.04.208.

[114] C. Reiner-Rozman, R. Hasler, J. Andersson, T. Rodrigues, A. Bozdogan, J. Bintinger, P. Aspermair, The top performer: Towards optimized parameters for reduced graphene oxide uniformity by spin coating, Micro Nano Lett. 16 (2021) 436–442. https://doi.org/10.1049/mna2.12070.

[115] X. Li, L. Colombo, R.S. Ruoff, Synthesis of Graphene Films on Copper Foils by Chemical Vapor Deposition, Adv. Mater. 28 (2016) 6247–6252. https://doi.org/10.1002/adma.201504760.

[116] X. Zhang, Q. Yuan, H. Shu, F. Ding, Mechanisms of Graphene Chemical Vapor Deposition (CVD) Growth, in: Graphene Chem., John Wiley & Sons, Ltd, 2013: pp. 255–290. https://doi.org/10.1002/9781118691281.ch12.

[117] G. Deokar, J. Avila, I. Razado-Colambo, J.-L. Codron, C. Boyaval, E. Galopin, M.-C. Asensio, D. Vignaud, Towards high quality CVD graphene growth and transfer, Carbon 89 (2015) 82–92. https://doi.org/10.1016/j.carbon.2015.03.017.

[118] Y. Song, W. Zou, Q. Lu, L. Lin, Z. Liu, Graphene Transfer: Paving the Road for Applications of Chemical Vapor Deposition Graphene, Small 17 (2021) 2007600. https://doi.org/10.1002/smll.202007600.

[119] T. Yamada, M. Ishihara, J. Kim, M. Hasegawa, S. Iijima, A roll-to-roll microwave plasma chemical vapor deposition process for the production of 294 mm width graphene films at low temperature, Carbon 50 (2012) 2615–2619. https://doi.org/10.1016/j.carbon.2012.02.020.

[120] X. Li, L. Colombo, R.S. Ruoff, Synthesis of Graphene Films on Copper Foils by Chemical Vapor Deposition, Adv. Mater. 28 (2016) 6247–6252. https://doi.org/10.1002/adma.201504760.

[121] Y. Zhang, L. Zhang, C. Zhou, Review of Chemical Vapor Deposition of Graphene and Related Applications, Acc. Chem. Res. 46 (2013) 2329–2339. https://doi.org/10.1021/ar300203n.

[122] Large-Area Synthesis of High-Quality and Uniform Graphene Films on Copper Foils | Science, (n.d.). https://www.science.org/doi/full/10.1126/science.1171245?casa_token=8s5LAW8HAacAAAAA%3A9oAjAA3YVsnEW_lNDsXKo1v_yeTCOR-VNGrS5AGLwnt3-6j6Y6nayYiFkmS9JxXvo--Uxd6vM-tR (accessed August 7, 2024).

[123] J. Jorudas, D. Pashnev, I. Kašalynas, I. Ignatjev, G. Niaura, A. Selskis, V. Astachov, N. Alexeeva, Green Removal of DUV-Polarity-Modified PMMA for Wet Transfer of CVD Graphene, Nanomaterials 12 (2022) 4017. https://doi.org/10.3390/nano12224017.

[124] S. Nikkho, M. Mirzaei, J. Karimi Sabet, M.A. Moosavian, S.M. Hedayat, Enhanced quality of transfer-free graphene membrane for He/CH4 separation, Sep. Purif. Technol. 232 (2020) 115972. https://doi.org/10.1016/j.seppur.2019.115972.

[125] J. Yang, E.L. Lim, L. Tan, Z. Wei, Ink Engineering in Blade-Coating Large-Area Perovskite Solar Cells, Adv. Energy Mater. 12 (2022) 2200975. https://doi.org/10.1002/aenm.202200975.

[126] T. Kobayashi, M. Bando, N. Kimura, K. Shimizu, K. Kadono, N. Umezu, K. Miyahara, S. Hayazaki, S. Nagai, Y. Mizuguchi, Y. Murakami, D. Hobara, Production of a 100-m-long high-quality graphene transparent conductive film by roll-to-roll chemical vapor deposition and transfer process, Appl. Phys. Lett. 102 (2013) 023112. https://doi.org/10.1063/1.4776707.

[127] L. Liu, X. Liu, Z. Zhan, W. Guo, C. Xu, J. Deng, D. Chakarov, P. Hyldgaard, E. Schröder, A. Yurgens, J. Sun, A Mechanism for Highly Efficient Electrochemical Bubbling

Delamination of CVD-Grown Graphene from Metal Substrates, Adv. Mater. Interfaces 3 (2016) 1500492. https://doi.org/10.1002/admi.201500492.

[128] L.-P. Ma, S. Dong, H.-M. Cheng, W. Ren, Breaking the Rate-Integrity Dilemma in Large-Area Bubbling Transfer of Graphene by Strain Engineering, Adv. Funct. Mater. 31 (2021) 2104228. https://doi.org/10.1002/adfm.202104228.

[129] Y. Huang, Q. Li, J. Zhang, Y. Qi, H. Wang, P. Zhao, Y. Meng, Effect of airborne contaminants on the macroscopic anti-wear performance of chemical vapor deposition graphene, Surf. Coat. Technol. 383 (2020) 125276. https://doi.org/10.1016/j.surfcoat.2019.125276.

[130] B. Kulyk, M.A. Freitas, N.F. Santos, F. Mohseni, A.F. Carvalho, K. Yasakau, A.J.S. Fernandes, A. Bernardes, B. Figueiredo, R. Silva, J. Tedim, F.M. Costa, A critical review on the production and application of graphene and graphene-based materials in anti-corrosion coatings, Crit. Rev. Solid State Mater. Sci. 47 (2022) 309–355. https://doi.org/10.1080/10408436.2021.1886046.

[131] Y. Ma, J. Han, M. Wang, X. Chen, S. Jia, Electrophoretic deposition of graphene-based materials: A review of materials and their applications, J. Materiomics 4 (2018) 108–120. https://doi.org/10.1016/j.jmat.2018.02.004.

[132] O.O.V. der Biest, L.J. Vandeperre, ELECTROPHORETIC DEPOSITION OF MATERIALS, Annu. Rev. Mater. Res. 29 (1999) 327–352. https://doi.org/10.1146/annurev.matsci.29.1.327.

[133] A.R. Boccaccini, J. Cho, J.A. Roether, B.J.C. Thomas, E. Jane Minay, M.S.P. Shaffer, Electrophoretic deposition of carbon nanotubes, Carbon 44 (2006) 3149–3160. https://doi.org/10.1016/j.carbon.2006.06.021.

[134] M. Atiq Ur Rehman, Q. Chen, A. Braem, M.S.P. Shaffer, A.R. Boccaccini, Electrophoretic deposition of carbon nanotubes: recent progress and remaining challenges, Int. Mater. Rev. 66 (2021) 533–562. https://doi.org/10.1080/09506608.2020.1831299.

[135] S.-J. Park, M.-K. Seo, Chapter 1 - Intermolecular Force, in: S.-J. Park, M.-K. Seo (Eds.), Interface Sci. Technol., Elsevier, 2011: pp. 1–57. https://doi.org/10.1016/B978-0-12-375049-5.00001-3.

[136] P. Amrollahi, J. Krasinski, R. Vaidyanathan, L. Tayebi, D. Vashaee, Electrophoretic Deposition (EPD): Fundamentals and Applications from Nano-to Micro-Scale Structures, in: 2015: pp. 1–27. https://doi.org/10.1007/978-3-319-15207-3_7-1.

[137] S.A. Hasan, J.L. Rigueur, R.R. Harl, A.J. Krejci, I. Gonzalo-Juan, B.R. Rogers, J.H. Dickerson, Transferable Graphene Oxide Films with Tunable Microstructures, ACS Nano 4 (2010) 7367–7372. https://doi.org/10.1021/nn102152x.

[138] L. Besra, M. Liu, A review on fundamentals and applications of electrophoretic deposition (EPD), Prog. Mater. Sci. 52 (2007) 1–61. https://doi.org/10.1016/j.pmatsci.2006.07.001.

[139] C. Zhang, H. Li, Y. Su, Q. Zhang, Y. Li, J. Lu, Controllable and Versatile Electrophoretic Deposition Technology for Monolithic Organic Memory Devices, ACS Appl. Mater. Interfaces 12 (2020) 15482–15490. https://doi.org/10.1021/acsami.0c02190.

[140] H. Akbulut, G. Hatipoglu, H. Algul, M. Tokur, M. Kartal, M. Uysal, T. Cetinkaya, Co-deposition of Cu/WC/graphene hybrid nanocomposites produced by electrophoretic deposition, Surf. Coat. Technol. 284 (2015) 344–352. https://doi.org/10.1016/j.surfcoat.2015.07.080.

[141] J.H. Park, J.M. Park, Photo-generated cathodic protection performance of electrophoretically Co-deposited layers of TiO2 nanoparticles and graphene nanoplatelets on steel substrate, Surf. Coat. Technol. 258 (2014) 62–71. https://doi.org/10.1016/j.surfcoat.2014.10.002.

[142] A.A. Sadeghi Ghazvini, E. Taheri-Nassaj, B. Raissi, R. Riahifar, M. Sahba Yaghmaee, M. Shaker, Co-electrophoretic deposition of Co3O4 and graphene nanoplates for supercapacitor electrode, Mater. Lett. 285 (2021) 129195. https://doi.org/10.1016/j.matlet.2020.129195.

[143] P. Zhao, L.J. LeSergent, J. Farnese, J.Z. Wen, C.L. Ren, Electrophoretic deposition of carbon nanotubes on semi-conducting and non-conducting substrates, Electrochem. Commun. 108 (2019) 106558. https://doi.org/10.1016/j.elecom.2019.106558.

[144] Y. Dong, W. Sun, X. Liu, M. Ma, Y. Zhang, Y. Liu, Electrophoretic-Deposition of Graphene and Microstructure and Friction Behavior of Ni–Graphene Composite Coatings, Adv. Eng. Mater. 21 (2019) 1900327. https://doi.org/10.1002/adem.201900327.

[145] B. Wu, B. Xu, B. Zhang, X. Jing, C. Liu, Automatic brush plating: An update on brush plating, Mater. Lett. 60 (2006) 1673–1677. https://doi.org/10.1016/j.matlet.2005.11.098.

[146] S. Qi, X. Li, Z. Zhang, H. Dong, Fabrication and characterisation of electro-brush plated nickel-graphene oxide nano-composite coatings, Thin Solid Films 644 (2017) 106–114. https://doi.org/10.1016/j.tsf.2017.06.064.

[147] D. Zhang, X. Cui, G. Jin, Y. Jiao, D. Li, Preparation, deposited behavior and hydrophobic property of modified graphene oxide reinforced Ni composite coatings by magnetic field assisted electro-brush plating, Surf. Coat. Technol. 403 (2020) 126363. https://doi.org/10.1016/j.surfcoat.2020.126363.

[148] B. Subramanian, C. Sanjeeviraja, M. Jayachandran, Brush plating of tin(II) selenide thin films, J. Cryst. Growth 234 (2002) 421–426. https://doi.org/10.1016/S0022-0248(01)01697-9.

[149] E. Rudnik, L. Burzyńska, Ł. Dolasiński, M. Misiak, Electrodeposition of nickel/SiC composites in the presence of cetyltrimethylammonium bromide, Appl. Surf. Sci. 256 (2010) 7414–7420. https://doi.org/10.1016/j.apsusc.2010.05.082.

[150] P.K. Rai, A. Gupta, Investigation of surface characteristics and effect of electrodeposition parameters on nickel-based composite coating, Mater. Today Proc. 44 (2021) 1079–1085. https://doi.org/10.1016/j.matpr.2020.11.182.

[151] A. Joseph, B. Kirubasankar, A.M. Mathew, M. Narayanasamy, C. Yan, S. Angaiah, Influence of pulse reverse current parameters on electrodeposition of copper-graphene nanocomposite coating, Appl. Surf. Sci. Adv. 5 (2021) 100116. https://doi.org/10.1016/j.apsadv.2021.100116.

[152] J. Yu, L. Wang, Z. Liu, J. Xu, Y. Zong, Electrodeposition-based fabrication of graphene/copper composites with excellent overall properties, J. Alloys Compd. 924 (2022) 166610. https://doi.org/10.1016/j.jallcom.2022.166610.

[153] S. Qi, X. Li, H. Dong, Reduced friction and wear of electro-brush plated nickel composite coatings reinforced by graphene oxide, Wear 426–427 (2019) 228–238. https://doi.org/10.1016/j.wear.2018.12.069.

[154] P. Xu, X. Shen, G. Xin, Electro-brush plating Ni-Graphene oxide composite coating enhanced corrosion resistance of fluoride ion, Mater. Res. Express 8 (2021) 026406. https://doi.org/10.1088/2053-1591/abe2e1.

[155] B. Jiang, B. Xu, S. Dong, Y. Yi, P. Ding, Contact fatigue behavior of nano-ZrO2/Ni coating prepared by electro-brush plating, Surf. Coat. Technol. 202 (2007) 447–452. https://doi.org/10.1016/j.surfcoat.2007.06.003.

[156] X. Li, X. Wang, R. Gao, L. Sun, Study of deposition patterns of plating layers in SiC/Cu composites by electro-brush plating, Appl. Surf. Sci. 257 (2011) 10294–10299. https://doi.org/10.1016/j.apsusc.2011.07.045.

[157] M. Xu, S. Zhu, H. Ding, X. Qi, Influence of electric contact strengthening on the microstructure and properties of electro brush plating Ni-P/nano-WC composite coatings, Int. J. Refract. Met. Hard Mater. 62 (2017) 70–77. https://doi.org/10.1016/j.ijrmhm.2016.10.017.

[158] X. Qi, Y. Wang, C. Wang, R. Zhang, Microstructure and Performance of Nano-WC Particle-Strengthened Ni Coatings by Electro-brush Plating, J. Mater. Eng. Perform. 27 (2018) 6069–6079. https://doi.org/10.1007/s11665-018-3684-0.

[159] Y. Huang, Z. Huang, Y. Zhou, Development of Dry Lubricant Nickel-MoS2 Composite Through Brush Plating, in: Y. Wei, S. Chng (Eds.), Proc. 2nd Int. Conf. Adv. Surf. Enhanc. INCASE 2021, Springer, Singapore, 2022: pp. 142–145. https://doi.org/10.1007/978-981-16-5763-4_31.

[160] W. Xiaohe, L. Biao, H. Zhenfeng, X. Binshi, Effects of n-Al2O3 Particles Content on Structure and Performance of Electro-Brush Plating Ni-Co Alloy Composite Coatings, Rare Met. Mater. Eng. 45 (2016) 36–41. https://doi.org/10.1016/S1875-5372(16)30042-X.

[161] M. Gao, Z. Pei, G. Song, Z. Liu, H. Li, J. Gong, Wear resistance of Ni/nano-Al2O3 composite coatings by brush electroplating, J. Mater. Sci. 59 (2024) 7009–7027. https://doi.org/10.1007/s10853-024-09563-y.

[162] H. Liu, X. Wang, H. Ji, Fabrication of lotus-leaf-like superhydrophobic surfaces via Ni-based nano-composite electro-brush plating, Appl. Surf. Sci. 288 (2014) 341–348. https://doi.org/10.1016/j.apsusc.2013.10.030.

[163] D. Zhang, X. Cui, G. Jin, D. Li, Y. Fang, X. Wen, G. Ma, H. Wang, B. Xu, Comparison of MWCNTs and GO reinforced electro-brush plated Ni nanocomposite coatings: structural variations of carbon-based reinforcements and tribological behavior, J. Alloys Compd. 832 (2020) 154941. https://doi.org/10.1016/j.jallcom.2020.154941.

[164] X. Jiang, X. Xie, Z. Xu, Double glow surface alloying of low carbon steel with electric brush plating Ni interlayer for improvement in corrosion resistance, Surf. Coat. Technol. 168 (2003) 156–160. https://doi.org/10.1016/S0257-8972(02)00861-7.

[165] L. Mostafapour, S. Baghshahi, M. Rajabi, M.S. Siahpoosh, F. Esfehani, Kinetic evaluation of YSZ/Al2O3 nanocomposite coatings fabricated by electrophoretic deposition on a nickel-based superalloy, Process. Appl. Ceram. 15 (2021) 1–10.

[166] L. Wu, Electrodeposition and Tribological Behavior of Ni-MoS2 Composite Coatings, M.S., 2022. https://www.proquest.com/docview/2800164157/abstract/631DAC565E54452PQ/1 (accessed August 9, 2024).

[167] M.R. Hosseini, M. Ahangari, M.H. Johar, S.R. Allahkaram, Optimization of nano HA-SiC coating on AISI 316L medical grade stainless steel via electrophoretic deposition, Mater. Lett. 285 (2021) 129097. https://doi.org/10.1016/j.matlet.2020.129097.

[168] L. Shi, M. Li, Z. Liu, Z. Zhan, Z. Yuan, X. Wang, Fabrication of yttria-stabilized zirconia/La2O3 composite coating by electrophoretic deposition to improve high-temperature oxidation resistance of stainless steel, Ceram. Int. 50 (2024) 10641–10650. https://doi.org/10.1016/j.ceramint.2023.12.378.

[169] L.H. Prado, S. Virtanen, Cu–MoS2 Superhydrophobic Coating by Composite Electrodeposition, Coatings 10 (2020) 238. https://doi.org/10.3390/coatings10030238.

[170] M.R. Gorji, S. Sanjabi, C. Edtmaier, Combination of electrophoretic and electroless depositions to fabricate Ni/TiC cladding, Surf. Eng. 36 (2020) 929–935. https://doi.org/10.1080/02670844.2019.1653010.

[171] H. Yang, S.Y. Dong, B.S. Xu, Microstructure and Properties of Brush Electroplated Nano-SiC-Al2O3/Ni Composite Coating, Key Eng. Mater. 373–374 (2008) 285–288. https://doi.org/10.4028/www.scientific.net/KEM.373-374.285.

[172] M. Gao, Z. Pei, G. Song, Z. Liu, H. Li, J. Gong, Wear resistance of Ni/nano-Al2O3 composite coatings by brush electroplating, J. Mater. Sci. 59 (2024) 7009–7027. https://doi.org/10.1007/s10853-024-09563-y.

[173] M. Xu, S. Zhu, H. Ding, X. Qi, Influence of electric contact strengthening on the microstructure and properties of electro brush plating Ni-P/nano-WC composite coatings, Int. J. Refract. Met. Hard Mater. 62 (2017) 70–77. https://doi.org/10.1016/j.ijrmhm.2016.10.017.

[174] M. Gao, Z. Pei, G. Song, Z. Liu, H. Li, J. Gong, Wear resistance of Ni/nano-Al2O3 composite coatings by brush electroplating, J. Mater. Sci. 59 (2024) 7009–7027. https://doi.org/10.1007/s10853-024-09563-y.

[175] S. Qi, X. Li, Z. Zhang, H. Dong, Fabrication and characterisation of electro-brush plated nickel-graphene oxide nano-composite coatings, Thin Solid Films 644 (2017) 106–114. https://doi.org/10.1016/j.tsf.2017.06.064.

[176] Y. Raghupathy, A. Kamboj, M.Y. Rekha, N.P. Narasimha Rao, C. Srivastava, Copper-graphene oxide composite coatings for corrosion protection of mild steel in 3.5% NaCl, Thin Solid Films 636 (2017) 107–115. https://doi.org/10.1016/j.tsf.2017.05.042.

[177] M.A. Raza, Z.U. Rehman, F.A. Ghauri, A. Ahmad, R. Ahmad, M. Raffi, Corrosion study

of electrophoretically deposited graphene oxide coatings on copper metal, Thin Solid Films 620 (2016) 150–159. https://doi.org/10.1016/j.tsf.2016.09.036.

[178] A.K. Behera, A. Mallik, Ultrasound assisted electroplating of nano-composite thin film of Cu matrix with electrochemically in-house synthesized few layer graphene nano-sheets as reinforcement, J. Alloys Compd. 750 (2018) 587–598. https://doi.org/10.1016/j.jallcom.2018.03.264.

[179] C. Wang, M. Zhao, J. Li, J. Yu, S. Sun, S. Ge, X. Guo, F. Xie, B. Jiang, E.K. Wujcik, Y. Huang, N. Wang, Z. Guo, Silver nanoparticles/graphene oxide decorated carbon fiber synergistic reinforcement in epoxy-based composites, Polymer 131 (2017) 263–271. https://doi.org/10.1016/j.polymer.2017.10.049.

[180] S. Park, J. An, J.R. Potts, A. Velamakanni, S. Murali, R.S. Ruoff, Hydrazine-reduction of graphite- and graphene oxide, Carbon 49 (2011) 3019–3023. https://doi.org/10.1016/j.carbon.2011.02.071.

[181] S. Stankovich, D.A. Dikin, R.D. Piner, K.A. Kohlhaas, A. Kleinhammes, Y. Jia, Y. Wu, S.T. Nguyen, R.S. Ruoff, Synthesis of graphene-based nanosheets via chemical reduction of exfoliated graphite oxide, Carbon 45 (2007) 1558–1565. https://doi.org/10.1016/j.carbon.2007.02.034.

[182] P.-G. Ren, D.-X. Yan, X. Ji, T. Chen, Z.-M. Li, Temperature dependence of graphene oxide reduced by hydrazine hydrate, Nanotechnology 22 (2010) 055705. https://doi.org/10.1088/0957-4484/22/5/055705.

[183] V.S. Sapner, P.P. Chavan, A.V. Munde, U.S. Sayyad, B.R. Sathe, Heteroatom (N, O, and S)-Based Biomolecule-Functionalized Graphene Oxide: A Bifunctional Electrocatalyst for Enhancing Hydrazine Oxidation and Oxygen Reduction Reactions, Energy Fuels 35 (2021) 6823–6834. https://doi.org/10.1021/acs.energyfuels.0c04298.

[184] M. Pinzón, O. Avilés-García, A.R. de la Osa, A. de Lucas-Consuegra, P. Sánchez, A. Romero, New catalysts based on reduced graphene oxide for hydrogen production from ammonia decomposition, Sustain. Chem. Pharm. 25 (2022) 100615. https://doi.org/10.1016/j.scp.2022.100615.

[185] M.J. Fernández-Merino, L. Guardia, J.I. Paredes, S. Villar-Rodil, P. Solís-Fernández, A. Martínez-Alonso, J.M.D. Tascón, Vitamin C Is an Ideal Substitute for Hydrazine in the Reduction of Graphene Oxide Suspensions, J. Phys. Chem. C 114 (2010) 6426–6432. https://doi.org/10.1021/jp100603h.

[186] I.M. Leo, E. Soto, F. Vaquero, N. Mota, B. Garcia, D. Liuzzi, R. Guil-López, R.M. Navarro, J.L.G. Fierro, Influence of the Reduction of Graphene Oxide with Hydroiodic

Acid on the Structure and Photoactivity of CdS–rGO Hybrids, Top. Catal. 60 (2017) 1183–1195. https://doi.org/10.1007/s11244-017-0799-8.

[187] W. Liu, G. Speranza, Chemical Reduction of GO: Comparing Hydroiodic Acid and Sodium Borohydride Chemical Approaches by X-ray Photoelectron Spectroscopy, C 8 (2022) 20. https://doi.org/10.3390/c8020020.

[188] M.J. McAllister, J.-L. Li, D.H. Adamson, H.C. Schniepp, A.A. Abdala, J. Liu, M. Herrera-Alonso, D.L. Milius, R. Car, R.K. Prud'homme, I.A. Aksay, Single Sheet Functionalized Graphene by Oxidation and Thermal Expansion of Graphite, Chem. Mater. 19 (2007) 4396–4404. https://doi.org/10.1021/cm0630800.

[189] H.C. Schniepp, J.-L. Li, M.J. McAllister, H. Sai, M. Herrera-Alonso, D.H. Adamson, R.K. Prud'homme, R. Car, D.A. Saville, I.A. Aksay, Functionalized Single Graphene Sheets Derived from Splitting Graphite Oxide, J. Phys. Chem. B 110 (2006) 8535–8539. https://doi.org/10.1021/jp060936f.

[190] C.-S. Lee, S.H. Yu, T.H. Kim, One-Step Electrochemical Fabrication of Reduced Graphene Oxide/Gold Nanoparticles Nanocomposite-Modified Electrode for Simultaneous Detection of Dopamine, Ascorbic Acid, and Uric Acid, Nanomaterials 8 (2018) 17. https://doi.org/10.3390/nano8010017.

[191] A.-M.J. Haque, H. Park, D. Sung, S. Jon, S.-Y. Choi, K. Kim, An Electrochemically Reduced Graphene Oxide-Based Electrochemical Immunosensing Platform for Ultrasensitive Antigen Detection, Anal. Chem. 84 (2012) 1871–1878. https://doi.org/10.1021/ac202562v.

[192] S.Y. Toh, K.S. Loh, S.K. Kamarudin, W.R.W. Daud, Graphene production via electrochemical reduction of graphene oxide: Synthesis and characterisation, Chem. Eng. J. 251 (2014) 422–434. https://doi.org/10.1016/j.cej.2014.04.004.

[193] V. Babaahmadi, M. Montazer, W. Gao, Surface modification of PET fabric through *in-situ* reduction and cross-linking of graphene oxide: Towards developing durable conductive fabric coatings, Colloids Surf. Physicochem. Eng. Asp. 545 (2018) 16–25. https://doi.org/10.1016/j.colsurfa.2018.02.018.

[194] A.G. Marrani, R. Zanoni, R. Schrebler, E.A. Dalchiele, Toward Graphene/Silicon Interface via Controlled Electrochemical Reduction of Graphene Oxide, J. Phys. Chem. C 121 (2017) 5675–5683. https://doi.org/10.1021/acs.jpcc.7b00749.

[195] Z. Wang, S. Wu, J. Zhang, P. Chen, G. Yang, X. Zhou, Q. Zhang, Q. Yan, H. Zhang, Comparative studies on single-layer reduced graphene oxide films obtained by electrochemical reduction and hydrazine vapor reduction, Nanoscale Res. Lett. 7 (2012)

161. https://doi.org/10.1186/1556-276X-7-161.

[196] X.-Y. Peng, X.-X. Liu, D. Diamond, K.T. Lau, Synthesis of electrochemically-reduced graphene oxide film with controllable size and thickness and its use in supercapacitor, Carbon 49 (2011) 3488–3496. https://doi.org/10.1016/j.carbon.2011.04.047.

[197] C. Lee, X. Wei, Q. Li, R. Carpick, J.W. Kysar, J. Hone, Elastic and frictional properties of graphene, Phys. Status Solidi B 246 (2009) 2562–2567. https://doi.org/10.1002/pssb.200982329.

[198] N. Fan, J. Guo, G. Jing, C. Liu, Q. Wang, G. Wu, H. Jiang, B. Peng, A hillock-like phenomenon with low friction and adhesion on a graphene surface induced by relative sliding at the interface of graphene and the SiO 2 substrate using an AFM tip, Nanoscale Adv. 2 (2020) 2548–2557. https://doi.org/10.1039/C9NA00660E.

[199] W. Guo, J. Yin, H. Qiu, Y. Guo, H. Wu, M. Xue, Friction of low-dimensional nanomaterial systems, Friction 2 (2014) 209–225. https://doi.org/10.1007/s40544-014-0064-0.

[200] H.S. Dong, S.J. Qi, Realising the potential of graphene-based materials for biosurfaces – A future perspective, Biosurface Biotribology 1 (2015) 229–248. https://doi.org/10.1016/j.bsbt.2015.10.004.

[201] D. Marchetto, C. Held, F. Hausen, F. Wählisch, M. Dienwiebel, R. Bennewitz, Friction and Wear on Single-Layer Epitaxial Graphene in Multi-Asperity Contacts, Tribol. Lett. 48 (2012) 77–82. https://doi.org/10.1007/s11249-012-9945-4.

[202] Y. Peng, Z. Wang, C. Li, Study of nanotribological properties of multilayer graphene by calibrated atomic force microscopy, Nanotechnology 25 (2014) 305701. https://doi.org/10.1088/0957-4484/25/30/305701.

[203] H. Lee, N. Lee, Y. Seo, J. Eom, S. Lee, Comparison of frictional forces on graphene and graphite, Nanotechnology 20 (2009) 325701. https://doi.org/10.1088/0957-4484/20/32/325701.

[204] Z. Chen, A. Khajeh, A. Martini, S.H. Kim, Origin of High Friction at Graphene Step Edges on Graphite, ACS Appl. Mater. Interfaces 13 (2021) 1895–1902. https://doi.org/10.1021/acsami.0c18098.

[205] Z.-L. Cheng, Y.-C. Kong, L. Fan, Z. Liu, Ultrasound-assisted Li+/Na+ co-intercalated exfoliation of graphite into few-layer graphene, Ultrason. Sonochem. 66 (2020) 105108. https://doi.org/10.1016/j.ultsonch.2020.105108.

[206] J. Li, T. Gao, J. Luo, Superlubricity of Graphite Induced by Multiple Transferred Graphene Nanoflakes, Adv. Sci. 5 (2018) 1700616. https://doi.org/10.1002/advs.201700616.

[207] T. Filleter, J.L. McChesney, A. Bostwick, E. Rotenberg, K.V. Emtsev, Th. Seyller, K. Horn, R. Bennewitz, Friction and Dissipation in Epitaxial Graphene Films, Phys. Rev. Lett. 102 (2009) 086102. https://doi.org/10.1103/PhysRevLett.102.086102.

[208] D. Berman, A. Erdemir, A.V. Zinovev, A.V. Sumant, Nanoscale friction properties of graphene and graphene oxide, Diam. Relat. Mater. 54 (2015) 91–96. https://doi.org/10.1016/j.diamond.2014.10.012.

[209] J. Llorente, B. Román-Manso, P. Miranzo, M. Belmonte, Tribological performance under dry sliding conditions of graphene/silicon carbide composites, J. Eur. Ceram. Soc. 36 (2016) 429–435. https://doi.org/10.1016/j.jeurceramsoc.2015.09.040.

[210] S.K. Singh, S. Samanta, A.K. Das, R.R. Sahoo, Electrodeposited SiC-graphene oxide composite in nickel matrix for improved tribological applications, Surf. Topogr. Metrol. Prop. 7 (2019) 035004. https://doi.org/10.1088/2051-672X/ab302d.

[211] Y. Du, Z. Zhang, D. Wang, L. Zhang, J. Cui, Y. Chen, M. Wu, R. Kang, Y. Lu, J. Yu, N. Jiang, Enhanced tribological properties of aligned graphene-epoxy composites, Friction 10 (2022) 854–865. https://doi.org/10.1007/s40544-021-0496-2.

[212] A. Toosinezhad, M. Alinezhadfar, S. Mahdavi, Tribological behavior of cobalt/graphene composite coatings, Ceram. Int. 46 (2020) 16886–16894. https://doi.org/10.1016/j.ceramint.2020.03.267.

[213] A. Roy, L. Mu, Y. Shi, Tribological properties of polyimide-graphene composite coatings at elevated temperatures, Prog. Org. Coat. 142 (2020) 105602. https://doi.org/10.1016/j.porgcoat.2020.105602.

[214] E. Thangavel, S. Ramasundaram, S. Pitchaimuthu, S.W. Hong, S.Y. Lee, S.-S. Yoo, D.-E. Kim, E. Ito, Y.S. Kang, Structural and tribological characteristics of poly(vinylidene fluoride)/functionalized graphene oxide nanocomposite thin films, Compos. Sci. Technol. 90 (2014) 187–192. https://doi.org/10.1016/j.compscitech.2013.11.007.

[215] Y. Shang, X. Wu, Y. Liu, Z. Jiang, Z. Wang, Z. Jiang, H. Zhang, Preparation of PEEK/MWCNTs composites with excellent mechanical and tribological properties, High Perform. Polym. (2018). https://doi.org/10.1177/0954008317750726.

[216] H.G. Prashantha Kumar, M. Anthony Xavior, Effect of graphene addition and

tribological performance of Al 6061/graphene flake composite, Tribol. - Mater. Surf. Interfaces 11 (2017) 88–97. https://doi.org/10.1080/17515831.2017.1329920.

[217] Y. Min, C.-L. Kim, D.-E. Kim, Tribological properties of the hierarchically structured graphene oxide composite coatings reinforced with polyvinyl alcohol, Wear 490–491 (2022) 204212. https://doi.org/10.1016/j.wear.2021.204212.

[218] Kavita, A.K. Singh, N. Shukla, D.K. Verma, B. Kumar, S. Singh, R.B. Rastogi, Polyaniline intercalated vanadium pentoxide nanosheets for the improvement of lubricity of base oil, Colloids Surf. Physicochem. Eng. Asp. 642 (2022) 128644. https://doi.org/10.1016/j.colsurfa.2022.128644.

[219] T. Bao, Z. Wang, Y. Zhao, Y. Wang, X. Yi, Improving tribological performance of epoxy composite by reinforcing with polyetheramine-functionalized graphene oxide, J. Mater. Res. Technol. 12 (2021) 1516–1529. https://doi.org/10.1016/j.jmrt.2021.03.091.

[220] Effect of graphene addition and tribological performance of Al 6061/graphene flake composite - H. G. Prashantha Kumar, M. Anthony Xavior, 2017, (n.d.). https://journals.sagepub.com/doi/full/10.1080/17515831.2017.1329920?casa_token=QSFJUWOU1RAAAAAA%3A5DE_FpjCT0w69nBIsGs4R-ZHiy03K3yXEra6BmzUMaHtDAmZUDCaDM2yWtToEx4S2NJfUjmpyLrV (accessed December 4, 2024).

[221] Z. Pan, L. He, L. Qiu, A.H. Korayem, G. Li, J.W. Zhu, F. Collins, D. Li, W.H. Duan, M.C. Wang, Mechanical properties and microstructure of a graphene oxide–cement composite, Cem. Concr. Compos. 58 (2015) 140–147. https://doi.org/10.1016/j.cemconcomp.2015.02.001.

[222] A.K. Pathak, M. Borah, A. Gupta, T. Yokozeki, S.R. Dhakate, Improved mechanical properties of carbon fiber/graphene oxide-epoxy hybrid composites, Compos. Sci. Technol. 135 (2016) 28–38. https://doi.org/10.1016/j.compscitech.2016.09.007.

[223] B.L. Dasari, M. Morshed, J.M. Nouri, D. Brabazon, S. Naher, Mechanical properties of graphene oxide reinforced aluminium matrix composites, Compos. Part B Eng. 145 (2018) 136–144. https://doi.org/10.1016/j.compositesb.2018.03.022.

[224] N.V. Medhekar, A. Ramasubramaniam, R.S. Ruoff, V.B. Shenoy, Hydrogen Bond Networks in Graphene Oxide Composite Paper: Structure and Mechanical Properties, ACS Nano 4 (2010) 2300–2306. https://doi.org/10.1021/nn901934u.

[225] F. Nazeer, Z. Ma, L. Gao, F. Wang, M.A. Khan, A. Malik, Thermal and mechanical properties of copper-graphite and copper-reduced graphene oxide composites, Compos. Part B Eng. 163 (2019) 77–85. https://doi.org/10.1016/j.compositesb.2018.11.004.

[226] S. Baradaran, E. Moghaddam, W.J. Basirun, M. Mehrali, M. Sookhakian, M. Hamdi, M.R.N. Moghaddam, Y. Alias, Mechanical properties and biomedical applications of a nanotube hydroxyapatite-reduced graphene oxide composite, Carbon 69 (2014) 32–45. https://doi.org/10.1016/j.carbon.2013.11.054.

[227] H. Asgharzadeh, M. Sedigh, Synthesis and mechanical properties of Al matrix composites reinforced with few-layer graphene and graphene oxide, J. Alloys Compd. 728 (2017) 47–62. https://doi.org/10.1016/j.jallcom.2017.08.268.

[228] A.B. Filizzola, J.L.N. Pereira, P.R. dos Santos, F. da S. Medeiros, S.Z.S. do Amparo, C.K.B. de Vasconcelos, G.G. Silva, Enhanced wear resistance of epoxy coatings on steel using graphene oxide, J. Coat. Technol. Res. 21 (2024) 215–228. https://doi.org/10.1007/s11998-023-00811-5.

[229] Z. Xu, L. Chen, X. Shi, Q. Zhang, A.M.M. Ibrahim, W. Zhai, J. Yao, Q. Zhu, Y. Xiao, Formation of Friction Layers in Graphene-Reinforced TiAl Matrix Self-Lubricating Composites, Tribol. Trans. 58 (2015) 668–678. https://doi.org/10.1080/10402004.2014.1002596.

[230] Y. Li, Q. Wang, T. Wang, G. Pan, Preparation and tribological properties of graphene oxide/nitrile rubber nanocomposites, J. Mater. Sci. 47 (2012) 730–738. https://doi.org/10.1007/s10853-011-5846-4.

[231] Z. Tai, Y. Chen, Y. An, X. Yan, Q. Xue, Tribological Behavior of UHMWPE Reinforced with Graphene Oxide Nanosheets, Tribol. Lett. 46 (2012) 55–63. https://doi.org/10.1007/s11249-012-9919-6.

[232] X.-J. Shen, X.-Q. Pei, Y. Liu, S.-Y. Fu, Tribological performance of carbon nanotube–graphene oxide hybrid/epoxy composites, Compos. Part B Eng. 57 (2014) 120–125. https://doi.org/10.1016/j.compositesb.2013.09.050.

[233] J.S. Bunch, S.S. Verbridge, J.S. Alden, A.M. van der Zande, J.M. Parpia, H.G. Craighead, P.L. McEuen, Impermeable Atomic Membranes from Graphene Sheets, Nano Lett. 8 (2008) 2458–2462. https://doi.org/10.1021/nl801457b.

[234] V. Berry, Impermeability of graphene and its applications, Carbon 62 (2013) 1–10. https://doi.org/10.1016/j.carbon.2013.05.052.

[235] N.-W. Pu, G.-N. Shi, Y.-M. Liu, X. Sun, J.-K. Chang, C.-L. Sun, M.-D. Ger, C.-Y. Chen, P.-C. Wang, Y.-Y. Peng, C.-H. Wu, S. Lawes, Graphene grown on stainless steel as a high-performance and ecofriendly anti-corrosion coating for polymer electrolyte membrane fuel cell bipolar plates, J. Power Sources 282 (2015) 248–256. https://doi.org/10.1016/j.jpowsour.2015.02.055.

[236] R.R. Nair, H.A. Wu, P.N. Jayaram, I.V. Grigorieva, A.K. Geim, Unimpeded Permeation of Water Through Helium-Leak–Tight Graphene-Based Membranes, Science 335 (2012) 442–444. https://doi.org/10.1126/science.1211694.

[237] D.C. Marcano, D.V. Kosynkin, J.M. Berlin, A. Sinitskii, Z. Sun, A. Slesarev, L.B. Alemany, W. Lu, J.M. Tour, Improved Synthesis of Graphene Oxide, ACS Nano 4 (2010) 4806–4814. https://doi.org/10.1021/nn1006368.

[238] D.C. Marcano, D.V. Kosynkin, J.M. Berlin, A. Sinitskii, Z. Sun, A.S. Slesarev, L.B. Alemany, W. Lu, J.M. Tour, Correction to Improved Synthesis of Graphene Oxide, ACS Nano 12 (2018) 2078–2078. https://doi.org/10.1021/acsnano.8b00128.

[239] D.C. Marcano, D.V. Kosynkin, J.M. Berlin, A. Sinitskii, Z. Sun, A. Slesarev, L.B. Alemany, W. Lu, J.M. Tour, Improved synthesis of graphene oxide, ACS Nano 4 (2010) 4806–4814.

[240] Correction to Improved Synthesis of Graphene Oxide | ACS Nano, (n.d.). https://pubs-acs-org.bham-ezproxy.idm.oclc.org/doi/full/10.1021/acsnano.8b00128 (accessed December 16, 2023).

[241] X. Li, Y. Zhao, W. Wu, J. Chen, G. Chu, H. Zou, Synthesis and characterizations of graphene–copper nanocomposites and their antifriction application, J. Ind. Eng. Chem. 20 (2014) 2043–2049. https://doi.org/10.1016/j.jiec.2013.09.029.

[242] Scherrer Equation - an overview | ScienceDirect Topics, (n.d.). https://www.sciencedirect.com/topics/materials-science/scherrer-equation (accessed December 14, 2023).

[243] K.S. Novoselov, V.I. Fal′ko, L. Colombo, P.R. Gellert, M.G. Schwab, K. Kim, A roadmap for graphene, Nature 490 (2012) 192–200. https://doi.org/10.1038/nature11458.

[244] B.C. Smith, Fundamentals of Fourier transform infrared spectroscopy, CRC press, 2011.

[245] D. Torres, L. Madriz, R. Vargas, B.R. Scharifker, Electrochemical formation of copper phosphide from aqueous solutions of Cu(II) and hypophosphite ions, Electrochimica Acta 354 (2020) 136705. https://doi.org/10.1016/j.electacta.2020.136705.

[246] J.C. Meyer, A.K. Geim, M.I. Katsnelson, K.S. Novoselov, T.J. Booth, S. Roth, The structure of suspended graphene sheets, Nature 446 (2007) 60–63. https://doi.org/10.1038/nature05545.

[247] S. Pei, H.-M. Cheng, The reduction of graphene oxide, Carbon 50 (2012) 3210–3228.

[248] S.Y. Toh, K.S. Loh, S.K. Kamarudin, W.R.W. Daud, Graphene production via electrochemical reduction of graphene oxide: synthesis and characterisation, Chem. Eng. J. 251 (2014) 422–434.

[249] A.K. Behera, A. Mallik, Ultrasound assisted electroplating of nano-composite thin film of Cu matrix with electrochemically in-house synthesized few layer graphene nano-sheets as reinforcement, J. Alloys Compd. 750 (2018) 587–598.

[250] H.L. Yu, Y. Xu, P.J. Shi, B.S. Xu, X.L. Wang, Q. Liu, H.M. Wang, Characterization and nano-mechanical properties of tribofilms using Cu nanoparticles as additives, Surf. Coat. Technol. 203 (2008) 28–34. https://doi.org/10.1016/j.surfcoat.2008.07.032.

[251] Y. Zhao, K. Feng, C. Yao, P. Nie, J. Huang, Z. Li, Microstructure and tribological properties of laser cladded self-lubricating nickel-base composite coatings containing nano-Cu and h-BN solid lubricants, Surf. Coat. Technol. 359 (2019) 485–494. https://doi.org/10.1016/j.surfcoat.2018.12.017.

[252] M. Terheci, Microscopic investigation on the origin of wear by surface fatigue in dry sliding, Mater. Charact. 45 (2000) 1–15. https://doi.org/10.1016/S1044-5803(00)00045-0.

[253] G. Meneghetti, L. Susmel, R. Tovo, High-cycle fatigue crack paths in specimens having different stress concentration features, Eng. Fail. Anal. 14 (2007) 656–672. https://doi.org/10.1016/j.engfailanal.2006.02.004.

[254] T. Sumigawa, T. Shishido, T. Murakami, T. Kitamura, Interface crack initiation due to nano-scale stress concentration, Mater. Sci. Eng. A 527 (2010) 4796–4803. https://doi.org/10.1016/j.msea.2010.04.002.

[255] N. Savjani, V.O. Mercadillo, D. Hodgeman, G. Paterakis, Y. Deng, C. Vallés, G. Anagnostopoulos, C. Galiotis, M.A. Bissett, I.A. Kinloch, Tribology of Copper Metal Matrix Composites Reinforced with Fluorinated Graphene Oxide Nanosheets: Implications for Solid Lubricants in Mechanical Switches, ACS Appl. Nano Mater. 6 (2023) 8202–8213. https://doi.org/10.1021/acsanm.3c00399.

[256] Y. Deng, A.D. Handoko, Y. Du, S. Xi, B.S. Yeo, In Situ Raman Spectroscopy of Copper and Copper Oxide Surfaces during Electrochemical Oxygen Evolution Reaction: Identification of CuIII Oxides as Catalytically Active Species, ACS Catal. 6 (2016) 2473–2481. https://doi.org/10.1021/acscatal.6b00205.

[257] A. V, K. Pavani, K. Mahesh, Corrosion Analysis of Friction Stir-Welded Brass-Brass and Copper-Copper Plates, J. Corros. Sci. Eng. 19 (2016).

[258] M. Galai, K. Dahmani, M. Ebn Touhami, R. Hsissou, F. Benhiba, M. Rbaa, M. Ouakki, R. Lachhab, S.M. Alharbi, Corrosion inhibition of brass electrode in 3% NaCl medium using novel quinoline derivatives based on D-glucose: Synthesis, characterization, and mechanistic insights through experimental and computational approaches, Mater. Sci. Eng. B 298 (2023) 116843. https://doi.org/10.1016/j.mseb.2023.116843.

[259] Z. Ahmad, CHAPTER 4 - TYPES OF CORROSION: Materials and Environments, in: Z. Ahmad (Ed.), Princ. Corros. Eng. Corros. Control, Butterworth-Heinemann, Oxford, 2006: pp. 120–270. https://doi.org/10.1016/B978-075065924-6/50005-2.

[260] G.A. EL-Mahdy, A.K.F. Dyab, A.M. Atta, H.A. Al-Lohedan, Brass Corrosion under a single droplet of NaCl, Int. J. Electrochem. Sci. 8 (2013) 9858–9867. https://doi.org/10.1016/S1452-3981(23)13018-5.

[261] M.B. Radovanović, Ž.Z. Tasić, M.B.P. Mihajlović, A.T. Simonović, M.M. Antonijević, Electrochemical and DFT studies of brass corrosion inhibition in 3% NaCl in the presence of environmentally friendly compounds, Sci. Rep. 9 (2019) 16081. https://doi.org/10.1038/s41598-019-52635-2.

[262] O. Kozaderov, K. Shikhaliev, C. Prabhakar, A. Tripathi, D. Shevtsov, A. Kruzhilin, E. Komarova, A. Potapov, I. Zartsyn, Y. Kuznetsov, Corrosion of α-Brass in Solutions Containing Chloride Ions and 3-Mercaptoalkyl-5-amino-1H-1,2,4-triazoles, Appl. Sci. 9 (2019) 2821. https://doi.org/10.3390/app9142821.

[263] A.M. Dimiev, S. Eigler, Graphene oxide: fundamentals and applications / edited by Ayrat M. Dimiev, Siegfried Eigler., John Wiley and Sons, Incorporated., Chichester, West Sussex, 2017. https://ebookcentral.proquest.com/lib/bham/detail.action?docID=4698010 (accessed January 15, 2024).

[264] A. Klechikov, J. Yu, D. Thomas, T. Sharifi, A. V. Talyzin, Structure of graphene oxide membranes in solvents and solutions, Nanoscale 7 (2015) 15374–15384. https://doi.org/10.1039/C5NR04096E.

[265] S.A. Hasan, J.L. Rigueur, R.R. Harl, A.J. Krejci, I. Gonzalo-Juan, B.R. Rogers, J.H. Dickerson, Transferable Graphene Oxide Films with Tunable Microstructures, ACS Nano 4 (2010) 7367–7372. https://doi.org/10.1021/nn102152x.

[266] W. He, L. Zhu, H. Chen, H. Nan, W. Li, H. Liu, Y. Wang, Electrophoretic deposition of graphene oxide as a corrosion inhibitor for sintered NdFeB, Appl. Surf. Sci. 279 (2013) 416–423. https://doi.org/10.1016/j.apsusc.2013.04.130.

[267] C. Örnek, C. Leygraf, J. Pan, Passive film characterisation of duplex stainless steel using scanning Kelvin probe force microscopy in combination with electrochemical

measurements, Npj Mater. Degrad. 3 (2019) 1–8. https://doi.org/10.1038/s41529-019-0071-8.

[268] C.-O.A. Olsson, D. Landolt, Passive films on stainless steels—chemistry, structure and growth, Electrochimica Acta 48 (2003) 1093–1104. https://doi.org/10.1016/S0013-4686(02)00841-1.

[269] L.J. Durney, Electroplating engineering handbook., 4th ed. / edited by Lawrence J. Durney., Wokingham : Van Rostrand Reinhold, New York, 1984.

[270] X.-Y. Peng, X.-X. Liu, D. Diamond, K.T. Lau, Synthesis of electrochemically-reduced graphene oxide film with controllable size and thickness and its use in supercapacitor, Carbon 49 (2011) 3488–3496. https://doi.org/10.1016/j.carbon.2011.04.047.

[271] V. Agarwal, P.B. Zetterlund, Strategies for reduction of graphene oxide – A comprehensive review, Chem. Eng. J. 405 (2021) 127018. https://doi.org/10.1016/j.cej.2020.127018.

[272] S. Houam, A.M. Affoune, I. Atek, F. Kesri, R. Saad Guermeche, M.L. Chelaghmia, M. Nacef, O. Khelifi, C.E. Banks, Determination of the standard rate constant for soluble-soluble quasi-reversible electrochemical systems by linear sweep voltammetry: Application to the electrochemical oxidation on screen-printed graphite electrodes, Electrochimica Acta 449 (2023) 142200. https://doi.org/10.1016/j.electacta.2023.142200.

[273] N. Bisht, M. Patel, N. Dwivedi, P. Kumar, D.P. Mondal, A.K. Srivastava, C. Dhand, Bio-inspired polynorepinephrine based nanocoatings for reduced graphene oxide/gold nanoparticles composite for high-performance biosensing of Mycobacterium tuberculosis, Environ. Res. 227 (2023) 115684. https://doi.org/10.1016/j.envres.2023.115684.

[274] S. Ahadi, Y. Ghorbani, A. Dolati, Electrochemical characterization of 3D N-rGO with cobalt phthalocyanine as redox mediator toward oxygen reduction reaction, J. Appl. Electrochem. 53 (2023) 2197–2212. https://doi.org/10.1007/s10800-023-01918-8.

[275] F. Mazzara, B. Patella, G. Aiello, C. Sunseri, R. Inguanta, Ascorbic Acid determination using linear sweep voltammetry on flexible electrode modified with gold nanoparticles and reduced graphene oxide, in: 2020 IEEE 20th Mediterr. Electrotech. Conf. MELECON, 2020: pp. 406–410. https://doi.org/10.1109/MELECON48756.2020.9140684.

[276] Y. Ma, J. Han, M. Wang, X. Chen, S. Jia, Electrophoretic deposition of graphene-based materials: A review of materials and their applications, J. Materiomics 4 (2018) 108–120. https://doi.org/10.1016/j.jmat.2018.02.004.

[277] L.P. Yeo, T.D. Nguyen, H. Ling, Y. Lee, D. Mandler, S. Magdassi, A.I.Y. Tok, Electrophoretic deposition of reduced graphene oxide thin films for reduction of cross-sectional heat diffusion in glass windows, J. Sci. Adv. Mater. Devices 4 (2019) 252–259. https://doi.org/10.1016/j.jsamd.2019.04.002.

[278] Z. Ren, N. Meng, K. Shehzad, Y. Xu, S. Qu, B. Yu, J.K. Luo, Mechanical properties of nickel-graphene composites synthesized by electrochemical deposition, Nanotechnology 26 (2015) 065706. https://doi.org/10.1088/0957-4484/26/6/065706.

[279] M. Aghaee Malayeri, H. Koohestani, M. Tajally, Improving the properties of nickel/graphene oxide coated copper plate by changing the electroplating process conditions, Results Eng. 18 (2023) 101167. https://doi.org/10.1016/j.rineng.2023.101167.

[280] N. Sharma, Mohd. Arif, S. Monga, Mohd. Shkir, Y.K. Mishra, A. Singh, Investigation of bandgap alteration in graphene oxide with different reduction routes, Appl. Surf. Sci. 513 (2020) 145396. https://doi.org/10.1016/j.apsusc.2020.145396.

[281] A.G. Marrani, A. Motta, R. Schrebler, R. Zanoni, E.A. Dalchiele, Insights from experiment and theory into the electrochemical reduction mechanism of graphene oxide, Electrochimica Acta 304 (2019) 231–238. https://doi.org/10.1016/j.electacta.2019.02.108.

[282] H. Algul, M. Tokur, S. Ozcan, M. Uysal, T. Cetinkaya, H. Akbulut, A. Alp, The effect of graphene content and sliding speed on the wear mechanism of nickel–graphene nanocomposites, Appl. Surf. Sci. 359 (2015) 340–348. https://doi.org/10.1016/j.apsusc.2015.10.139.

[283] X. You, A. Yan, Y. Liu, Q. Zhao, Y. Fan, Y. Liu, C. Li, J. Yi, A comparison study of the strengthening effect of carbon nanomaterial reinforcements in the 3D skeleton-reinforced copper matrix composites, Diam. Relat. Mater. 141 (2024) 110580. https://doi.org/10.1016/j.diamond.2023.110580.

[284] H. Akbulut, G. Hatipoglu, H. Algul, M. Tokur, M. Kartal, M. Uysal, T. Cetinkaya, Co-deposition of Cu/WC/graphene hybrid nanocomposites produced by electrophoretic deposition, Surf. Coat. Technol. 284 (2015) 344–352. https://doi.org/10.1016/j.surfcoat.2015.07.080.

[285] Y.J. Mai, M.P. Zhou, H.J. Ling, F.X. Chen, W.Q. Lian, X.H. Jie, Surfactant-free electrodeposition of reduced graphene oxide/copper composite coatings with enhanced wear resistance, Appl. Surf. Sci. 433 (2018) 232–239. https://doi.org/10.1016/j.apsusc.2017.10.014.

[286] S. Fu, X. Chen, P. Liu, Preparation of CNTs/Cu composites with good electrical conductivity and excellent mechanical properties, Mater. Sci. Eng. A 771 (2020) 138656.

https://doi.org/10.1016/j.msea.2019.138656.

[287] H. Deng, J. Yi, C. Xia, Y. Yi, Mechanical properties and microstructure characterization of well-dispersed carbon nanotubes reinforced copper matrix composites, J. Alloys Compd. 727 (2017) 260–268. https://doi.org/10.1016/j.jallcom.2017.08.131.

[288] P. Yang, X. You, J. Yi, D. Fang, R. Bao, T. Shen, Y. Liu, J. Tao, C. Li, S. Tan, S. Guo, Simultaneous achievement of high strength, excellent ductility, and good electrical conductivity in carbon nanotube/copper composites, J. Alloys Compd. 752 (2018) 431–439. https://doi.org/10.1016/j.jallcom.2018.03.341.

[289] S.K. Ghosh, A.K. Grover, G.K. Dey, M.K. Totlani, Nanocrystalline Ni–Cu alloy plating by pulse electrolysis, Surf. Coat. Technol. 126 (2000) 48–63. https://doi.org/10.1016/S0257-8972(00)00520-X.

[290] S. Kaiser, A. Ahmed, R. Sharmila, M.S. Kaiser, Effect of Long Used Machine Oil on the Tribological Behaviour of Cu-Based Gear Materials, Appl. Mech. Mater. 919 (2024) 139–154. https://doi.org/10.4028/p-DGl3Xv.

[291] P.L. Menezes, Kishore, S.V. Kailas, Influence of roughness parameters on coefficient of friction under lubricated conditions, Sadhana 33 (2008) 181–190. https://doi.org/10.1007/s12046-008-0011-8.

[292] M. Sedlaček, B. Podgornik, J. Vižintin, Influence of surface preparation on roughness parameters, friction and wear, Wear 266 (2009) 482–487. https://doi.org/10.1016/j.wear.2008.04.017.

[293] B. Bachchhav, H. Bagchi, Effect of surface roughness on friction and lubrication regimes, Mater. Today Proc. 38 (2021) 169–173. https://doi.org/10.1016/j.matpr.2020.06.252.

[294] A. Moshkovich, V. Perfilyev, I. Lapsker, L. Rapoport, Friction, wear and plastic deformation of Cu and α/β brass under lubrication conditions, Wear 320 (2014) 34–40. https://doi.org/10.1016/j.wear.2014.08.016.

[295] Y.H. Zhao, X.Z. Liao, Y.T. Zhu, Z. Horita, T.G. Langdon, Influence of stacking fault energy on nanostructure formation under high pressure torsion, Mater. Sci. Eng. A 410–411 (2005) 188–193. https://doi.org/10.1016/j.msea.2005.08.074.

[296] L. Meshi, S. Samuha, S.R. Cohen, A. Laikhtman, A. Moshkovich, V. Perfilyev, I. Lapsker, L. Rapoport, Dislocation structure and hardness of surface layers under friction of copper in different lubricant conditions, Acta Mater. 59 (2011) 342–348.

https://doi.org/10.1016/j.actamat.2010.09.038.

[297] Y. Deng, A.D. Handoko, Y. Du, S. Xi, B.S. Yeo, In Situ Raman Spectroscopy of Copper and Copper Oxide Surfaces during Electrochemical Oxygen Evolution Reaction: Identification of CuIII Oxides as Catalytically Active Species, ACS Catal. 6 (2016) 2473–2481. https://doi.org/10.1021/acscatal.6b00205.

[298] A.R. Marlinda, G.S.H. Thien, M. Shahid, T.Y. Ling, A. Hashem, K.-Y. Chan, M.R. Johan, Graphene as a Lubricant Additive for Reducing Friction and Wear in Its Liquid-Based Form, Lubricants 11 (2023) 29. https://doi.org/10.3390/lubricants11010029.

[299] A.R. Marlinda, G.S.H. Thien, M. Shahid, T.Y. Ling, A. Hashem, K.-Y. Chan, M.R. Johan, Graphene as a Lubricant Additive for Reducing Friction and Wear in Its Liquid-Based Form, Lubricants 11 (2023) 29. https://doi.org/10.3390/lubricants11010029.

[300] D. Berman, A. Erdemir, A.V. Zinovev, A.V. Sumant, Nanoscale friction properties of graphene and graphene oxide, Diam. Relat. Mater. 54 (2015) 91–96. https://doi.org/10.1016/j.diamond.2014.10.012.

[301] A. Klemenz, L. Pastewka, S.G. Balakrishna, A. Caron, R. Bennewitz, M. Moseler, Atomic Scale Mechanisms of Friction Reduction and Wear Protection by Graphene, Nano Lett. 14 (2014) 7145–7152. https://doi.org/10.1021/nl5037403.

[302] X. Zeng, Y. Peng, H. Lang, A novel approach to decrease friction of graphene, Carbon 118 (2017) 233–240. https://doi.org/10.1016/j.carbon.2017.03.042.

[303] A.A. Abdel-Rehim, S. Akl, S. Elsoudy, Investigation of the Tribological Behavior of Mineral Lubricant Using Copper Oxide Nano Additives, Lubricants 9 (2021) 16. https://doi.org/10.3390/lubricants9020016.

[304] J. Zhao, G. Yang, Y. Zhang, S. Zhang, C. Zhang, C. Gao, P. Zhang, Controllable synthesis of different morphologies of CuO nanostructures for tribological evaluation as water-based lubricant additives, Friction 9 (2021) 963–977. https://doi.org/10.1007/s40544-020-0382-3.

[305] V. Berry, Impermeability of graphene and its applications, Carbon 62 (2013) 1–10. https://doi.org/10.1016/j.carbon.2013.05.052.

[306] Y. Su, V.G. Kravets, S.L. Wong, J. Waters, A.K. Geim, R.R. Nair, Impermeable barrier films and protective coatings based on reduced graphene oxide, Nat. Commun. 5 (2014) 4843. https://doi.org/10.1038/ncomms5843.

[307] M.R. Hasan, B. Kim, Molecular transportation phenomena of simple liquids through a nanoporous graphene membrane, Phys. Rev. E 102 (2020) 033110. https://doi.org/10.1103/PhysRevE.102.033110.

[308] Z. Ahmad, CHAPTER 4 - TYPES OF CORROSION: Materials and Environments, in: Z. Ahmad (Ed.), Princ. Corros. Eng. Corros. Control, Butterworth-Heinemann, Oxford, 2006: pp. 120–270. https://doi.org/10.1016/B978-075065924-6/50005-2.

[309] A.Y. Nalivaiko, A.N. Arnautov, S.V. Zmanovsky, A.A. Gromov, Electrochemical synthesis of Al–Al2O3 composites for selective laser melting, Mater. Res. Express 6 (2019) 116580. https://doi.org/10.1088/2053-1591/ab493d.